

AD-A136 242

MICROHARDNESS FRICTION AND WEAR OF SIC AND Si3N4  
MATERIALS AS A FUNCTION OF (U) CAMBRIDGE UNIV (ENGLAND)  
DEPT OF METALLURGY AND MATERIALS SCI.

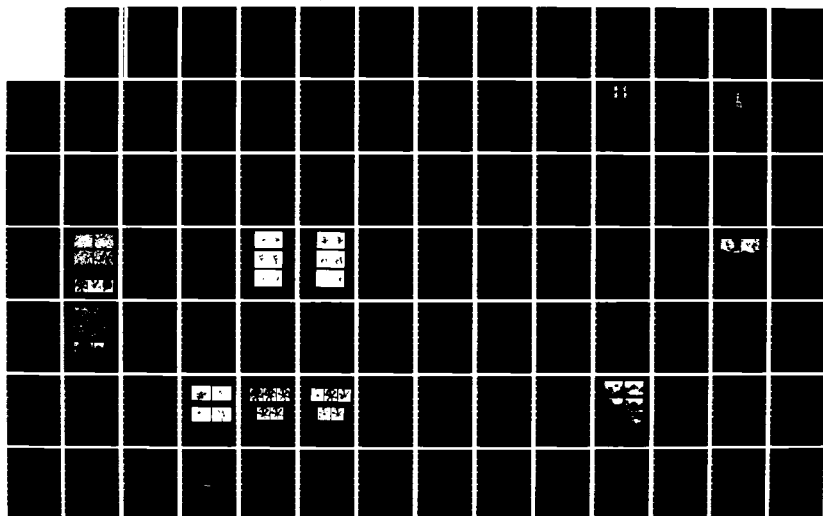
1/3

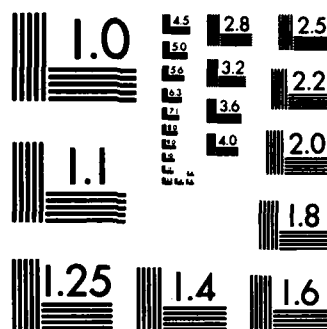
UNCLASSIFIED

M G NAYLOR ET AL. OCT 81 DA-ERO-78-G-010

F/G 11/2

NL





MICROCOPY RESOLUTION TEST CHART  
NATIONAL BUREAU OF STANDARDS-1963-A

12

AD

MICROHARDNESS, FRICTION AND WEAR OF SiC AND  
Si<sub>3</sub>N<sub>4</sub> MATERIALS AS A FUNCTION OF LOAD,  
TEMPERATURE AND ENVIRONMENT

THIRD ANNUAL TECHNICAL REPORT

By

M.G.S. Naylor and T.F. Page

October 1981

EUROPEAN RESEARCH OFFICE  
United States Army,  
London, NW1 5TH,  
England.

GRANT NUMBER DA-ERO-78-G-010

DTIC  
ELECTE  
DEC 22 1983  
S  
A

University of Cambridge,  
England.

Approved for Public Release; distribution unlimited

83 12 22 001

AD-A236242

DTIC FILE COPY

UNCLASSIFIED

i

SECURITY CLASSIFICATION OF THIS PAGE (When Data Entered)

REPORT DOCUMENTATION PAGE		READ INSTRUCTIONS BEFORE COMPLETING FORM
1. REPORT NUMBER	2. GOVT ACCESSION NO.	3. RECIPIENT'S CATALOG NUMBER
4. TITLE (and Subtitle) MICROHARDNESS, FRICTION AND WEAR OF SiC AND Si <sub>3</sub> N <sub>4</sub> MATERIALS AS A FUNCTION OF LOAD, TEMPERATURE AND ENVIRONMENT.		5. TYPE OF REPORT & PERIOD COVERED Annual Technical Report 1 October 80 - 30 Sep. 81
		6. PERFORMING ORG. REPORT NUMBER
7. AUTHOR(s)  M.G.S. NAYLOR and T.F. PAGE		8. CONTRACT OR GRANT NUMBER(s)  DAERO-78-G-010
9. PERFORMING ORGANIZATION NAME AND ADDRESS  Department of Metallurgy and Materials Science, University of Cambridge, Pembroke St., Cambridge.		10. PROGRAM ELEMENT, PROJECT, TASK AREA & WORK UNIT NUMBERS  6.11.02A 1T161102BH57-04
11. CONTROLLING OFFICE NAME AND ADDRESS		12. REPORT DATE October 1981
		13. NUMBER OF PAGES 258
14. MONITORING AGENCY NAME & ADDRESS (if different from Controlling Office)		15. SECURITY CLASS. (of this report) UNCLASSIFIED
		15a. DECLASSIFICATION/DOWNGRADING SCHEDULE
16. DISTRIBUTION STATEMENT (of this Report)  Approved for public release: distribution unlimited.		
17. DISTRIBUTION STATEMENT (of the abstract entered in Block 20, if different from Report)		
18. SUPPLEMENTARY NOTES		
19. KEY WORDS (Continue on reverse side if necessary and identify by block number) SiC, Si <sub>3</sub> N <sub>4</sub> , Si, sialon, B <sub>4</sub> C, hardness, microhardness, temperature dependence of hardness, indentation plasticity, indentation fracture, fracture toughness, crack nucleation, wear of ceramics, load sensitivity of hardness, microstruc- tural control of hardness, microstructural control of fracture, impurity effects on plasticity.		
20. ABSTRACT (Continue on reverse side if necessary and identify by block number) Plasticity and fracture processes in engineering ceramics based on silicon carbide, silicon nitride, a sialon and boron carbide have been investigated as a function of temperature (in the range 25 ~ 1000°C) using indentation micro- hardness techniques. The effects of specimen microstructure on indentation processes were determined by using materials formed by a wide range of fabrication routes (sintering, hot-pressing, reaction-bonding and pyrolytic deposition) and comparison was made with the behaviour of single crystals		

cont'd

UNCLASSIFIED

SECURITY CLASSIFICATION OF THIS PAGE(When Data Entered)

>(SiC and Si). Microstructural characterization was carried out by light microscopy, electron-optical and X-ray techniques.

The variation of Vickers and, in some cases, Knoop microhardness with temperature was measured, and deformation structures around indentations were examined optically and by scanning electron microscopy. Indentation plasticity in silicon carbide was further investigated by measuring Knoop hardness anisotropy on basal and non-basal faces of single crystal SiC at various temperatures. The effect of dopant on hardness was investigated for Si and SiC.

Indentation fracture was found to become more severe with increasing temperature for most materials, due to increased residual stresses around indentations, in turn caused by increasing plasticity. Currently-available indentation fracture mechanics models have been used to determine fracture toughness ( $K_{IC}$ ) values, which in most cases remained constant with changing temperature.

The resistance of each material to crack initiation ( $K_{IC}$  measures the resistance to crack propagation) was determined as a function of temperature and specimen microstructure, in terms of the critical values of applied load ( $P^*$ ) required to form cracks.  $P^*$  was found to increase with increasing temperature, sometimes sharply.

The relevance of indentation plasticity and fracture to abrasive and erosive wear processes in ceramics is discussed, and the concept of "brittleness" is reviewed, both in general terms and in the specific case of abrasive/erosive wear resistance. The dependence of wear resistance on temperature, contact load and specimen microstructure is predicted.

UNCLASSIFIED

SECURITY CLASSIFICATION OF THIS PAGE(When Data Entered)

### Acknowledgements

I wish to thank Dr. T.F. Page for asking the right questions and for pointing me at (hopefully) some of the right answers. I also acknowledge many useful discussions with past and present members of the Ceramics Group in Cambridge, and especially with Dr. E.H. Yoffe. Thanks are also due to Prof. R.W.K. Honeycombe for provision of laboratory facilities and to the assistant staff of the Department of Metallurgy and Materials Science (especially Messrs. B. Barber, J. Reich, M. Stocker and Ms. V. Kohler) for invaluable technical assistance. I am grateful to Dr. K. Gove for advice and co-operation concerning the construction of the hot-hardness tester, which was funded by the Science Research Council. The help and sponsorship of the European Research Office of the U.S. Army (Grant No. DAERO-78-G-010) is also gratefully acknowledged. For supplies of specimen materials I thank Dr. R.N. Katz (AMMRC, Watertown, U.S.A.), Mr. P. Kennedy (U.K.A.E.A., Springfields Division), Dr. D.J. Godfrey, (AMTE, Holton Heath), Dr. R.J. Lumby (Lucas Group Services Ltd., Solihull), Prof. H. Suzuki (Tokyo Institute of Technology), Le Carbone (G.B.) Ltd. and Texas Instruments (U.K.) Ltd. Finally, I am grateful to Mrs. E. Palmer and Mrs. P. Summerfield for help with the typing of this thesis.

M.G.S. Naylor: Ph.D. Thesis.  
Department of Metallurgy & Materials Science,  
University of Cambridge.

August 1982



Accession For	
NTIS - NSAS	
DTIC - R	
Unpublished	
Classification	
Distribution/	
Availability Codes	
Avail and/or	
Special	

THE EFFECTS OF TEMPERATURE ON HARDNESS AND WEAR PROCESSES IN  
ENGINEERING CERAMICS

M.G.S. NAYLOR

SUMMARY

Plasticity and fracture processes in engineering ceramics based on silicon carbide, silicon nitride, a sialon and boron carbide have been investigated as a function of temperature (in the range 25 - 1000°C) using indentation microhardness techniques.

The effects of specimen microstructure on indentation processes were determined by using materials formed by a wide range of fabrication routes (sintering, hot-pressing, reaction-bonding and pyrolytic deposition) and comparison was made with the behaviour of single crystals (SiC and Si). Microstructural characterization was carried out by light microscopy, electron optical and X-ray techniques.

The variation of Vickers and, in some cases, Knoop microhardness with temperature was measured, and deformation structures around indentations were examined optically and by scanning electron microscopy. Indentation plasticity in silicon carbide was further investigated by measuring Knoop hardness anisotropy on basal and non-basal faces of single crystal SiC at various temperatures. The effect of dopant on hardness was investigated for Si and SiC.

Indentation fracture was found to become more severe with increasing temperature for most materials, due to increased residual stresses around indentations, in turn caused by increasing plasticity. Currently-available indentation fracture mechanics models have been used to determine fracture toughness ( $K_{IC}$ ) values, which in most cases remained constant with changing temperature.

The resistance of each material to crack initiation ( $K_{IC}$  measures the resistance to crack propagation) was determined as a function of temperature and specimen microstructure, in terms of the critical values of applied load ( $P^*$ ) required to form cracks.  $P^*$  was found to increase with increasing temperature, sometimes sharply.

The relevance of indentation plasticity and fracture to abrasive and erosive wear processes in ceramics is discussed, and the concept of "brittleness" is reviewed, both in general terms and in the specific case of abrasive/erosive wear resistance. The dependence of wear resistance on temperature, contact load and specimen microstructure is predicted.

## CONTENTS

Preface	i
Acknowledgements	iii
Summary	iv
Contents	v
List of Figures	ix
List of Tables	xii

<u>CHAPTER 1</u>	<u>INTRODUCTION</u>	1
1.1	GENERAL AIMS OF THE PROJECT	1
1.2	ENGINEERING CERAMICS	2
1.2.1	The Need for 'Special' Ceramics	2
1.2.2	Properties and Applications of 'Special' Ceramics	3
1.2.2.1	Silicon Carbide	3
1.2.2.2	Silicon Nitride	5
1.2.2.3	Sialon	6
1.2.2.4	Boron Carbide	6
1.2.3	Crystal Structures	7
1.2.3.1	Silicon Carbide	7
1.2.3.2	Silicon Nitride	8
1.2.3.3	Sialon	9
1.2.3.4	Boron Carbide	10
1.2.4	Fabrication Routes	12
1.2.4.1	Sintering	12
1.2.4.2	Hot-Pressing	13
1.2.4.3	Reaction-Bonding	14
1.2.4.4	Vapour Deposition	15
1.2.5	Grain Boundary Engineering	16
1.3	PROJECT PHILOSOPHY	18
1.4	REFERENCES	20

<u>CHAPTER 2</u>	<u>EXPERIMENTAL</u>	24
2.1	SPECIMEN PREPARATION	24
2.2	SCANNING ELECTRON MICROSCOPY	26
2.2.1	Backscattered (Primary) Electron Imaging	26
2.2.2	Secondary Electron Imaging	29
2.2.3	Stereoscopic Imaging	30

2.3	MICROSTRUCTURAL CHARACTERIZATION	33
2.3.1	Silicon	33
2.3.2	Silicon Carbide	33
2.3.2.1	Single Crystal SiC	33
2.3.2.2	Hot-Pressed SiC	33
2.3.2.3	Sintered SiC	34
2.3.2.4	Reaction-Bonded SiC	34
2.3.3	Silicon Nitride	35
2.3.3.1	Pyrolytically-Deposited $\text{Si}_3\text{N}_4$	35
2.3.3.2	Hot-Pressed $\text{Si}_3\text{N}_4$	35
2.3.3.3	Reaction-Bonded $\text{Si}_3\text{N}_4$	36
2.3.4	Sialon	36
2.3.5	Boron Carbide	36
2.4	INDENTATION TECHNIQUES	38
2.5	APPENDIX: SECONDARY ELECTRON SEM CONTRAST IN 'REFEL'	41
	REACTION-BONDED SiC	
2.6	REFERENCES	45
CHAPTER 3	<u>INDENTATION PLASTICITY</u>	47
3.1	PLASTICITY IN BRITTLE MATERIALS	47
3.1.1	Grain Processes	47
3.1.2	Grain Boundary Processes	49
3.2	HARDNESS AND YIELD STRESS	51
3.3	INDENTATION PLASTICITY IN BRITTLE MATERIALS	55
3.3.1	Experimental Hot-Hardness Behaviour of Single Crystals	56
3.3.2	Theoretical Interpretation: the Role of Slip	69
3.3.2.1	Deformation Maps	71
3.3.2.2	The Peierls' Stress	74
3.3.2.3	Surface Slip Steps at High Temperatures	77
3.3.3	The Low-Temperature Regime: Athermal Deformation Mechanisms	79
3.3.4	Summary	83
3.4	HARDNESS ANISOTROPY OF SINGLE CRYSTALS	84
3.4.1	Effective Resolved Shear Stress Models	84
3.4.2	Temperature Effects	87
3.4.3	Results for Silicon Carbide	89
3.4.4	Summary	97

3.5	DOPANT EFFECTS ON PLASTICITY	99
3.5.1	Theories	99
3.5.2	Results for {111} Silicon	100
3.5.3	Results for Silicon Carbide	102
3.5.4	Conclusions	103
3.6	THE EFFECTS OF MICROSTRUCTURE ON HOT-HARDNESS OF POLYCRYSTALLINE CERAMICS	104
3.6.1	Results for Silicon Carbide	104
3.6.2	Results for Silicon Nitride	109
3.6.3	Results for Sialon	112
3.6.4	Results for Boron Carbide	112
3.6.5	The Effects of Grain Size	117
3.6.6	The Effects of Grain Boundary Phases	120
3.6.7	The Effects of Porosity	121
3.6.8	Summary	125
3.7	INDENTATION SIZE EFFECTS	126
3.7.1	The Meyer Index	126
3.7.2	Theoretical Interpretations	127
3.7.3	Temperature Effects	129
3.7.4	The Effects of Surface Abrasion Damage	132
3.8	INDENTATION CREEP	135
3.8.1	Theoretical Analysis	135
3.8.2	Results for {111} Silicon	137
3.9	EFFECTS OF CHEMICAL ENVIRONMENT	141
3.10	CONCLUSIONS	142
3.11	REFERENCES	145
<u>CHAPTER 4</u>	<u>CRACK PROPAGATION</u>	154
4.1	BRITTLE FRACTURE	154
4.2	INDENTATION FRACTURE	157
4.2.1	Crack Geometries	157
4.2.2	Elastic Stress Fields	159
4.2.3	Residual Stress	161
4.3	INDENTATION FRACTURE MECHANICS	164
4.3.1	The Dependence of Crack Size on Contact Load	164
4.3.2	Fracture Toughness	167
4.4	TEMPERATURE EFFECTS	170
4.4.1	The Variation of Crack Sizes with Temperature	170
4.4.2	The Variation of Fracture Toughness with Temperature	180
4.4.3	Discussion	185

4.5	MICROSTRUCTURAL EFFECTS	186
4.5.1	Fracture of Single Crystals	186
4.5.2	Fracture of Polycrystalline Silicon Carbides	191
4.5.3	Fracture of Polycrystalline Silicon Nitrides	198
4.5.4	Fracture of Polycrystalline Sialon	204
4.5.5	Fracture of Polycrystalline Boron Carbide	204
4.5.6	Microstructural Control of Fracture Toughness	204
4.6	SUMMARY	207
4.7	REFERENCES	209
<u>CHAPTER 5</u>	<u>CRACK INITIATION</u>	212
5.1	INTRODUCTION	212
5.2	CRACK NUCLEATION THEORIES	212
5.3	TEMPERATURE EFFECTS	215
5.4	MICROSTRUCTURAL EFFECTS	219
5.5	CONCLUSIONS	221
5.6	REFERENCES	223
<u>CHAPTER 6</u>	<u>FRICTION AND WEAR</u>	224
6.1	INTRODUCTION	224
6.2	FRICTION	224
6.3	WEAR MODELS	227
6.3.1	Adhesive Wear	227
6.3.2	Abrasive Wear	228
6.3.3	Corrosive Wear	229
6.3.4	Surface Fatigue Wear	230
6.3.5	Delamination	231
6.3.6	Erosion	232
6.4	ABRASIVE WEAR OF CERAMICS	234
6.4.1	The Fracture-Controlled Wear Regime	235
6.4.2	The Plasticity-Controlled Wear Regime	235
6.5	APPLICATION OF QUASI-STATIC INDENTATION RESULTS	237
6.5.1	Friction	237
6.5.2	The Plasticity-Controlled Wear Regime	238
6.5.3	The Fracture-Controlled Wear Regime	239
6.6	REFERENCES	248
<u>CHAPTER 7</u>	<u>CONCLUSIONS</u>	252
7.1	SUMMARY OF HOT-HARDNESS RESULTS	252
7.2	SUMMARY OF INDENTATION FRACTURE RESULTS	254
7.3	SUGGESTIONS FOR FURTHER WORK	256

LIST OF FIGURES

Fig. 1	The crystal structures of four common polytypes of SiC.	9
Fig. 2	The crystal structures of $\alpha$ - and $\beta$ -Si <sub>3</sub> N <sub>4</sub> .	9
Fig. 3	The crystal structure of B <sub>4</sub> C.	11
Fig. 4	Optical and scanning electron micrographs of 'REFEL' reaction-bonded SiC.	28
Fig. 5	Selected area channelling patterns for {111} Si, (0001) SiC and {1010} SiC.	28
Fig. 6	Stereo pair SEM images of Vickers indentations in various materials.	31
Fig. 7	The temperature/environment-controlled microhardness tester.	39
Fig. 8	Secondary electron SEM images of 'REFEL' reaction-bonded silicon carbides with controlled additions of various impurities.	42
Fig. 9	The expanding spherical cavity model for indentation of elastic/plastic solids.	53
Fig. 10	The variation of Vickers hardness with temperature for n-type {111} single crystal silicon.	57
Fig. 11	Slip activity around Vickers indentations in {111} single crystal silicon as a function of temperature ( as revealed by Nomarski differential interference contrast ).	58
Fig. 12	Selected area electron channelling patterns from regions around room temperature and 800°C Vickers indentations in {111} single crystal silicon.	59
Fig. 13	The variation of Vickers and Knoop hardness with temperature for single crystals of SiC.	62
Fig. 14	Slip activity around 800°C Knoop indentations in single crystal SiC as a function of crystallographic orientation ( Nomarski differential interference contrast ).	65
Fig. 15	Activation energy plots of the hot-hardness data of Niihara and Hirai for single crystal $\alpha$ -Si <sub>3</sub> N <sub>4</sub> at four different indenter:crystal orientations.	68
Fig. 16	Deformation mechanism maps for MgO of grain size 10 $\mu$ m and Si of grain size 100 $\mu$ m.	72

Fig. 17	Knoop hardness anisotropy of $\{0001\}$ single crystals of SiC at room temperature and 800°C.	90
Fig. 18	Knoop hardness anisotropy of $\{10\bar{1}0\}$ single crystal SiC at room temperature and 800°C.	92
Fig. 19	Knoop hardness anisotropy of $\{11\bar{2}0\}$ single crystal SiC at room temperature, 400°C and 800°C.	93
Fig. 20	Predicted hardness anisotropies for various crystal sections of $\alpha$ -SiC and for various slip systems.	95
Fig. 21	A schematic interpretation of the variation in critical temperature $T_c$ with indenter orientation on single crystal SiC.	98
Fig. 22	The variation of Vickers hardness with temperature for single crystal and polycrystalline forms of SiC.	105
Fig. 23	The variation of Knoop hardness with temperature for single crystal and polycrystalline forms of SiC.	108
Fig. 24	The variation of Vickers hardness with temperature for polycrystalline forms of $Si_3N_4$ .	110
Fig. 25	The variation of Vickers hardness with temperature for a sintered sialon.	113
Fig. 26	The variation of Vickers hardness with temperature for two forms of sintered $B_4C$ .	114
Fig. 27	Vickers indentations in porous materials.	122
Fig. 28	Indentation creep in $\{111\}$ single crystal silicon at 600°C, 700°C and 800°C.	138
Fig. 29	Schematic diagrams of crack geometries formed by Vickers indentations.	158
Fig. 30	The Boussinesq elastic stress field: stress trajectories and contours of principal normal stresses.	160
Fig. 31	Surface hoop stress distributions ( elastic, plastic and residual ) proposed by Evans for indentation of brittle materials.	163
Fig. 32	Radial and lateral crack radii as functions of temperature and load for $\{111\}$ single crystal silicon.	171
Fig. 33	Radial crack radius as a function of temperature and load for SiC materials.	172
Fig. 34	Radial crack radius as a function of temperature and load for $Si_3N_4$ materials.	175

Fig. 35	Radial crack radius as a function of temperature and load for a sintered sialon.	177
Fig. 36	Radial crack radius as a function of temperature and load for two forms of sintered $B_4C$ .	178
Fig. 37	Vickers indentations made at various temperatures on {111} single crystal Si with one indenter axis parallel to $\langle 1\bar{1}0 \rangle$	187
Fig. 38	Fracture around Knoop and Vickers indentations on (0001) single crystal SiC with one indenter axis parallel to $\langle 11\bar{2}0 \rangle$	190
Fig. 39	Fracture around Knoop and Vickers indentations in Norton NC203 hot-pressed SiC.	192
Fig. 40	Fracture around Vickers indentations in Carborundum sintered $\alpha$ -SiC.	194
Fig. 41	Fracture around Vickers indentations in 'Suzuki' sintered $\beta$ -SiC.	195
Fig. 42	Fracture around Knoop and Vickers indentations in 'REFEL' reaction-bonded SiC.	196
Fig. 43	Fracture around Vickers indentations in pyrolytically-deposited $Si_3N_4$	199
Fig. 44	Fracture around Vickers indentations in Norton NC132 hot-pressed $Si_3N_4$ ( MgO additive ).	200
Fig. 45	Fracture around Vickers indentations in Norton NCX34 hot-pressed $Si_3N_4$ ( $Y_2O_3$ additive ).	202
Fig. 46	Fracture around Vickers indentations in two forms of reaction-bonded $Si_3N_4$ : Ford '2.7' and Norton NC350.	203
Fig. 47	Fracture around Vickers indentations in a sintered sialon ( Lucas SYALON 342 ).	205
Fig. 48	Fracture around Vickers indentations in two forms of $B_4C$ sintered to different densities.	205
Fig. 49	The temperature sensitivity of $P^*$ , the critical load required for radial crack nucleation: {111} single crystal silicon.	216
Fig. 50	The temperature sensitivity of $P^*$ : SiC materials.	216
Fig. 51	The temperature sensitivity of $P^*$ : $Si_3N_4$ and sialon materials.	217
Fig. 52	The temperature sensitivity of $P^*$ : $B_4C$ materials.	217

Fig. 53	The variation of $(H/K_{IC})$ with temperature for {111} silicon.	241
Fig. 54	The variation of $(H/K_{IC})$ with temperature for SiC materials.	241
Fig. 55	The variation of $(H/K_{IC})$ with temperature for $Si_3N_4$ and sialon materials.	242
Fig. 56	The variation of $(H/K_{IC})$ with temperature for $B_4C$ materials.	243
Fig. 57	The variation of 'indentation brittleness' $(c^{3/2}P^{-1})$ with temperature for {111} single crystal Si.	244
Fig. 58	The variation of 'indentation brittleness' $(c^{3/2}P^{-1})$ with temperature for SiC materials.	245
Fig. 59	The variation of 'indentation brittleness' $(c^{3/2}P^{-1})$ with temperature for $Si_3N_4$ and sialon materials.	245
Fig. 60	The variation of 'indentation brittleness' $(c^{3/2}P^{-1})$ with temperature for $B_4C$ materials.	246

#### LIST OF TABLES

Table 1	Typical polishing schedule used.	25
Table 2	Properties of the materials investigated.	37
Table 3	Activation energies calculated from high-temperature ( $T > T_C$ ) hot-hardness data for single crystals of SiC as functions of crystal colour, indenter orientation and indenter profile.	67
Table 4	Activation energies calculated from the high-temperature ( $T > T_C$ ) Knoop hot-hardness data of Niihara and Hirai for single crystals of $\alpha$ - $Si_3N_4$ as a function of indenter orientation.	67
Table 5	Best fit parameters for Gilman's theory of low-temperature plastic flow in covalent materials.	76
Table 6	The effect of dopant on the Vickers hardness of {111} single crystal silicon as a function of temperature.	101
Table 7	The effect of dopant on the room-temperature Vickers hardness of $\alpha$ and $\beta$ 'REFEL' reaction-bonded silicon carbides.	101
Table 8	Activation energies for the variation of hardness with temperature above $T_C$ for a variety of ceramic materials.	116

Table 9	A comparison between the Knoop hardness of single crystal and polycrystalline SiC materials at room temperature and 800°C.	119
Table 10	The effects of porosity on hardness for two sintered boron carbides and two RBSN materials at room temperature and 800°C.	119
Table 11	Variation of Meyer index with temperature for Vickers indentations in the load range 100gf-1kgf	130
Table 12	Variation of Meyer index with temperature for Knoop indentations in SiC materials.	131
Table 13	The effect of surface finish on the room temperature Vickers hardness of alpha 'REFEL' reaction-bonded silicon carbide.	134
Table 14	Activation energies taken from the literature for various deformation mechanisms in Si, SiC and Si <sub>3</sub> N <sub>4</sub> materials.	139
Table 15	The ratio (c/a) of radial crack radius to Vickers indentation radius at room temperature and 800°C over the stated indenter load ranges for various Si, SiC, Si <sub>3</sub> N <sub>4</sub> , sialon and B <sub>4</sub> C materials.	181
Table 16	The ratio (c/b) of radial crack radius to calculated plastic zone radius for 1 kgf Vickers indentations in a variety of brittle materials at room temperature and at 800°C.	182
Table 17	The exponent q in the relation $P \propto c^q$ calculated from indentation fracture data for various brittle materials as a function of temperature.	183
Table 18	The variation of indentation fracture toughness with temperature for various Si, SiC, Si <sub>3</sub> N <sub>4</sub> , sialon and B <sub>4</sub> C materials.	184
Table 19	The critical flaw sizes (c*) required for median crack nucleation in a variety of Si, SiC, Si <sub>3</sub> N <sub>4</sub> , sialon and B <sub>4</sub> C materials at 25°C and 800°C.	220

## CHAPTER 1

### INTRODUCTION

#### 1.1 GENERAL AIMS OF THE PROJECT

Engineering ceramics have been developed primarily for high-temperature applications such as gas turbine components (e.g. 1-4), but have also found increasing use as bearing and abrasion-resistant surfaces (5-7) due to their excellent friction and wear characteristics in severe, and often unlubricated environments (8).

Abrasive and erosive wear damage is controlled by some combination of fundamental deformation mechanisms, such as localized plasticity (e.g. 9,10) often coupled with various crack arrays in brittle solids (e.g. 11,12). These mechanisms are most conveniently investigated and quantified experimentally by means of indentation tests (either quasi-static hardness tests or sliding stylus wear tests).

The primary aim of the work described in this thesis was to investigate, using indentation techniques, some of the variables influencing plasticity and fracture processes in engineering ceramics, with a view to predicting their effects on wear behaviour. The main variables considered were: specimen material, specimen microstructure, temperature, contact load and gaseous environment.

To this end, a range of microstructural forms of several materials (mostly silicon-based, and including Si, SiC, Si<sub>3</sub>N<sub>4</sub>, sialon and also B<sub>4</sub>C) have been subjected to a variety of indentation tests performed using a controlled-atmosphere, temperature-variable microhardness tester commissioned especially for this project (13). In parallel with these investigations, a range of light-optical and electron-optical and X-ray diffraction techniques were utilized for characterization of specimen microstructures and contact-induced deformation structures.

Although prediction of wear characteristics is the major theme of the project, many of the results are of much wider significance to the deformation behaviour of engineering ceramics and its dependence on microstructure and temperature.

The philosophy adopted in this investigation is discussed in more detail in section 1.3, but first a short review of the development and applications of 'engineering ceramics' is presented.

## 1.2 ENGINEERING CERAMICS

### 1.2.1 The need for 'special' ceramics

Ceramic materials\* have many useful physical, chemical and mechanical properties which render them potential engineering materials. These properties, which are a direct consequence of the atomic bonding (predominantly ionic or covalent), often include:

- high hardness (often above  $1000\text{kgfmm}^{-2}$ , and extending up to  $\sim 10,000\text{kgfmm}^{-2}$  for diamond), generally maintained to high temperatures,
- good abrasive wear resistance in severe environments,
- low coefficients of friction when in contact with many surfaces,
- high melting/dissociation temperatures (typically  $2000\text{--}3000^{\circ}\text{C}$ ),
- good chemical stability in a wide range of environments,
- low density (e.g.  $2.5 \sim 5\text{gcm}^{-3}$ , but with exceptions, e.g. WC,  $\text{UO}_2$ ),
- high stiffness (Young's modulus  $E \sim 200\text{--}1000\text{ GPa}$ ),
- high strength in compression.

However, a major drawback with all ceramic materials is their inherent brittleness when subjected to tensile stress, since local stress concentrations may not generally be relieved by plastic flow. A further consequence is that the strength (e.g. bend strength) of a ceramic (which may be quite high on average) is often subject to a wide statistical scatter from specimen to specimen due to variations in critical flaw sizes (e.g. 14-16).

For these reasons, traditional ceramics are not generally used where large tensile stresses (mechanically or thermally induced) are anticipated. Over the past 10-20 years, great efforts have been made to develop a range of 'special' ceramics with better and, especially, more reproducible mechanical properties. In addition, special ceramics have been developed for their extreme properties,

---

\*Ceramic materials are taken to include all inorganic substances with predominantly covalent or ionic bonding. This classification includes glasses, glass-ceramics, cermets, conventional refractories, whitewares and claywares and also concretes, as well as the 'special' ceramics discussed in this project.

such as high hardness, low or high thermal or electrical conductivity, etc. The leading candidates which have emerged for high-performance engineering applications are silicon carbide, silicon nitride and, more recently, a whole range of materials derived from 'alloying' silicon nitride with alumina and other oxides - the so-called 'sialon' materials. The underlying reasons for the superiority of these materials are their high resistance to thermal shock and thermal fatigue (a consequence of high thermal conductivity and low thermal expansion coefficients), comparatively good mechanical properties (e.g. modulus of rupture, toughness, creep strength) and also good oxidation resistance maintained to high temperatures. These features are discussed at greater length in the following section. In addition, fabrication of complex shapes by a variety of methods is possible for these materials (section 1.2.4).

## 1.2.2 Properties and Applications of 'Special' Ceramics

### 1.2.2.1 Silicon Carbide

Silicon carbide decomposes at a temperature of  $2830^{\circ}\text{C}$  (17), has high thermal conductivity (usually in the range  $K \sim 50-100 \text{ Wm}^{-1}\text{K}^{-1}$ , depending on microstructure and purity (2,18)), and has a small coefficient of thermal expansion ( $\alpha \sim 4-5 \times 10^{-6} \text{ K}^{-1}$  (2)). This combination of properties, combined with high chemical stability, makes SiC a useful refractory material. In particular, SiC is highly resistant to failure by thermal shock, due to high  $K$  and low  $\alpha$ , compared with many ceramic materials, and this is an essential property of any high-temperature engineering material.

Whilst SiC is chemically inert in many environments, it is extremely reactive towards many molten metals, such as Ti, V, Cr, Mn, Fe, Co, Ni (19), dissolving as carbides and silicides, both of which react with dissolved oxygen (hence the major volume use of SiC is in deoxidation of steels (19)).

SiC itself is very resistant to oxidation at temperatures up to  $\sim 1400^{\circ}\text{C}$  (e.g. 20,21), which again favours its use as a high-temperature ceramic. In this connection, the etching behaviour of SiC by electrolytic oxidation has been found to be impurity-sensitive (22): p-type SiC being more resistant to oxidation than either n-type or intrinsic material. This may be of significance in further

improvement of the oxidation resistance of SiC.

SiC is a wide band gap semiconductor of particular importance for two reasons: (a) it is a highly refractory material which shows relatively little change in electronic properties with changing temperature; (b) it is thought to be the only material capable of blue laser action (at suitable dopant levels of Al and possibly other impurities) (23). The uses of SiC in electronic devices have been summarized by Ryan in the proceedings of the 1973 conference on SiC (24).

SiC has been developed for nuclear applications such as fuel cladding because of its extremely low neutron capture cross-section (7,25).

Partly because of its extreme hardness, SiC has found numerous uses in tribological applications, either as an abrasive (where its conchoidal mode of fracture renders abrasive grains self-sharpening (19)) or as a highly wear-resistant material. Thus, SiC has been used in applications such as seal faces, bearings, die-liners and spinnerets (e.g. 7,25).

The brittle nature of SiC is utilized in light armour against high-velocity armour-piercing bullets (19), the impact energy being effectively absorbed by brittle fracture (unless of course the armour is hit in the same place twice!).

SiC is a material of exceptional mechanical properties, including: (a) very high stiffness, Young's modulus being typically 400-500 GPa, which, coupled with the low density of the material ( $3.3\text{gcm}^{-3}$ ), means that high stiffness:weight ratios are possible. (b) Silicon carbides generally have high strength: moduli of rupture in four-point bending are typically 300-700 MPa at room temperature, depending on microstructure (2). (c) For most forms of SiC, the strength is fairly reproducible from sample to sample, Weibull moduli (15,16) in excess of 15 being common. (d) Strength is maintained to very high temperatures (to  $1000^{\circ}\text{C}$ , and often above). (e) SiC has high resistance to creep and slow crack growth.

These properties, coupled with good thermal shock resistance and chemical stability, make SiC a promising material for use in high-temperature applications such as turbine components (1-4). Indeed, the development of materials based on SiC and  $\text{Si}_3\text{N}_4$  received great impetus in the 1970's when the United States Government's Advanced Research Projects Agency (ARPA) financed a research program whose

major aim was to develop a small gas-turbine engine to run at high temperatures, using the excellent high-temperature properties afforded by ceramic components (e.g. 2,27). The advantages include better running efficiency and fuel consumption (due to higher running temperatures), greater power per unit weight, and potentially smaller cost compared to current superalloys, especially since ceramic components require less efficient (or even non-existent) cooling systems.

However, the inherent brittleness of ceramics raises huge problems, which have not yet been fully solved, in design and construction of such high-temperature engines. Despite these, a variety of ceramic components have been successfully tested in laboratory test rigs and in some instances in commercial engines (e.g. 2,26,27, 37).

#### 1.2.2.2 Silicon Nitride

Silicon nitride is a competitor to SiC for many applications (e.g. turbine components, tribological applications), though there are important differences in properties between the two materials:

- a)  $\text{Si}_3\text{N}_4$  dissociates at a much lower temperature ( $1750\text{--}1900^\circ\text{C}$ ) than SiC, which may limit ultra-high temperature applications, and makes pressureless sintering a more difficult process (see 1.2.4.1).
- b)  $\text{Si}_3\text{N}_4$  has lower thermal conductivity than SiC ( $K \sim 10\text{--}50 \text{ W m}^{-1}\text{K}^{-1}$ ), but since the coefficient of thermal expansion is also very low ( $\alpha \sim 2.5 \times 10^{-6} \text{ K}^{-1}$ ), thermal shock and thermal fatigue resistance is even better than for SiC;
- c)  $\text{Si}_3\text{N}_4$  is an electrical insulator (resistivity  $\sim 10^{-2} (\Omega \text{ m})^{-1}$ ), and finds applications as encapsulants and in metal-nitride-oxide-semiconductor (MNOS) memory devices (28);
- d)  $\text{Si}_3\text{N}_4$  is less reactive towards molten metals than SiC, and is used in molten metal storage and handling applications (29);
- e)  $\text{Si}_3\text{N}_4$  is rather less stiff than SiC:  $E \sim 200\text{--}300 \text{ GPa}$ , depending on microstructure;
- f) silicon nitrides are generally stronger (i.e. have higher modulus of rupture and toughness) than equivalent forms of SiC (four point bend strengths are typically  $\sim 700 \text{ MPa}$  for dense forms of  $\text{Si}_3\text{N}_4$  at room temperature (2,27)), although the decrease in strength with increasing temperature is usually much more pronounced for  $\text{Si}_3\text{N}_4$  than for SiC (2,27);
- g) resistance to high-temperature oxidation, creep and subcritical crack growth is generally less for  $\text{Si}_3\text{N}_4$  than for SiC (2,29), although still

excellent by comparison with other materials.

#### 1.2.2.3 SIALON

The sialons are a more recently developed class of materials than either SiC or  $\text{Si}_3\text{N}_4$ , and there remains a great deal of work to be carried out to investigate the full range of compositions over which these materials may be formed, to characterize the microstructures which may be developed and finally to relate properties to structure and composition (28-31).

Sialon materials are alloys of  $\text{Si}_3\text{N}_4$  with oxides, notably with  $\text{Al}_2\text{O}_3$  but also with oxides such as  $\text{MgO}$ ,  $\text{Y}_2\text{O}_3$ ,  $\text{CeO}$  - indeed, the background to sialon development lay in understanding oxide-nitride interactions and the formation of grain boundary oxynitride glasses in hot-pressed  $\text{Si}_3\text{N}_4$  (see 1.2.5). The object of sialon development is to produce materials with better physical and/or chemical and/or mechanical properties than currently available forms of  $\text{Si}_3\text{N}_4$ . This is possible for a number of reasons: a) sintering to theoretical density is generally much easier for sialons than for  $\text{Si}_3\text{N}_4$ ; b) microstructures are more controllable and may be varied to a greater extent; c) in particular, oxide alloying enables better control of grain boundary phases to be achieved (see 1.2.5); d) sialon materials have inherently greater resistance to high temperature oxidation, creep and slow crack growth than  $\text{Si}_3\text{N}_4$  materials (29,30).

Sialon materials are likely to find increasing engineering uses, since the combinations of properties required for a given application might be specially developed by suitable choice of composition, heat treatment, etc. (subject, of course, to the limitations of the system: sialon materials will never be as hard or stiff, for instance, as SiC).

Proposed applications for sialon materials include holding and conveying of molten metals (28), tool bits for machining certain materials (31), turbine components (27) and tribological applications (31).

#### 1.2.2.4 Boron Carbide

Boron carbide has been used largely for its nuclear characteristics (as a neutron absorber) (32,33) but has many other

useful properties.  $B_4C$  has a melting point of  $2425^{\circ}C$ , has lower thermal conductivity than  $SiC$  ( $K \sim 33 \text{ Wm}^{-1}K^{-1}$  (35)), but has good thermal shock resistance because of its low thermal expansion coefficient ( $\alpha \sim 4-8 \times 10^{-6} K^{-1}$  (34)). High stiffness ( $E \sim 460 \text{ GPa}$  for fully dense material (33)) and low density ( $2.5 \text{ gcm}^{-3}$ ) favour its use in high stiffness: weight fibre composites. The material has high strength ( $\sim 280-410 \text{ MPa}$  at room temperature, often with good strength retention up to  $1400^{\circ}C$  (35)). However, it has been reported (36) that  $B_4C$  may not be used at temperatures above  $450^{\circ}C$  in air, presumably because of low oxidation resistance.

$B_4C$  is extremely hard (approximately as hard as  $SiC$  at room temperature) and is again highly resistant to abrasive and erosive wear (it is used, for example, in sand-blast nozzles (36)). The material has also been used in ceramic armour for helicopter seats (37).

### 1.2.3 Crystal Structures

#### 1.2.3.1 Silicon Carbide

The crystal structure of  $SiC$  is more fully reviewed by Verma and Krishma (38) and by Jepps and co-workers (e.g. 39-41). All  $SiC$  structures consist of primary tetrahedral co-ordination units of silicon and carbon atoms ( $SiC_4$  or  $CSi_4$ ), the bonding being largely covalent. The tetrahedra are stacked in positions analogous to those occupied by spheres in close-packed structures, and linked through their vertices to form a relatively open, polar structure.

The stacking sequence of layers of tetrahedra may be varied in two ways: by translating adjacent layers with or without rotations of  $\pi$ . In extreme cases, this generates cubic zinc blende and hexagonal wurtzite structures: 3C and 2H in Ramsdell notation (42). In this notation, a structure is described by a number representing the number of layers in the unit cell, and a letter giving the Bravais lattice type (C = cubic, H = hexagonal, R = rhombohedral).

By introducing variation in the one-dimensional stacking sequence, a whole range of crystal structures, termed polytypes are possible, and over a hundred such variants have been identified to date (38,41).

The most commonly occurring polytypes of  $SiC$  are short-period structures such as 3C (often called  $\beta$ - $SiC$ ) and also

6H, 15R, 4H and 2H (the hexagonal, rhombohedral and disordered structures are collectively known as  $\alpha$ -SiC). The structures of some of these polytypes are illustrated in fig.1. Long-period structures are observed more infrequently, and may often be regarded as regular arrays of stacking faults in the simpler polytypes.

The occurrence, stability and transformations of some of the polytypes of SiC have been reviewed by Jepps and Page (41). It appears that 6H is the more stable high-temperature polytype, whilst 3C is favoured at temperatures between 1400 and 1600°C. Impurities are known to affect the relative stability of SiC polytypes: nitrogen, for example, stabilizes 3C (43), whilst aluminium tends to stabilize 4H (44). Further research in this interesting area will be required before full understanding of polytypism in SiC, or the stabilizing effect of impurities, is achieved.

#### 1.2.3.2 Silicon Nitride

Crystalline silicon nitride exists in two hexagonal modifications ( $\alpha$  and  $\beta$ ) (e.g. 29,45) (see fig.2). In both forms, the basic unit is the silicon-nitrogen tetrahedron, joined so that each nitrogen is shared by three tetrahedra. The bonding in  $\text{Si}_3\text{N}_4$  has been estimated to be ~70% covalent in character (46).  $\alpha$ - $\text{Si}_3\text{N}_4$  has a unit cell c dimension approximately twice that of  $\beta$ - $\text{Si}_3\text{N}_4$ , the a dimensions being similar. Grievson et al. (47) have suggested that  $\alpha$ - $\text{Si}_3\text{N}_4$  is not a binary silicon nitride, but a defect structure with approximately one in every 30 nitrogen atoms replaced by oxygen, and to maintain electrical neutrality, the equivalent number of Si sites remains vacant. However, structure determinations indicate that  $\alpha$ - $\text{Si}_3\text{N}_4$  need not contain oxygen (46).

It is currently thought that the  $\alpha$  and  $\beta$  forms of  $\text{Si}_3\text{N}_4$  are polymorphs and that  $\alpha$ - $\text{Si}_3\text{N}_4$  has slightly the higher free energy at the formation temperature (46). However, the development of one or other of the two forms is probably determined more by kinetic than thermodynamic considerations.

#### 1.2.3.3 Sialon

Sialon compounds may be thought of as  $\text{Si}_3\text{N}_4$  with replacement

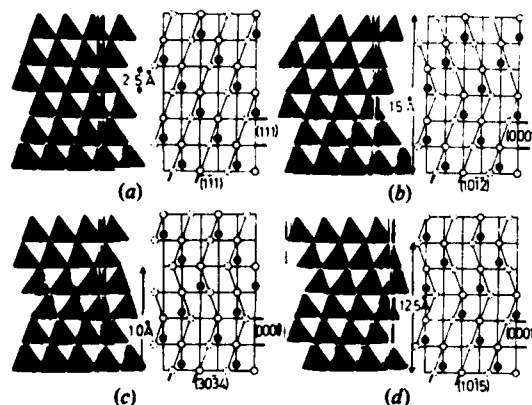


**Figure 1.** The crystal structures of four common polytypes of SiC, after Jepps et al. ( 40 ): (a) 3C viewed along  $\langle 1\bar{1}0 \rangle$ , (b) 6H viewed along  $\langle 12\bar{1}0 \rangle$ , (c) 4H viewed along  $\langle 12\bar{1}0 \rangle$ , (d) 15R viewed along  $\langle 12\bar{1}0 \rangle$ . Only those tetrahedral face planes in the zone of the viewing direction are shown on the stacking sequence diagrams. All the Si atomic positions are shown ( those in the plane of the plan as open circles, those above and below as closed circles ), but only those C positions ( filled circles ) in the plane of the plan are included.

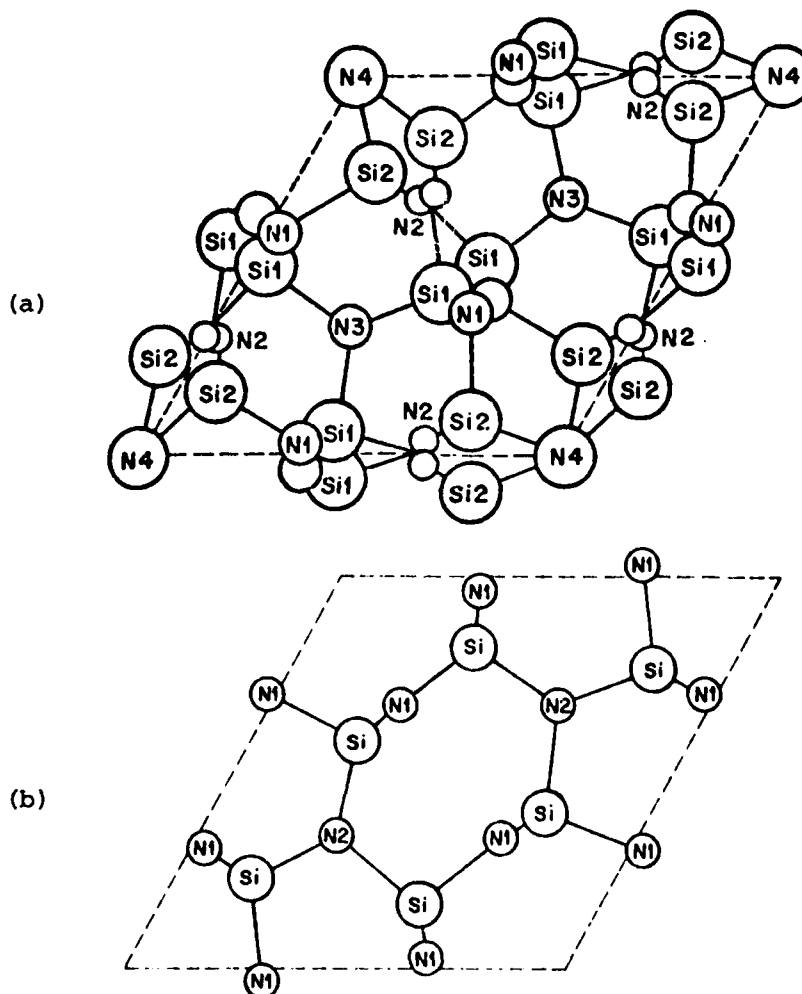


**Figure 2.** The crystal structures of  $\alpha$ - and  $\beta$ - $\text{Si}_3\text{N}_4$ , after Edington et al. ( 45 ). (a) Projection of the unit cell of  $\alpha$ - $\text{Si}_3\text{N}_4$  in the basal plane. There are four different nitrogen atomic sites ( N1-N4 ) and two different silicon sites ( S1, S2 ). (b) Projection of the unit cell of  $\beta$ - $\text{Si}_3\text{N}_4$  in the basal plane. All N atoms are labelled N1 except the special cases where the atom is at the centre of an equilateral triangle of Si atoms.

of silicon atoms by trivalent metal atoms (often Al) and nitrogen atoms by oxygen, such that charge neutrality is maintained. Effectively, various defective layer structures (or 'polytypes') are formed. Sialon materials are made by sintering or hot-pressing mixtures of compounds such as AlN, SiO<sub>2</sub>, Si<sub>3</sub>N<sub>4</sub> and Al<sub>2</sub>O<sub>3</sub> in appropriate proportions. The phase diagram is complex, containing the following phases (29):

β'-sialon - has composition Si<sub>6-z</sub> Al<sub>z</sub> O<sub>z</sub> N<sub>8-z</sub> where 0 < z ≤ 4.2, and has a distorted β-Si<sub>3</sub>N<sub>4</sub> structure (with Al replacing Si and O replacing N);

O'-sialon - is similarly based on the Si<sub>2</sub>N<sub>2</sub>O structure (29), with addition of Al<sub>2</sub>O<sub>3</sub>;

X-phase - the composition and structure of this phase are the subject of some controversy in the literature, having variously been described as triclinic, orthorhombic and monoclinic (29);

Y-phase - occurs as a minor phase in the hot-pressing of AlN-rich β' sialons, and is based on the 15R polytype of AlN. Other possible phases include 8H, 12H, 21R and 27R (29).

Commercially, the β'-sialons are of greatest interest because they are more readily sintered to full density (29). Often, densification aids (especially MgO and Y<sub>2</sub>O<sub>3</sub>) are added to promote liquid-phase sintering, thus complicating the phase diagram. Magnesium spinel (MgAl<sub>2</sub>O<sub>4</sub>) or equimolar mixtures of MgO and Al<sub>2</sub>O<sub>3</sub> react with silicon nitride to give β'-magnesium sialons. In general, the phases occurring in the basic sialon system occur in the Mg-sialon system to greater or lesser extents, but other new phases are also found. Thus, in addition to β' phase, α' (isostructural with α-Si<sub>3</sub>N<sub>4</sub>), X, 12H, 15R and a nitrogen spinel occur (29).

#### 1.2.3.4 Boron Carbide

The crystal structure of boron carbide has been described by Wyckoff (48). B<sub>4</sub>C forms rhombohedral crystals with three B<sub>4</sub>C units per cell, unit cell dimensions being a=5.19Å, γ=66°18'. Corresponding to this is a hexagonal unit cell containing nine molecular units, with a'=5.60Å, c'=12.12Å (see fig.3). The structure may be considered as a rhombohedrally distorted NaCl-like grouping of linear C<sub>3</sub> and icosahedral B<sub>12</sub> groups. Alternatively, the boron atoms may be visualized as forming a three-dimensional network, with

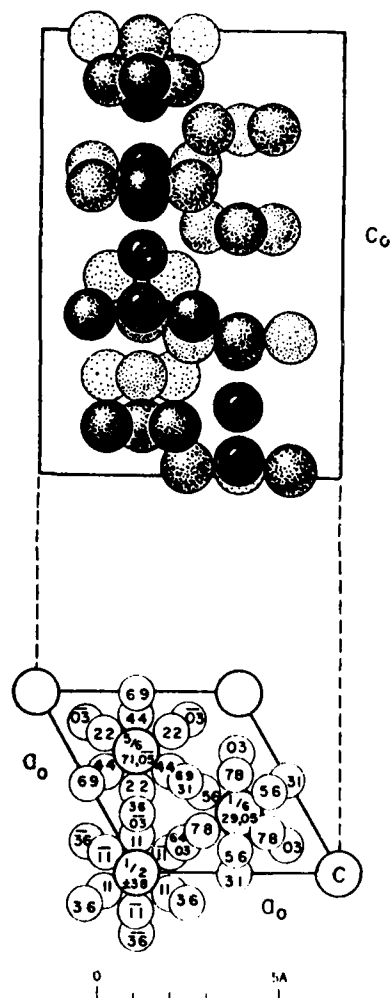


**Figure 3.** The crystal structure of  $B_4C$ , after Wyckoff ( 48 ): two projections of the hexagonal unit cell. In the upper projection, the carbon atoms are black.

the linear  $C_3$  groups filling the largest holes. Bonding is largely covalent.

#### 1.2.4 Fabrication Routes

Almost all ceramics are fabricated by powder forming methods. Since machining costs for ceramics are high, good dimensional tolerance is required for any commercially viable fabrication route, and the requirement of optimum mechanical properties for the finished component usually requires a ceramic of close to full density. Brief descriptions of commercial fabrication routes are given below and microstructural characterization of specimens actually used in the investigation is detailed in section 2.3.

##### 1.2.4.1 Sintering

Without very high pressures, pure SiC and  $Si_3N_4$  powders do not sinter (e.g. 49): at very high temperatures, both compounds merely dissociate without melting, surface and volume diffusion coefficients being insufficient for diffusive sintering mechanisms. For this reason, the use of additives is required to promote liquid phase and/or diffusive sintering at reasonable temperatures.

Thus,  $\beta$ -SiC is often sintered with small amounts (typically 0.5-1wt%) of boron and carbon at temperatures of  $\sim 2000$ - $2100^\circ C$  in inert atmospheres (e.g. helium) (49). The role of the additives is by no means well-established, Prochazka (e.g. 49) having presented a thermodynamic argument that C removes surface SiO from the SiC grains, thus raising the surface energy. Boron was thought to segregate to grain boundaries, thus lowering the grain boundary energy and ensuring a large thermodynamic driving force for sintering. Greskovich et al. (50) and Suzuki et al. (51,52) favour the kinetic argument that a B-C compound ( $\sim 8\text{\AA}$  thick) is formed on the surface of SiC grains, and solid-state sintering then occurs by material transport through this phase, which then dissolves in the bulk material at temperatures above  $1950^\circ C$ , leaving B- and C-rich regions at triple grain junctions (52). Sintering is thought to be facilitated by inhibition of surface diffusion by the B-C layer, preventing the anomalous grain growth of  $\alpha$ -SiC (e.g. 53) which otherwise occurs if original  $\beta$ -SiC grains undergo a phase transformation (49, 53-56). This may be prevented by the use of highly phase-pure

$\beta$ -SiC (with  $<0.1\%$   $\alpha$ -SiC (49)) or, more recently, by the use of  $\alpha$ -SiC powder (developed by the Carborundum Company in the U.S.A. (27)). The starting powder must have submicron particle size in order to ensure a sufficiently high surface energy to provide the necessary driving force for sintering (49) and to minimize diffusion distances.

$\text{Si}_3\text{N}_4$  is difficult to sinter because of its relatively low dissociation temperature ( $1750$ - $1900^\circ\text{C}$ ), but this problem has been overcome recently by use of powder sintering beds and nitrogen overpressures (e.g. 57-60). The sintering additives used are refractory glass-forming oxides such as  $\text{MgO}$ ,  $\text{Y}_2\text{O}_3$  and  $\text{CeO}_2$  (57-59), which react with surface  $\text{SiO}$  present on  $\text{Si}_3\text{N}_4$  grains to form a glass phase which is liquid at the sintering temperature (typically in the range  $1650$ - $1800^\circ\text{C}$ ).

A major advantage of pressureless sintering as a fabrication route is that complex shapes are possible by mixing the starting powder with a polymeric binder and shaping by conventional plastic forming methods, finally burning out the binder prior to sintering. High dimensional tolerances may be achieved if the shrinkage which occurs on sintering is allowed for (58).

The disadvantages of sintering are that some residual porosity is almost invariably left in the material, and this may limit mechanical properties and reduce oxidation resistance if the porosity is 'open'. Residual grain boundary phases resulting from sintering additives may further limit the high-temperature properties of sintered materials (see 1.2.5).

#### 1.2.4.2 Hot-Pressing

Hot-pressing involves the simultaneous application of high temperatures and pressures (either isostatic or uniaxial) to the starting powder (61). Additives are again required to promote sintering: for SiC either boron and carbon or  $\text{Al}_2\text{O}_3$  are used commercially, the hot-pressing temperature being typically  $1900$ - $2000^\circ\text{C}$  with pressures of the order of 35 MPa (27). The additives used in hot-pressed  $\text{Si}_3\text{N}_4$  include  $\text{MgO}$ ,  $\text{Y}_2\text{O}_3$ ,  $\text{ZrO}_2$ ,  $\text{Be}_3\text{N}_2$  and  $\text{BeSiN}_2$  (27,62,63). with pressures in excess of  $\sim 14$  MPa and temperatures in the range  $1650$ - $1750^\circ\text{C}$  (27). During hot-pressing of  $\alpha$ - $\text{Si}_3\text{N}_4$ , a phase change to the  $\beta$  polymorph occurs which is favoured because the resultant grains are often elongated, and this has been found to result in higher

values of toughness (27).

An advantage of hot-pressing is that full density may be achieved, and hence excellent mechanical properties are possible. Disadvantages are that only simple shapes may be formed, except where 'powder vehicle' techniques are used (e.g. 61), for which shape distortion is often a problem. The material may have a pronounced texture (due to packing of plate-like crystals or plastic deformation (81)) if the pressure was applied uniaxially (resulting in anisotropic mechanical properties) and also the grain boundary phase may degrade high-temperature properties (this has been found to be the case for  $\text{Si}_3\text{N}_4$  especially).

#### 1.2.4.3 Reaction-Bonding

In this process, grains are bound together by new material formed by chemical reaction. The processes used for SiC and  $\text{Si}_3\text{N}_4$  are different and will be described separately: for further details, see e.g. (64,13) (SiC) and e.g. (46,65) ( $\text{Si}_3\text{N}_4$ ).

For reaction-bonded SiC, a starting mixture of commercial SiC grit, colloidal graphite and polymeric binder is used, the proportions being carefully controlled for optimum formability and for other reasons (see below). The mixture is shaped by conventional plastic forming methods (e.g. injection moulding, extrusion, etc.) and the binder is then removed by heating in air to produce a 'green compact' containing SiC grit, carbon and porosity. The ratio of SiC to C is important since it determines the ratio of original SiC to new SiC formed in the subsequent reaction stage. Here, the green compact is infiltrated with molten silicon in a vacuum induction furnace, such that the silicon reacts with graphite to form new SiC which ideally (66) deposits epitaxially on the SiC grit 'seeds', binding the material together.

The resulting material is fully dense, but contains ~10-15 vol.% residual silicon in a connected network (this is necessary to ensure complete infiltration of the compact, hence complete reaction). Because the volume change associated with the reaction may be accommodated by the porosity within the green compact (determined by the amount of polymeric binder used in the starting mixture), volume changes on reaction of ~0.1% are possible (64).

Reaction-bonded silicon nitride is formed by nitriding a

porous compact of silicon powder. The compact may be shaped by, for example, slip casting, dry pressing, flame spraying, injection moulding, etc. and then lightly sintered to a readily machineable 'pre-form', which is then nitrided in an atmosphere of either  $N_2$  or  $N_2 + H_2$ . The nitriding sequence is typically in two or three stages, at temperatures from  $1250-1450^{\circ}C$  (46). Often, impurities (especially iron) are added to help densification. The reactions which occur during nitridation of silicon have been reviewed elsewhere (e.g. 46, 65).

As with reaction-bonded SiC, there is very little change in dimensions on reaction. The final product contains at least 10-20 vol.% residual porosity (mostly  $<0.1\mu m$  in diameter), the silicon nitride being largely (60-90%)  $\alpha-Si_3N_4$ , often with some finely-dispersed residual silicon.

The advantages of reaction-bonding processes are that shape tolerance is very good indeed and fairly complex shapes may be formed. Thus, the amount of subsequent machining required is usually minimal, so the material is relatively cheap. However, reaction-bonded SiC contains 10-15 vol.% residual silicon which melts at  $\sim 1450^{\circ}C$ , causing a sharp drop in strength at higher temperatures, and the porosity in reaction-bonded silicon nitride results in low strength and high susceptibility to oxidation.

#### 1.2.4.4 Vapour Deposition

In this process, material is formed entirely from the vapour phase by the reaction of silicon-bearing gases such as  $SiH_4$ ,  $SiCl_4$ , or  $CH_3SiCl_3$  (for SiC) with e.g.  $H_2$ , propane (for SiC),  $NH_3$  (for  $Si_3N_4$ ) (67, 68). Although the major use of vapour deposition is to form coatings, free-standing components with complex shapes may be made by deposition onto graphite substrates, which are subsequently removed by oxidation (67).

Advantages of the process are that the material formed is very pure (e.g. for electronic applications), fully dense and often very hard (see 3.6.5) compared to other forms (hence its use in abrasion-resistant coatings). Disadvantages are that the process is slow, very expensive and produces large, columnar grains (69), often with a pronounced texture and containing large residual stresses.

A new development - "controlled nucleation thermal deposition (CNTD)" (68) may remove some of these problems: by

continually interrupting the deposition by some form of chemical instability, very fine grain sizes are produced, which can result in very high strengths (1400 MPa for SiC in four point bending (68)) which are retained to high temperatures, perhaps because of the absence of any impurity phases.

#### 1.2.5 Grain Boundary Engineering

A major problem with ceramic powder fabrication is that in order to densify materials, some form of additive is often needed to promote liquid-phase sintering. The additives react with the oxide layer always present on grains of the material to form a grain boundary second phase, usually amorphous, and often based on silicates with segregation of impurities such as Ca, Na, etc. Such phases are found especially in sintered and hot-pressed materials, the most extensively studied being  $\text{Si}_3\text{N}_4$  hot-pressed with MgO, in which a thin  $\text{MgSiO}_3$  glass phase (10-20 Å thick) forms along boundaries, with thicker regions at triple junctions (e.g. 70-73).

These grain boundary layers are known to degrade high temperature properties (2,74) by, for example, viscous flow and triple point cavitation (e.g. 75), which result in greater creep susceptibility and faster subcritical crack growth (e.g. 76) and also by providing a highly diffusive path for oxygen which results in greater oxidation rates. Low-temperature properties such as environment-controlled subcritical crack growth and the microstructural control of fracture paths may also be sensitive to the amount and composition of grain boundary phases.

Following Katz and Gazza (74), there are various ways of minimizing these problems by 'grain boundary engineering'. Firstly, we might reduce the concentration of impurities such as Ca and Na in order to make the silicate boundary phase more refractory (e.g. 77,78). This involves purification of the starting materials which is, in practice, expensive. Another approach is to develop a densification aid which yields a more refractory glass. Thus,  $\text{Y}_2\text{O}_3$  represents an improvement over MgO in the hot-pressing of  $\text{Si}_3\text{N}_4$  (63). In addition,  $\text{Y}_2\text{O}_3$ -based phases can accommodate relatively large amounts of impurities such as Ca and may, in some cases, be crystallized by suitable heat treatment (although the concentration of  $\text{Y}_2\text{O}_3$  must be carefully controlled to avoid phase instability problems at  $\sim 1000^\circ\text{C}$  (2)).

A further method of grain boundary engineering lies in developing a non-glass boundary phase, for example by employing a heat treatment to either diffuse impurities into the bulk or to crystallize a separate boundary phase. Indeed, it is this concept which underlies the tremendous potential for the sialon materials (see section 1.1.2.3).

The importance of Mg-sialons lies in the fact that the oxide layer always present on grains of  $\text{Si}_3\text{N}_4$  prevents the formation of homogeneous, single-phase hot-pressed  $\text{Si}_3\text{N}_4$ , whereas by alloying  $\text{Si}_3\text{N}_4$  with appropriate amounts of  $\text{Al}_2\text{O}_3$  and  $\text{AlN}$ , together with just sufficient  $\text{MgO}$  to react with the surface silica, a homogeneous  $\beta'$ -magnesium sialon can be formed. An added advantage is that magnesium silicate reacts first with silicon nitride to produce a liquid which aids densification by liquid phase sintering. Then, by suitable heat-treatment, it is possible to incorporate this phase in solid solution as single-phase  $\beta'$ -sialon (29). Thus, greater control of grain boundary phases may be achieved in this class of material, although a Mg- and O-rich 'segregate' layer, which has adverse effects on high-temperature properties, may still be detected (30).

For this reason, and because fabrication by pressureless sintering is desirable (see 1.2.4), a new range of materials, known as SYALON ceramics (a trademark of Lucas Industries Ltd.) has recently been developed (30, 31). These materials are based on  $\beta'$ -sialon, with a relatively small substitution level ( $z < 0.5$ , see 1.2.3.3) and with large ( $\sim 6\text{wt}\%$ ) additions of  $\text{Y}_2\text{O}_3$ . At the sintering temperature, large amounts of liquid phase are present to facilitate pressureless liquid phase sintering whilst, on cooling, a refractory glassy phase is formed. In one such material, the amorphous material may be crystallized by heat treatment just below the sintering temperature, to form a silicon-substituted yttrium aluminium garnet (YAG) (30, 31). The low substitution level of the  $\beta'$ -sialon matrix is required to accommodate excess Si or Al which may result from crystallization of a stoichiometric second phase from a non-stoichiometric melt (30).

Finally, it might be possible to dispense with grain boundary glass phases, either in part or in whole, by moving away from conventional powder forming methods, possibly towards either reaction-bonding processes (where impurity levels are relatively low) or, better still, towards chemical deposition (especially CNTD) where

essentially pure materials are formed. To the author's knowledge, grain boundaries in such materials remain uncharacterized. Coincident site boundary structures (as observed in some metals) are thought to be at least possible for many ceramic materials (e.g. 83). However, it is often extremely difficult to establish whether thin grain boundary phases are present or not (84), although periodic structures have been observed at some grain boundaries in some materials (e.g. 85).

### 1.3 PROJECT PHILOSOPHY

In this project, plasticity and fracture processes in a range of ultra-brittle solids (largely based on silicon, and including Si, SiC, Si<sub>3</sub>N<sub>4</sub>, sialon and also B<sub>4</sub>C) have been investigated as a function of temperature (in the range 25-1000°C) and of specimen microstructure. The principal experimental technique (described in detail in Chapter 2) was that of controlled-environment, temperature-variable indentation microhardness testing, which was considered to be particularly suitable for reasons discussed below.

Indentation tests are often the only way of inducing plastic responses in a brittle material at low temperatures (82). The study of plasticity in ceramics is important both from a fundamental materials science standpoint and also because plasticity is known to play an important part in wear processes and in crack nucleation. Thus, Chapter 3 of this thesis is devoted to a review of indentation plasticity and its temperature dependence, together with experimental hot-hardness results obtained for a wide range of brittle materials including single crystals of Si and SiC (sections 3.3, 3.4 and 3.5) and commercially-available polycrystalline forms of SiC, Si<sub>3</sub>N<sub>4</sub>, sialon and B<sub>4</sub>C (section 3.6 - microstructural characterization of each of the materials tested is described in section 2.3). Indentation plasticity was also investigated by single crystal hardness anisotropy measurements on SiC (3.4) and by measuring the variations of hardness with applied load (3.7) and with indenter dwell time (3.8).

Indentation tests may also be used to induce well-defined local crack arrays in brittle solids, allowing the study of both crack propagation and initiation processes (described in Chapters 4

and 5 respectively). Fracture processes are, of course, crucial in determining the general mechanical behaviour of ceramic materials, and toughness (or lack of it) is an all-important engineering parameter. For this reason, the development of indentation fracture mechanics (e.g. 79,80), whereby the dependence of (radial) crack extent on applied indenter load may be related to fracture toughness ( $K_{IC}$ ), is a great advance. Toughness values have been derived as functions of temperature for all the materials investigated and direct observations of fracture patterns around indentations have further established where microstructurally preferred crack paths exist.

Many of the surface and near-surface plasticity and fracture processes which occur in response to penetration by sharp indenters are also observed to occur in abrasive and erosive wear situations involving surface contact by sharp asperities (e.g. 9-12). Thus, the results of indentation tests may be applied to predicting wear behaviour, and this theme is developed in Chapter 6.

Experimentally, there are further advantages of micro-hardness tests over other mechanical tests, in that they are non-destructive, require only small amounts of test material and are relatively quick and simple to perform. Whilst the treatment of data is often theoretically complex, a large amount of materials information may often be extracted from a small number of measurements. Perhaps surprisingly, therefore, there have been relatively few previous attempts to study the variation of hardness with temperature for ceramic materials, very few attempts to systematically investigate the effects of microstructure (3.6), and almost no previous investigations of the effects of temperature on indentation fracture (4.4).

Because of this, the project has developed along fairly broad lines: the approach taken was to compare the behaviour of as many different microstructural forms of material as possible, establishing microstructural and temperature effects, from which deductions were made as to probable mechanisms. Much of the work described in this thesis is a necessary preliminary to more detailed examinations required to precisely determine the deformation mechanisms operating in response to indentation of highly brittle materials. Suggestions for such work are included in Chapter 7, along with a summary of the main results of this study.

1.4 REFERENCES

1. J.J. Burke, A.E. Gorum and R.N. Katz, 1974, "Ceramics for High Performance Applications" (U.S. Army Materials Technology Conference Series), Brook Hill.
2. R.N. Katz, 1980, Proceedings of the Third International Conference on Mechanical Behaviour of Materials, 20th. August, 1979, Volume 1, eds. K.J. Miller and R.F. Smith, Pergamon Press.
3. Idem, 1977, in "Nitrogen Ceramics", ed. R.L. Riley, NATO Adv. Study Inst. Series E, No. 23 (Noordhoff, Leyden), p.643.
4. D.J. Godfrey, 1977, *ibid.*, p.647.
5. E. Gugel, 1977, *ibid.*, p.659.
6. "Silicon Nitride as a Bearing Material", Program Review: U.S. Naval Air Systems Command and U.S. Office of Naval Research, July 1974 (Proc. of a meeting held at SKF, King of Prussia, Pa. 9-10 July, 1974).
7. P. Kennedy and J.V. Shennan, 1973, *Atom* (No. 206), 260.
8. J.W. Edington, D.J. Rowcliffe and J.L. Henshall, 1975, *Powder Powder Met. Int.* 7, 136.
9. R. Stickler and G.R. Booker, 1962, *Phil. Mag.* 8, 859.
10. B.J. Hockey and S.M. Wiederhorn, 1979, Proceedings of the Fifth International Conference on Erosion by Liquid and Solid Impact (ELSI V), 3-6th. September 1979, Newnham College Cambridge. Publ. Cavendish Laboratory, Cambridge, p. 26.
11. J.D.B. Veldkamp, N. Hattu and V.A.C. Snijders, 1978, in "Fracture Mechanics of Ceramics" Vol.3, eds. R.C. Bradt, D.P.H. Hasselman and F.F. Lange, Plenum Press, p.273.
12. A.G. Evans, M.E. Gulden and M. Rosenblatt, 1978, *Proc. Roy. Soc. Lond.* A361, 343.
13. M.G.S. Naylor, 1978, M. Phil Thesis, University of Cambridge, Department of Metallurgy and Materials Science.
14. A.A. Griffith, 1920, *Phil. Trans. Roy. Soc. Lond.* A221, 163.
15. A. De S. Jayatilaka and K. Trustrum, 1977, *J. Mater. Sci.* 12, 1426.
16. B.R. Lawn and T.R. Wilshaw, 1975, "Fracture of Brittle Solids", Cambridge Solid State Science Series, Cambridge University Press.
17. R.C. Marshall, J.W. Faust Jr. and C.E. Ryan (eds.). 1973, "Silicon Carbide-1973", Proc. 3rd. Int. Conf. on SiC, Florida, University of South Carolina Press, p.668.
18. B. North and K.E. Gilchrist, 1981, *Am. Ceram. Soc. Bull.* 60, 549.
19. P.T.B. Shaffer, 1973, in ref. 17, p. 343.

20. G.Q. Weaver and B.A. Olson, 1973, in ref. 17, p.367.
21. M.J. Bennett and G.H. Chaffey, 1971, J. Nucl. Mat. 39, 253.
22. N.W. Jepps and T.F. Page, 1981, J. Microsc. 124, 227.
23. J.F. Scott, D.J. Toms and W.J. Choyke, 1980, Phys. Rev. B 21, 3432.
24. C.E. Ryan, 1973, in ref. 17, p.651.
25. P. Kennedy and J.V. Shennan, 1973, in ref. 17, p.359.
26. V. de Biasi, 1977, Gas Turbine World, July 1977, 12.
27. R.N. Katz, 1980, Science 208, 841.
28. J. Robertson, 1981, Phil. Mag. B 44, 215.
29. K.H. Jack, 1976, J. Mater. Sci. 11, 1135.
30. M.H. Lewis, A.R. Bhatti, R.J. Lumby and B. North, 1980, *ibid.* 15, 103.
31. M.H. Lewis, R. Fung and D.M.R. Taplin, 1981, *ibid.* 16, 3437.
32. G.W. Hollenberg, 1980, Am. Ceram. Soc. Bull. 59, 538.
33. G.W. Hollenberg and G. Walther, 1980, J. Am. Ceram. Soc. 63, 610.
34. F. Singer and S.S. Singer, 1963, "Industrial Ceramics", Chapman and Hall, London, p.1146.
35. S.K. Dutta, 1975, quoted in ref.33.
36. F.H. Norton, 1974, "Elements of Ceramics", Addison Wesley, p.256.
37. R.N. Katz, 1980, U.S. Army Research, Development and Acquisition Magazine, Nov./Dec. 1980, p.1.
38. A.R. Verma and P. Krishma, 1966, "Polymorphism and Polytypism in Crystals", J. Wiley Inc., p.93.
39. D.J. Smith, N.W. Jepps and T.F. Page, 1978, J. Microsc. 114, 1.
40. N.W. Jepps, D.J. Smith and T.F. Page, 1979, Acta Cryst. A35, 916.
41. N.W. Jepps and T.F. Page, 1980, J. Microsc. 119, 177.
42. L.S. Ramsdell, 1947, Am. Min. 32, 64.
43. A.R. Kieffer, P. Ettmayer, P. Gugel and A. Schmidt, 1969, Mat. Res. Bull. 4, S153.
44. M. Mitomo, Y. Inomata and M. Kumanomido, 1970, Yogyo-Kyokai-Shi 78, 224.

45. J.W. Edington, D.J. Rowcliffe and J.L. Henshall, 1975, Powder Met. Int. 7, 82.
46. A.J. Moulson, 1979, J. Mater. Sci. 14, 1017.
47. P. Grievson, K.H. Jack and S. Wild, 1968, in "Special Ceramics 4" ed. P. Popper, B. Ceram. R.A., Stoke-on-Trent, p.237.
48. R.W.G. Wyckoff, 1964, "Crystal Structures" vol.2, Interscience (John Wiley and Sons), p.138.
49. S. Prochazka, 1974, in "Special Ceramics 6", ed. P. Popper, B. Ceram. R.A., Stoke-on-Trent, p.171.
50. C. Greskovich and J.H. Rosolowski, 1976, J. Am. Ceram. Soc. 59, 336.
51. T. Hase, H. Suzuki and I. Tomizuka, 1979, Yogyo-Kyokai-Shi 87, 317.
52. H. Suzuki and T. Hase, 1980, J. Am. Ceram. Soc. 63, 349.
53. S. Prochazka, 1973, in ref. 17, p.394.
54. N.W. Jepps and T.F. Page, 1979, J. Microsc. 116, 159.
55. S. Shinozaki and K.R.Kinsman, 1977, Proc. Crystalline Ceramics Conf., N. Carolina State University, N.C. (Sept. 1977).
56. A.H. Heuer, G.A. Fryburg, L.U. Ogbuji, T.E. Mitchell and S. Shinozaki, 1978, J. Am. Ceram. Soc. 61, 406.
57. A. Giachello, P.C. Martinengo, G. Tommasini and P. Popper, 1979, J. Mater. Sci. 14, 2825.
58. Idem, 1980, Am. Ceram. Soc. Bull. 59, 1212.
59. A. Arias, 1981, J. Mater. Sci. 16, 787.
60. C. Greskovich, 1981, J. Am. Ceram. Soc. 64, 725.
61. F.F. Lange and G.R. Terwilliger, 1973, Am. Ceram. Soc. Bull. 52, 563.
62. C. Greskovich, 1979, J. Mater. Sci. 14, 2427.
63. G.E. Gazza, 1975, Am. Ceram. Soc. Bull. 54, 778.
64. C.W. Forrest, P. Kennedy and J.V. Shennan, 1972, in "Special Ceramics 5", ed. P. Popper, B. Ceram. R.A., Stoke-on-Trent, p.99.
65. A.J.S. Edmonds, 1979, Ph.D. Thesis, University of Cambridge.
66. G.R. Sawyer and T.F. Page, 1978, J. Mater. Sci. 13, 885.

67. K.C. Pitman and D.J. Godfrey, 1978, Proc. Brit. Ceram. Soc. 26, 225.
68. S. Dutta, R.W. Rice, H.C. Graham and M.C. Mendiratta, 1980, J. Mater. Sci. 15, 2183.
69. S. Shinozaki and H. Sato, 1978, J. Am. Ceram. Soc. 61, 425.
70. D.R. Clarke and G.R. Thomas, 1977, *ibid.* 60, 491.
71. A.H. Heuer, V. Lou, L. Ogbuji and T.E. Mitchell, 1977, J. Microsc. Spectrosc. Electron 2, 475.
72. D.R. Clarke and G.R. Thomas, 1978, J. Am. Ceram. Soc. 61, 114.
73. O. Krivanek, T.M. Shaw and G. Thomas, 1979, *ibid.* 62, 585.
74. R.N. Katz and G.E. Gazza, 1979, as ref. 3, p.417.
75. A.G. Evans and A. Rana, 1980, Acta. Metall. 28, 129.
76. B.S.B. Karunaratne and M.H. Lewis, 1980, J. Mater. Sci. 15, 1781.
77. R. Kossowsky, 1973, *ibid.* 8, 1603.
78. D.W. Richerson, 1973, Am. Ceram. Soc. Bull. 52, 560.
79. A.G. Evans, 1980, ASTM Special Technical Publication No. 678, ed. S.W. Freiman, p.115.
80. B.R. Lawn, A.G. Evans and D.B. Marshall, 1980, J. Am. Ceram. Soc. 63, 574.
81. S.C. Martin, 1981, Ph.D. Thesis, University of Cambridge.
82. D.M. Marsh, 1964, Proc. Roy. Soc. Lond. A279, 420.
83. Z. Inoue, Y. Uemura and Y. Inomata, 1981, J. Mater. Sci. 16, 2297.
84. N.W. Jepps, W.M. Stobbs and T.F. Page, 1981, Inst. Phys. Conf. Ser. No. 61: Chapter 10, paper presented at EMAG, Cambridge, 7-10 September 1982, p.453.
85. R.W. Balluffi, P.D. Bristowe and C.P. Sun, 1981, J. Am. Ceram. Soc. 64, 23.

## CHAPTER 2

### EXPERIMENTAL

#### 2.1 SPECIMEN PREPARATION

Sections of each of the polycrystalline samples were cut using a high-speed annular diamond saw (Capco, model Q35 Mk (II) (1). As-grown basal habit single crystals of SiC were selected and from some of these were cut  $\{10\bar{1}0\}$  and  $\{11\bar{2}0\}$  slices, by sectioning either parallel or perpendicular to well-defined  $\{10\bar{1}0\}$  faces. Samples from  $\{111\}$  single crystal silicon wafers were made by cleaving after diamond scribing and, in this case, the specimens were tested in the as-received condition since one face had already been polished to mirror finish (presumably by chemical and mechanical polishing procedures commonly used in the semiconductor industry (2)).

Sectioned specimens were mounted in electrically-conducting resin and diamond lapped and polished on Kent polishing machines to  $0.25\mu\text{m}$  finish or better, according to the approximate schedule given in table 1. Some experiments to determine the effects of surface finish on indentation hardness are described in 3.7.4 but, in summary, it was found that the polishing procedure had no effect on measured hardness values for surface finishes of  $1\mu\text{m}$  or better. Coarser surface finishes were observed to produce hardening effects.

After polishing, specimens were examined optically (using either a Zeiss Universal or Zeiss Neophot 2 microscope) and by SEM (using either a Cambridge Stereoscan Mark IIA or an ISI system 100A). For SEM examination, specimen mounts were glued to aluminium stubs with electrically-conducting glue ('Durofix' plus graphite) and conducting silverdag strips were painted from a corner of the specimen surface to the stub. Electrically insulating specimens ( $\text{Si}_3\text{N}_4$ , sialon and  $\text{B}_4\text{C}$ ) were sputter-coated with gold to an approximate thickness of  $100\text{\AA}$ . These specimens were viewed at normal incidence, so as to image the material through the coating: with a tilted specimen, the secondary electron image was found to contain no information about the specimen, the majority of the detected electrons presumably coming from the gold coating.

Porosity and residual silicon contents were measured

Diamond Compound	Cloth or lapping wheel	Applied weight (kg)	Approximate time (minutes)
14 $\mu$ m	Cast iron lap	1.75, progressively reduced to 0.5	5
6 $\mu$ m	" " "	1.75, progressively reduced to 0.5	10
6 $\mu$ m	Copper lap	1.75, progressively reduced to 0.5	15
6 $\mu$ m	Hyprocel Pellon cloth	1.75, later reduced to 1	30-45
1 $\mu$ m	Microcloth	1.75	15
0.25 $\mu$ m	Microcloth	1.75	15
0.1 $\mu$ m	Microcloth	1.75	15

**Table 1** Typical polishing schedule used. Polishing times were dependent on specimen, the state of the polishing cloth, the amount of diamond compound used, etc. After the lapping stages, specimens were examined by optical microscopy before progressing to each new stage of polishing. Generally, the surface appeared shiny after use of the 6 $\mu$ m cloth and was mirror-finish after 1 $\mu$ m and subsequent stages.

directly from optical images using a Quantimet 720 System 23C image analyzer, and grain sizes were estimated from SEM micrographs of the specimens.

## 2.2 SCANNING ELECTRON MICROSCOPY

For several reasons, scanning electron microscopy was found to be an ideal technique for examination of specimens: a) the available resolution is much higher in a scanning electron microscope (SEM) than in optical microscopes (important when determining indentation crack paths or crack termination sites, for example); b) depth of field is also much greater, so that topographic features such as chips formed by indentation fracture may be imaged in focus at all points; c) the SEM image is formed by contrast mechanisms completely different from those giving rise to optical images, in many cases allowing a great deal of extra information to be extracted. This often led to useful microstructural observations, especially in the case of REFEL reaction-bonded SiC (see 2.5); d) stereoscopic techniques (2.2.3) are particularly applicable to SEM imaging, allowing a better appreciation of lateral crack depths, for example; e) energy dispersive X-ray (EDX) systems can be employed for elemental analysis of microstructural features; f) signal processing is readily available in the SEM for contrast enhancement in certain situations.

Some examples of the usefulness of various SEM techniques to this investigation will now be given. For detailed discussion of theoretical and practical aspects of SEM imaging, the reader is referred to the standard textbooks (e.g. 4,5).

### 2.2.1 Backscattered (Primary) Electron Imaging

In this mode, only the incident electrons scattered elastically and inelastically (by Rutherford or Coulomb scattering) by the specimen into the detector are imaged. Such electrons are high-energy (they retain most of the energy imparted to them in forming the original beam) and are scattered (6) from a volume of material typically 0.3-0.5 $\mu$ m in depth, with a similar lateral spread (the precise dimensions depend on the incident beam energy and the material). Hence, the backscattered signal has comparatively poor lateral and depth resolution, but is nevertheless useful since it carries the

following information (6):

i) atomic number contrast

The backscattered signal increases monotonically with the mean atomic number of the material, the contrast increasing by  $\sim 1\%$  per unit increase in atomic number (6). Figure 4b is a backscattered image of REFEL reaction-bonded silicon carbide which shows atomic number contrast between iron-rich particles (identified by EDX analysis), residual silicon and SiC. The particles appear bright because of their relatively high atomic number compared to SiC and Si, these phases also showing a weak (approximately 4%) contrast difference, the silicon appearing brighter. By comparison, optical images (e.g. fig. 4a) merely display contrast between Si (bright) and SiC (darker).

ii) crystallographic (channelling) contrast

When an electron probe hits a crystal at the Bragg angle, it is diffracted (channelled) into the specimen and the backscattered signal typically decreases (6). This gives rise to crystallographic or channelling contrast which is generally weak ( $\sim 5\%$ ) and may be seen as intergranular contrast in polycrystalline specimens (faintly observable in fig. 4b). A channelling pattern may be visible in low-magnification backscattered images of large single crystals, where the variations in the angle of incidence of the electron probe as it rasters across the specimen are sufficiently large (i.e.  $> 2\theta_B$  for several different plane stacks).

This contrast mechanism is utilized in the technique of selected area electron channelling, where the incident beam is caused to 'rock' about a single point on the specimen. The variation in angle of incidence generates an image which is the exact analogue of a Kikuchi electron diffraction pattern (7). Selected area channelling patterns (SACPs) of various single crystals ( $\{111\}$  silicon,  $\{0001\}$  and  $\{10\bar{1}0\}$  SiC) are shown in fig. 5.

The spatial resolution limit of this technique is governed primarily by spherical aberration and is usually of the order of  $10\mu\text{m}$ , but was found to be much worse for the instrument used in this study (ISI 100A) at the minimum value of beam divergence usable. The technique is obviously unsuitable for polycrystalline materials with grain size smaller than the spatial resolution limit (this was the

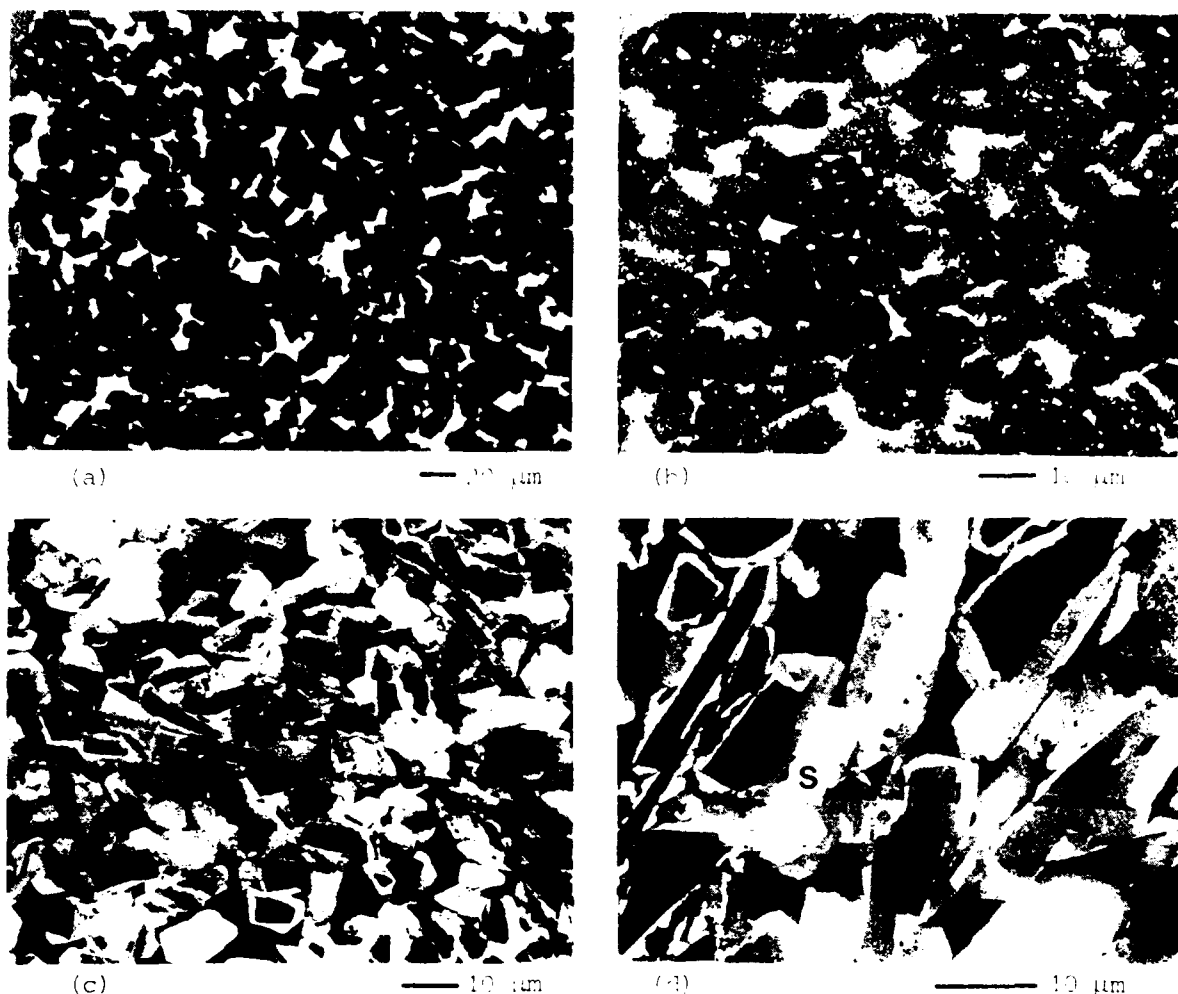


Figure 4 Optical and scanning electron micrographs of 'REFEL' reaction-bonded SiC. (a) Light micrograph showing contrast between SiC ( dark ) and residual Si ( light ). (b) Backscattered electron SEM image revealing contrast between SiC ( dark ), residual Si ( lighter ) and iron-rich inclusions ( white ). Faint grain to grain channelling contrast may be seen within the SiC crystal array. (c) Secondary electron SEM image revealing contrast between SiC grain cores ( usually dark ), epitaxial SiC ( light ) and residual Si ( dark ). (d) as (c) but revealing highly pronounced 'sandwich contrast' within the SiC grains and a 'striped' grain core (S) ( see text ).

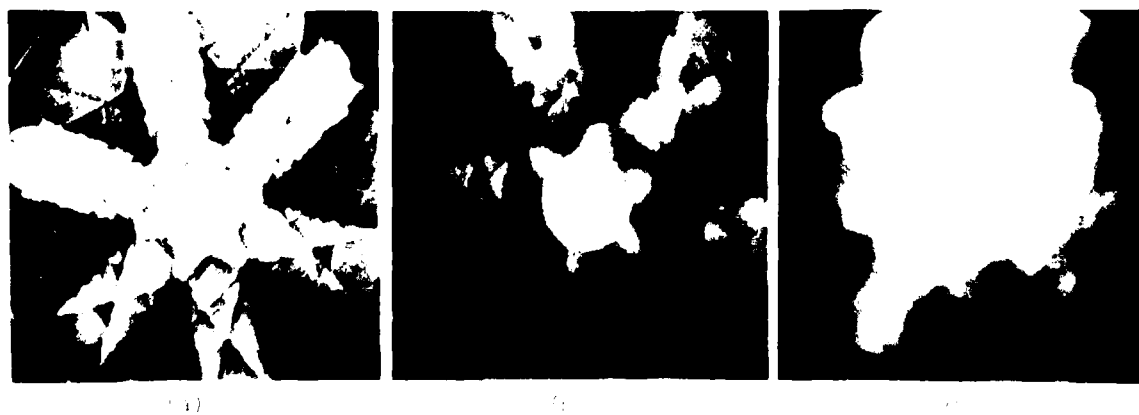


Figure 5 Selected area electron channelitter patterns. (a) 111-111 Si, (b) (001) SiC and (c) 111-111 SiC. Scattered state selected, low resolution.

case for all the polycrystalline materials examined).

The contrast is also highly sensitive to defects in the crystal structure of the specimen surface (8), which probably accounts for the lack of clarity in SACPs of mechanically-polished SiC specimens (figs. 5b, c) compared to those obtained from the (presumed) chemically-polished Si wafer (fig. 5a). This effect may be used to provide information about near-surface defect structures and mechanical strain around indentations (9) or worn surfaces (10, 11) and attempts to do this for high and low temperature indentations in {111} silicon are described in 3.3.1.

### iii) topographic contrast

Backscattered images obtained from a non-symmetrically placed detecting system display topographic contrast (6) originating from the geometry of electron scattering. The effect was not used in this study, since secondary electron imaging was found to be more suitable (see below) but, as a point of interest, fig. 4b shows surface relief in a diamond-polished section of reaction-bonded SiC, especially at the interfaces between SiC and the softer residual Si phase.

## 2.2.2 Secondary Electron Imaging

In this imaging mode, two signals are commonly detected simultaneously by the usual Everhart-Thornley detecting system (4, 5): firstly, a proportion of the backscattered signal discussed previously and, secondly, a higher proportion of the low-energy (typically up to 50 eV) secondary electrons emitted by the specimen as a consequence of electron fluorescence and also inelastic and multiple scattering of primary electrons. Secondary electrons may only escape from a small depth ( $\sim 50-500\text{\AA}$ , depending on material) beneath the specimen surface, and are not generally subject to substantial beam-spreading effects, so the available resolution in this imaging mode is greater than for backscattered imaging (except for the case where substantial numbers of secondaries are generated by emerging backscattered electrons).

Secondary electron generation is theoretically not well understood, but is known (e.g. 4,5,12) to be a function of probe voltage, specimen material, stray electric or magnetic fields and also to specimen topography. The types of contrast most useful to

this project were:

i) topographic contrast

Secondary electrons may only escape from a very thin ( $\sim 50-500\text{\AA}$ ) surface layer, and a surface inclined to the electron probe has rather more of this layer contained in the beam-affected volume than a less-inclined surface (4,5). Thus, the secondary electron signal is a function of surface tilt, hence of specimen topography. Secondary electron imaging has therefore been useful in examining microhardness indentations made in otherwise flat surfaces, and especially in characterizing crack patterns (see figs. 37-48).

ii) material-dependent contrast

The secondary electron coefficient  $\delta$ , defined (4,5) as the number of secondary electrons emitted per incident primary electron, varies strongly with material.  $\delta$  is often low ( $\sim 0.5$ ) for metals (although  $\delta \sim 1-5$  for Au, Ag, Pt, Pd, etc.) and high for insulators ( $\delta \sim 20$  for NaCl and LiF, and is even higher for some rare earth oxides). For metals,  $\delta$  generally increases slowly with increasing atomic number (4,5).

Silicon carbide has been found to exhibit highly impurity-sensitive secondary electron contrast which is particularly striking in the case of 'REFEL' reaction-bonded SiC (1). This is discussed more fully in section 2.5.

### 2.2.3 Stereoscopic Imaging

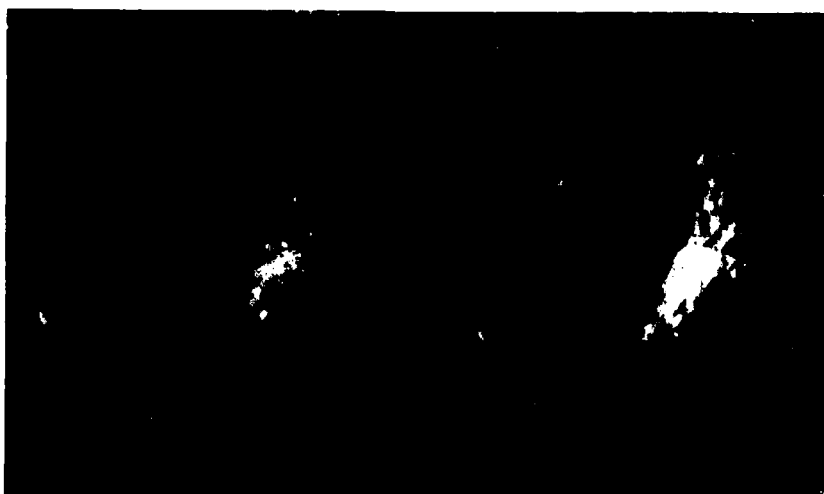
With their high depth of field (typically of the order of the field width), SEM images often contain a lot of useful topographic information. This is best interpreted using stereoscopic techniques (e.g. 18,5), since these are the only means of accurately perceiving and measuring depth effects. For this, stereo-pair images are required, that is to say images of the same area of specimen, at exactly the same magnification but viewed from different tilt angles (typically differing by  $6-10^\circ$ ). The simplest system for viewing stereo-pairs involves mounting photographs side by side, with the tilt axis vertical, and observing them through a simple lens or prism viewer. A further requirement is that the observer should have 'stereopsis': the ability to 'see' in three dimensions (approximately 8% of the population do not have stereopsis). A variety of stereo-



— 10  $\mu\text{m}$  (a)



— 10  $\mu\text{m}$  (b)



— 10  $\mu\text{m}$  (c)

**Figure 6** Stereo pair SEM images of 1 kgf Vickers indentations in various materials. Tilt axis vertical, LH micrographs at normal incidence ( $0^\circ$ ), RH micrographs tilted  $10^\circ$ , except for (c) LH -  $37^\circ$ , RH -  $45^\circ$  and (e) LH -  $0^\circ$ , RH -  $8^\circ$ . (a)  $\{111\}$  Si, room temperature, showing extensive radial and deep lateral cracking, with partially removed debris lying above the indentation. (b) as (a), showing more extensive lateral fracture around a  $200^\circ\text{C}$  indentation. (c) Norton NC 203 hot-pressed SiC,  $800^\circ\text{C}$ , revealing intergranular radial and lateral fracture, whole grains of material having become detached.



— 10  $\mu\text{m}$  (d)



— 10  $\mu\text{m}$  (e)



— 10  $\mu\text{m}$  (f)

**Figure 6 continued.** (d) Carborundum sintered  $\alpha$ -SiC, 800°C, revealing surface tilting due to a lateral crack. (e) Pyrolytically-deposited  $\text{Si}_3\text{N}_4$ , 800°C. A deep lateral chip, part of which has become detached, is visible. (f) Norton NC 350 reaction-bonded  $\text{Si}_3\text{N}_4$ , room temperature. A lip of material overhangs the indentation profile, perhaps indicating differential elastic recovery ( see text ).

pairs of indentations in ceramic materials is displayed in figure 6.

### 2.3. MICROSTRUCTURAL CHARACTERIZATION

#### 2.3.1 Silicon

Single crystals were obtained from Texas Instruments (U.K.) Ltd., in the form of standard, transistor-grade {111} wafers, polished on one side. Two crystals were used: an n-type sample doped with  $5.3 \times 10^{14}$  atoms  $\text{cm}^{-3}$  of antimony (resistivity 9.15  $\Omega\text{cm}$ ) and a p-type sample doped with  $1.9 \times 10^{15}$  atoms  $\text{cm}^{-3}$  of boron (resistivity 7.05  $\Omega\text{cm}$ ) (46).

#### 2.3.2 Silicon Carbide

##### 2.3.2.1 Single Crystal SiC

Single crystals of silicon carbide were extracted from aggregates of abrasive-grade material obtained from Arendal Smelteverk (Norway). Two forms of material were available: one being opaque and coloured blue-black (suggesting both Fe and Al as impurities (19)), the other green in colour and transparent (suggesting nitrogen as an impurity (19)). Both forms displayed a hexagonal, platelike habit and samples from the same batch of blue-black crystals have been previously established (from X-ray rotation photographs) to be faulted, but of predominantly 6H polytype (12, 20). The green crystals have also been found to comprise largely 6H SiC, with rather more faulting than in the blue-black crystals (21).

Light microscopy and scanning electron microscopy (SEM) showed the polished specimens to be featureless except for occasional large pores and globular patches of a more reflective phase—possibly residual silicon or glass. These patches were more common in the green specimens, and were avoided in microhardness tests.

##### 2.3.2.2 Hot-pressed SiC

One form of hot-pressed SiC was available: Norton NC203, with  $\text{Al}_2\text{O}_3$  as the pressing additive. Other impurities are listed by Quinn (22), the most notable being tungsten, in the form of small ( $\approx 1\mu\text{m}$ ) globular particles of WC situated at the grain boundaries. These particles are thought to originate from the ball-milling stage in the fabrication of the material, and are particularly visible

(as specular white particles) in SEM micrographs (see figure 39) due to the high atomic number of W compared to the matrix (composed of Si, C, Al, etc.) - see 2.2. Energy dispersive X-ray (EDX) analysis (Link 860 system) confirmed the high proportion of W in these particles.

NC203 is a fully-dense form of SiC (predominantly  $\alpha$  polytypes (23)) with a grain size of approximately  $5\mu\text{m}$  as revealed by faint intergranular contrast observable in SEM secondary images.

#### 2.3.2.3 Sintered SiC

Two forms were examined: sintered  $\alpha$ -SiC ex Carborundum Co. and an experimental material prepared by Prof. H. Suzuki (of the Tokyo Institute of Technology).

The Carborundum sample was of early 1978 vintage, sintered with boron and carbon additives, the major impurity being Fe at 0.3wt.%(22). The sample was found to have a grain size of  $\sim 10\mu\text{m}$ , and about 4.5vol% residual porosity (see figure 40), homogeneously distributed across the specimen. The porosity is thought to be largely intergranular, again as revealed by faint intergranular contrast observable in SEM secondary images.

The 'Suzuki' sample was prepared (24) from submicron  $\beta$ -SiC powder, sintered for 1 hour at  $2100^\circ\text{C}$  in pure helium with 1wt% amorphous boron and 1wt% carbon black. It is claimed that this material has no grain boundary glassy phase (24). The material consists of elongated needle- or plate-like grains (approximate length  $20\mu\text{m}$ , width  $\sim 2\mu\text{m}$ ) with substantial ( $\sim 9\text{vol.}\%$ ) intergranular porosity (figure 41). The grain morphology suggests that the  $\beta$ -SiC has undergone a transformation to  $\alpha$ -SiC, accompanied by rapid grain growth during sintering (e.g.25).

#### 2.3.2.4 Reaction-Bonded SiC

Various samples of 'REFEL' reaction-bonded SiC were obtained from the United Kingdom Atomic Energy Authority, Springfields Division. Microstructures of this material have previously been described in detail by Sawyer and Page (1).

Two types of specimen, having different grain sizes ( $\sim 10\mu\text{m}$  and  $\sim 5\mu\text{m}$ ), were used. Both materials contained an interconnected network of residual silicon, 12-14% by volume, the

remainder being SiC of predominantly  $\alpha$  polytypes (1). Optically, the Si appears white and the SiC crystal array grey. The microstructure revealed by SEM micrographs (e.g. figs. 4, 8, 42) is described in section 2.5. Typical impurity contents in the SiC are listed in references 1, 13 and 17, the major impurities being Al, Fe, Ti, V in concentrations of the order of 100-300ppm, the SiC formed in the reaction being generally purer than that comprising the grit 'seed' particles (see 1.2.4.3).

A special series of doped materials (described in ref. 13) was also examined. Specimens were prepared by UKAEA (Springfields Division) using highly pure SiC grits ( $\alpha$  and  $\beta$ ) and transistor-grade silicon, with and without controlled additions of dopants such as boron carbide, aluminium and aluminium nitride (see 2.5).

### 2.3.3 Silicon Nitride

#### 2.3.3.1 Pyrolytically-Deposited $\text{Si}_3\text{N}_4$

The fabrication of this material has been described by Pitman and Godfrey (26) and samples were obtained from the Admiralty Marine Technology Establishment (Holton Heath). The specimens were green in colour and transparent (hence very pure) - the equiaxed grain structure of the material could be clearly revealed by viewing the material in reflection between crossed polars (see figure 43). The grain size was  $\sim 50\mu\text{m}$ , with a very small amount of porosity (not measured) at grain boundaries. The material has been reported to consist entirely of  $\alpha\text{-Si}_3\text{N}_4$  (26).

#### 2.3.3.2 Hot-Pressed $\text{Si}_3\text{N}_4$

Two forms of hot-pressed  $\text{Si}_3\text{N}_4$  ex Norton Co. (USA) were available, designated NC132 (1977 vintage) and NCX 34 (1978 vintage). Both materials were fully dense and have been reported to comprise largely  $\beta\text{-Si}_3\text{N}_4$  (22).

NC132 contains  $\sim 5\text{wt}\%$  MgO (pressing additive) (22) and secondary and backscattered SEM images (fig. 44) also revealed specular white particles, apparently distributed around  $\sim 5\mu\text{m}$  sized grains, similar to those observed in Norton NC203 hot-pressed SiC. EDX analysis of the particles showed them to be rich in W, Si and often Fe and/or Ni. The presence of such particles has been reported previously (e.g. 27), and they are again presumed to originate from

ball-milling of the starting powder used in the fabrication procedure.

NCX 34, containing 8wt%  $Y_2O_3$  (22), was also found to contain W-rich particles, but SEM images (figure 45) also revealed networks of diffuse light-imaging material clearly delineating the grain structure and revealing occasional large ( $\sim 20\mu m$ ) grains. These light regions were found by EDX analysis to be rich in yttrium, and are assumed to correspond to a thick grain boundary phase.

#### 2.3.3.3 Reaction Bonded $Si_3N_4$

Two materials were examined: Norton NC350 (reference number Con 6 FY78 QE) and Ford '2.7' reaction-bonded silicon nitrides. Both materials were highly porous (21vol% porosity for NC350 and 13vol% for Ford '2.7' (22)). The porosity in NC350 was fine-scale (typical pore size  $\sim 1\mu m$ ) and homogeneously distributed, whereas in the Ford material, large pores or clusters of pores were often observed (fig. 46). Very little residual silicon was observed in either sample and grain sizes appeared to be of the order of  $1\mu m$  or less in both materials.

NC350 has been reported to comprise 72wt%  $\alpha-Si_3N_4$  (the remainder being  $\beta-Si_3N_4$ ), whilst Ford '2.7' has a slightly higher proportion of 80wt%  $\alpha-Si_3N_4$  (22) and contains fairly high proportions of Fe, due to the 3wt%  $Fe_2O_3$  addition used to enhance nitridation (22).

#### 2.3.4. Sialon

The single material examined was Lucas SYALON ceramic 342, of the type described in 1.2.5, with  $z = 0.5$  and containing  $\beta'$ -sialon, an yttrium-containing glass, with minor amounts of SiC and possibly silicides (28,29). The material was pressureless sintered. SEM micrographs (fig. 47) revealed a predominantly fine grain size of  $\sim 1\mu m$  but with several large grains (often elongated) up to  $10\mu m$  in size. Grains were surrounded by a phase showing diffuse white contrast, as in NCX 34 hot-pressed  $Si_3N_4$ . The material also contained a small amount of residual porosity.

#### 2.3.5. Boron Carbide

Two forms of sintered boron carbide, designated S1143

MATERIAL	SOURCE	Main Polycrystalline	Grain Size #	Porosity #	ROOM TEMPERATURE VALUES			
					Young's Modulus (GPa)	Vickers Hardness (HV)	Fracture Toughness ( $K_{IC}$ ) (MPa $\sqrt{m}$ )	Poisson's Ratio ( $\nu$ )
<u>SILICON CARBIDE</u> (001) single crystal	Arendal Smelterwerk (Norway)	a (20)	-	-	446 (30)	34.5 [±1]	3.4 (34)	0.2 (19)
Hot-pressed	Norton MC203	a (23)	~5µm	-	438 (31)	31.7 [±0.7]	6.1 (34) 4.0 (35)	0.17 (22)
Sintered (a)	Carborundum Co.	a (*)	~10µm	4.5 vol. %	406 (*)	29.9 [±0.4]	4.6 (*)	0.15 (*)
(b)	Experimental batch from Prof. H. Suzuki (130)	a (24)	Needles or plates: Length ~20µm Width ~2µm	9 vol. %	400 (estimated)	25.7 [±0.3]	-	-
Reaction-bonded	UKAEA, Springfield	a (1)	a) ~10µm b) ~5µm	None, but 12-14 vol. % unreacted silicon	400 (+)	a) 21.3 [±0.5] b) 27 [±2]	4.4 (34)	0.24 (+)
<u>SILICON NITRIDE</u> Pyrolytically-deposited	Admiralty Marine Technology Estab., Bolton leath.	a (26)	~50µm	small amount (not measured)	312 (26)	37.0 [±1]	-	-
Reaction-bonded (a)	Ford '2.7'	80wt% 20wt% B (22)	~1µm	13 vol. % (22)	210 (22)	15.3 [±0.3]	-	0.22 (22)
(b)	Norton MC350	72wt% 28wt% B (22)	~1µm	21 vol. % (22)	180 (22)	8.8 [±0.2]	1.7-2.1 (35-38)	0.22 (22)
Hot-pressed (a)	Norton MC132	largely B (22)	~5µm	-	320 (22)	21.7 [±0.3]	4-6.2 (22, 35, 39, 40)	0.27 (22)
(b)	Norton MCX34	largely B (22)	~5µm - some grains ~20µm	-	310 (22)	18.1 [±0.2]	5.9 (22)	0.27 (22)
<u>SIALON</u> Sintered SYALON	Lucas 342	B' (29)	~1µm; some grains ~10µm	small amount (not measured)	~300 (45)	16.2 [±0.2]	5-6 (29) 3.1-4.9 (41)	Not known
<u>SIC</u> Sintered (a)	Le Carbone S1143	-	~5µm	2.8 vol. %	383 (32)	33.5 [±0.4]	1.8 (32)	0.14 (32)
(b)	Le Carbone S1138	-	~5µm	22.5 vol. %	240 (32)	14.1 [±1]	-	-
<u>SILICON</u> (111) single crystal	Texas Instruments (U.K.)	-	-	-	168 (33)	11 [±0.1]	0.8 (42)	0.27 (43) (polycrystalline value)

Table 2. Properties of the materials investigated. Vickers hardness values were obtained in this investigation and have been averaged over the load range used and finally expressed as a projected area Vickers hardness value.

\* Carborundum Technical Data Sheet  
+ UKAEA Technical Data Sheet  
# Measured from optical/SEM images

(density  $2.40 \text{ gcm}^{-3}$ ) and S1138 (density  $2.05 \text{ gcm}^{-3}$ ), were obtained from Le Carbone (GB) Ltd. Both materials were porous, the denser form containing 2.5vol% porosity, the less dense form 22.5vol% porosity. The porosity was inhomogeneously distributed in both samples (fig. 48), with pore sizes of up to  $\sim 7 \mu\text{m}$ . Whilst clear intergranular contrast was not observed optically or in the SEM, grain shapes were occasionally delineated by the porosity in the less dense form, indicating a grain size of approximately  $5 \mu\text{m}$ .

#### 2.4. INDENTATION TECHNIQUES

Where only microhardness measurements made at room temperature and under ambient conditions were required, a Leitz "Miniload" microhardness tester, fitted with either Vickers or Knoop indenter, was used. Hardness values measured with this instrument were found to be the same (within experimental errors) as obtained using the hot-hardness tester described below.

Hot-hardness experiments were carried out in a Wilberforce Scientific Developments (Coventry, U.K.) high-temperature microhardness tester coupled to a four-inch oil diffusion pump with liquid nitrogen trapping (fig. 7). The instrument consists of specimen and indenter assemblies together with heating furnaces and water cooling systems contained in a sealed stainless steel vessel capable of evacuation to  $\sim 2 \times 10^{-7}$  torr to  $10^{-6}$  torr (with the furnaces outgassed and running at  $800^\circ\text{C}$ ), with gas-bleed facilities for operating in controlled gaseous environments, typically Ar or  $\text{N}_2$ . All the experiments described here were performed 'in vacuo' to prevent furnace oxidation and indenter graphitization and to exclude (as far as possible) any environmental or 'Rebinder' effects which are important in some ceramic materials (e.g. 3).

Polished specimens were bonded to a stainless steel stub with a refractory aluminium orthophosphate cement\* which was cured at  $\sim 200^\circ\text{C}$  for a few hours. The stub, to which a chromel alumel thermocouple was spot-welded, was then screwed onto a pedestal in the bottom of the specimen furnace assembly within the instrument (fig. 7d).

---

Footnote: \* The cement was formed by mixing 100 and 200 mesh alumina powders in equal amounts and mixing to a stiff paste with dilute (1:5 v/v in water) orthophosphoric acid.

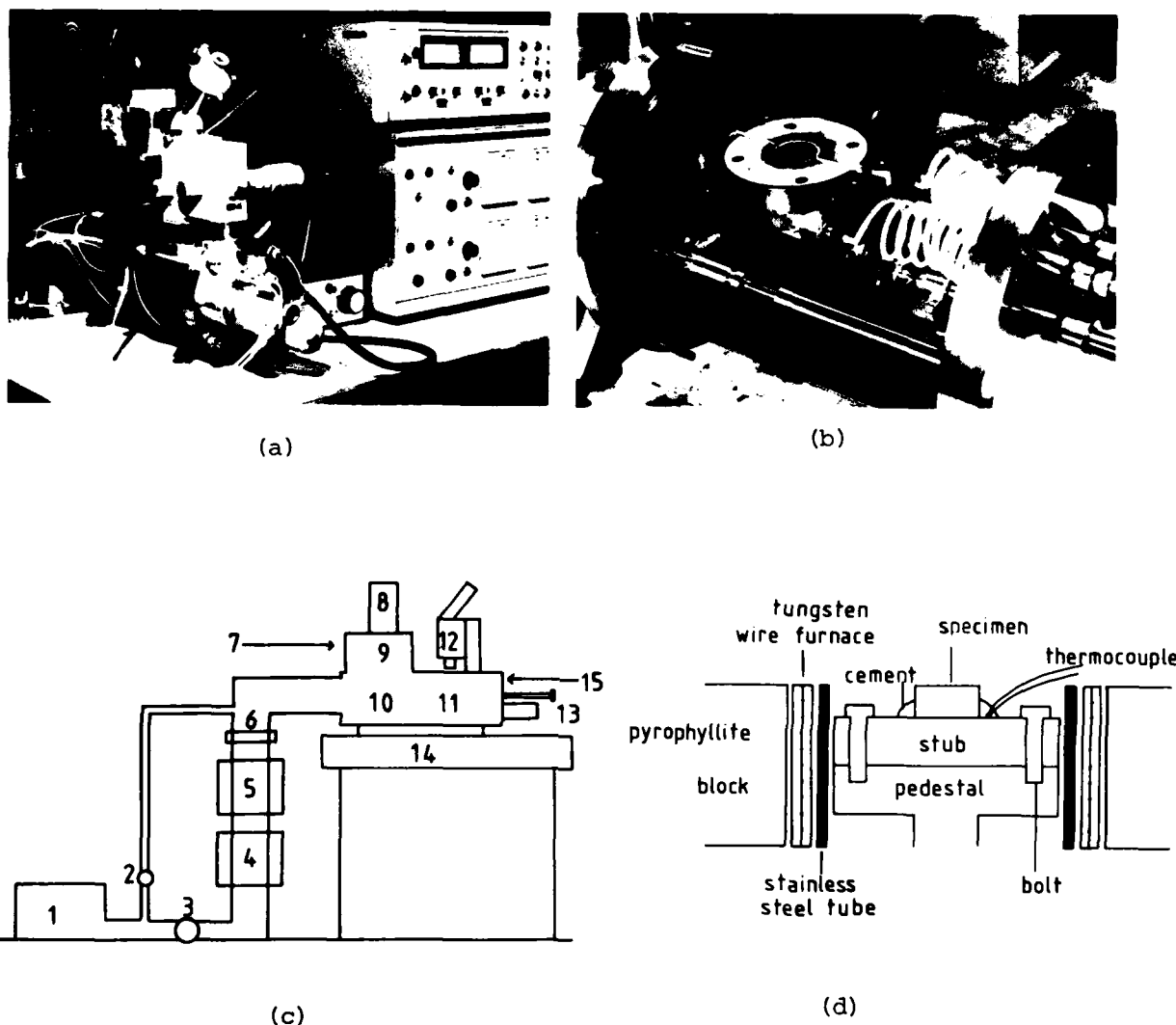


**Figure 7** The temperature/environment-controlled microhardness tester.

(a) General view showing the control consoles. (b) The specimen furnace assembly. (c) Schematic layout of the system ( see key below ).

(d) Schematic layout of the specimen furnace assembly.

Key: (1) rotary pump, vacuum switch, Pirani head, (2) roughing valve, (3) backing valve, (4) 4" oil diffusion pump, (5) liquid nitrogen trap, (6) 1/4 swing butterfly valve, Pirani and Penning guage heads, air inlet valve, (7) gas bleed location ( coupled to leak valves ), water cooling and electrical feed-throughs to indenter furnace, (8) loading system, (9) indenter plus heater assembly with external dashpot, (10) specimen furnace assembly in the 'indent' position, (11) specimen furnace assembly in the 'view' position beneath the quartz window, (12) microscope with long working distance objective, (13) specimen traverse/rotate controls, (14) concrete bench, (15) water cooling and electrical inlets to specimen furnace.

The entire specimen assembly was capable of rotation and translation in orthogonal directions controlled by external micrometers. In the 'viewing' position (fig.7c), the specimen could be examined through a water-cooled 1.8 mm quartz window by a Zeiss Epignost II microscope fitted with a Leitz long working distance objective lens and a screw micrometer measuring-eyepiece. For heating, the whole furnace unit could be translated to a position directly underneath the indenter assembly, which comprised a mechanically-retained diamond (Knoop or Vickers profile) on a stainless steel shank contained in its own separately-controlled furnace and loaded by a series of weights stacked in a stepped cylinder. Winding this cylinder down resulted in progressively more weights being lowered onto a collar in the indenter shank. An external oil dashpot controlled the descent of the indenter, and various electrical contacts on the supporting double cantilever assembly enabled the loading time to be controlled for each indentation.

Vickers and Knoop hot-hardness experiments were generally performed at loads of 100, 200, 500 and 1000gf with a constant indenter dwell time of 15 seconds. Normally, 5 indentations were made at each of the lower loads, 10 at 1000gf. Measurements were generally made at 100°C or 200°C intervals (as considered appropriate), with at least half an hour being allowed for matching and stabilization of indenter and specimen temperatures prior to indentation. The maximum operating temperature was found, in practice, to be ~1000°C due to the short lifetime of the tungsten wire furnaces at this temperature (continuous currents of 3-5A being required to maintain 1000°C). It was this limitation which made high-temperature indentation creep experiments (performed by varying the indenter dwell time at constant load and temperature) infeasible for long dwell times. Vickers indentations on single crystals were made at constant crystallographic orientation: for (0001) SiC, the two indenter diagonals were aligned along  $\langle 11\bar{2}0 \rangle$  and  $\langle 10\bar{1}0 \rangle$ ; for {111} Si, the chosen directions were  $\langle 1\bar{1}0 \rangle$  |  $\langle \bar{1}\bar{1}2 \rangle$ . Knoop hardness anisotropy experiments are described in section 3.4.3.

In all cases, indentations were observed at temperature and subsequently examined both optically and by SEM. Measurements were often made at temperature, although this was not generally found to be

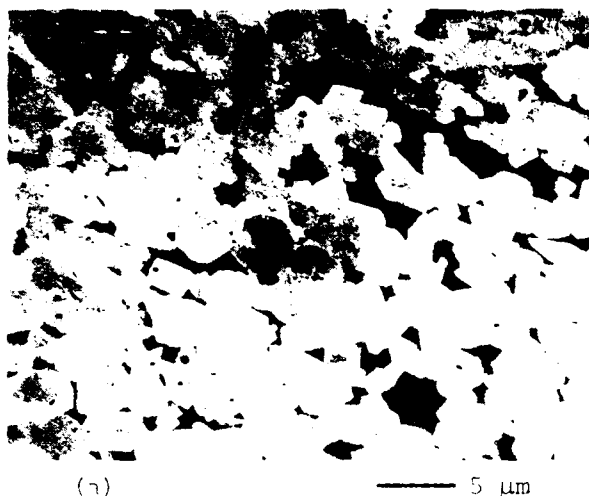
necessary, since indentation/crack sizes did not change appreciably with time or subsequent heating.

## 2.5 APPENDIX: SECONDARY ELECTRON SEM CONTRAST IN 'REFEL' REACTION-BONDED SiC

'REFEL' reaction-bonded SiC has previously been shown to exhibit unusual secondary electron SEM contrast (1) - see fig.4c (corresponding to exactly the same area as the backscattered image shown in fig. 4b). In the secondary image, SiC grains (as revealed by the channelling contrast in fig.4b) are seen to comprise bright outer regions and angular central cores, which are usually dark, but sometimes light. The boundaries between dark cores and light coatings are always sharp. Residual silicon appears as dark irregular patches.

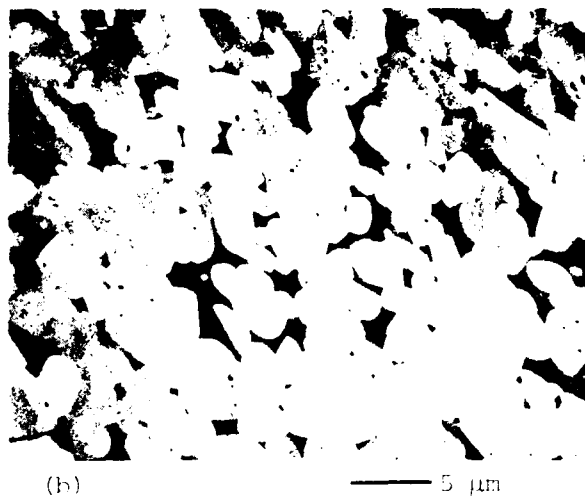
It has been demonstrated (1) that the grain cores correspond to the SiC grit 'seed' particles used in the fabrication procedure (see 1.2.4.3), and the coatings to 'new' SiC, formed in the reaction-bonding process, and depositing mainly epitaxially on the seeds (1). It has been further suggested (1) that the contrast is due to the distribution of trace impurities (especially aluminium) within the SiC, the darker cores being substantially less pure (with ~100ppm of Al, Fe, V, Ti) than the epitaxial reaction-formed material. A mechanism has been proposed (1, 12) to account for this phenomenon, in which donor and (especially) acceptor states created by impurities in the band gap of the material are thought to be responsible for increased secondary electron scattering probability, hence decreased escape probability. By this means, pure material was predicted to have a higher value of  $\delta$  than impure SiC, although donors might also act to increase the supply of secondary electrons.

For this investigation, a series of specially-prepared samples of 'REFEL', with varying impurity content, was available (see 2.3.2.4), thus providing an opportunity to test the above hypothesis. Figure 8 shows secondary electron images of these samples: in fig.8a, a material prepared from comparatively pure starting materials (the  $\alpha$ -SiC grit contained ~300ppm Al, ~90 ppm N and ~20ppm B (13)) is seen to exhibit relatively little contrast within the SiC, save for occasional light grain cores. The above model would predict light epitaxial material surrounding light grain cores (assuming the specially-prepared starting grit to be



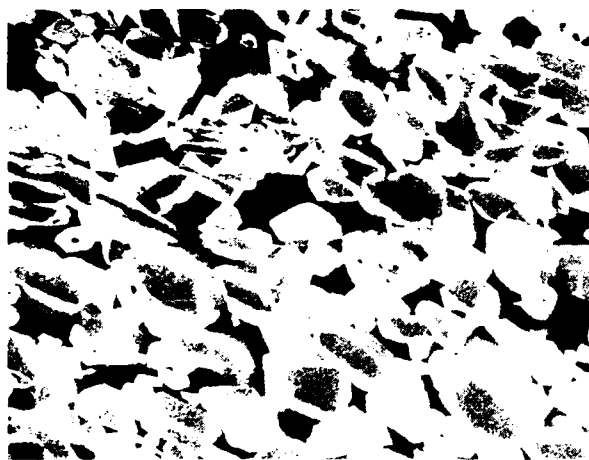
(a)

5 μm



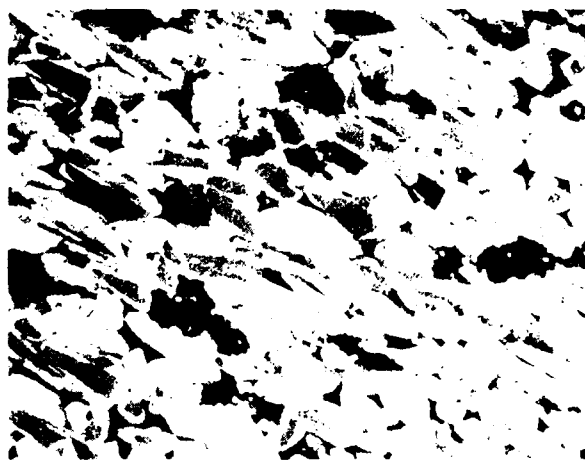
(b)

5 μm



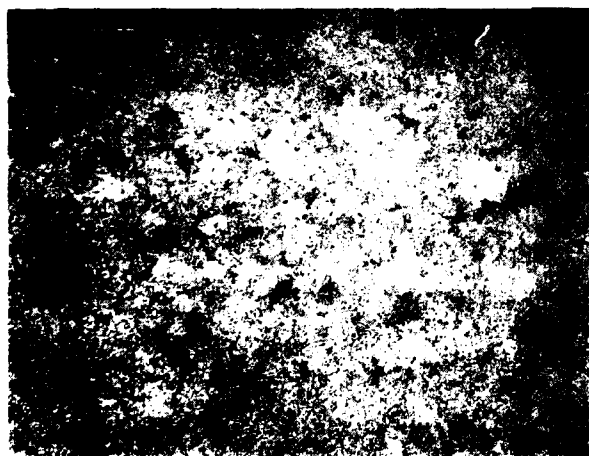
(c)

5 μm



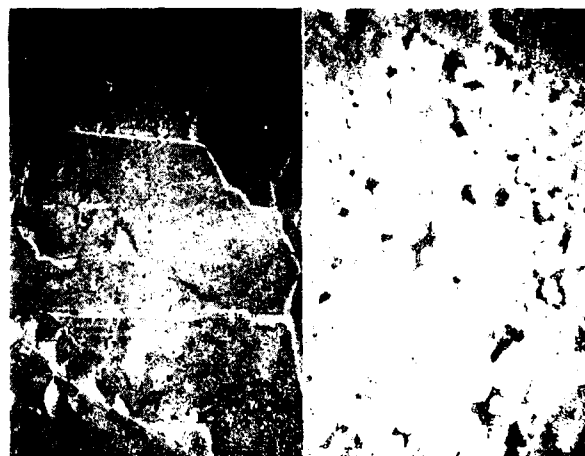
(d)

5 μm



(e)

5 μm



(f)

5 μm

Figure 1. Scanning electron micrographs of silicon carbide surfaces after 1000 h of thermal oxidation at 1400°C. (a) 100% SiC, (b) 100% SiC, (c) 100% SiC, (d) 100% SiC, (e) 100% SiC, (f) 100% SiC.

Figure 1. Scanning electron micrographs of silicon carbide surfaces after 1000 h of thermal oxidation at 1400°C. (a) 100% SiC, (b) 100% SiC, (c) 100% SiC, (d) 100% SiC, (e) 100% SiC, (f) 100% SiC.

sufficiently pure). Figure 8b shows a material prepared from the same constituents as the 'pure' sample, but with additives of boron (as 2wt%  $B_4C$  present in the green compact, corresponding to  $\sim 1000\text{ppm}$  B in the final material (13)). The secondary electron image is similar to that observed for the 'pure' sample, but with rather more light grain cores. The model predicts light grain cores\* with dark (p-type) epitaxial material, which would be a fair interpretation of fig.8b. However, the same results would be expected for doping with Al, and in this case the observed image (fig.8c) is the exact opposite, showing the contrast normally observable in commercial samples: predominantly dark cores with light epitaxial material. Similar results were obtained for the AlN doped materials (fig.8d), which would be expected to behave like undoped samples, since AlN should have no net electrical effect. Images similar to figs. 8c and 8d were observed for dopant levels ranging from 0.1wt% to 5wt% of dopant present in the green compact (0.1wt% Al produced  $\sim 600\text{ppm}$  in the final material; 0.1wt% AlN produced  $\sim 300\text{ppm}$  Al (13)).

Additionally, fig.8e shows undoped 'REFEL' made from  $\beta$ -SiC starting grit (little contrast and comparatively little residual silicon) and fig.8f shows the same form of material doped with  $B_4C$ . This has evidently resulted in a phase transformation accompanied by rapid grain growth of large plates of  $\alpha$ -SiC, hundreds of microns across, the remaining  $\beta$ -SiC again showing little or no secondary electron contrast.

The implications of these results are that the contrast is indeed impurity-sensitive, but in a different or more complex way to the model proposed by Sawyer and Page (1). Ostensibly, it is only the presence of Al (added either elementally or as AlN) which causes the epitaxial layer to have a higher value of secondary electron coefficient than the grain cores, in contradiction of the above model. However, interpretation of fig.8 might be misleading without knowledge of the precise impurity contents of each microstructural feature: for instance North et al. (13,44) have reported that the Al-doped materials may have preferentially absorbed nitrogen from the atmosphere inside the reaction chamber (air at 1-2 mmHg),

---

Footnote: \*diffusion distances during the reaction-bonding process are thought to be too small for diffusion of impurities into the grit seeds (1).

rendering the epitaxial material effectively intrinsic. There is a great need for high resolution chemical analysis, for example by secondary ion mass spectrometry (SIMS) (14) (impurity levels are far too low for X-ray analysis). Equally, it would be desirable to make precise measurements of the image grey levels of grain cores and epitaxial coatings for each sample under identical instrument conditions. In addition, it may prove instructive to relate the secondary electron contrast to electrolytic etching behaviour, which has also been found to be impurity-sensitive for SiC (15).

There are further puzzling aspects to the contrast observed: for instance, in a very small percentage of grain cores, parallel-sided bands of light or dark material occur (fig.4d). This contrast would appear to be in some way crystallographic (possibly due to twins), although the bands do not extend into the epitaxial material, which might be expected to have the same crystallographic stacking sequence as the seed (1, 16). Another interesting observation is that, in some cases, the outside region of the epitaxial material images dark, giving rise to a 'sandwich' effect (1). This occurs particularly near the outer edges of a material (17), which suggests that the diffusion of some gaseous species in from the furnace atmosphere is responsible. In some cases (such as fig.4d), the effect is so pronounced that only thin, often discontinuous, layers of white epitaxial material are present around the grain cores.

In summary, SEM secondary images of REFEL SiC display contrast which is sensitive to trace impurity levels far below those required for conventional X-ray microanalysis. Experiments with specially-doped materials indicate (but do not prove) that Al is likely to be the active dopant. A model to account for this will probably have to await a more detailed theoretical understanding of secondary electron emission. Similar behaviour is observable in other microstructural forms of SiC (e.g. 15,17), although the contrast levels are generally lower than in REFEL SiC. The technique of secondary electron imaging may be useful in studying such phenomena as high-temperature diffusion of impurities or impurity segregation during phase transformations in SiC (15).

2.6. REFERENCES

1. G.R. Sawyer and T.F. Page, 1978, J. Mater. Sci. 13, 885.
2. J.B. Brinton, 1982, Electronics, January 13th 1982, p.40.
3. A.R.C. Westwood, J.S. Ahearn and J.J. Mills, 1981, Colloids and Surfaces 2, 1.
4. G.R. Booker, 1970, in "Modern Diffraction and Imaging Techniques in Materials Science", eds. S. Amelinckx, R.Gevers, G. Remaut and J. van Landuyt (North-Holland), p.553.
5. J.I. Goldstein, D.E. Newbury, P. Echlin, D.C. Joy, C. Fiori and E. Lifshin, 1981, "Scanning Electron Microscopy and X-ray Microanalysis", Plenum Press.
6. G.R. Booker, 1970, as ref. 4, p.613.
7. H. Niedrig, 1978, Scanning 1, 17.
8. P. Morin, M. Pitaval, D.Besnard and G. Fontaine, 1979, Phil. Mag. A 40, 511.
9. J. Lankford and D.L. Davidson, 1979, J. Mater. Sci. 14, 1675.
10. A.W. Ruff, 1976, Wear 40, 59.
11. Idem, 1978, ibid. 46, 251.
12. G.R. Sawyer, 1979, Ph.D. thesis, University of Cambridge.
13. B. North and K.E. Gilchrist, 1981, Am. Ceram. Soc. Bull. 60, 549.
14. S.J.B. Reed, 1980, Scanning 3, 119.
15. N.W. Jepps and T.F. Page, 1981, J. Microsc. 124, 227.
16. G.R. Sawyer and T.F. Page, 1980, J. Mater. Sci. 15, 1850.
17. M.G.S. Naylor, 1978, M. Phil. thesis, University of Cambridge, Department of Metallurgy and Materials Science.
18. A. Boyde, 1973, J. Microsc. 98, 452.
19. R.C. Marshall, J.W. Faust, Jr. and C.E. Ryan (eds.), 1973, "Silicon Carbide - 1973", Proc. 3rd. Int. Conf. on SiC Florida, University of South Carolina Press.
20. G.R. Sawyer, P.M. Sargent and T.F. Page, 1980, J. Mater. Sci. 15, 1001.
21. S.G. Roberts, 1982, private communication.
22. G.D. Quinn, 1980, Technical Report to U.S. Department of Energy by AMMRC, Interagency Agreement EC-76-A-1017.

23. O.O. Adewoye, 1976, Ph.D. thesis, University of Cambridge.
24. H. Suzuki, 1980, private communication.
25. S. Prochazka, 1973, in ref. 19, p.394.
26. K.C. Pitman and D.J. Godfrey, 1978, Proc. Brit. Ceram. Soc. 26, 225.
27. R.L. Tsai and R. Raj, 1980, J. Am. Ceram. Soc. 63, 513.
28. R.J. Lumby, 1980, private communication.
29. M.H. Lewis, A.R. Bhatti, R.J. Lumby and B. North, 1980, J. Mater. Sci. 15, 103.
30. R.W. Rice, 1977, Treatise on Materials Science and Technology 11, ed. R.K. MacCrone, Academic Press, p.199.
31. J.W. Edington, D.J. Rowcliffe and J.L. Henshall, 1975, Powder Met. Int. 7, 82.
32. G.W. Hollenberg and G. Walther, 1980, J. Am. Ceram. Soc. 63, 610.
33. B.R. Lawn, A.G. Evans and D.B. Marshall, 1980, *ibid.* 63, 574.
34. J.L. Henshall, 1975, Ph.D. thesis, University of Cambridge.
35. G.R. Anstis, P. Chantikul, B.R. Lawn and D.B. Marshall, 1981, J. Am. Ceram. Soc. 64, 533.
36. D.R. Messier, L.J. Schioler and G.D. Quinn, 1981, Am. Ceram. Soc. Bull. 60, 812.
37. D.C. Larsen and G.C. Walther, 1978, Illinois Institute of Technology Interim. Tech. Report No. 5. IITRI-D6614-ITR-30.
38. R.R. Wills, M.G. Mendiratta and J.J. Petrovic, 1976, J. Mater. Sci. 11, 1330.
39. G.K. Bansal, 1977, in "Ceramic Microstructures 1976", eds. R.M. Fulrath and J.A. Pask, Westview Press, Boulder, Colorado, p.860.
40. G.K. Bansal and W.H. Duckworth, 1980, Am. Ceram. Soc. Bull. 59, 254.
41. M.H. Lewis, R. Fung and D.M.R. Taplin, 1981, J. Mater. Sci. 16, 3437.
42. C.P. Chen and H. Leipold, 1980, Am. Ceram. Soc. Bull. 59, 469.
43. A. Kelly, 1966, "Strong Solids", Clarendon Press, Oxford.
44. B. North and P. Kennedy, 1981, private communication.
45. R.N. Katz, 1980, Science 208, 841.
46. P.J.C. Mathis, 1982, private communication.

### CHAPTER 3

#### INDENTATION PLASTICITY

In this chapter, plasticity mechanisms in ultra-brittle ceramic materials are examined using the results of indentation hardness tests. The subject is highly complex, with a large body of relevant literature (e.g. 1-1971) incorporating many different theoretical interpretations of experimental results. For this reason, the length of this chapter is perhaps disproportionately great. In some sections (notably 3.3), conclusions are drawn from a combination of results obtained in this investigation and from the literature. Experimental data obtained in this study are summarized at the end of each relevant section and again in the concluding section (3.10).

#### 3.1 PLASTICITY IN BRITTLE MATERIALS

In this section, the term plasticity is used loosely to refer to any irreversible deformation mechanism, excluding brittle fracture. A full review of plasticity in ceramics is not attempted here- the subject is immense and has been extensively reviewed elsewhere (e.g. 1-4). The purpose of this section is merely to provide a background to the more detailed discussions of indentation plasticity in brittle materials presented later.

Plastic deformation may be divided into two broad categories, namely grain processes (including dislocation glide, climb, kinking and also twinning) and grain boundary processes (e.g. grain boundary sliding, diffusional and viscous creep). Grain processes will be considered first.

##### 3.1.1 Grain Processes

Dislocation activity may be observed in all ceramics, albeit on limited slip systems (e.g. 5), for instance  $\text{Si}_3\text{N}_4$  forms  $\{10\bar{1}0\}\langle 0001 \rangle$  dislocations (5,6) which (if glissile) would produce two independent slip systems only. Secondary slip systems are as yet unknown. 6H SiC shows prismatic slip ( $\{10\bar{1}0\}\langle 11\bar{2}0 \rangle$ ) (5,7) with basal ( $(0001)\langle 11\bar{2}0 \rangle$ ) (7) secondary slip, which would produce a total of four independent shear strains if they act independently.

Neither material satisfies the von Mises criterion ( 8 ) of five independent slip systems for a general small, homogeneous strain without change in volume. In principle,  $\beta$ -SiC, in common with other sphalerite materials ( e.g. diamond, Si, Ge ), has twelve available  $\{111\}\langle\bar{1}\bar{1}0\rangle$  slip systems, however the von Mises criterion is not satisfied until slip may occur homogeneously within each grain and the various slip systems may interpenetrate freely ( 9 ). All these materials are brittle at room temperature, the critical resolved shear stress ( CRSS ) for dislocation glide being large ( e.g. 3 ).

High CRSS values are generally a consequence of high Peierls' stresses in covalent materials ( e.g. 10 ) and dislocation-impurity and dislocation-dislocation interactions in ionic materials ( e.g. 11-13 ). These factors arise from the nature of atomic bonding in ceramics, which give rise to problems of charge neutrality in ionic solids and bond breaking and stretching in covalent materials.

Dislocation structures in tetrahedrally co-ordinated cubic semiconductors ( e.g. Si,  $\beta$ -SiC ) have been reviewed by Hirsch ( 14 ) and further observations of dislocations in semiconductors may be found in ref. 15. It seems that dislocations are often resolved into partials and that bond reconstruction may take place in the core structure of these partials, minimizing ( or even eliminating ) the need for dangling bonds.

Dislocation movement is thought to occur by the formation and lateral propagation of double kinks on dislocation lines ( e.g. 14-17 ). The Peierls' mechanism in covalent materials has been modelled by Gilman ( 16,17 ) in terms of phonon-assisted quantum mechanical tunnelling of bonding electrons into non-bonding states. Activation barriers for double kink formation and migration have been modelled by various authors ( e.g. 18-23 ) in the context of predicting dopant effects on plasticity ( see section 3.5 ). The Peierls' mechanism in an ionic material ( MgO ) has been modelled atomistically by Woo and Puls ( 24 ).

Strain-hardening has been reported in ionic materials ( e.g. 11, 12, 25, 26 ), mechanisms being either dislocation dipole interactions ( athermal ) or dislocation-vacancy interactions ( thermally activated ) or both. High concentrations of both types of defect may be formed as 'dislocation debris' by cross glide of

screw dislocations, which are more mobile than edge dislocations at low temperatures ( 11,12 ). Strain-hardening and recovery effects are also observed in covalent materials such as Si and Ge tested in compression at high temperatures ( 10 ), the resolved shear stress versus shear strain curves showing up to five distinct stages ( depending on temperature and strain rate ) ( 27 ).

Finally, on the subject of dislocation glide, it is worth emphasizing that limited slip may actually nucleate cracks ( e.g. 28-31 ), for instance at the intersection of slip bands with grain boundaries ( 32-34 ) or by slip band interaction ( 28-30, 35-37 ). The potential role of plasticity in crack propagation has been recently reviewed ( 38 ), with the conclusion that crack tip micro-plasticity probably does not occur at room temperature in Si, Ge, SiC and  $Al_2O_3$  . For many ceramic materials , slip planes are also cleavage planes, which might reflect preferential fracture along planar slip bands ( as observed in some metal alloys ( e.g. 39 ) ).

Twinning, another potentially important grain deformation process, is observed in some materials ( e.g.  $Al_2O_3$  ( 41 ) and Si ( 42 ) ). Twinning may or may not produce strain, and may cause premature fracture due to stress concentration if not accommodated by other mechanisms ( 4 ).

A deformation mechanism which is well-known in the field of rock mechanics is that of microcracking ( e.g. 40 ). Whilst this is not true plastic deformation, large strains ( of the order of 10% ) may be produced in otherwise brittle rocks when tested in compression with confining pressures, simply by the arrested growth of large numbers of microcracks. This mechanism may operate with or without accompanying plastic flow ( depending on temperature, material, etc. ), and may be important wherever significant crack-arresting stresses exist ( e.g. in indentation ).

### 3.1.2 Grain Boundary Processes

Whilst grain processes have received most attention in previous fundamental studies of deformation in ceramics, grain boundary processes are not well understood. This is unfortunate, since such processes dominate under many conditions of applied stress/strain rate/temperature ( e.g. 13, 71, 72 ). Studies of grain boundary

deformation mechanisms are hindered by the comparative lack of information on boundary structure, which have only been investigated for certain ceramics, such as Si and Ge ( e.g. 43-47 ), oxides ( e.g. 48-51 ), SiC ( e.g. 52-54 ) and  $\text{Si}_3\text{N}_4$  and sialon materials sintered or hot-pressed with various additives ( e.g. 6, 55-62 ). In the latter case, thin ( usually 10-20 Å ) glassy films have been observed along boundaries and especially at triple grain junctions. Unambiguous evidence for periodic boundary structures similar to those observed in metals ( see e.g. 51 ) seems to be limited to artificially-produced bicrystals ( e.g. 43-48, 51, 54 ) and to low-angle grain boundaries in polycrystalline materials of high purity ( i.e. where thick glassy films are not present ) ( e.g. 49-51 ).

Grain boundaries are known to play a particularly significant role in high-temperature processes such as creep: Coble creep involves mass transport along boundaries from compressive to tensile regions, and has been postulated to occur in SiC above 1900°C ( 63 ). Nabarro-Herring creep involves mass transport through grains with the boundaries acting as vacancy sources/sinks ( 64,65 ). Where grain boundary phases are present, creep often occurs by high-temperature grain boundary sliding accompanied by viscous and/or diffusive growth of grain boundary cavities ( especially at triple junctions ) ( 66 ). Design of grain boundaries to minimize these effects has been described in section 1.2.5.

High-temperature subcritical crack growth often involves viscous cavity nucleation ( and growth ) by grain boundary sliding ahead of the primary crack tip ( 67 ). In the absence of boundary glass phases, slow crack growth perhaps involves thermally-activated intergranular bond rupture at the crack tip or diffusion-controlled cavity growth from triple junctions ( 61 ). Although boundary sliding is essential for cavity nucleation, it is not necessarily the rate-limiting step ( 68 ). In some temperature regimes, boundary sliding may cause crack blunting, decreasing the rate of subcritical crack growth ( 67 ).

Whether grain boundary sliding, in its own right, may be considered a deformation mechanism contributing plastic strain is reviewed by Dokko and Pask ( 4 ), the conditions for such a contribution being unclear. Grain boundary sliding in MgO above 1700°C has been described in detail by Day and Stokes ( 69 ).

Boundary porosity was found to promote sliding by (a) providing the source, (b) decreasing the interfacial contact area and (c) preventing grain boundary migration, which produces corrugations in the interface which interfere with sliding. Boundary migration may, in other systems, act to relieve the stress concentrations caused by sliding, and may also facilitate slip transfer across boundaries ( 4 ). The effect of sliding and migration on grain boundary structure is unclear.

An interesting observation is that grain boundaries in MgO may initiate dislocations at a stress independent of the grain size and below the microyield stress ( 70 ). It is uncertain whether this effect occurs generally.

To summarize, plastic deformation in ceramics may take place by grain or grain boundary processes, which may act independently, co-operatively, or even competitively. There is a great need for further investigations of both the processes themselves and their interactions with each other, as a function of material parameters ( e.g. microstructure, impurity content, etc. ) and external variables ( e.g. applied stress, strain rate, temperature, chemical environment, etc. ).

### 3.2 HARDNESS AND YIELD STRESS

In order to measure the indentation hardness  $H$  of a solid, a hard indenter of specified shape is pressed with load  $P$  onto a specimen surface, forming a permanent impression of area  $A$  ( which may be defined either as the projected or actual area ). The hardness is then defined as  $H = P/A$ , the mean pressure over the indentation. Since the indentation is formed by plastic deformation,  $H$  may be related to the plastic properties of the material ( 73, 74 ).

For fully strain-hardened metals, where the indentation process itself produces no increase in flow stress, the material approximates to a rigid-plastic solid, for which plasticity slip-line theory may be used. For blunt\*, wedge-shaped indenters, this model predicts  $H = k Y_0$  where  $Y_0$  is the yield stress for the material

---

\* indenters with large semi-apical angle  $\psi$ , including Vickers, Knoop and Rockwell indenters.

and the constraint factor  $k=3$  ( 73 ). For materials which are not fully strain-hardened,  $H \approx 3Y$ , where  $Y$  is the uniaxial flow stress at an effective strain which is calculated to be  $\sim 8-10\%$  for Vickers indenters ( 73 ).

The above solution assumes a rigid hinterland constraining the plastic region beneath the indenter, but if the hinterland can deform elastically, the constraint on plastic flow is reduced and  $k < 3$ . Indeed, for Vickers indentations in many solids, material is observed to be displaced radially into the bulk rather than outward towards the surface to form a lip of material piled up around the indentation (as predicted by slip-line theory). This has been modelled by Marsh ( 75 ), who considered indentation as equivalent to expansion of a spherical cavity into an elastic-plastic solid, a model originally developed by Dugdale ( 197 ) and subsequently by Hill ( 76 ) and others. In this model, the material in a hemispherical core immediately beneath the indenter is assumed to be under a hydrostatic pressure equal to the indentation pressure  $H$ . Surrounding this core is a plastically-deformed shell over which the plastic strains diminish radially until they match the plastic strains in the hinterland at the elastic-plastic zone boundary ( see fig. 9 and ref. 77 ). Marsh ( 75 ) derived an expression for the constraint factor:

$$(H/Y) = 2/3(1 + \ln \left[ \frac{E}{3(1-\nu)Y} \right]) \quad \text{for } 2/3 \leq (H/Y) < 3$$

where  $E$  = Young's modulus and  $\nu$  = Poisson's ratio.

$(H/Y)$  thus increases with increasing  $(E/Y)$  ratio, until a limiting value of 3 is reached for materials of high  $(E/Y)$  ratio ( metals ) in which there is little elastic strain in the hinterland and material displaced by the indenter is accommodated by piling up around the indentation ( surface-directed displacement ). Ceramic materials generally have low values of  $(E/Y)$  and exhibit radial displacement of material ( 75 ).

Subsequently, the above model has been refined by various workers: Hirst and Howse ( 78 ) obtained data for wedge indenters of varying angles, concluding that the plastic-rigid approximation was valid only for acute indenter angles and materials of low elasticity ( high  $(E/Y)$  ratio ). For blunter indenters and elastic materials, indentation was observed to become elastic-plastic in nature and the

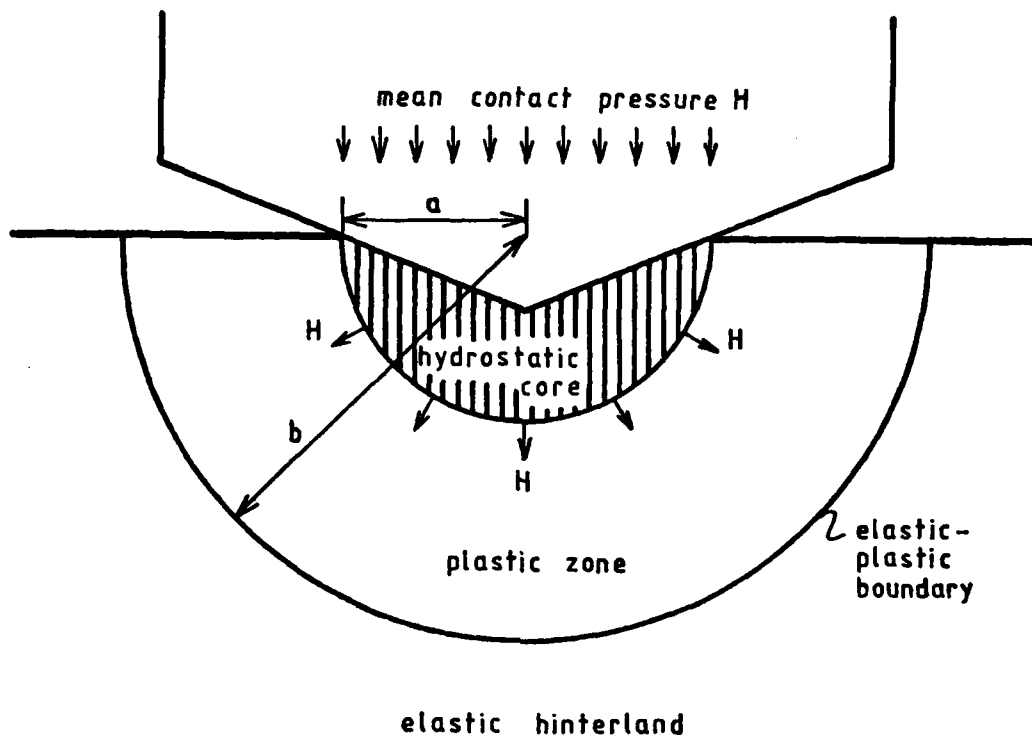


**Figure 9.** The expanding spherical cavity model for indentation of elastic-plastic solids ( after Johnson ( 77 ) ). The indentation process is regarded as the expansion of a hemispherical core where the pressure ( =  $H$  ) is assumed to be hydrostatic. Surrounding this is a plastically deformed region which is confined by the elastic hinterland.

expanding cavity model applies. In the limit of very blunt indenters and highly elastic materials, the process becomes entirely elastic. Johnson ( 77 ) introduced an indenter shape term into the expanding cavity model by assuming no surface pile-up of material and that the volume of the indentation is accommodated in the elastic hinterland. This model was further refined by assuming that the hemispherical core is a region in which the stresses change from purely hydrostatic to values which satisfy the von Mises yield criterion ( 79 ). For conical or pyramidal indenters:

$$(H/Y) = 0.5 + 2/3 \left( 1 + \ln \left[ \frac{Ecot\psi}{3Y} \right] \right) \quad \text{for } \nu = 0.5.$$

All the above models assume no strain-hardening of the material. This effect has been considered by Gerk ( 80 ) using a true-strain approach and simple strain-dependent flow stress relations.

More recently, the applicability of expanding cavity models to elastic-plastic indentation has been questioned ( e.g. 81 ) because in some regards they are physically unreasonable ( for instance, such models neglect entirely the free-surface ). Both the rigid-plastic and expanding cavity theories require the uniform distribution of stresses across the face of the indenter, which is only found to be the case for acute indenter angles and materials of high (E/Y) ratio ( 76 ). The indentation model due to Perrott ( 81 ) assumes radial displacement of material, but not necessarily uniform outward movement. Perrott's stress field is essentially the elastic Boussinesq ( 82 ) solution for surface contact by sharp indenters, modified by incorporation of the von Mises yield criterion. The analysis gave:

$$(H/Y) = 0.494 + 0.577 \ln \left[ \frac{Ecot\psi}{Y(1-\nu^2)} \right] \quad \text{for } (H/Y) < 3.$$

A model based on elastic-plastic indentation stresses has recently been developed by Chiang et al. ( 196 ) by modifying Hill's spherical cavity solution to eliminate stresses normal to the free surface and also in-plane shear stresses at the surface, by application of suitable point forces. The analysis provided an improved correlation between (H/Y) and (E/Y), but the relation may not be written in simple form ( see ref. 196 ).

Further improvement of such theories must await better modelling of indentation stress fields, which may shortly be forthcoming ( 83 ). In addition, the effects of friction between indenter and specimen must be considered ( see ref. 77 ). In order to illustrate some of the deficiencies in current theories, two examples are given.

Single crystal of the halite structure ( e.g. KCl ) have been found ( 84 ) to have  $(H/Y) \approx 35$ , where  $Y$  is the yield stress on the primary slip system. This has been attributed to strain-hardening by Gerk ( 85 ), but a better explanation has been described by Gilman ( 84 ). The strain around an indentation requires five independent shears ( 8 ), whilst the primary slip system in halite structure crystals is usually  $\{110\}\langle 1\bar{1}0 \rangle$ , which has only three independent shears ( 9 ). Thus, the activation of secondary slip, probably on  $\{100\}\langle 1\bar{1}0 \rangle$  systems, is required ( or else a different deformation mode entirely ). The critical resolved shear stress for yield on such systems may be significantly ( e.g. a hundred times ) higher than that of the primary ( e.g. 87 ), resulting in higher hardness values.

The anomalous indentation behaviour of metallic glasses has been well documented ( e.g. 86 ): such materials have  $(H/Y)$  values close to three and exhibit surface-directed displacement ( pile-up ) around indentations. Theory predicts  $(H/Y)$  values around half the above value and radial displacement of material. Possible explanations ( e.g. work-softening, shear band deformation ) have been considered by Sargent ( 86 ).

In the final analysis, the flow stress measured by an indentation experiment is that for whatever deformation mechanism ( or combination of mechanisms ) operates beneath the indenter. For brittle materials at low temperatures, this is often ( as will be seen in following sections ) not simply dislocation glide.

### 3.3 INDENTATION PLASTICITY IN BRITTLE MATERIALS

Even the most brittle materials form permanent plastic impressions in response to surface contact by hard, sharp indenters ( e.g. 88-90, 94 ). This is a consequence of the stress field generated by indentation ( section 4.2 ), which generally contains large, localized shear components ( causing slip ) and local hydrostatic compression ( inhibiting massive cracking ). Various tensile stresses are also generated, causing arrested growth of a number of crack geometries ( discussed in Chapter 4 ).

Thus, indentation hardness measurements provide the easiest method of studying plasticity in brittle solids ( section 1.3 ). In this section, the influence of temperature on plasticity mechanisms in ultra-brittle ceramic materials is examined by considering the

hot-hardness behaviour of single crystal materials ( Si, SiC and  $\text{Si}_3\text{N}_4$  ), using results from this study and from the literature.

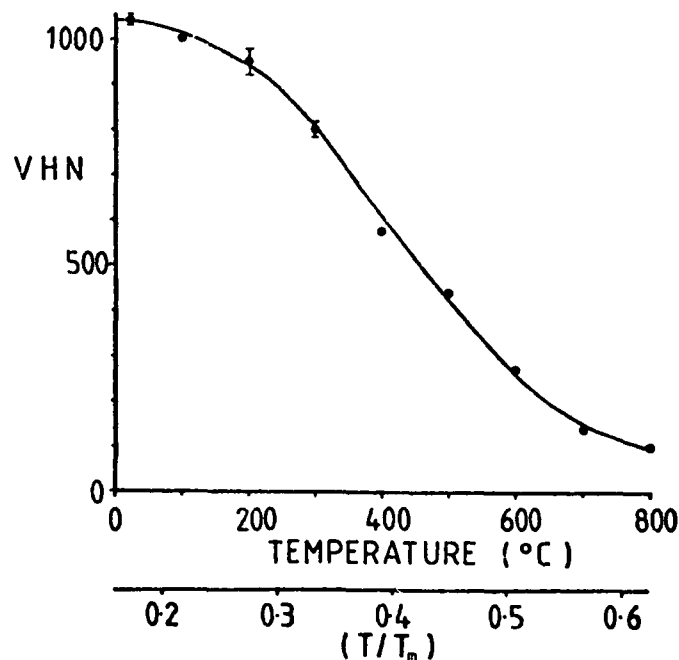
### 3.3.1 Experimental Hot-Hardness Behaviour of Single Crystals

The hot-hardness behaviour of covalent crystals of the diamond structure ( termed sphalerites, and including Si, Ge and  $\beta\text{-SiC}$  ) is typified by that of silicon ( see refs. 91, 92 and fig. 10 ). At low temperatures, hardness decreases only weakly with temperature, whilst at high temperatures, hardness decreases strongly with increasing temperature. For silicon, the transition temperature  $T_c$  is approximately  $0.4 - 0.5 T_m$  ( 91-93 ): for the {111} crystal investigated here,  $T_c$  was found to be  $\sim 350^\circ\text{C}$  (  $0.36 T_m$  ) ( fig. 10c ). The change is often described as a 'ductile-brittle' transition ( e.g. 93 ), but care must be exercised in this. Indentation fracture ( possibly caused by dislocation interaction ) persists up to  $700^\circ\text{C}$  for 1 kgf Vickers indentations ( section 4.4.1 ), the fracture toughness remaining constant over the whole temperature range ( section 4.4.2 ). Thus, the transition is not a conventional ductile-brittle transition: it reflects a change from stress-activated to thermally activated plastic deformation under the stress state peculiar to indentation, rather than a change from fully brittle to fully plastic behaviour.

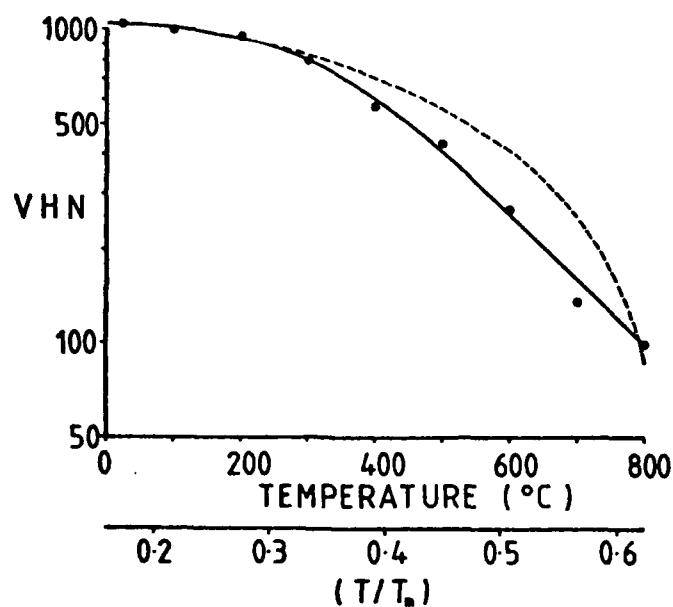
At temperatures slightly above  $T_c$ , direct evidence for substantial dislocation activity around indentations in {111} silicon is observable ( fig. 11 ) in the form of slip steps along  $\langle 1\bar{1}0 \rangle$  directions ( {111} traces ). Slip steps formed spontaneously at indentation temperatures of  $600^\circ\text{C}$  and above. At  $500^\circ\text{C}$ , slip steps formed over a time scale of a few minutes after indentation, suggesting limited dislocation mobility at this temperature. Slip steps were observed to move further away from indentations with increasing anneal time at  $500^\circ\text{C}$  ( indentation times were kept constant at 15s ) ( figs. 11 b,c ). Slip steps were also observed to form around indentations made at lower temperatures which were heated to  $500^\circ\text{C}$  or above.

These observations confirm previous dislocation etch-pitting studies ( e.g. 42, 94-97 ) and are further confirmed by selected area electron channelling pattern ( SACP ) studies. Figures 12 a-e show SACP's taken at various distances from a room temperature Vickers indentation in {111} silicon, whilst figs. 12 f-j were taken at similar distances from an  $800^\circ\text{C}$  indentation. Degradation of the

(a)



(b)



(c)

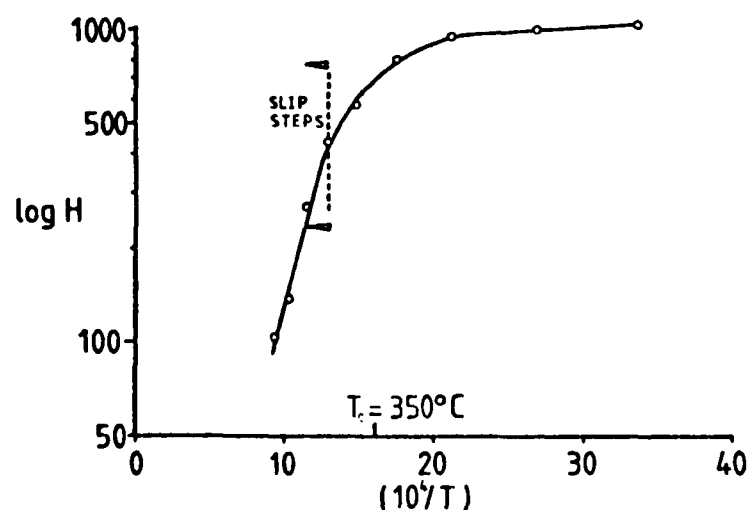
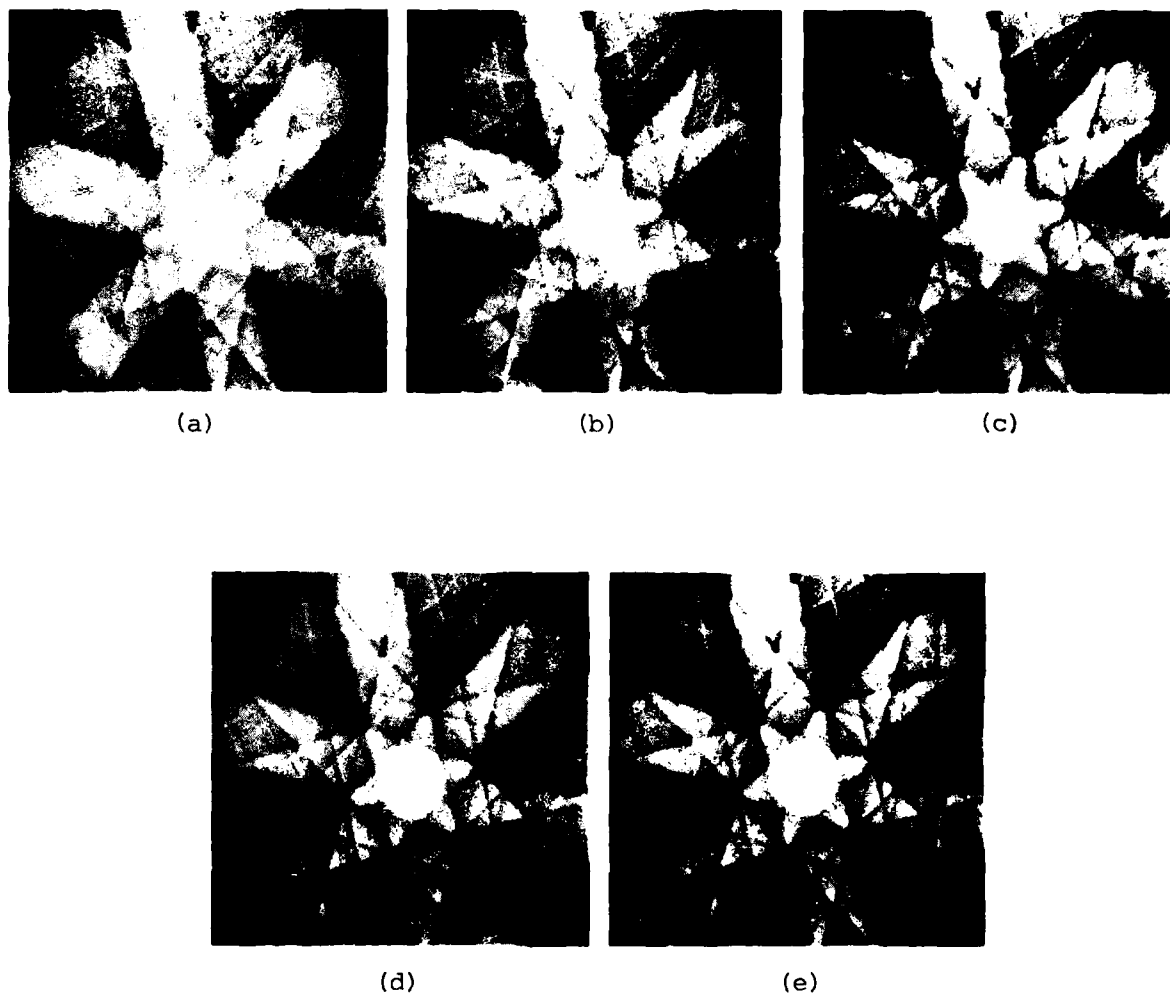


Figure 10. The variation of Vickers hardness ( 100 gf applied load and 15s dwell time ) with temperature for n-type {111} single crystal silicon: (a) linear plot, (b) logarithmic hardness scale ( dashed curve represents best fit hardness values calculated from the Gilman expression ( section 3.3.2.2 ) ), (c) activation energy plot of  $\log H$  against  $(10^4/T)$ . Error bars indicate one standard error in the mean



**Figure 11** Slip activity around Vickers indentations ( 1 kgf load ) in  $\{111\}$  single crystal silicon as a function of temperature, as revealed by Nomarski differential interference contrast. Indentations were aligned with one indenter diagonal parallel to  $\langle 1\bar{1}0 \rangle$ . (a) Room temperature indentation displaying severe indentation fracture. (b) 500°C indentation cooled within a few minutes of the indentation being made.  $\langle 1\bar{1}0 \rangle$  slip steps are visible but are of limited extent. (c) as (b) but with the specimen held at 500°C for  $\sim 20$  minutes after indentation. More extensive slip steps are evident. (d) 800°C indentation showing extensive and clearly-defined  $\langle 1\bar{1}0 \rangle$  slip steps but no indentation fracture.



**Figure 12** Selected area electron channelling patterns ( SACPs ) from regions around room temperature and 800°C Vickers indentations ( 1 kgf load ) in {111} single crystal silicon ( solid state detector, 40 kV beam voltage ). ( a-e ) SACPs taken at progressively greater distances from a line of room temperature indentations, which is visible as three blurred images superimposed on the channelling pattern. In (e), the closest indentation is at an approximate distance of twice the pattern radius out from the centre. Note the degradation of the pattern in image (a).

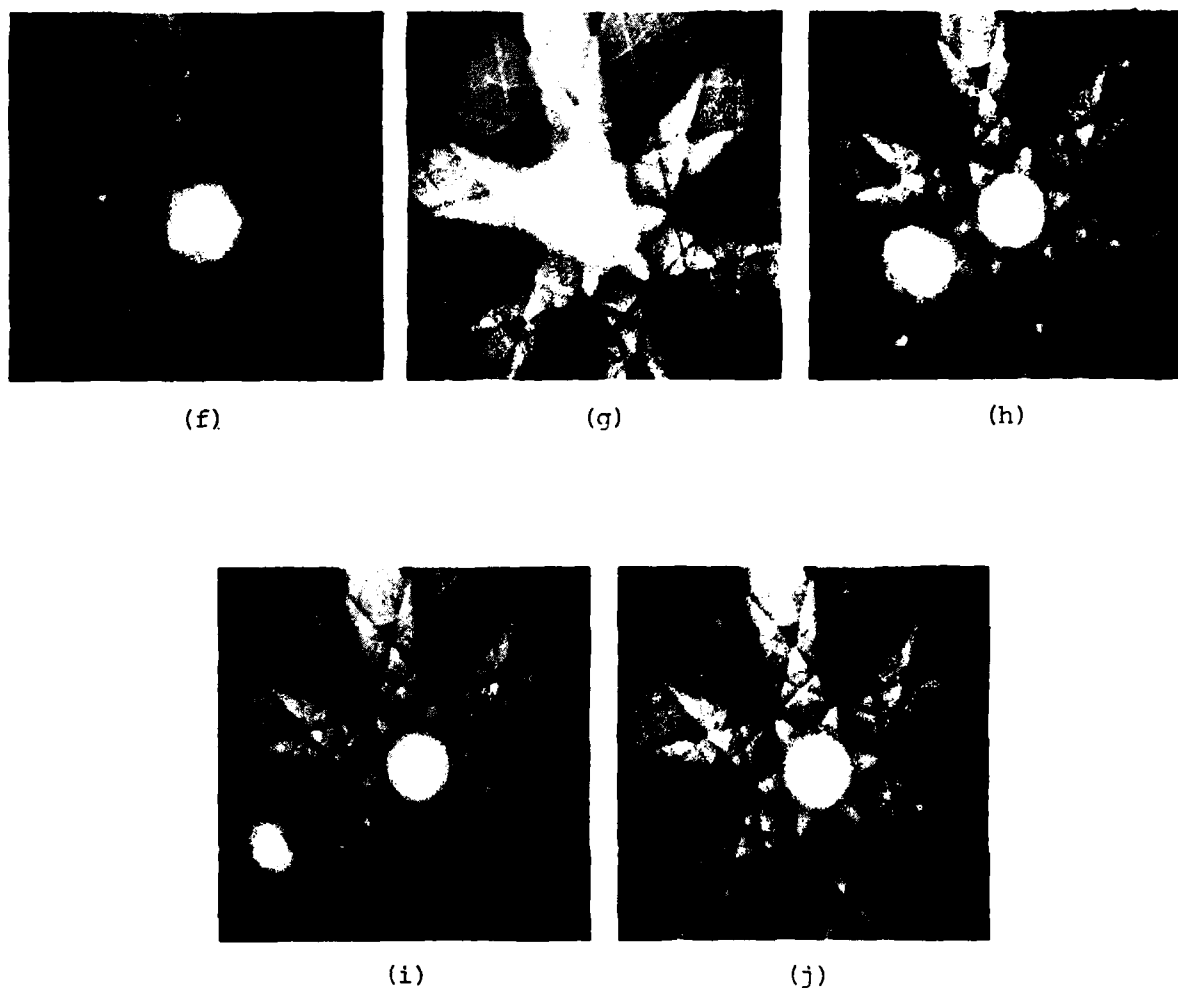


Figure 12 continued. ( f-j ) SACPs at increasing distances from an 800°C indentation ( approximate diagonal length 110  $\mu\text{m}$  ). Image j was taken at a distance of roughly twice the pattern radius away from the indentation. Note the degradation of high order lines in images f, g and possibly h.

patterns ( e.g. absence of high order lines ) persists to greater distances from the  $800^{\circ}\text{C}$  indentation ( although the poor spatial resolution of these images spoils the effect ), suggesting greater slip activity at  $800^{\circ}\text{C}$ .

The form of hardness/temperature response observed for silicon is by no means common to all materials. Silicon carbide, for example, has a transition temperature  $T_c$  of only  $0.15 - 0.25 T_m$  ( ref. 98 and fig. 13 ). The precise value of  $T_c$  was found in this investigation to depend on various factors, including indenter:crystal orientation ( fig. 13 d ), discussed in section 3.4, and crystal colour ( i.e. specimen purity ) ( fig. 13 c ), discussed in section 3.5.

Silicon carbide does not form slip steps until temperatures substantially higher than the transition temperature observed in hot-hardness curves: slip steps around indentations are not observed below  $800^{\circ}\text{C}$  (  $\sim 0.35 T_m$  ) ( ref. 98 and fig. 14 ). For  $800^{\circ}\text{C}$  Knoop indentations in prismatic faces of SiC single crystals, slip steps were observed along (0001) traces only ( figs. 14 b-f ). Thus, it is likely that basal slip ( (0001) $\langle 11\bar{2}0 \rangle$  ) is the dominant slip system in SiC at high temperatures ( see section 3.4.3 ). Polycrystalline forms of SiC were also observed to form slip steps ( presumably basal ) around Vickers and Knoop indentations made at  $800^{\circ}\text{C}$  and above ( figs. 39,40,42 ). Basal faces of both green and blue/black SiC did not form slip steps around indentations made at or above  $800^{\circ}\text{C}$ , and substantial lateral cracking was observed around such indentations ( fig. 14 a ). Evidently, basal slip does not provide the necessary displacements of material required for the formation of indentations in basal sections ( this is more fully discussed in section 3.4 ).

By plotting hot-hardness data for prismatic faces on a  $\log H$  versus  $(1/T)$  plot ( fig. 13 e ), it was established that no second change in activation energy occurred due to the formation of slip steps at  $800^{\circ}\text{C}$  ( since few data were obtained for temperatures greater than  $800^{\circ}\text{C}$  in this investigation, the Vickers hot-hardness data of Hirai and Niihara ( 99 ) have been included in fig. 13 e ). Thus, the appearance of surface slip steps is unlikely to reflect a change in deformation mechanism, and is discussed in section 3.3.2.3.

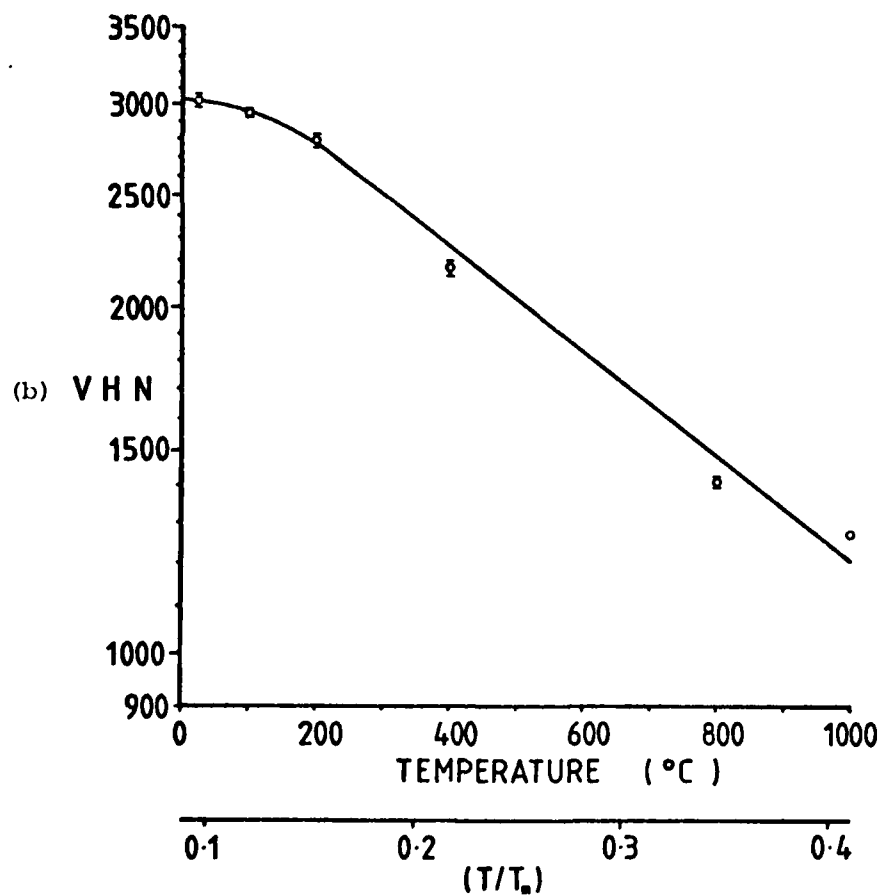
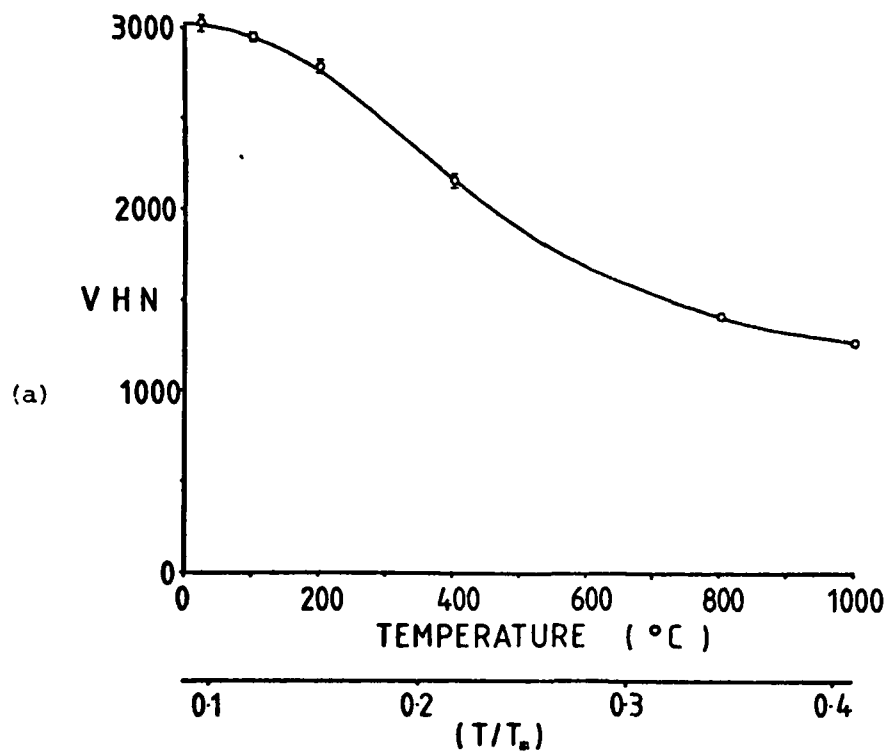


Figure 13. The variation of Vickers and Knoop hardness ( various loads, 15s dwell time ) with temperature for single crystals of SiC: (a) Vickers hardness ( 1 kgf load ) of blue-black (0001) SiC, linear plot, (b) as (a), logarithmic hardness scale. Error bars indicate one standard error in the mean for approximately 5 - 10 indentations.

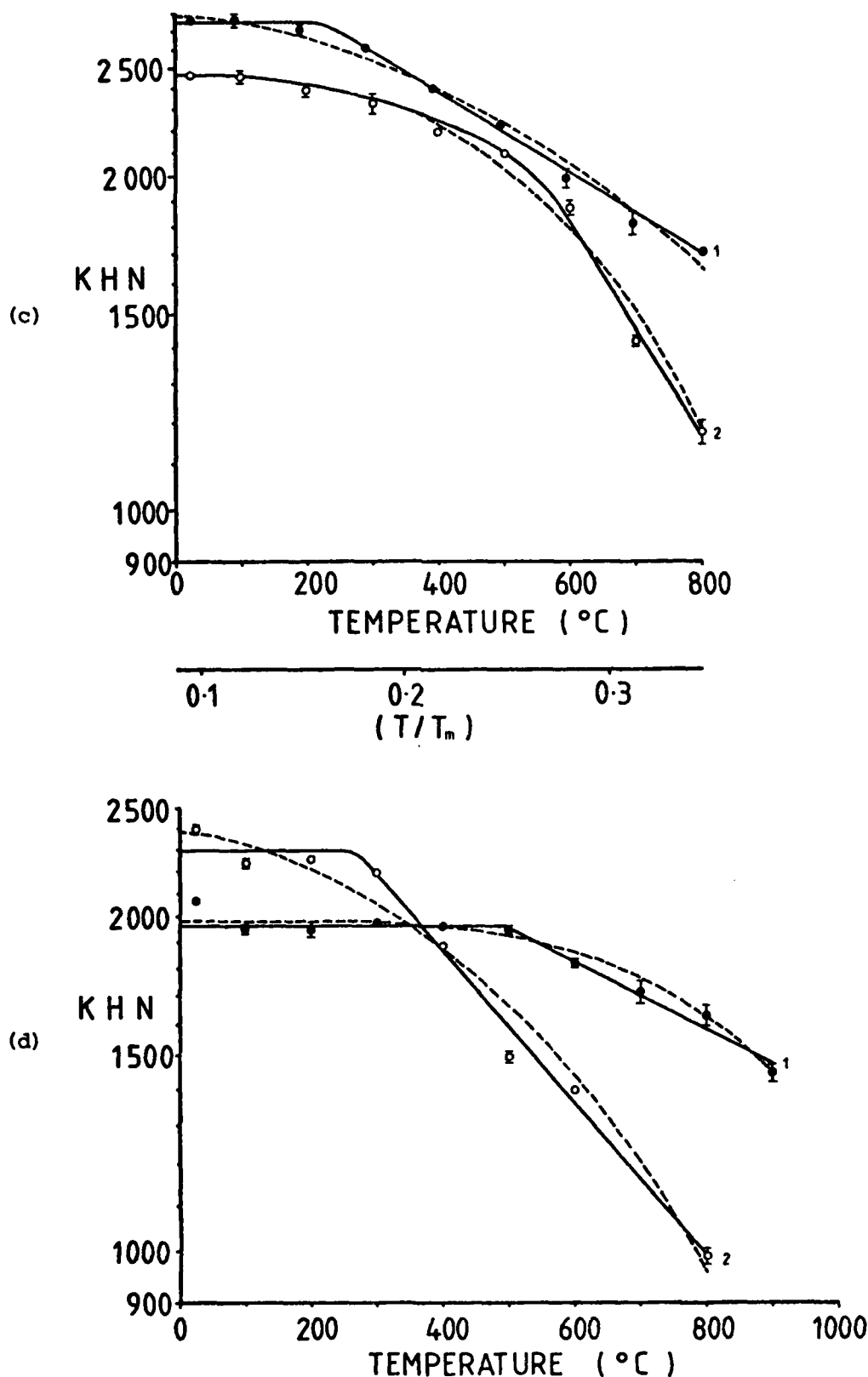


Fig. 13 (c) The variation of Knoop hardness ( 200 gf load, 15s dwell time, logarithmic scale ) with temperature for (0001) single crystals of SiC: curve 1 = blue-black SiC, curve 2 = green SiC. Dashed curves represent best fit hardness values calculated from the Gilman expression ( section 3.3.2.2 ). (d) Knoop hardness ( 200 gf load, 15s dwell time, logarithmic scale ) versus temperature for green  $\{11\bar{2}0\}$  single crystal SiC: curve 1 = long indenter axis parallel to [0001], curve 2 =  $\langle 10\bar{1}0 \rangle$  orientation. Dashed curves as above. Error bars indicate one standard error in the mean for approximately 5 indentations.

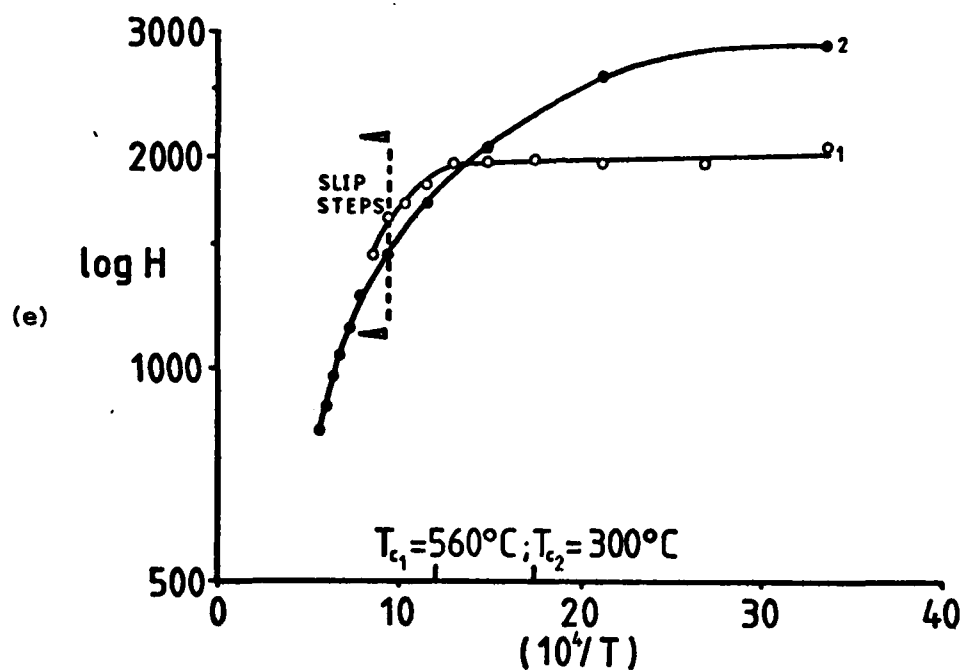


Fig. 13 (e) Activation energy plots of log H against  $(10^4/T)$  for  $\{11\bar{2}0\}$  single crystal SiC: curve 1 = Knoop hardness ( 200 gf load, 15s dwell time ), experimental data from this investigation, curve 2 = Vickers hardness ( 100 gf load, 10s dwell time ), data of Hirai and Niihara ( 99 ). In both cases, one indenter diagonal ( the long one for Knoop indentations ) was aligned along  $[0001]$ . Note that the appearance of surface slip steps at  $800^{\circ}\text{C}$  does not cause a discontinuity in activation energy.



Figure 14 Slip activity around 800°C Knoop indentations ( 200 gf load ) in single crystal SiC as a function of crystallographic orientation ( Nomarski differential interference contrast ). (a) (0001) face, long indenter axis 40° from  $\langle 11\bar{2}0 \rangle$ . No slip steps are evident and severe indentation fracture is apparent. (b)  $\{11\bar{2}0\}$  face, indentation along  $\langle 10\bar{1}0 \rangle$ . Note the slip steps parallel to the indentation. (c)  $\{11\bar{2}0\}$  face, indentations 30° from  $\langle 10\bar{1}0 \rangle$ . (d)  $\{10\bar{1}0\}$  face, indentation along  $\langle 11\bar{2}0 \rangle$ . Slip steps lie parallel to the indentation. Subsurface lateral fracture is evident. (e)  $\{10\bar{1}0\}$  face, indentation 40° from  $\langle 11\bar{2}0 \rangle$ . (f)  $\{10\bar{1}0\}$  face, indentation parallel to  $[0001]$ . Slip steps are along  $\langle 11\bar{2}0 \rangle$  and are less extensive than in (d) or (e).

Activation energies for the variation of hardness with temperature in the high-temperature ( $T > T_c$ ) region were calculated from the slopes of  $\log H$  versus  $(1/T)$  plots for the single crystal SiC samples (table 3). There were found to be differences in activation energy for different indenter:crystal orientations (section 3.4.3) and for differently coloured materials (which may be an impurity effect as discussed in section 3.5), but little variation due to indenter profile. For comparison, the activation energy calculated for {111} silicon (data in fig. 10), with Vickers indentation diagonals along  $\langle 1\bar{1}0 \rangle$  and  $\langle \bar{1}\bar{1}2 \rangle$ , was  $35 (\pm 3) \text{ kJmol}^{-1}$  above  $400^\circ\text{C}$ . The calculation and interpretation of activation energies from hot-hardness data is further discussed in section 3.8.

The Knoop hot-hardness of single crystal  $\alpha\text{-Si}_3\text{N}_4$  has been measured in the range  $25\text{-}1500^\circ\text{C}$  by Niihara and Hirai (100). Plotting their results as  $\log H$  versus  $T$ , they found no transition in behaviour as described above. However, the slope of the  $\log H$  versus  $T$  plot is not related directly to the activation energy (although large changes in activation energy are often revealed by such plots). Accordingly, some of the experimental data of Niihara and Hirai (for four different orientations) has been re-plotted as  $\log H$  versus  $(1/T)$  in figure 15, which reveals a transition in activation energy occurring over the temperature range  $400\text{-}700^\circ\text{C}$  ( $\sim 0.3\text{-}0.45 T_m$ ). High-temperature ( $T > T_c$ ) activation energies calculated from these data are presented in table 4, the values being similar to those determined for SiC (table 3), although the variation with indenter orientation is less pronounced for  $\text{Si}_3\text{N}_4$ .

Slip steps around indentations were not found by Niihara and Hirai for any orientation or temperature, for reasons discussed in section 3.3.2.3.

In order to explain the differences in hot-hardness behaviour described in this section, we must first account for the general form of the hot-hardness plot, which involves a knowledge of the deformation mechanisms acting within each temperature regime.

Crystal Colour:	Crystal face:	Indenter diagonal parallel to:	Indenter profile:	Activation Energy (kJmol <sup>-1</sup> ):
Blue-Black	(0001)	$\langle 11\bar{2}0 \rangle$	Vickers	5.2 ( $\pm 0.9$ )
Blue-Black	(0001)	$\langle 11\bar{2}0 \rangle$	Knoop	5.9 ( $\pm 0.2$ )
Green	(0001)	$\langle 11\bar{2}0 \rangle$	Knoop	13.6 ( $\pm 2.2$ )
Green	$\{11\bar{2}0\}$	[0001]	Knoop	6.1 ( $\pm 1.2$ )
Green	$\{11\bar{2}0\}$	$\langle 10\bar{1}0 \rangle$	Knoop	9.3 ( $\pm 1.2$ )

**Table 3** Activation energies calculated from high-temperature ( $T > T_c$ ) hot-hardness data for single crystals of SiC as functions of crystal colour, indenter orientation and indenter profile. Indentation load 200gf in each case; indenter dwell time = 15s. Errors are one standard error in the mean.

Crystal face:	Indenter diagonal parallel to:	Activation Energy (kJmol <sup>-1</sup> ):
(0001)	$\langle 11\bar{2}0 \rangle$	7.9 ( $\pm 1.1$ )
(0001)	$\langle 10\bar{1}0 \rangle$	8.4 ( $\pm 0.7$ )
$\{10\bar{1}0\}$	[0001]	6.9 ( $\pm 0.4$ )
$\{10\bar{1}0\}$	$\langle 11\bar{2}0 \rangle$	9.3 ( $\pm 1.1$ )
$\{11\bar{2}0\}$	[0001]	7.6 ( $\pm 0.5$ )
$\{11\bar{2}0\}$	$\langle 10\bar{1}0 \rangle$	8.6 ( $\pm 0.9$ )

**Table 4** Activation energies calculated from the high-temperature ( $T > T_c$ ) Knoop hot-hardness data of Niihara and Hirai (100) for single crystals of  $\alpha$ -Si<sub>3</sub>N<sub>4</sub> as a function of indenter orientation. Indentation load 100gf in each case; indenter dwell time = 10s. Errors are one standard error in the mean.

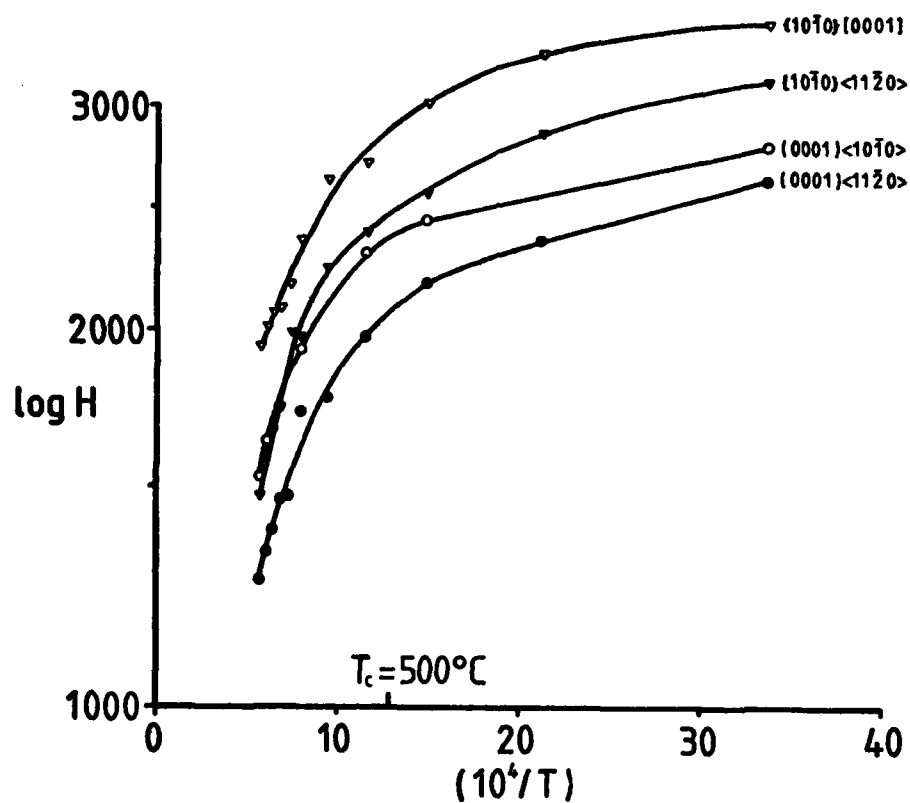


Figure 15. Activation energy plots of the hot-hardness data of Niihara and Hirai ( 100 ) for single crystal  $\alpha$ - $\text{Si}_3\text{N}_4$  at four different indenter:crystal orientations ( Knoop hardness, 100 gf load, 10s dwell time ).

### 3.3.2 Theoretical Interpretations: the Role of Slip

Before considering the various slip mechanisms which have been proposed to account for the variation of hardness with temperature, we must first review the evidence for slip occurring at all in brittle solids. From the foregoing evidence and from other high-temperature indentation studies ( e.g. 42, 94, 97, 105 ), it is reasonable to assume that deformation is controlled by thermally activated slip processes in the high-temperature domain. However, it has been established by a wide variety of techniques that even the most brittle materials exhibit some form of slip response, however localized, to indentation, abrasion and erosive impact at low temperatures also ( e.g. 42, 89, 90, 94-97, 101-117 ).

The technique most often used for revealing dislocation structures around indentations is dislocation etch-pitting ( e.g. 42, 89, 94, 96, 97, 104-108 ). Thus, etch rosettes corresponding to rays of dislocation half-loops are observed to form around indentations in semi-brittle solids ( e.g. MgO, LiF, NaCl, etc. ) at room temperature. The technique has been used extensively to study dislocation mobility as a function of dislocation character, slip system, temperature, dopant, irradiation damage and chemical environment ( e.g. 94 ). Brittle materials such as Si, Ge, etc. only show similar behaviour at high temperatures ( 42, 94, 97, 105 ). At low temperatures, etching only results in preferential attack of the indentation profile ( e.g. 89, 108, 94 ). High-temperature annealing of room temperature indentations followed by etching results in the formation of dislocation etch rosettes ( e.g. 94, 96, 107 ). The problem facing early workers was whether annealing resulted in increased mobility of dislocations formed by the indentation process ( allowing them to move under the action of the residual stresses around the indentation ) or whether high temperatures simply allowed nucleation of new dislocations to relieve the residual stress.

This problem was resolved by transmission electron microscopy ( TEM ) of defect structures around indentations, which has established that highly localized dislocation networks are indeed formed beneath room temperature indentations ( e.g. 38, 42, 89, 90, 94, 104, 109-112 ), scratches ( e.g. 111, 113-115 ) and erosive

impact sites ( e.g. 38, 116, 117 ) in materials such as Si, SiC and  $\text{Al}_2\text{O}_3$  . Annealing ( above  $550^\circ\text{C}$  for Si ( 94, 110 ) ) has been observed to cause dislocation rearrangement to form more mobile configurations which then propagate away from the indentation ( 110 ) . Eremenko and Nikitenko ( 42 ) have reported that dislocation lengths are independent of indentation temperature up to  $350^\circ\text{C}$  for silicon, whilst Hill and Rowcliffe ( 110 ) ( studying deeper-lying dislocations beneath larger indentations ) observed that dislocation loops beneath indentations made at  $300^\circ\text{C}$  ( again in Si ) were significantly longer than those beneath room temperature indentations, and were bowed out slightly.

Further techniques have been found useful for studying dislocations around indentations or beneath abraded/eroded surfaces, notably selected area electron channelling ( e.g. 102, 115 ) . X-ray topography ( 101 ) has been used, but is suited only to the study of extensive dislocation activity around high-temperature indentations or beneath abraded surfaces, due to lack of resolution. Finally, cathodoluminescence ( e.g. 86, 103, 104 ) has been used to determine the extent of plastic deformation around indentations, and is thought to be sensitive to changes in point defect concentration caused by dislocations, rather than to the dislocations themselves ( 103, 104 ) .

Whilst evidence for the formation of dislocations by indentation is irrefutable, there is controversy as to what extent slip processes determine final measured hardness values. Many observations suggest that indentation hardness is highly dependent on slip: for instance, single crystal hardness anisotropy is clearly related to active slip systems ( see section 3.4 ) even for materials such as SiC at room temperature ( e.g. 7 ) . Evidence for deformation mechanisms other than slip is presented in section 3.3.3.

Slip mechanisms which have been proposed to account for the temperature-sensitivity of hardness may be summarized as follows:

1) the low-temperature regime

- stress-activation of dislocations over the Peierls' barrier by ( phonon-assisted ) quantum mechanical electron tunnelling from bonding to non-bonding states ( covalent materials ) ( 16, 17 );
- athermal behaviour of the critical resolved shear stress ( CRSS ) for dislocation glide due to long-range interactions between dislocations and, for example, large precipitates or other dislocations

on parallel slip planes ( ionic materials ) ( 13, 71, 72 ).

ii) the high-temperature regime

- diminution of the CRSS for dislocation glide. This may involve a decrease in the Peierls' stress ( covalent materials ) or increased diffusion of short-range pinning mechanisms such as solute atoms ( ionic materials ), and is almost certainly a function of dislocation character;

- thermal activation of secondary slip systems, or even a complete change in primary slip system ( see section 3.4.2 );

- thermally activated cross slip and climb effects ( 4, 9 ), which may act in two ways. Firstly, dislocations may be released from obstacles ( other than the Peierls' barrier ) in the primary glide plane by cross slip or climb. Secondly, the operation of primary slip with cross slip and climb may fulfil the von Mises ( 8 ) criterion without the need for secondary slip systems with substantially higher CRSS values.

Some of the above mechanisms will now be discussed in greater detail.

### 3.3.2.1 Deformation Maps

Transitions between deformation modes are best considered by the deformation map approach ( e.g. 13, 71, 72 ), where normalized shear stress (  $\sigma_s/\mu$  ) is plotted as a function of homologous temperature (  $T/T_m$  ) for a selected grain size and for varying strain rates. By using the best available constitutive equations to describe each of the known ( or assumed ) deformation mechanisms, the maps are then divided into fields of temperature space within which a single mechanism dominates the deformation behaviour. Examples of such maps taken from the literature are shown in fig. 16 for MgO ( grain size  $10\ \mu\text{m}$  ) and silicon ( grain size  $100\ \mu\text{m}$  ).

Considering MgO firstly, it may be seen from fig. 16a that, at low temperatures, (  $\sigma_s/\mu$  ) is a strong function of temperature and strain rate (  $\dot{\epsilon}$  ) ( 71 ). In this region, deformation is thought to be controlled by dislocation glide which must be thermally activated to overcome obstacles in the glide plane having short-range stress fields ( e.g. solute atoms or the Peierls' barrier ) ( 71 ). Of course, under most stress conditions, the material would fracture in a brittle manner at stresses well below those required for slip

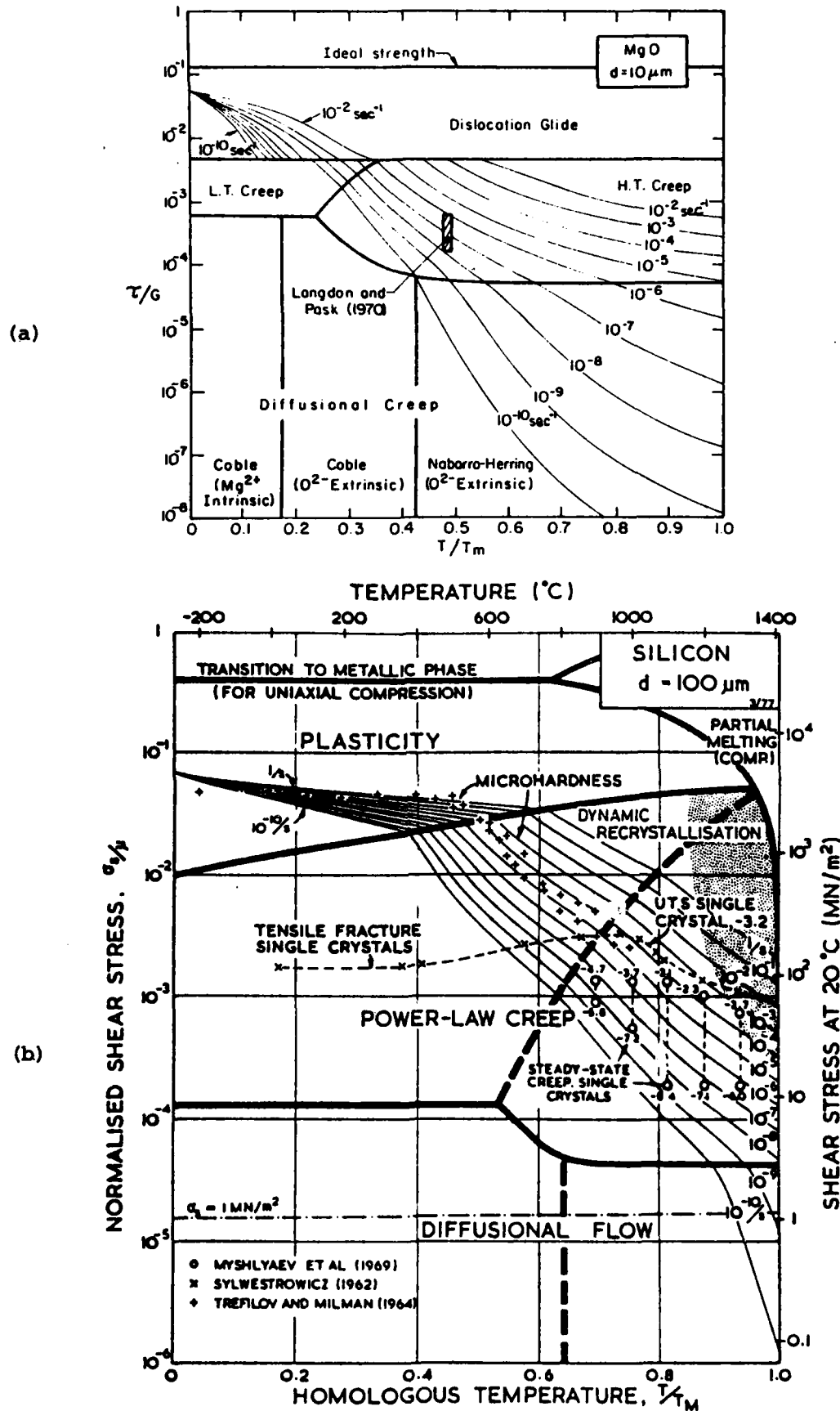


Figure 16. Deformation mechanism maps for (a) MgO of grain size 10 μm (after Langdon and Mohamed ( 71 )) and (b) silicon of grain size 100 μm (after Frost and Ashby ( 72 )).

to be observed ( see section 4.1 ). It is the combination of high shear stresses and high crack-inhibiting hydrostatic stresses which promote slip in indentation hardness tests.

At higher temperatures, MgO shows an athermal region, where dislocation mobility is limited by long-range stress fields due, for example, to large precipitates or dislocation-dislocation interactions ( 71 ).

At still higher temperatures, the deformation becomes thermally activated and highly strain rate sensitive once more. Here, the deformation is dominated by diffusion-controlled creep processes. The transition temperature is highly strain rate sensitive: a low strain rate favours time-dependent creep mechanisms, hence a lower transition temperature ( and vice versa ). In the low-temperature creep region for MgO ( fig. 16a ), dislocations are thought to be released from obstacles by climb involving vacancy diffusion along dislocation cores, whereas high-temperature creep involves climb by lattice diffusion ( 71 ).

At very high temperatures and low stresses, deformation may occur entirely by stress-directed diffusional flow through the structure ( Nabarro-Herring creep ). Coble creep ( diffusional flow of either  $Mg^{2+}$  or  $O^{2-}$  along grain boundaries ) would occur at lower homologous temperatures, but only at very low strain rates (  $<10^{-10} s^{-1}$  ), much lower than those required in indentation.

Silicon ( fig. 16b ) is thought to exhibit substantially different behaviour to MgO, the initial temperature and strain rate sensitive region extending up to higher temperatures, but with a comparatively small dependence of shear stress on temperature or strain rate ( 72 ). Deformation of silicon in the low-temperature regime is assumed to be limited largely by the Peierls' barrier ( short-range obstacles to glide ) ( 10 ). The athermal region ( long-range obstacles to glide ) determined for MgO is vanishingly small for silicon ( 72 ) and the transition to diffusion-controlled creep mechanisms is predicted to occur between  $0.4 T_m$  ( at  $\dot{\epsilon} = 10^{-10} s^{-1}$  ) and  $0.6 T_m$  ( at  $\dot{\epsilon} = 1 s^{-1}$  ). For strain rates above  $\sim 10^{-8} s^{-1}$ , deformation is predicted to occur by glide plus climb all the way up to the melting point, with insignificant Nabarro-Herring or Coble creep.

Applying these theories to the hot-hardness behaviour of silicon, a sharp increase in activation energy is predicted to

occur at  $\sim 0.55 T_m$  ( for  $\dot{\epsilon} = 10^{-2} s^{-1}$ , corresponding to a 10% strain produced over a 10s indenter dwell time ). The transition is thought to correspond to a change from dislocation glide limited by the Peierls' barrier to glide plus climb limited by pipe diffusion.

A similar interpretation is postulated for f.c.c. metals, which have hot-hardness curves similar to that of silicon ( e.g. 93 ). In this case, deformation at low temperatures is by dislocation glide and, because of high dislocation mobility, the flow rate is limited by strain-hardening effects. Dislocation-dislocation interactions are long-range and elastic in f.c.c. metals, hence hardness is only weakly dependent on temperature in the low-temperature regime ( e.g. 84 ). Above the transition temperature, deformation occurs by glide plus climb, as above.

However, there are a number of reservations about the above arguments for covalent materials such as silicon. Most importantly, the dependence of hardness on temperature in the low-temperature regime is far less than can be explained using realistic values of the activation energy for the Peierls' stress ( 72 ). For covalent semiconductors, the activation energy for low-temperature glide is thought to equal twice the band gap (  $2E_g$  ) per atom ( 16, 17 ), which is  $220 \text{ kJmol}^{-1}$  for silicon ( Frost and Ashby assume a value of  $430 \text{ kJmol}^{-1}$  ),  $550 \text{ kJmol}^{-1}$  for 6H SiC and  $980 \text{ kJmol}^{-1}$  for  $\text{Si}_3\text{N}_4$ . A theory which accounts for this behaviour in terms of a stress-activated Peierls' mechanism is discussed in the following section. Models which consider the low-temperature athermal region in terms of deformation mechanisms other than slip are discussed in section 3.3.3.

### 3.3.2.2 The Peierls' Stress

Dislocation glide in covalent ceramics is thought to occur by the formation and migration of double kinks, which involves breaking of atomic bonds ( e.g. 20-22 ). Due to the high strength and directionality of covalent bonds, the Peierls' stress is extremely high. The dependence of low-temperature hardness on bond-strength has been demonstrated by Garbato and Rucci ( 118 ) and by Gilman ( 16, 17 ), who found a linear relationship between room-temperature hardness and glide plane shear stiffness for a wide range of covalent solids. Further, the activation energy for dislocation glide was found to be twice the band gap, indicating that kink pair formation

involves the transfer of two electrons from bonding to non-bonding states ( 16, 17 ).

Plastic flow of covalent solids at low temperatures has been modelled by Gilman ( 16, 17 ) in terms of double kink motion by phonon-assisted quantum mechanical tunnelling of electrons across a potential barrier which may be taken either as the band gap (  $E_g$  ) or the elastic energy of the dislocation (  $\frac{1}{2}Gb^2$  per atom length ). This largely stress-activated mechanism was proposed to be more favourable than conventional thermally activated flow processes at low temperatures ( 16 ). Although electron tunnelling is an athermal process, a temperature dependence was predicted because of the effect of temperature on phonon energies: phonons were considered to facilitate electron transfer by momentarily stretching bonds. The flow stress predicted by this model is essentially the Peierls' stress ( although pinning effects could also be considered ), and assuming that hardness is proportional to flow stress, the temperature dependence of hardness was given by:

$$(H/H_0) = 1 - \frac{2k\theta}{U_0}(\coth(\theta/T) - 1)$$

where  $H_0$  = hardness at absolute zero ( 0K ),

$k$  = Boltzmann's constant,

$\theta$  = a characteristic temperature for phonon cutoff,

$U_0$  = an energy barrier at 0K, given by:

$$U_0 = \frac{2m^*E_g^2b^2}{\hbar^2}$$

where  $m^*$  = electronic effective mass,

$E_g$  = band gap,

$b$  = Burgers vector,

$\hbar$  = Planck's constant  $h/2\pi$

This equation was found to fit experimental hot-hardness data for silicon ( 17 ), although  $U_0$  was difficult to determine accurately, and so was obtained by best fit to experimental data. The characteristic temperature  $\theta$  was calculated to be 750K for silicon, which is close to the Debye temperature (  $\theta_D = 650K$  ). Thus, hardness was considered to become nearly independent of temperature below  $\theta_D$ .

Hardness values calculated from the above theory are shown in fig. 10b ( dashed curve ) using a value of  $H_0$  which best fitted the data and the values of  $\theta$  and  $(2k\theta/U_0)$  determined by Gilman ( 17 )

Material	Indenter	Orientation	$H_0$ (kgfmm <sup>-2</sup> )	$\theta$ (K)	(2k $\theta/U_0$ )
{111} silicon	Vickers	<1 $\bar{1}$ 0>	a) 1060	750	1.40
			b) 1255	200	0.2124
(0001) SiC (blue-black)	Knoop	<11 $\bar{2}$ 0>	2797	795	0.694
(0001) SiC (green)	Knoop	<11 $\bar{2}$ 0>	2466	1440	3.56
{11 $\bar{2}$ 0} SiC (green)	Knoop	[0001]	1980	2500	9.36
		<10 $\bar{1}$ 0>	2401	740	0.894

**Table 5** Best fit parameters for Gilman's theory of low-temperature plastic flow in covalent materials. Values were fitted to experimental hot-hardness curves determined for single crystals of silicon and silicon carbide using various indenters and crystallographic orientations. For silicon, two sets of parameters were determined: (a) best fit  $H_0$  using  $\theta$  and (2k $\theta/U_0$ ) values given by Gilman (17); (b) best fit values of  $H_0$ ,  $\theta$  and (2k $\theta/U_0$ ).

( see table 5 ). Agreement with the observed hardness variation ( solid line, fig. 10b ) is good at low and high temperatures, with some deviation between  $300^{\circ}\text{C}$  and  $800^{\circ}\text{C}$ . Better fit to the present data is obtained if a lower value of  $\theta$  ( 200K ) is used, with different values of  $H_0$  and  $(2k\theta/U_0)$  ( table 5 ).

Attempts have been made to fit the above model to experimental Knoop hot-hardness data obtained in this investigation for single crystals of SiC ( the Vickers hot-hardness curve was not fitted because of insufficient data points ). Because the transition from athermal to temperature-sensitive behaviour occurred at markedly different temperatures for different materials and crystal orientations, there is no single value of characteristic temperature  $\theta$  which will fit all the measured data. The approach taken was to determine best fit curves by suitable choice of  $H_0$ ,  $\theta$  and  $(2k\theta/U_0)$  for each hot-hardness curve ( dotted curves in figs. 13c and d, parameters listed in table 5 ). Thus,  $\theta$  was found to vary between 740K and 2500K. For comparison, the Debye temperature for  $\alpha$ -SiC is 1200K (  $\sim 0.4 T_m$  ) ( for  $\beta$ -SiC,  $\theta_D = 1440\text{K}$  ) ( 119 ), and  $(2k\theta/U_0)$  is calculated theoretically to be 0.041 for 6H SiC. Possible explanations for the variations in  $\theta$  are discussed in sections 3.4 and 3.5. It may be seen from figs. 10b, 13c and 13d that the shapes of the hardness/temperature plots are well-modelled by the form of the Gilman expression, even allowing for the fact that the theoretical parameters were obtained by fitting the experimental data.

The above analysis should be compared with recent models to account for the effects of electrically-active impurities on plastic flow in covalent semiconductors ( see section 3.5 ). In the theory due to Hirsch ( e.g. 20-22 ), the activation energy for glide is considered to be the difference between the Fermi energy and energy levels formed within the band gap by the presence of double kinks. Thus, kink migration probably involves more complex electron transitions than envisaged in the theory of Gilman.

### 3.3.2.3 Surface Slip Steps at High Temperatures

Observations of high-temperature indentations in Si and SiC established that surface slip steps were not formed until temperatures substantially higher than  $T_c$  ( section 3.3.1 ). For {111} silicon,  $T_c$  was  $\sim 350^{\circ}\text{C}$  but slip steps were not formed until  $500^{\circ}\text{C}$

and for non-basal single crystal SiC, slip steps were formed at 800°C with  $T_c$  in the range 200-600°C.

The key to understanding this behaviour is that dislocation activity around the indentation profile on the specimen surface will only be observed where the plastic zone radius (  $b$  ) exceeds the indentation radius\* (  $a$  ) ( see fig. 9 ). Now the expanding spherical cavity model for indentation ( discussed in section 3.2 ) predicts ( 76 ) the relation

$$(b/a) \propto (E/H)^m \quad \text{where } m \text{ is approximately } 0.5.$$

Thus, surface slip steps would first become visible at  $(b/a) = 1$ , which occurs at some critical value of  $(E/H)$ . For silicon at 500°C,  $(E/H)$  was calculated to be  $\sim 35$  and for SiC at 800°C,  $(E/H)$  was  $\sim 28$ . These values are reasonably similar, but more precise determination of the critical  $(E/H)$  ratio must await observations of the exact temperatures at which slip step formation begin. Observations of the extent of slip steps as a function of temperature in single crystal silicon and polycrystalline silicon carbides ( figs. 39, 40, 42 ) suggest a constant of proportionality in the above relation ( assuming  $m = \frac{1}{2}$  ) of approximately 0.4.

A critical observation is that  $Si_3N_4$  has been found by Niihara and Hirai ( 100 ) not to form slip steps even at their maximum experimental temperature of 1500°C. Considering the highest temperature and softest orientation used by Niihara and Hirai, the highest  $(E/H)$  value obtaining in their investigation was  $\sim 21$ , which is lower than the values at which Si and SiC were observed to form slip steps in this investigation. Thus,  $Si_3N_4$  is predicted not to form slip steps until very high temperatures indeed, mainly because of the low temperature sensitivity of hardness in this material ( fig. 15 ).

A further possible explanation of the above observations exists, namely a transition from radial displacement of material beneath the indenter at low temperatures to surface-directed displacement ( pile-up ) at high temperatures ( section 3.2 ). This transition is expected to occur as a critical value of  $(E/Y) = 114$  ( corresponding to  $(H/Y) = 2.75$  and  $(E/H) = 41$  ) is exceeded ( 86 ). For silicon at 500°C, the yield stress  $Y$  was calculated ( from the theory due to Perrott ( 81 ), described in section 3.2 ) to be  $\sim 1.8$  GPa with  $(E/Y) = 87$  and  $(H/Y) = 2.5$ . For SiC at 800°C,  $Y = 6.7$  GPa,  $(E/Y) = 64$  and

---

\* In this thesis,  $a$  is taken as half the Vickers indentation diagonal length.

$(H/Y) = 2.3$ . These values are somewhat lower than those thought to be required for surface-directed displacement, although  $\{111\}$  silicon would be predicted to show this type of behaviour above  $530^{\circ}\text{C}$ . Possible evidence for surface pile-up may be found in fig. 37, which includes Nomarski differential interference micrographs ( highly sensitive to changes in surface height ) of Vickers indentations in silicon. Light contrast, presumed to be caused by topographic effects, may be observed around high-temperature ( $\geq 500^{\circ}\text{C}$ ) indentation profiles, becoming more extensive with increasing temperature. Stereo pair SEM images were not found very useful in this situation because of the lack of surface features on this specimen, rendering stereo perception difficult.

For SiC, the temperature at which pile-up should be observed is predicted to be above the temperature range investigated, although surface perturbation was observed around  $800^{\circ}\text{C}$  indentations in polycrystalline materials ( figs. 39f and 40d ).

### 3.3.3 The Low-Temperature Regime: Athermal Deformation Mechanisms

Despite the above arguments, many workers consider that dislocation mobilities are too low and dislocation structures too localized for slip to account for a significant part of the deformation at low temperatures. Rather, slip is considered to play a secondary role in accommodating material displaced by other athermal deformation mechanisms ( e.g.  $91, 110$  ). We must remember that the von Mises criterion ( 8 ) requires the operation of five independent shears for the formation of an indentation without change in volume ( i.e. assuming no densification ). Most brittle materials have less than five independent primary slip systems ( 9 ), and even where this is not the case ( e.g.  $\{111\}\langle 11\bar{0}\rangle$  slip in Si ), the Peierls' stress may be enormous and slip interpenetration difficult ( 10 ). Elasticity may or may not provide a sufficient number of extra shear strains ( 86 ), and it is thought that stress-activated secondary slip and/or cross slip and/or some other ( athermal ) deformation mechanism(s) may be required for the formation of permanent indentations in many brittle materials at low temperatures. Possible alternative deformation mechanisms will now be reviewed.

#### (a) Pressure-Sensitive Densification

Material displaced by the indenter might be accommodated

by densification of the surrounding region. This might occur by, for example, compaction of a porous material ( modelled in section 3.6.7 ) or by densification of the crystal structure. The analogue of this latter effect is observed in certain silicate glasses which are relatively free of network modifying ions ( the so-called "anomalous glasses", including silica and borosilicate glass ) ( 86, 120-123 ). Although mechanisms are as yet unclear, it has been established that densification may account for about half the plastic strain in such materials ( 123 ).

A pressure-sensitive densification mechanism has been proposed for sphalerite ( zinc-blende structure ) crystals such as diamond, Si, Ge, InSb,  $\beta$ -SiC, etc. ( 91 ). At low temperatures, the hardness is thought to be of the order of the transition pressure required for localized formation ( by an essentially martensitic transformation ( 124, 125 ) ) of a dense metallic phase beneath the indenter due to the high hydrostatic pressure. Trefilov et al. ( 98 ) have tentatively suggested that  $\alpha$ -SiC may also densify in this way, whilst Velednitskaya et al. ( 104 ) and Rozhanskii et al. ( 126 ) have postulated a similar 'crowdionic plasticity mechanism' in MgO and Al<sub>2</sub>O<sub>3</sub> respectively. Materials such as GaAs, where the phase-transition pressure is thought to be much higher than the hardness, are not observed to have an athermal region in the hardness/temperature plot ( 91 ).

There is good evidence that such phase transitions are possible on thermodynamic grounds ( 127 ) and from calculation of interatomic force constants ( 124, 125 ), and also from direct experimental observations using high-pressure cells ( 128 ) or shock-wave compression tests ( 129, 130 ). There is further evidence for such transformations occurring during indentation : Gridneva et al. ( 91 ) have measured a change in electrical resistivity that could be accounted for by a metallic layer  $\sim 500\text{\AA}$  thick occurring during indentation of a silicon crystal. The resistivity was found to decrease to its original value on removal of the load, indicating that the structure probably reverts and also that the change in resistivity was not due to formation of dislocations. Direct observation of the supposed remnants ( platelets of a hexagonal phase ) of such layers have been made by TEM by Eremenko and Nikitenko ( 42 ) and support for their findings has recently been provided by Tan et al. ( 131 ). Platelets were only observed beneath

indentations formed in the temperature range 400 - 700°C and it was proposed that residual stresses were insufficient to prevent the reverse transformation at lower temperatures ( see section 4.4 ), slip being the dominant deformation mechanism at higher temperatures. In SiC, small volumes of material beneath indentations have been observed ( by TEM ) to have suffered severe rotational strains and to contain unresolvably dense dislocation tangles ( 38, 109, 112 ). Such "mussed-up" zones may also be the result of reversion of a dense, metallic phase.

It seems unlikely that this deformation mechanism occurs in all sphalerite materials: Sargent ( 86 ) has made a detailed study of existing low-temperature hardness and phase transition data, concluding that, for most sphalerites, the hardness lies significantly below the phase transition pressure (  $P_c$  ). It was therefore considered to be coincidental that  $H = P_c$  was found for some materials ( e.g. for Si, Ge, InSb, CdS, Sn and SiC ). In addition, shock-wave testing of Ge indicates that the pressure required for plastic flow is only half that required for densification ( 129 ).

In conclusion, it seems that densification may well occur in some materials ( including Si and perhaps SiC ), but may not be the dominant plasticity mechanism ( 86 ).

(b) Block Shear

Estimates of the shear stresses beneath an indenter are close to the expected theoretical shear strength for some materials ( including SiC ( 7 ) ), and it is then possible that deformation occurs by block shear ( 110 ). In such cases, dislocations might be generated simultaneously at the edges of slipped zones ( 110 ).

(c) Deformation Twinning

Deformation twinning has been observed beneath Vickers indentations in silicon ( between 350 and 650°C ( 42 ) ) and in Al<sub>2</sub>O<sub>3</sub> and SiC at room temperature ( 38, 90, 94, 109, 111, 112, 132 ). Twinning is likely to be favoured at large grain sizes ( 31 ) in materials with low stacking fault energies ( especially true for SiC ( 133 ) ). The stress concentrations induced by twinning must be accommodated by some other deformation mechanism, such as slip or microcracking ( e.g. 4, 31 ).

(d) Microcracking

As discussed in section 3.1, microcracking may be a significant deformation mechanism where crack-arresting stresses are present, as they are in indentation, and microcracking has indeed been observed beneath room temperature indentations in many materials ( e.g. 42, 90, 109 ). For silicon, it has been reported that microcracks are not initiated by dislocations below  $400^{\circ}\text{C}$ , rather they nucleate separately, presumably because the stresses required for dislocation and crack nucleation are about equal ( approximately the theoretical shear strength ) ( 42 ).

(e) Grain Boundary Separation

Where less than five slip systems are operating in a polycrystalline material, limited dislocation motion in grains will cause pile-ups at grain boundaries accompanied by stress concentrations which must be relieved, for example by secondary slip or by grain boundary separation ( e.g. 4, 31, 37 ), depending on the strength of the boundary. Grain boundary cracking is observed in MgO bicrystals ( 132-134 ) at points where a boundary is intersected by a glide band: the deformation of a general boundary produced by a slip band in one grain cannot be accommodated by slip in the neighbouring grain due to strain incompatibility ( e.g. 9 ). This mechanism is considered further in section 3.6.5.

In addition, grain boundary sliding ( involving triple point cavitation ) might also occur, although this deformation mechanism is usually observed only at high temperatures ( 66 ). However, grain boundary sliding has been found beneath room temperature indentations in ZnS ( 134 ).

(f) Creep

Deformation by viscous flow processes, which are highly temperature- and strain rate- sensitive, may occur in some glasses but, in general, diffusional or viscous flow rates are too low for conventional creep mechanisms to operate significantly in the low-temperature regime ( 13, 71, 72 ). However, in the presence of certain chemical environments ( e.g. where polar species, especially water, may be adsorbed ) some materials exhibit surface softening and

AD-A136 242

MICROHARDNESS FRICTION AND WEAR OF SIC AND SI3N4  
MATERIALS AS A FUNCTION OF (U) CAMBRIDGE UNIV (ENGLAND)  
DEPT OF METALLURGY AND MATERIALS SCI.

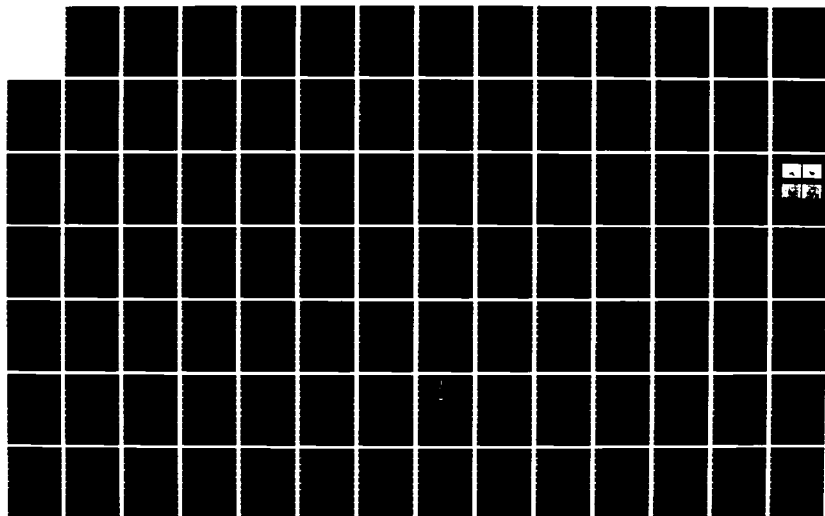
2/3

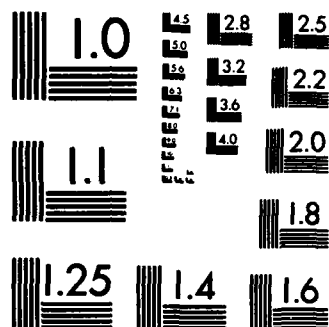
UNCLASSIFIED

M G NAYLOR ET AL. OCT 81 DA-ERO-78-G-010

F/G 11/2

NL





MICROCOPY RESOLUTION TEST CHART  
NATIONAL BUREAU OF STANDARDS-1963-A

anomalous indentation creep effects ( discussed in section 3.9 ). In order to eliminate these effects as far as possible, all hot-hardness experiments described in this thesis were performed in liquid nitrogen-trapped high vacuum (  $\sim 10^{-6}$  mmHg ).

#### 3.3.4 Summary

In this section, an attempt has been made to review the many theories to account for indentation plasticity in brittle materials, illustrated by considering the hot-hardness behaviour of single crystal materials. For many materials, the temperature sensitivity of hardness shows a transition from largely athermal behaviour at low temperatures to thermally activated deformation at high temperatures. The transition temperature  $T_c$  is approximately  $0.4 - 0.5 T_m$  for a variety of materials, including f.c.c. metals and sphalerites ( such as diamond, silicon, germanium, etc. ). In this investigation,  $T_c$  was found to be  $\sim 0.36 T_m$  (  $350^\circ\text{C}$  ) for Vickers indentations in {111} silicon. The transition is well understood for f.c.c. metals but open to various interpretations for sphalerites. There is evidence for extensive slip activity ( {111} slip steps ) around high-temperature (  $\gtrsim 500^\circ\text{C}$  ) indentations in Si, and plastic deformation is thought to occur by dislocation glide plus climb in this regime. Broadly, there are two types of model for deformation at low temperatures: (a) deformation by stress-activated dislocation glide, for which  $T_c$  is expected to be of the order of the Debye temperature  $\theta_D$  ( which happens to be  $\sim 0.4 T_m$  for Si ) and (b) the operation of some other, athermal deformation mechanism(s) such as densification, block shear, twinning, microcracking, etc. Post facto observations of deformation structures induced by indentation have as yet failed to resolve the matter conclusively.

For  $\alpha$ -SiC,  $T_c$  has been found in this investigation to be much lower on a homologous scale, lying in the range  $0.15 - 0.25 T_m$  (  $\sim 200 - 550^\circ\text{C}$  ) for single crystals, depending on indenter:crystal orientation and specimen purity.  $T_c$  is thus well below  $0.5 T_m$  or  $\theta_D$  ( which is also  $\sim 0.4 T_m$  for 6H SiC ). Slip steps were not formed around indentations until temperatures of  $\sim 0.35 T_m$  (  $800^\circ\text{C}$  ) or above, and were established to be caused by basal slip only. The formation of surface slip steps is thought to mark the point at which

the plastic zone radius becomes equal to the indentation radius on the specimen surface. This occurs as a critical value of  $(E/H)$  ( found to be approximately 30 ) is exceeded, and probably does not involve a change in deformation mechanism, as may be seen from activation energy plots.

By re-plotting some existing hot-hardness data for  $\alpha$ - $\text{Si}_3\text{N}_4$  single crystals, it has been established that this material shows a transition in activation energy at  $T_c \sim 0.3 - 0.45 T_m$ .  $\text{Si}_3\text{N}_4$  is predicted not to exhibit slip steps around indentations until very high temperatures indeed ( precise values cannot easily be determined since this involves extrapolation of data well beyond the experimental range ).

Before extending the discussion to include microstructural effects in polycrystalline materials ( section 3.6 ), further aspects of indentation plasticity in single crystals are considered. In section 3.5, the influence of electrical dopants on plasticity is discussed, whilst in the following section, a method is described for extracting information about active slip systems from single crystal hardness anisotropy measurements ( with particular emphasis on the temperature sensitivity of this effect for  $\alpha$ -SiC ).

### 3.4 HARDNESS ANISOTROPY OF SINGLE CRYSTALS

Anisotropy in the hardness of single crystal materials is well-established ( e.g. 135-137 ). Whilst the effects of elastic anisotropy and elastic recovery may exert some influence on the anisotropy\* ( 86 ), the dominant effect has been shown ( 138, 140 ) to be anisotropic plastic flow beneath the indenter. The most successful theoretical models consider the effective resolved shear stresses experienced by the various slip systems in the test crystal.

#### 3.4.1 Effective Resolved Shear Stress Models

In these models, the forces exerted by a loaded, stationary indenter are resolved onto each slip system in the crystal. The models consider only the effects of the indenter facets, the resolved shear

---

\* Sargent ( 86 ) has demonstrated that such effects are minimal for the long diagonals of Knoop indentations.

stresses due to each facet being combined for each indenter orientation ( 86, 139 ). The effects of the indenter edges and tip are neglected. For indenter:crystal orientations where one or more of the slip systems experiences a high resolved shear stress, the hardness is predicted to be low; where resolved shear stresses are low, the hardness is high ( 138, 140 ). Knowing the active slip systems in a crystal, we may predict the hardness anisotropy ( 138 ). Alternatively, we may determine the slip systems from hardness anisotropy experiments in the following manner.

Firstly, the Schmidt-Boas resolved shear stress (  $\tau$  ) is calculated for each slip system according to

$$\tau = (L/A) \cos \lambda \cos \phi$$

where  $L$  is the force on a cylindrical test element of cross-sectional area  $A$ ,  $\lambda$  is the angle between the stress axis and the slip direction in question and  $\phi$  is the angle between the stress axis and the slip plane normal. The direction of the tensile stress axis is considered to lie parallel to the line of steepest slope in each indenter facet. The model is illustrated schematically in fig. 7 of ref. 138.

The above relationship is then modified by a constraint factor (  $C$  ), which was introduced in order to allow for the constraints on plastic flow imposed by the presence of the indenter and the elastic hinterland ( 138, 140 ). Then

$$\begin{aligned} \text{ERSS} &= C\tau \\ &= (L/A) F(\lambda, \phi, \gamma, \psi) \end{aligned}$$

where  $\gamma$  is the angle between the slip direction and an axis parallel to the indenter facet and to the surface of the material and  $\psi$  is the angle between this axis and the axis of rotation of the slip plane ( fig. 7, ref. 138 ).

The constraint factor  $C$  was first introduced by Daniels and Dunn ( 140 ) in order to allow for slip plane rotation, this being easiest when the axis of rotation of the slip system lies in the plane of the indenter facet. This led to the use of  $C = \cos \psi$  in the formulation of their ERSS. This approach was found to be unsuccessful in some cases, and Brookes et al. ( 138 ) used a different constraint factor  $C = \frac{1}{2}(\cos \psi + \sin \gamma)$  which satisfied the boundary conditions  $C = 0$  when  $\gamma = 0^\circ$  (  $\psi = 90^\circ$  ),  
 $C = 1$  when  $\psi = 0^\circ$  (  $\gamma = 90^\circ$  ).

These boundary conditions were suggested because the constraint on plastic flow ought to be a minimum when the rotation axis of the slip system is parallel to the indenter facet, enabling material to flow upwards by slip ( 140 ). The constraint is maximum when the rotation axis is perpendicular to the horizontal line in the indenter facet, i.e. the slip direction is parallel to the facet.

Sawyer et al. ( 7 ) point out that any form of constraint factor which satisfies the boundary conditions might be used: that used by Brookes et al. ( 138 ) is one of the simplest, but is nevertheless highly successful. The Brookes et al. model is most appropriate for materials which form surface pile-ups around indentations, but other constraint factors might be more applicable to stiff, brittle ceramics, where material flows radially out from indentations ( section 3.2 ) ( 7 ). Further, Sawyer et al. consider that where the ERSS model predicts hardness anisotropies which are highly sensitive to the precise form of the constraint factor, it may not be used reliably.

Arnell ( 139 ) has developed a method of applying the ERSS model directly to the prediction of hardness anisotropies: ERSS values are calculated for each indenter facet using the above formulations, then the pressure acting over the indenter ( the hardness ) is taken to be proportional to the sum of the stresses over the four ( Knoop and Vickers ) facets:

$$H \propto \Sigma (L_i/A)$$

This assumes equal strains under each facet and no strain-hardening. For yield beneath the indenter to occur, the ERSS must equal the critical resolved shear stress ( CRSS ) on the relevant slip system, hence:

$$(L_i/A) = (CRSS)/F_i$$

Thus  $H \propto (CRSS) \times f$

where  $f = \Sigma (1/F_i)$ ;  $F_i = C_i \cos \lambda_i \cos \phi_i$

$f$  is therefore a geometrical factor, which is calculated for each slip system, for each crystal section under test and for every indenter orientation on that section.  $f$ -plots for various sections of  $\alpha$ -SiC and slip systems are given in ref. 7.

Before using the above model to interpret hardness anisotropy versus temperature data, it is useful to review some of the assumptions used in the above analysis:

(a) the model assumes that hardness is completely controlled

by slip processes, which may not be the case for brittle materials at low temperatures ( see section 3.3 );

(b) the model does not consider effects such as differing Peierls' stresses and mobilities of dislocations of different character on identical slip systems ( 7 );

(c) no account is taken of strain-hardening effects ( reviewed in ref. 7 );

(d) the stress state is assumed to be predominantly tensile in the plastic region, which may not be the case for brittle materials, for which a model based on compressive forces might be more appropriate. However, Brookes et al. ( 138 ) consider that their tensile stress model affords better correlation with experimental data than a compressive stress model.

Despite these shortcomings, the model has been used successfully to explain hardness anisotropies on a range of single-crystal materials, failing only where effects such as twinning or indentation creep occur ( 138 ).

#### 3.4.2 Temperature Effects

Single crystal hardness anisotropy experiments performed as a function of temperature are a valuable means of studying changes in slip behaviour with changing temperature. The technique has been used to study such changes in transition metal carbides, either by measuring the hardness of a single material as a function of temperature at a few orientations ( e.g. 141, 142 ), or by measuring the room temperature hardness anisotropies of a range of materials ( e.g. 143-145 ). Such experiments have established that stoichiometric Group V transition metal carbides ( e.g. TaC, NbC ) deform by  $\{111\}\langle\bar{1}\bar{1}0\rangle$  slip at all temperatures, whilst Group IV carbides ( e.g. TiC, VC, HfC ) and substoichiometric Group V carbides exhibit predominantly  $\{110\}\langle\bar{1}\bar{1}0\rangle$  slip ( with some  $\{111\}\langle\bar{1}\bar{1}0\rangle$  slip ) at room temperature ( 144 ). In these materials, ductility is found to be much greater ( i.e. hardness is lower and indentation fracture much less severe ) where  $\{111\}\langle\bar{1}\bar{1}0\rangle$  slip predominates ( 143, 144 ). For materials which exhibit  $\{110\}\langle\bar{1}\bar{1}0\rangle$  slip at low temperatures, a "brittle-ductile" transition occurs at higher temperatures ( usually at  $0.2 - 0.35 T_m$  ( 93, 141 )): the dominant slip system changes to  $\{111\}\langle\bar{1}\bar{1}0\rangle$ , surface slip steps are

observed, indentation fracture ceases and plasticity may even be detected in conventional mechanical tests ( 142,143 ). The transition is also reflected in an increase in activation energy in the hot-hardness plot ( 93, 141 ).

The greater ductility allowed by  $\{111\}\langle\bar{1}\bar{1}0\rangle$  slip probably arises because dislocation dissociation is much easier than for  $\{110\}\langle\bar{1}\bar{1}0\rangle$  slip systems ( 143 ).  $\{111\}\langle\bar{1}\bar{1}0\rangle$  slip is thought to be favoured by the more open crystal structures found in Group V carbides or in Group IV carbides at high temperatures, and is thought to be associated with largely metallic bonding ( 142, 143 ).  $\{110\}\langle\bar{1}\bar{1}0\rangle$  slip may be predicted by atomic radius ratio criteria assuming largely covalent bonding ( 142,143 ). Thus, the origin of the "ductile-brittle" transition in these materials is thought to be a change from predominantly covalent to predominantly metallic bonding with increasing temperature ( 142-144 ).

This behaviour should be compared with that of sphalerite materials ( described in section 3.3 ), where the dominant slip system remains  $\{111\}\langle\bar{1}\bar{1}0\rangle$  over the whole temperature range ( 10 ): the "ductile-brittle" transition is not necessarily caused by a change in slip system. Rather, a change in slip system may reflect changes in bonding which are themselves responsible for the transition.  $T_c$  is higher ( on a homologous scale ) for sphalerites than for transition metal carbides, which probably reflects the more covalent nature of interatomic bonding in the former. Also, plastic flow in transition metal carbides is thought to be more influenced by the mobility of carbon atoms than by changes in the Peierls' stress ( 93 ), since stoichiometry has been found to have a marked effect on hardness ( e.g. 93, 144, 145 ).

Of more relevance to the present study, the Knoop hardness anisotropy of single crystal  $\alpha\text{-Si}_3\text{N}_4$  has been measured as a function of temperature at various orientations by Nihara and Hirai ( 100 ), the active slip system being determined as  $\{10\bar{1}0\}[0001]$  from room temperature to  $1500^\circ\text{C}$ . However, the full variation of hardness with orientation was not determined for temperatures other than room temperature, and  $f$  factors were only calculated for certain orientations. Thus, details of any secondary slip systems cannot be determined from this investigation, since these systems only act over limited ranges of orientation ( where they experience high ERSS ).

### 3.4.3 Results for Silicon Carbide

Room temperature Knoop hardness anisotropies have previously been measured by Shaffer for  $\alpha$ -SiC ( 136 ) and for  $\beta$ -SiC ( 137 ). The results for  $\alpha$ -SiC were rationalized in terms of one possible slip system (  $\{10\bar{1}0\}\langle 11\bar{2}0\rangle$  ) by Brookes et al. ( 138 ). However, these investigations used only a limited number of orientations: a subsequent, more comprehensive study by Sawyer et al. ( 7 ) established that the controlling slip systems were  $\{10\bar{1}0\}\langle 11\bar{2}0\rangle$  and  $(0001)\langle 11\bar{2}0\rangle$  over different ranges of indenter orientation. Basal slip was further established to have a CRSS between 1.2 and 2.1 times that of the prismatic slip system ( 7 ). Hardness anisotropies were also considered to be consistent with slip on some pyramidal systems (  $\{h\bar{h}0\ell\}\langle 11\bar{2}0\rangle$  ), but the model due to Brookes et al. could not be used reliably for such systems because small changes in the form of the assumed constraint factor resulted in large changes in predicted hardness anisotropy ( 7 ). Thus, the operation of basal and prismatic slip was considered to be the simplest interpretation of the experimental data.

Some measurements of the Vickers hardness anisotropy of  $\alpha$ -SiC have been made by Hirai and Niihara ( 99 ), but again for a limited number of indenter orientations ( insufficient for accurate slip system determination ). The present study seeks to extend comprehensive hardness anisotropy measurements to higher temperatures in order to shed light on the hot-hardness behaviour of SiC.

Thus, Knoop hardness was measured at  $10^\circ$  intervals in orientation on  $(0001)$ ,  $\{10\bar{1}0\}$  and  $\{11\bar{2}0\}$  sections of green  $\alpha$ -SiC at room temperature and  $800^\circ\text{C}$  and also at  $400^\circ\text{C}$  for the  $\{11\bar{2}0\}$  section. In addition, hardness anisotropy ( at  $5^\circ$  intervals ) was measured for blue-black  $(0001)$  SiC at room temperature and  $800^\circ\text{C}$ . Orientations were established by aligning the long axis of the indenter relative to prominent crystal facets: for basal and  $\{10\bar{1}0\}$  faces, orientations were measured relative to  $\langle 11\bar{2}0\rangle$  directions, whilst for the  $\{11\bar{2}0\}$  section, orientations were measured relative to  $\langle 10\bar{1}0\rangle$ . The data are plotted in figs. 17-19. Each data point corresponds to a mean hardness value calculated for five indentations.

Room temperature hardness anisotropy curves were found to be very similar in shape to those determined by Sawyer et al. ( 7 ) ( who used samples from the same batch of crystals as used in this

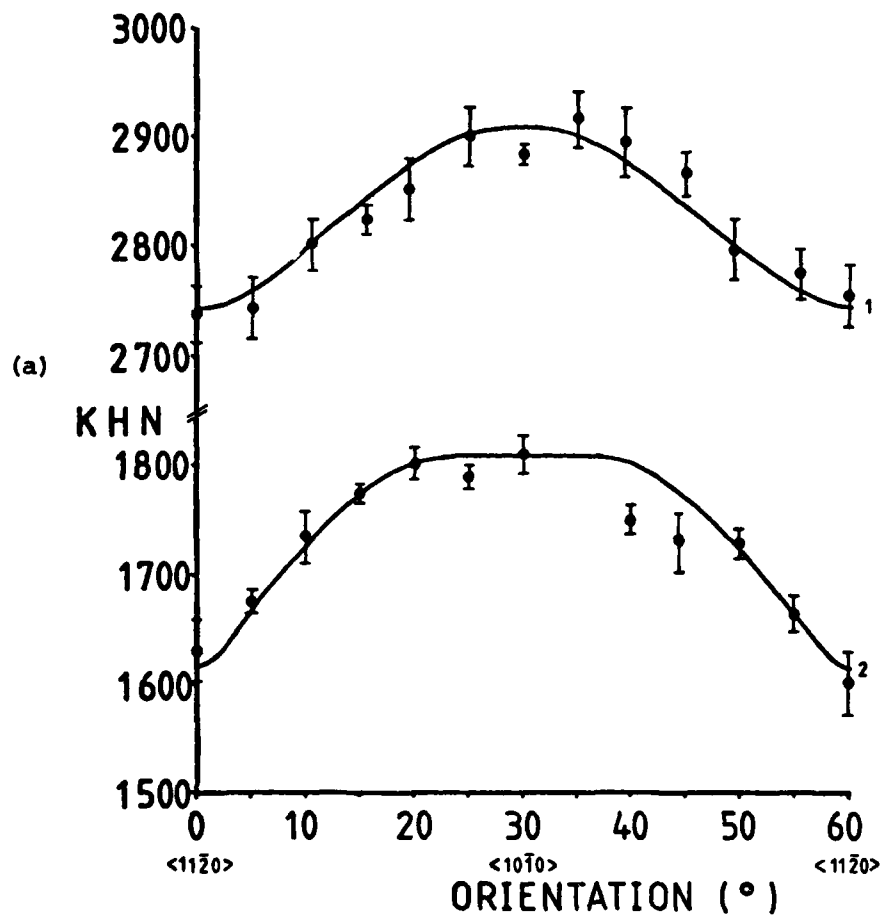


Figure 17. Knoop hardness anisotropy ( 200 gf load, 15s dwell time ) of (0001) single crystals of SiC at 25°C ( curve 1 ) and 800°C ( curve 2 ). Error bars represent one standard error in the mean calculated over approximately 5 indentations.  
(a) Blue-black SiC.

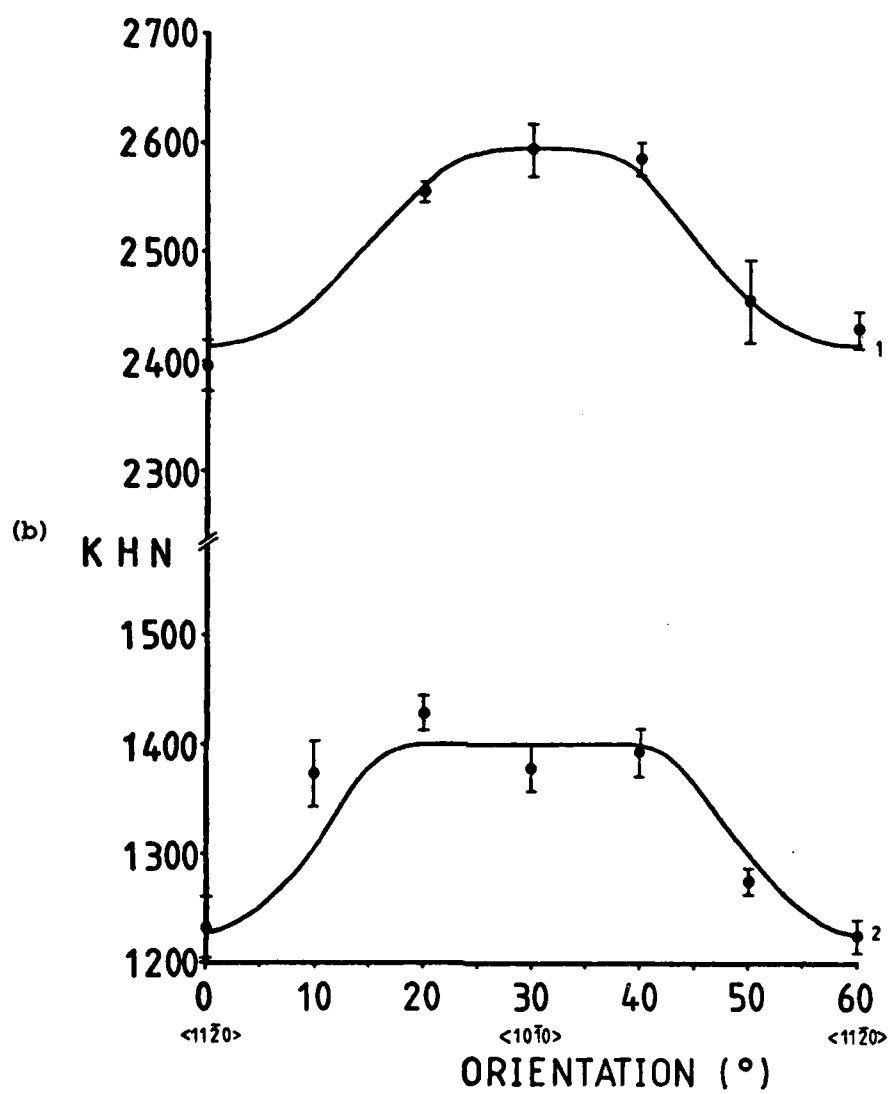


Fig. 17b. Green SiC.

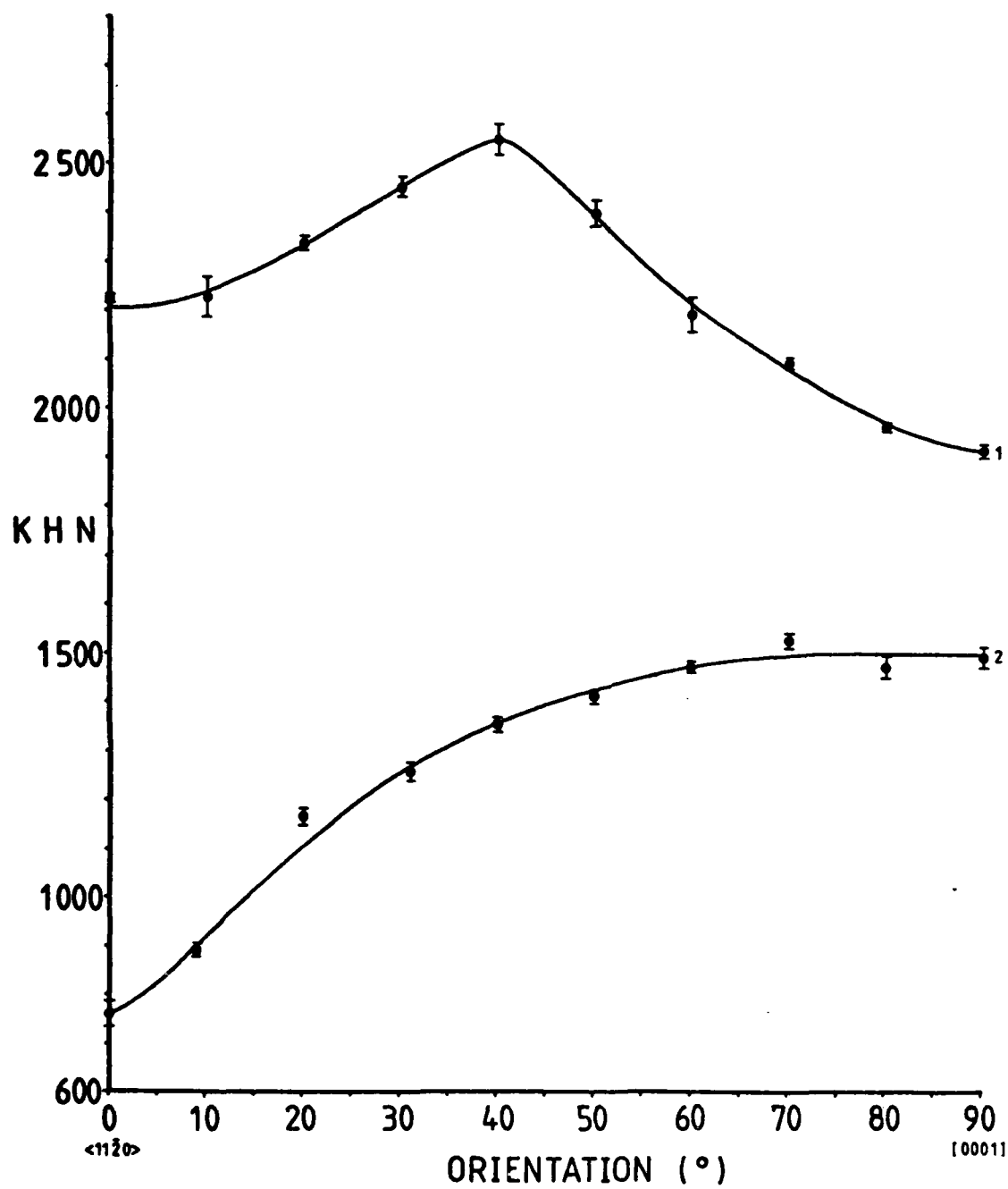


Figure 18. Knoop hardness anisotropy ( 200gf load, 15s dwell time ) of green  $\{10\bar{1}0\}$  single crystal SiC at 25°C ( curve 1 ) and 800°C ( curve 2 ). Error bars represent one standard error in the mean calculated over approximately 5 indentations.

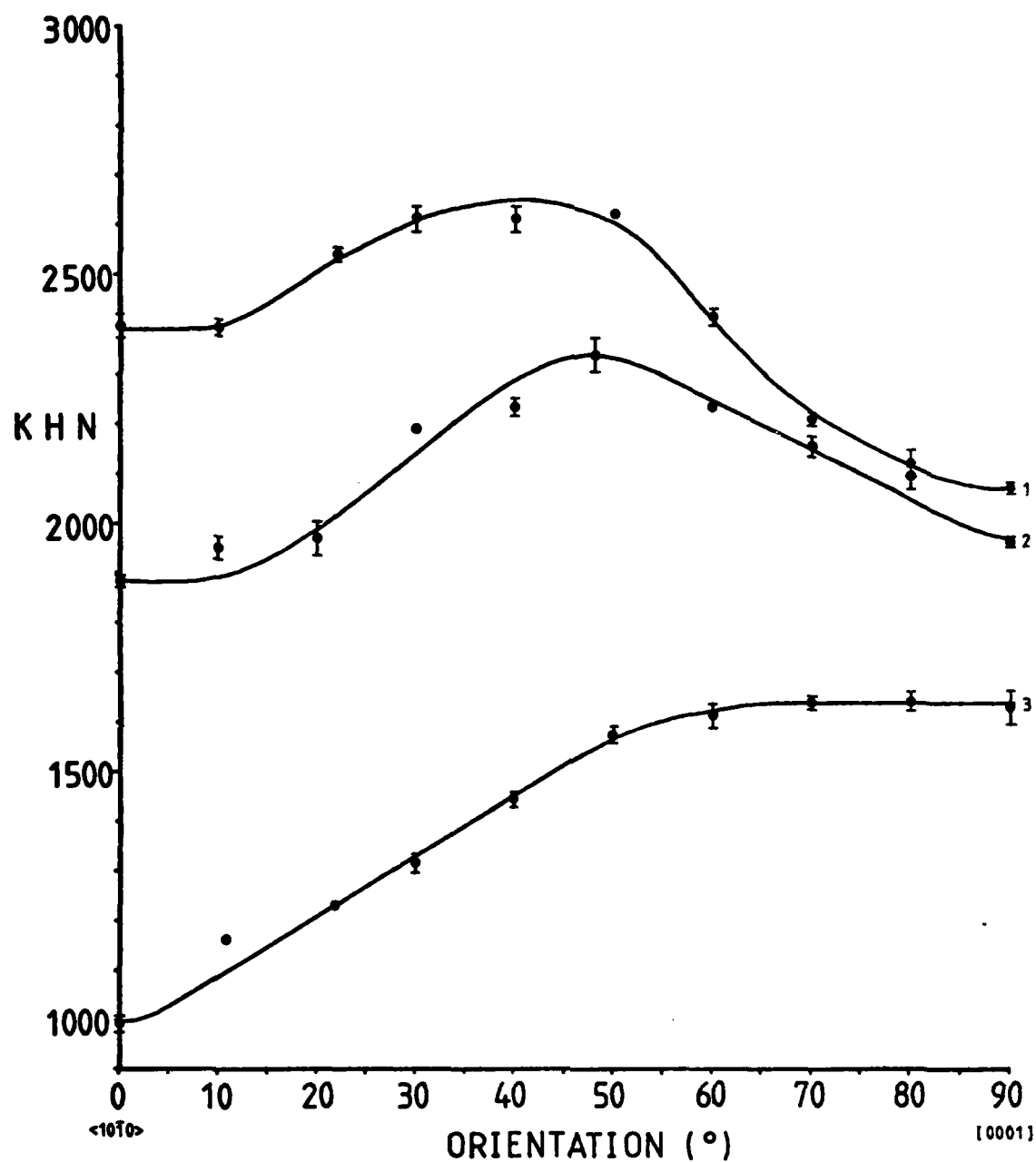


Figure 19. Knoop hardness anisotropy ( 200 gf load, 15s dwell time ) of green {11 $\bar{2}$ 0} single crystal SiC at 25°C ( curve 1 ), 400°C ( curve 2 ) and 800°C ( curve 3 ). Error bars represent one standard error in the mean calculated over approximately 5 indentations.

investigation ). Basal sections showed a small hardness anisotropy, with  $\langle 10\bar{1}0 \rangle$  indenter orientations hardest and  $\langle 11\bar{2}0 \rangle$  orientations softest. The prismatic sections showed greater variations in room temperature hardness, with a hardness maximum occurring at orientations approximately  $50^\circ$  away from  $[0001]$  for both sections.

At  $800^\circ\text{C}$ , the hardness anisotropy on  $(0001)$  remained similar to that found at room temperature ( transposed to lower hardness values ) for both green and blue-black SiC ( fig. 17 ). Possibly, the hardness peak is broader at  $800^\circ\text{C}$  than at room temperature, but the effect is marginal. In contrast, the prismatic faces both showed substantially different hardness anisotropy at  $800^\circ\text{C}$  ( figs. 18 and 19 ), with maximum hardness occurring at  $[0001]$  (  $90^\circ$  ) orientations and minimum hardness at  $0^\circ$  orientations (  $\langle 11\bar{2}0 \rangle$  for  $\{10\bar{1}0\}$  and  $\langle 10\bar{1}0 \rangle$  for  $\{11\bar{2}0\}$  ). At  $400^\circ\text{C}$ , the hardness anisotropy on the  $\{11\bar{2}0\}$  section was intermediate between that at room temperature and that at  $800^\circ\text{C}$ , with a peak in hardness at approximately  $40^\circ$  from  $[0001]$ . However, the hardness measured in the  $\langle 10\bar{1}0 \rangle$  orientation was much less at  $400^\circ\text{C}$  than at room temperature, whilst that measured in the  $[0001]$  orientation was almost the same as at room temperature ( fig. 18 ). This is better illustrated in fig. 13d, which shows the full variation of hardness with temperature for  $[0001]$  and  $\langle 10\bar{1}0 \rangle$  orientations on  $\{11\bar{2}0\}$ . As described in section 3.3, there is a difference in not only activation energy, but also in  $T_c$  between the two curves. Before discussing this, we must first apply the ERSS model to determine the probable changes in active slip systems.

As detailed in section 3.4.1, slip systems may be determined by comparing experimental hardness anisotropy curves with  $f$  factors predicted theoretically for various slip systems.  $f$ -plots calculated by Sawyer et al. ( 7 ) for basal sections and for basal and prismatic slip systems are shown in fig. 20. Additional  $f$ -plots may be found in ref. 7. Clearly, the anisotropies shown in fig. 17 are best described by  $\{10\bar{1}0\}\langle 11\bar{2}0 \rangle$  slip over the whole range of orientations at both room temperature and  $800^\circ\text{C}$ . Figure 20c illustrates schematically the interpretation of room temperature hardness anisotropy on prismatic sections\* in terms of  $\{10\bar{1}0\}\langle 11\bar{2}0 \rangle$  and  $(0001)\langle 11\bar{2}0 \rangle$  slip, as proposed by Sawyer

---

\* The argument applies equally to  $\{10\bar{1}0\}$  and  $\{11\bar{2}0\}$  sections because the  $f$ -plots for basal and prismatic slip are similar in shape for both ( 7 ).

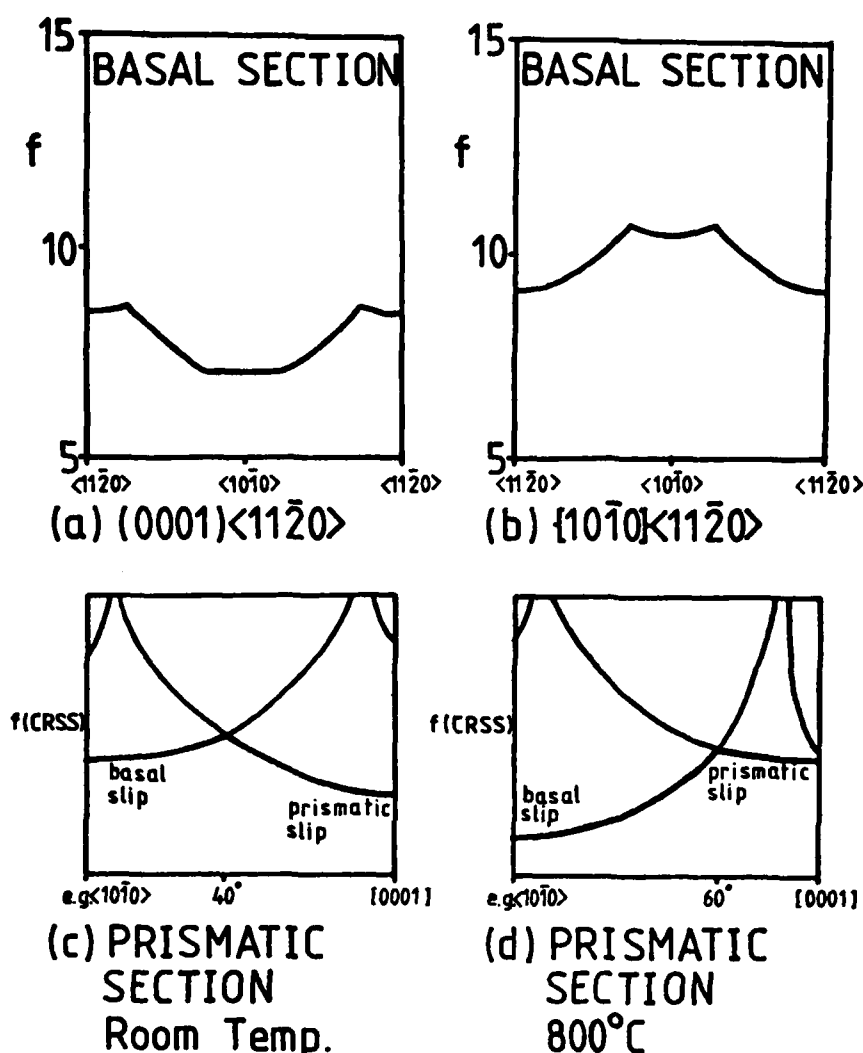


**Figure 20.** Predicted hardness anisotropies for various crystal sections of  $\alpha$ -SiC and for various slip systems. (a)  $f$ -plot for basal sections with  $(0001)\langle 11\bar{2}0 \rangle$  slip. (b)  $f$ -plot for basal sections with  $\{10\bar{1}0\}\langle 11\bar{2}0 \rangle$  slip. (c) Schematic interpretation of the hardness anisotropy on prismatic sections at room temperature: deformation is controlled by basal and prismatic slip over different ranges of indenter orientation, such that peak hardness occurs at  $\sim 50^\circ$  from the  $[0001]$  orientation. (d) As (c) for  $800^\circ\text{C}$ , where the crossover occurs at  $\sim 30^\circ$  from the  $[0001]$  orientation, suggesting that the CRSS for basal slip decreases with temperature much more rapidly than for prismatic slip.

et al. ( note that there is a typographical error in fig. 5 of Sawyer et al: fig. 5a shows the  $f$ -plot for prismatic slip on  $\{11\bar{2}0\}$  and fig. 5b shows that for basal slip, not vice versa as stated ). The y ordinate in fig. 20c is the  $f$  factor multiplied by the relevant value of CRSS for the two slip systems ( this is proportional to the hardness- see section 3.4.1 ). On this plot, the predicted hardness is given by the lowest of the two curves at any given orientation. Although the two CRSS values are not known, their ratio may be calculated by choosing values which best fit the observed anisotropy ( i.e. with a crossover at the  $40^\circ$  orientation at room temperature ) ( 7 ). From fig. 20c it may be seen that, at room temperature, prismatic slip controls the deformation for orientations up to  $50^\circ$  from  $[0001]$ , the remainder of the orientation range being controlled by basal slip.

The schematic diagram for hardness anisotropy of prismatic sections at  $800^\circ\text{C}$  ( fig. 20d ) must differ from the above because of the relative changes in CRSS for the two slip systems: the  $f$  factor is a purely geometrical term which is not sensitive to changes in temperature. The interpretation most consistent with the observed change in anisotropy is that the CRSS for basal slip diminishes more rapidly than for prismatic slip ( fig. 20d ). This is to be expected, since slip steps observed at  $800^\circ\text{C}$  on prismatic sections are clearly due to basal slip only ( section 3.3.1 ). Now the ratio of the CRSS values for the two slip systems may be estimated as a function of temperature from fig. 13d, using the following argument.

For the  $[0001]$  orientation on  $\{11\bar{2}0\}$  ( curve 1, fig. 13d ), the active slip system is always  $\{10\bar{1}0\}\langle 11\bar{2}0\rangle$  ( figs. 20c,d ). Then

$$H_{[0001]} \propto (\text{CRSS})_{\{10\bar{1}0\}} f_{\{10\bar{1}0\}}$$

$$\text{Similarly } H_{\langle 10\bar{1}0\rangle} \propto (\text{CRSS})_{(0001)} f_{(0001)}$$

$$\text{Hence } \frac{(\text{CRSS})_{(0001)}}{(\text{CRSS})_{\{10\bar{1}0\}}} = \frac{f_{\{10\bar{1}0\}}}{f_{(0001)}} \frac{H_{\langle 10\bar{1}0\rangle}}{H_{[0001]}}$$

Using the  $f$  factors determined by Sawyer et al. with the Brookes et al. constraint factor, we obtain a value for the above ratio of 1.1 at room temperature ( c.f. Sawyer et al. 1.2 - 2.1 ) and a value of 0.6 at  $800^\circ\text{C}$ .

Using exactly the same procedure for the  $\{10\bar{1}0\}$  section, values of 0.7 and 0.3 respectively were obtained. These calculations take no account of possible variations in  $f$  factor due to changes in

constraint factor, which must further limit the accuracy of the CRSS ratio. The above analysis also assumes that slip is entirely controlled by either basal or prismatic slip ( but not both ) at the two orientations (  $0^\circ$  and  $90^\circ$  ) of each prismatic crystal face. This may not always be the case: for example, the prismatic slip system is predicted to be dominant at orientations within  $\sim 30^\circ$  of  $[0001]$  at  $800^\circ\text{C}$  ( fig. 20d ), yet basal slip steps are clearly observable around such indentations ( fig. 14 ) ( although they are less extensive than those around indentations at different orientations ). Prismatic slip steps were never observed at  $800^\circ\text{C}$ , possibly because higher CRSS ( hence hardness ) entails a smaller plastic zone size ( see section 3.3.2.3 ).

Finally, the hot-hardness curves shown in fig. 13d for  $\{11\bar{2}0\}$  SiC at indenter orientations parallel to  $[0001]$  ( curve 1 ) and  $\langle 10\bar{1}0 \rangle$  ( curve 2 ) are effectively plots of the temperature sensitivity of the CRSS for prismatic and basal slip respectively, since the relevant  $f$  factors are almost the same for the two orientations ( 7 ). Thus, we see that CRSS values for the two slip systems have significantly different activation energies ( table 3 ) at high temperatures and also have different values of  $T_c$ . Whilst interpretation of this latter effect must await more detailed theoretical understanding of such transitions ( section 3.3 ), a number of points can be made. Firstly, if the transition corresponds to a change to slip-controlled behaviour from some other ( athermal ) deformation mechanism, it might be expected to occur at a lower critical temperature for the slip system with lowest CRSS, as shown in fig. 21. We must then try to account for the hardness anisotropy observed at low temperatures. Secondly, if the Gilman model for phonon-assisted dislocation glide ( see section 3.3.2.2 ) is correct, the difference in  $T_c$  would be due to a difference in characteristic temperature for phonon cutoff ( table 5 ). In order to test this hypothesis, details of the variation of phonon energy with crystallographic orientation would be required.

#### 3.4.4 Summary

The Knoop hardness anisotropy of single crystal  $\alpha$ -SiC was measured as a function of temperature in the range  $25$ - $800^\circ\text{C}$ . The data are best explained in terms of a combination of basal and prismatic slip acting over different indenter orientations, as suggested by

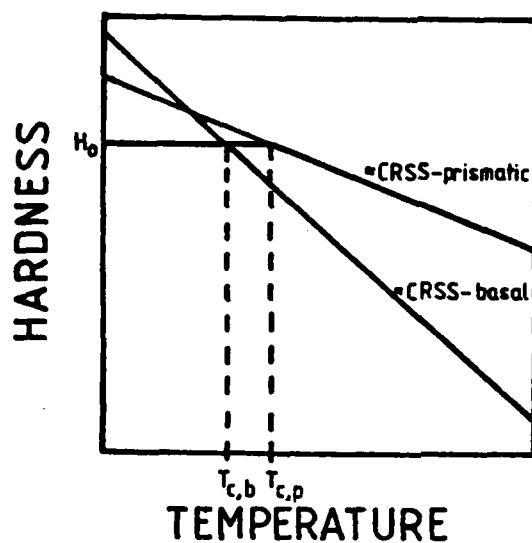


**Figure 21.** A schematic interpretation of the variation in critical temperature  $T_c$  with indenter orientation on single crystal SiC. Where one indenter orientation promotes basal slip and another prismatic slip, differences in  $T_c$  may occur because of the different temperature sensitivities of the CRSS values for the two systems, as shown above. It is assumed that the low-temperature hardness  $H_0$  is determined by some other deformation mechanism and is the same for all orientations.

Sawyer et al. ( 7 ) from room temperature experiments. The hardness anisotropy of non-basal crystal sections changed with temperature, indicating that the CRSS for basal slip decreases with increasing temperature much more rapidly than for prismatic slip. Thus, the ratio  $(CRSS)_{\text{basal}} : (CRSS)_{\text{prismatic}}$  was calculated to be 0.7 - 1.1 at room temperature and 0.3 - 0.6 at 800°C. In addition to the differences in thermal activation energy, the two slip systems were found to have different values of  $T_c$  for the transition from athermal to thermally activated behaviour -  $T_c$  was lower for basal slip. This effect is not fully understood.

### 3.5 DOPANT EFFECTS ON PLASTICITY

#### 3.5.1 Theories

Impurity effects on dislocation mobility have been reported for many brittle materials, especially ionic solids ( e.g. 11, 12, 24, 146-148 ). In MgO, for instance,  $Fe^{3+}$  impurities produce solid solution hardening effects ( 146 ), dislocation velocities being limited by the Peierls' stress below a concentration of  $\sim 200$  ppm  $Fe^{3+}$  at high resolved shear stresses ( 24 ). Trivalent impurities in MgO impede screw dislocations athermally, whilst divalent cations are thought to retard edge dislocations at high temperatures by the formation of Cottrell atmospheres ( 148 ). Dislocation pinning is often by impurity-vacancy dipoles in alkali halides ( e.g. 11 ), in which such hardening effects are more pronounced ( 146 ). At high impurity concentrations, precipitation hardening produces even larger effects ( e.g. 146, 147 ).

Dislocation velocities in silicon and germanium are also known to depend on the concentration of electrically-active impurities ( e.g. 149, 150 ), and this effect has been modelled in a number of ways ( e.g. 18-22 ), that due to Hirsch ( 20-22 ) being perhaps the most complete. This theory considers the energy levels created in the band gap of the material by the formation of dislocations. Additional deep-lying acceptor and donor levels are created in the gap between the dislocation levels by the formation of kinks: dislocation motion is observed to occur by the formation and migration of double kinks in these materials ( 10 ). This inevitably requires the breaking of bonds, i.e. electronic transitions from bonding to non-bonding states ( e.g. 22 ). The concentration of charged kinks is thought to depend

on an activation energy for kink formation which is the energy difference between the Fermi level and the kink levels. Impurities which change the Fermi level ( i.e. electrically-active dopants ) may thus influence dislocation mobilities by changing the total ( charged plus uncharged ) kink concentration. In addition, the mobilities of charged and uncharged kinks may differ due to differences in activation energy for migration.

In silicon, dislocation velocities are greater in both n- and p-type material ( above a critical dopant level of approximately  $10^{18}$  atoms  $\text{cm}^{-3}$  ) than in intrinsic material ( 151 ), and it is proposed that the kink levels lie near the middle of the band gap ( 20-22 ). In germanium, on the other hand, dislocation velocities are greater for n-type than for intrinsic material, and greater for intrinsic than for p-type material ( 150 ). Kink levels are thought to lie near the valence band for germanium ( 20-22 ). Similar effects may well occur in any material with a band gap ( semiconductors and insulators ) for which dislocation glide is limited by the Peierls' barrier ( 21 ).

An experimental study of various Si and SiC materials with different impurity contents was undertaken in an attempt to investigate these effects ( differences in dislocation velocity ought to be reflected in different hardness values ).

### 3.5.2 Results for {111} silicon

Unfortunately, the two materials available contained rather low dopant levels (  $5.3 \times 10^{14}$  atoms  $\text{cm}^{-3}$  of antimony for the n-type specimen and  $1.9 \times 10^{15}$  atoms  $\text{cm}^{-3}$  of boron for the p-type sample ). It has been reported ( 151 ) that dopant levels in excess of  $10^{18}$  atoms  $\text{cm}^{-3}$  are required for a noticeable effect on dislocation velocity and the two materials were found to have identical Vickers hardness at all temperatures ( in the range 24 - 800°C ) ( table 6 ), as expected. Clearly, further research is required using more highly doped materials, as well as intrinsic material ( both n- and p-type silicon are predicted to be softer than intrinsic material ).

Temperature (°C)	Vickers Hardness (kgfmm <sup>-2</sup> )	
	p-type Si (1.9x10 <sup>15</sup> atoms cm <sup>-3</sup> B)	n-type Si (5.3x10 <sup>14</sup> atoms cm <sup>-3</sup> Sb)
24	1029 (±7)	1041 (±12)
100	982 (±9)	1002 (±9)
200	965 (±38)	949 (±29)
300	800 (±4)	801 (±16)
400	574 (±7)	574 (±3)
500	446 (±4)	437 (±6)
600	282 (±1)	269 (±3)
700	159 (±3)	137 (±2)
800	98 (±1)	100 (±0.5)

**Table 6** The effect of dopant on the Vickers hardness of {111} single crystal silicon as a function of temperature. Applied load=100gf in each case. Errors are one standard error in the mean for approximately 10 indentations.

Material	Vickers Hardness (kgfmm <sup>-2</sup> )
Undoped α REFEL	2070 (±60)
Al-doped α REFEL	2060 (±40)
AlN-doped α REFEL	2060 (±60)
B-doped α REFEL	2145 (±110)
Undoped β REFEL	2560 (±30)
B-doped β REFEL	2350 (±70)

**Table 7** The effect of dopant on the room temperature Vickers hardness of α and β REFEL reaction-bonded silicon carbides. Applied load = 1kgf in each case. Errors are 95% confidence limits (10 indentations).

### 3.5.3 Results for Silicon Carbide

The hot-hardness behaviour of basal sections of green and blue-black  $\alpha$ -SiC single crystals has already been described in section 3.3 ( fig. 13c ). Although the precise nature of impurities in these two samples is unknown, the colour of SiC crystals is known to be a function of impurity ( e.g. 120 ). Thus, we can assume that the green sample contained nitrogen as the major impurity ( at fairly low concentration, since the material was semi-transparent ) and that the blue-black sample contained both Fe and Al as impurities ( at greater concentrations, since this material was largely opaque ). Care must be exercised in this, since Roberts ( 152 ) has found that the samples, although largely of the same polytype ( 6H SiC ), contained differing amounts of stacking disorder ( the green sample being more disordered than the blue-black sample ). Thus, any differences in hot-hardness behaviour cannot unambiguously be related to impurity effects.

Referring to figure 13c, the differences in hot-hardness behaviour between the two samples can be summarized as follows: (a) blue-black SiC has a slightly higher low-temperature hardness than green SiC, (b) green SiC has a somewhat higher value of  $T_c$  (  $500^\circ\text{C}$  ) than blue-black SiC (  $200^\circ\text{C}$  ), (c) the hardness/temperature variation for green SiC has a much higher activation energy at high temperatures ( table 3 ). Changes in activation energy for dislocation motion with dopant are indeed predicted by the Hirsch model, and by an argument analogous to that used in section 3.4.3 ( fig. 21 ), we would also expect differences in  $T_c$ . From fig. 13c, p-type SiC appears to be harder than n-type SiC over the whole temperature range ( as in Germanium ( 150 ) ). Interestingly, this same effect has been proposed by Gibbs and Page ( 153 ) to account for differential plastic wear behaviour observed in 'REFEL' reaction-bonded SiC, where the grain cores are thought to be p-type relative to the more pure epitaxially-formed outer layers ( see section 2.5 ).

Accordingly, a series of 'REFEL' silicon carbides ( described in section 2.5 ) of varying impurity content and major polytype was indented at room temperature under ambient conditions using a Leitz 'Miniload' microhardness tester ( 1 kgf Vickers indentations ), and the results are shown in table 7. Precise impurity levels were again

not known, but were of the order of 1000 ppm for each major dopant, the Al-doped specimen also containing ~500 ppm of nitrogen and the 'undoped' sample ~ 300 ppm of various impurities ( notably Fe, Al, N ) ( 154 ). Alpha materials showed no variation of hardness with dopant, whilst undoped  $\beta$ -REFEL appeared harder than B-doped ( p-type ) material. However, this latter effect might have been due to other microstructural factors, such as a comparative lack of residual Si in the undoped specimen ( see section 3.6.1 ). In any case, the major polytype present in the material appears to be more important in determining the room-temperature hardness than the impurity concentration for these samples. Unfortunately, no n-type materials were available for comparison with the p-type or intrinsic materials described above.

#### 3.5.4 Conclusions

Hot-hardness testing is a potentially powerful technique for investigating the effects of dopants on dislocation mobilities in semiconductors and insulators. The experiments described in this section were preliminary studies using the materials readily to hand - clearly, more comprehensive future investigations are required. However, in using the hardness test to study such effects, a number of factors must be borne in mind. Firstly, the effects are thought to depend on dislocation character, and dislocation structures generated beneath indentations are known to be complex. Also, the Hirsch theory applies strictly only to (a) low-stress, high-temperature and (b) high-stress, low-temperature situations, so it might not be applicable to indentation at high temperatures ( a high-stress, high-temperature situation ). At low temperatures ( below  $T_c$  ), hardness might not be a strong function of dislocation mobility at all ( for the reasons discussed in section 3.3.3 ). However, if the low-temperature glide mechanism proposed by Gilman ( 16, 17 ) operates, we might still expect dopant effects due to differences in the height of the energy barrier through which electrons tunnel when bonds are broken at kink sites. In this case, the precise form of the dependence of dislocation velocity on dopant would be quite different from that derived by Hirsch for thermally activated flow at higher temperatures.

### 3.6 THE EFFECTS OF MICROSTRUCTURE ON HOT-HARDNESS OF POLYCRYSTALLINE CERAMICS

In preceding sections, various aspects of the indentation plasticity of single crystal materials have been described. In this section, microstructural effects on hot-hardness behaviour are described for a range of commercial engineering ceramics. Very few studies of this nature have been made in the past ( see, for example, ref. 155 ), and results have often been contradictory ( e.g. grain size effects ( 86, 155 ) ). The study is considered to be important both from the fundamental standpoint of further understanding plasticity mechanisms in ceramics, and from the practical one of predicting wear rates for such materials when used in tribological applications ( Chapter 6 ).

No attempt was made to create specially 'tailored' microstructures for this investigation, since this would have been difficult in practice ( microstructural parameters such as porosity and grain size may seldom be varied independently in any case ( 156 ) ). Rather, the approach taken was to make deductions about microstructural effects from the hot-hardness behaviour of the materials available, which had different microstructures ( characterized in section 2.3 ) due to differences in fabrication routes ( section 1.2.4 ).

#### 3.6.1 Results for Silicon Carbide

The variations of Vickers hardness ( at 1 kgf load and 15 s dwell time ) with temperature for a variety of SiC materials are displayed in figure 22a ( linear hardness scale ) and figure 22b ( logarithmic hardness scale ). Notable features of these plots are summarized below.

(a) There was a fairly large spread in hardness due to the effects of microstructure (  $\sim 2\,000 - 3\,000\text{ kgf mm}^{-2}$  at room temperature ).

(b) The variation of hardness with temperature was marked for all materials, hardness typically decreasing by 50% between room temperature and  $800^{\circ}\text{C}$ .

(c) The single crystal ( blue-black SiC, basal face,  $\langle 11\bar{2}0 \rangle$  orientation ) was the hardest form of SiC over the whole temperature

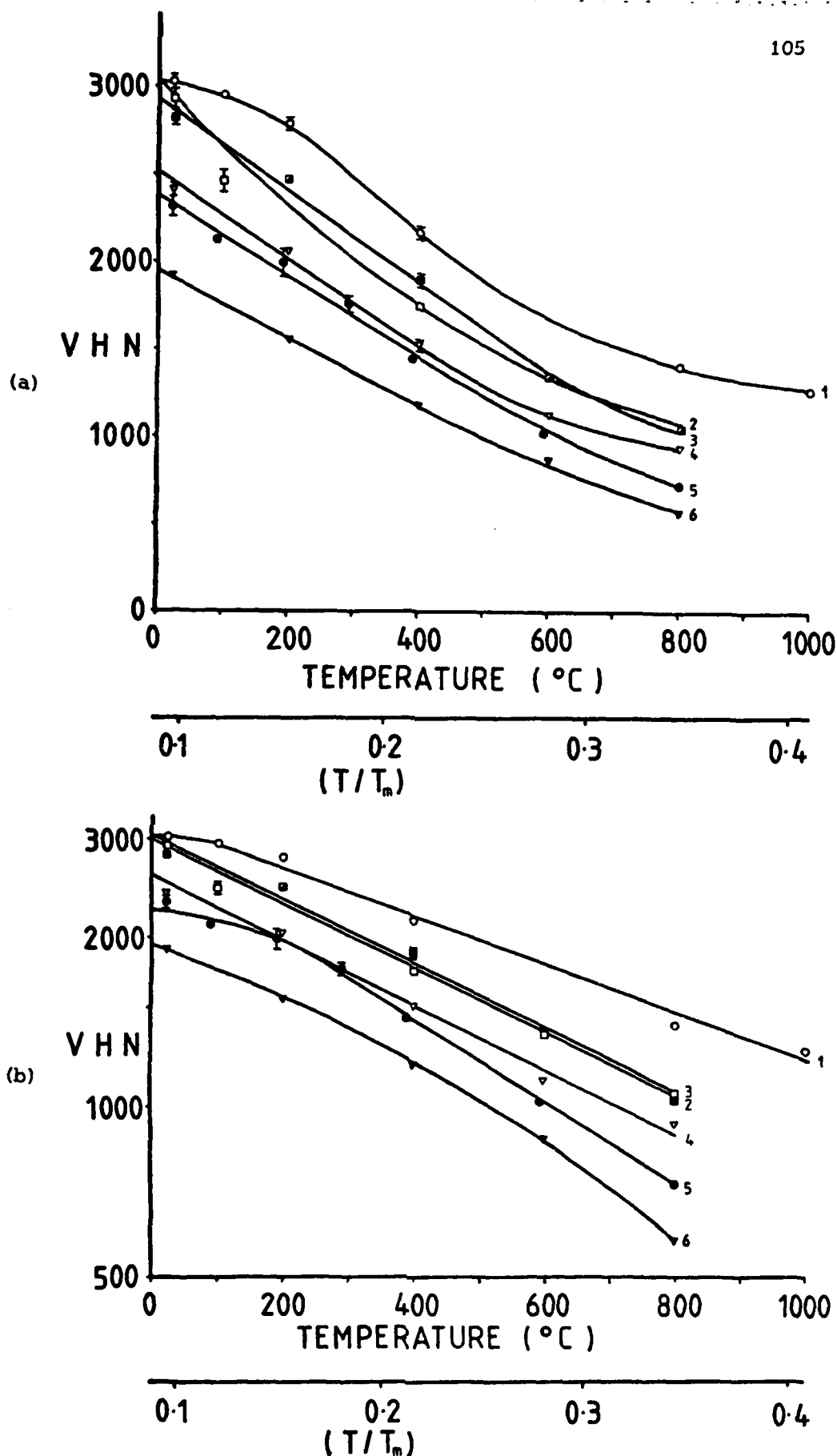


**Figure 22.** The variation of Vickers hardness (1 kgf applied load and 15s dwell time) with temperature for single crystal and polycrystalline forms of SiC: (a) linear plots, (b) logarithmic hardness scale. Error bars indicate one standard error in the mean for approximately 10 indentations. Curve 1 = blue-black (0001) single crystal, curve 2 = Norton NC203 hot-pressed SiC, curve 3 = Carborundum sintered  $\alpha$ -SiC, curve 4 = 'Suzuki' sintered SiC, curve 5 = 'REFEL' reaction-bonded SiC (grain size  $\sim 5 \mu\text{m}$ ), curve 6 = 'REFEL' reaction-bonded

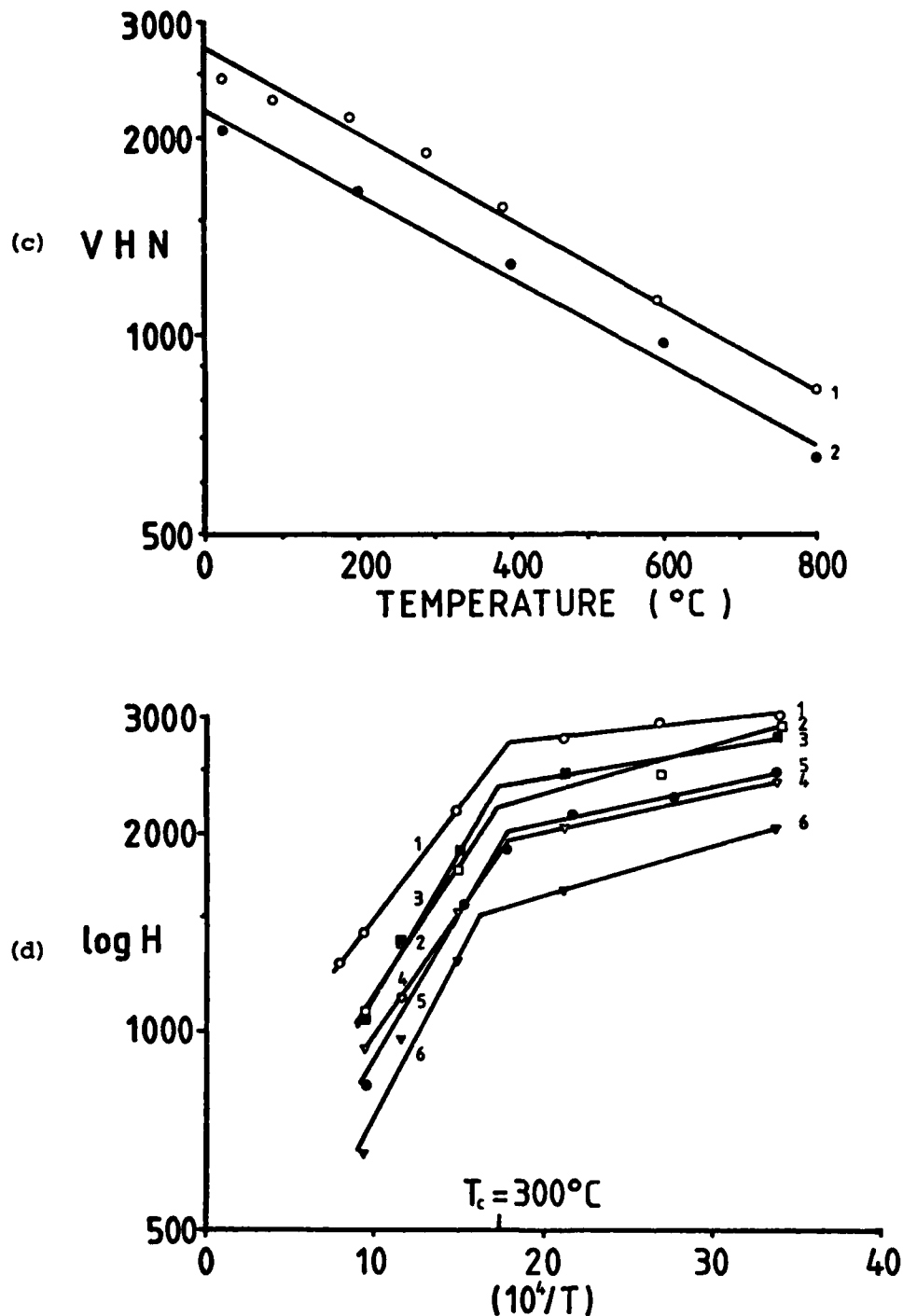


Fig. 22 (c) Hot-hardness plots ( logarithmic hardness scale ) for 'REFEL' reaction-bonded silicon carbides, corrected for the volume fraction of free silicon ( see text ). Curve 1 = 5  $\mu\text{m}$  grain size, curve 2 = 10  $\mu\text{m}$  grain size. (d) Activation energy plots of log H against  $(10^4/T)$  for all SiC materials ( REFEL curves corrected as above ). Curve 1 = blue-black (0001) single crystal, curve 2 = Norton NC203 hot-pressed SiC, curve 3 = Carborundum sintered  $\alpha$ -SiC, curve 4 = 'Suzuki' sintered SiC, curve 5 = 'REFEL' reaction-bonded SiC ( grain size  $\sim 5 \mu\text{m}$  ), curve 6 = 'REFEL' reaction-bonded SiC ( grain size  $\sim 10 \mu\text{m}$  ).

range. Because of the marked hardness anisotropy of SiC single crystals ( section 3.4.3 ), it is difficult to say whether or not grain boundaries have a softening effect ( although the hardness anisotropy for a Vickers indenter should be less than for a Knoop indenter ( 86 ) ). This is discussed further in section 3.6.5.

(d) Of the polycrystalline materials, the hot-pressed ( Norton NC203 ) and Carborundum sintered samples were the hardest, with almost identical hot-hardness curves. The more porous 'Suzuki' sintered specimen was slightly softer than these materials ( by  $\sim 400 \text{ kgf mm}^{-2}$  at  $25^\circ\text{C}$  and by  $\sim 100 \text{ kgf mm}^{-2}$  at  $800^\circ\text{C}$  ). 'REFEL' reaction-bonded silicon carbides were the softest, which was thought to be due to the  $\sim 13 \text{ vol } \%$  of residual silicon present in these samples ( section 1.2.4.3 ). Accordingly, an attempt was made to correct for this by applying a simple law of mixtures calculation, using hot-hardness data for {111} single crystal silicon ( fig. 10 ) ( the precise microstructural form of residual silicon in 'REFEL' materials is not known ). The results are shown in fig. 21c, which plots the hardness/temperature response of the SiC content of these two materials. These curves are much closer to those for other forms of SiC, although the  $10\mu\text{m}$  grain sized 'REFEL' sample was still considerably softer than other materials. The effects of such microstructural features as grain size, grain boundary phases and porosity are discussed in sections 3.6.5, 3.6.6 and 3.6.7, respectively.

Rather more information may be derived by plotting the results as  $\log H$  against  $(1/T)$  ( fig. 22d ), as described in section 3.3.1, so that changes in activation energy may be more clearly seen. Figure 22d reveals that microstructure has little effect on  $T_c$  (  $\approx 0.18 T_m$  or  $300^\circ\text{C}$  ) and that the curves appear to be transposed along the  $\log H$  axis from each other. Activation energies were reasonably constant from material to material within experimental errors ( see table 8 ), and were in the range  $6 - 10 \text{ kJ mol}^{-1}$ . Errors were relatively large because they were calculated from a limited number of data points ( i.e. from  $400 - 800^\circ\text{C}$  only ). As discussed in section 3.8, activation energies calculated directly from  $\log H$  versus  $(1/T)$  plots are not very useful because they ignore the effects of the stress exponent for creep. Where activation energies for two materials are similar, however, we might expect that the dominant deformation mechanism(s)

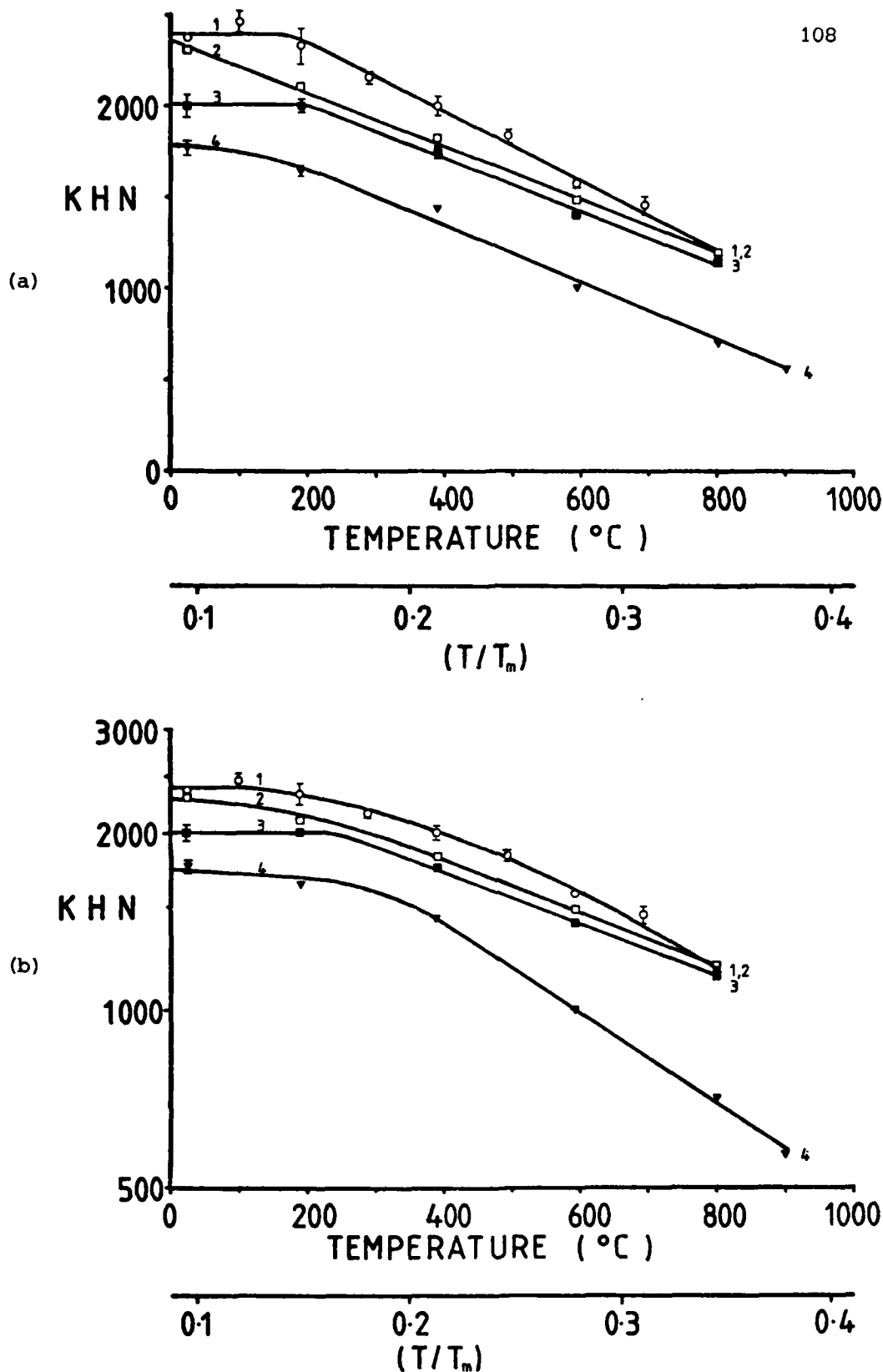


Figure 23. The variation of Knoop hardness ( 1 kgf applied load and 15s dwell time ) with temperature for single crystal and polycrystalline forms of SiC: (a) linear plots, (b) logarithmic hardness scale. Error bars indicate one standard error in the mean for approximately 5 indentations. Curve 1 = blue-black (0001) single crystal, curve 2 = Norton NC203 hot-pressed SiC, curve 3 = Carborundum sintered  $\alpha$ -SiC, curve 4 = 'REFEL' reaction-bonded SiC ( grain size  $\sim 10 \mu\text{m}$  ).

are the same for each.

Finally, the variations of Knoop hardness ( again at 1 kgf load and 15 s dwell time ) with temperature are shown in figure 23. The variation in Knoop hardness with microstructure is qualitatively the same as for Vickers indentations, although the actual hardness values are lower. Activation energies calculated from Knoop hot-hardness data are comparable with those for the Vickers indenter within experimental errors ( table 8 ).

### 3.6.2 Results for Silicon Nitride

Figure 24a shows the variation of Vickers hardness ( again at 1 kgf load and 15 s dwell time ) with temperature for the polycrystalline  $\text{Si}_3\text{N}_4$  materials described in section 2.3.3. The plots cover the homologous temperature range  $0.15 - 0.5 T_m$ . Comparing these curves with the results for SiC, a number of differences were observed:

- (a) The variation in hardness due to microstructure was much greater for  $\text{Si}_3\text{N}_4$  (  $800 - 3100 \text{ kgf mm}^{-2}$  at  $25^\circ\text{C}$  ) than for SiC.
- (b) The temperature sensitivity of hardness was much less for  $\text{Si}_3\text{N}_4$  than for SiC.
- (c) At room temperature, only pyrolytically-deposited  $\text{Si}_3\text{N}_4$  ( PDSN ) was of comparable hardness to the hardest forms of SiC, the other forms of  $\text{Si}_3\text{N}_4$  being generally much softer than corresponding forms of SiC. The comparatively high hardness of PDSN ( also reported in ref. 157 ) may be due to the relatively large grain size ( section 3.6.5 ) or possibly to impurity effects ( see section 3.5 ) in the other  $\text{Si}_3\text{N}_4$  materials: the PDSN sample was known to be relatively pure since it was semi-transparent whilst all the other samples were opaque.
- (d) Because of their smaller dependence of hardness on temperature, many of the nitrides became as hard as ( sometimes harder than ) corresponding forms of SiC at high temperatures. PDSN had superior hardness to all forms of SiC at temperatures above  $200^\circ\text{C}$ .

Plotting the results as  $\log H$  against  $(1/T)$  ( fig. 24c ), two types of behaviour were observed in  $\text{Si}_3\text{N}_4$  materials. The fully-dense materials ( PDSN and the two hot-pressed samples ) all showed a transition in activation energy at  $T_c \approx 330^\circ\text{C}$  (  $0.28 T_m$  ), with

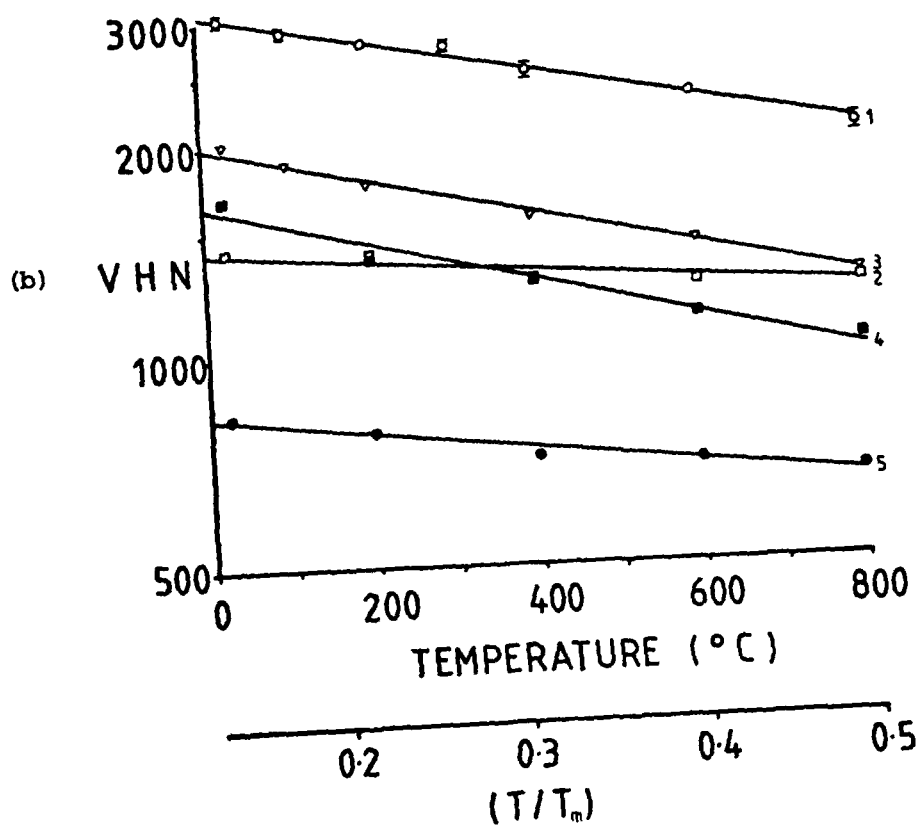
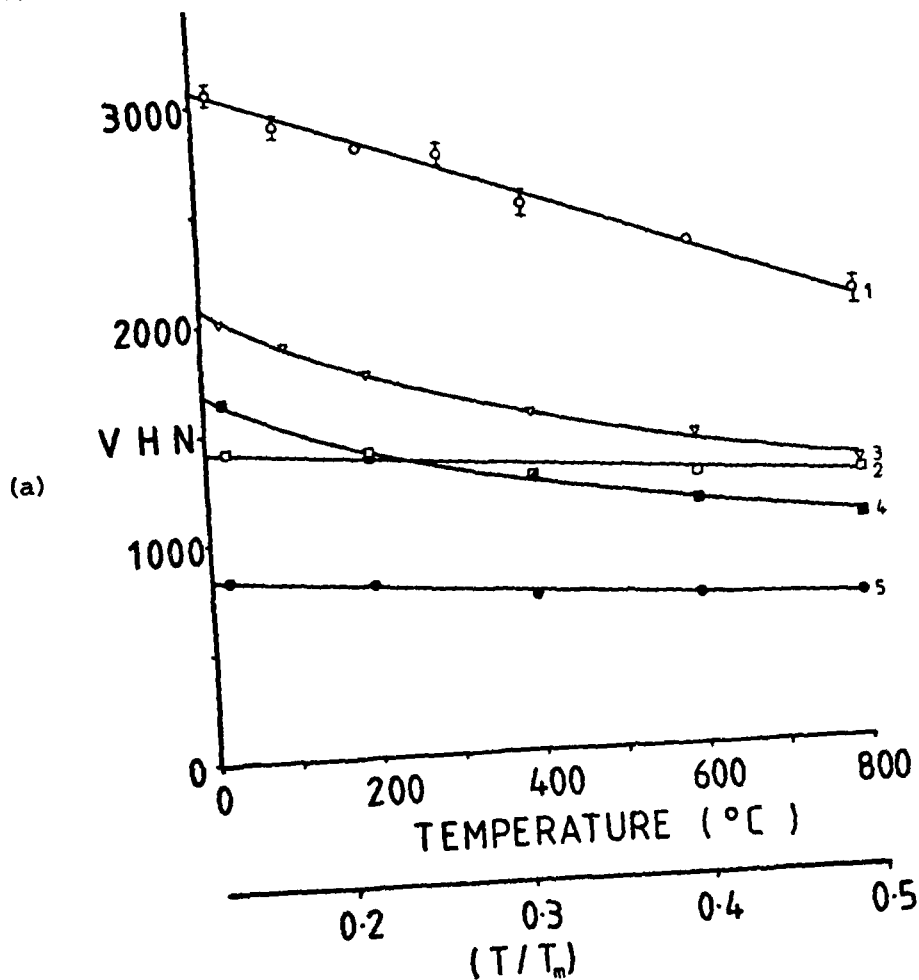


Figure 24. The variation of Vickers hardness (1 kgf applied load and 15s dwell time) with temperature for polycrystalline forms of  $\text{Si}_3\text{N}_4$ : (a) linear plots, (b) logarithmic hardness scale. Error bars indicate one standard error in the mean for approximately 10 indentations. Curve 1 = pyrolytically-deposited  $\text{Si}_3\text{N}_4$ , curve 2 = Norton NC132 hot-pressed  $\text{Si}_3\text{N}_4$  (MgO Ford '2.7' RBSN, curve 3 = Norton NC132 hot-pressed  $\text{Si}_3\text{N}_4$  (Y<sub>2</sub>O<sub>3</sub> pressing additive), curve 4 = Norton NCX34 hot-pressed  $\text{Si}_3\text{N}_4$  (Y<sub>2</sub>O<sub>3</sub> pressing additive).

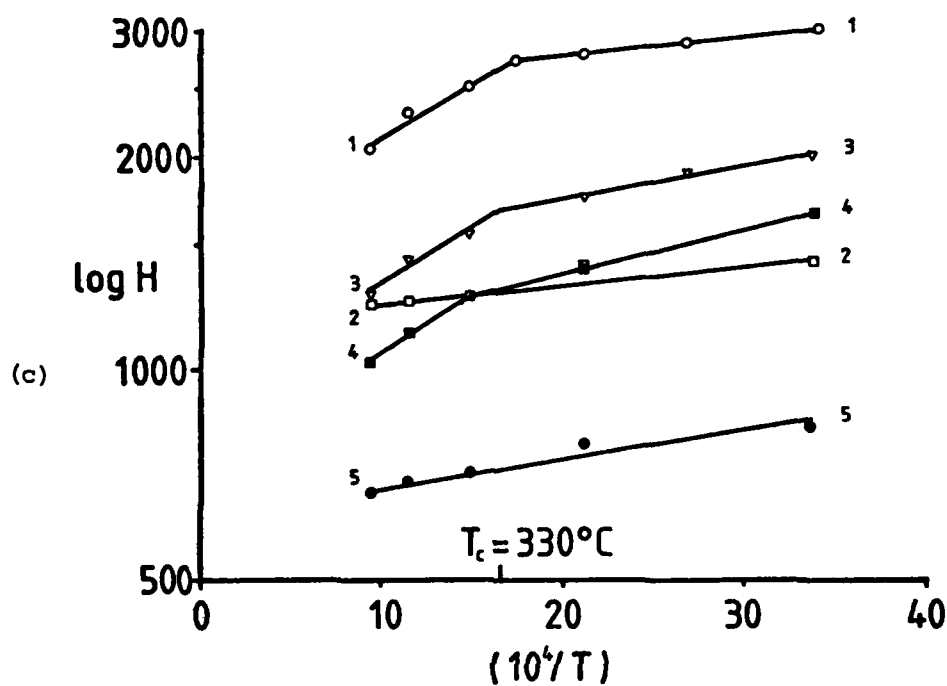


Fig. 24c. Activation energy plots of  $\log H$  against  $(10^4/T)$  for  $\text{Si}_3\text{N}_4$  materials. Curve 1 = pyrolytically-deposited  $\text{Si}_3\text{N}_4$ , curve 2 = Ford '2.7' RBSN, curve 3 = Norton NC132 hot-pressed  $\text{Si}_3\text{N}_4$  (MgO pressing additive), curve 4 = Norton NCX34 hot-pressed  $\text{Si}_3\text{N}_4$  ( $\text{Y}_2\text{O}_3$  pressing additive), curve 5 = Norton NC350 RBSN.

very similar high-temperature activation energies ( table 8 ) of approximately  $3 \text{ kJ mol}^{-1}$ . Figure 24c shows that the activation energy plots for these materials were all of similar shape but were transposed along the  $\log H$  axis from each other. This is especially significant for the two hot-pressed materials, which differed primarily in the amount and composition of grain boundary phases ( discussed in section 3.6.6 ).

Activation energies for the two highly porous RBSN materials were significantly lower (  $0.9 - 1.1 \text{ kJ mol}^{-1}$  ) than for fully-dense samples, and showed little or no change over the whole temperature range ( fig. 24c ). This is probably due to compaction effects ( section 3.6.7 ). A consequence of this behaviour was that RBSN materials, which were the softest forms of  $\text{Si}_3\text{N}_4$  at room temperature, showed little change in hardness with increasing temperature. Thus, Ford '2.7' RBSN became harder than Norton NCX 34 hot-pressed  $\text{Si}_3\text{N}_4$  ( HPSN ) at  $\sim 300^\circ\text{C}$  and as hard as Norton NC 132 HPSN at  $\sim 800^\circ\text{C}$ . Norton NC 350 RBSN ( of lower density than Ford '2.7' RBSN ) remained softer than all other forms of  $\text{Si}_3\text{N}_4$  over the whole temperature range.

### 3.6.3 Results for Sialon

The variation of Vickers hardness ( 1 kgf load, 15 s dwell time ) with temperature for Lucas sintered SYALON 342 is shown in figure 25. The hot-hardness curve was very similar to that for  $\text{Y}_2\text{O}_3$  hot-pressed  $\text{Si}_3\text{N}_4$  ( Norton NCX 34 HPSN ), with very little change in hardness with increasing temperature. The activation energy plot ( fig. 25c ) possibly shows a small change in slope at  $\sim 240^\circ\text{C}$  ( the melting point of this material is not known, so homologous temperatures could not be calculated ). The activation energy calculated from the high-temperature hot-hardness data was  $\sim 1.8 \text{ kJ mol}^{-1}$ , lower than the value for dense silicon nitrides ( table 8 ).

### 3.6.4 Results for Boron Carbide

In figure 26a, the Vickers hardness ( 1 kgf load, 15 s dwell time ) is shown as a function of temperature for two sintered boron carbides of different densities ( corresponding to 2.5 vol % and

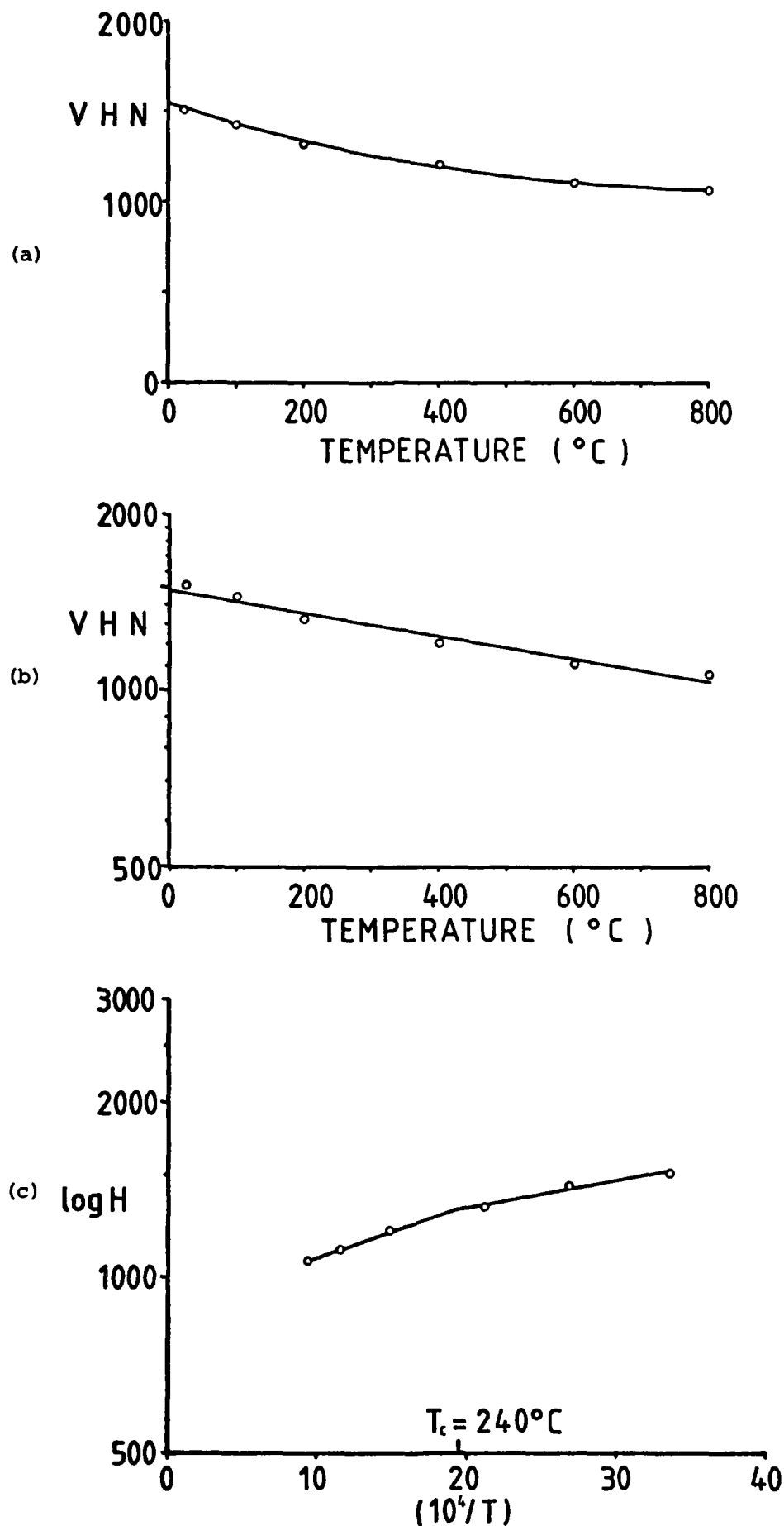


**Figure 25.** The variation of Vickers hardness ( 1 kgf applied load and 15s dwell time ) with temperature for a sintered sialon ( Lucas SYALON 342 ): (a) linear plot, (b) logarithmic hardness scale and (c) activation energy plot of log H against  $(10^4/T)$ . Error bars indicate one standard error in the mean for approximately 10 indentations.

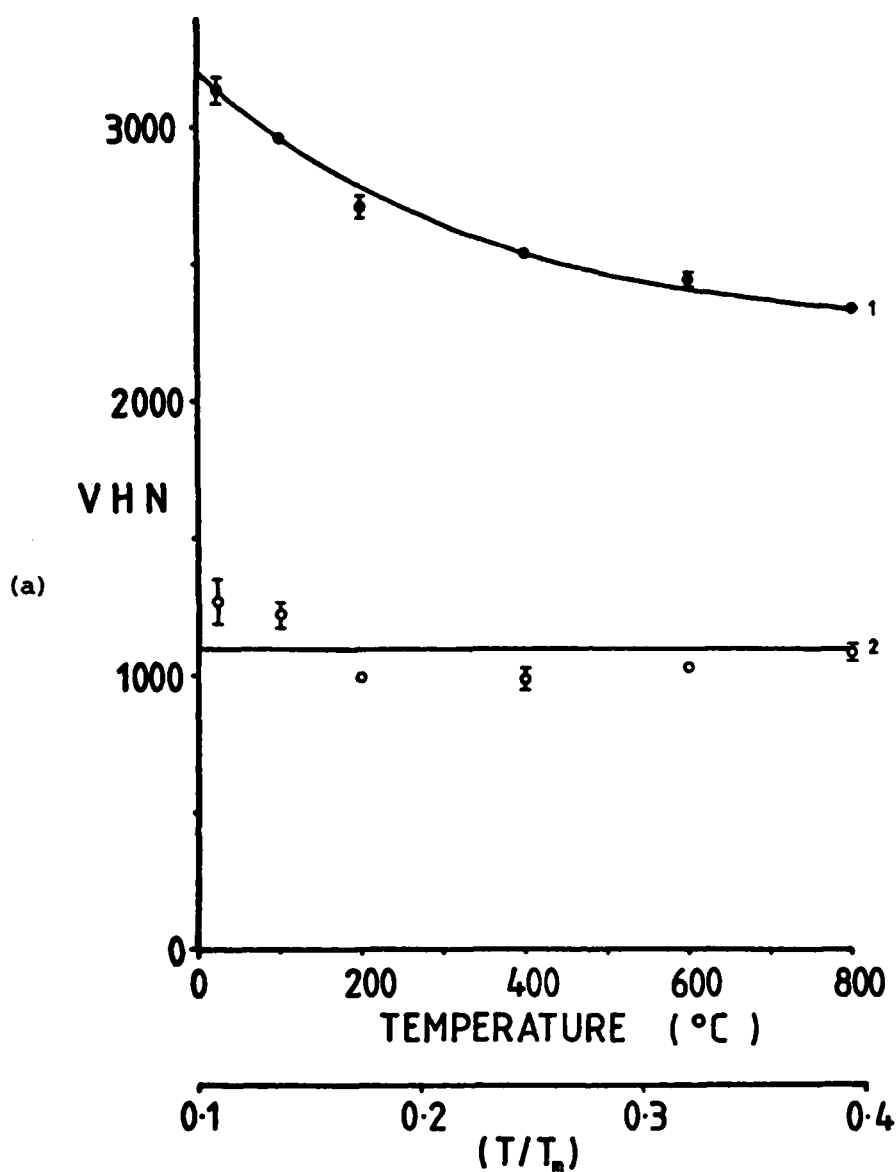


Figure 26. The variation of Vickers hardness ( 1 kgf applied load and 15s dwell time ) with temperature for two forms of sintered  $B_4C$ : (a) linear plots. Error bars indicate one standard error in the mean for approximately 10 indentations. Curve 1 = Le Carbone sintered  $B_4C$  grade S1143 ( density  $2.4 \text{ gcm}^{-3}$  ), curve 2 = Le Carbone sintered  $B_4C$  grade S1138 ( density  $2.05 \text{ gcm}^{-3}$  ).

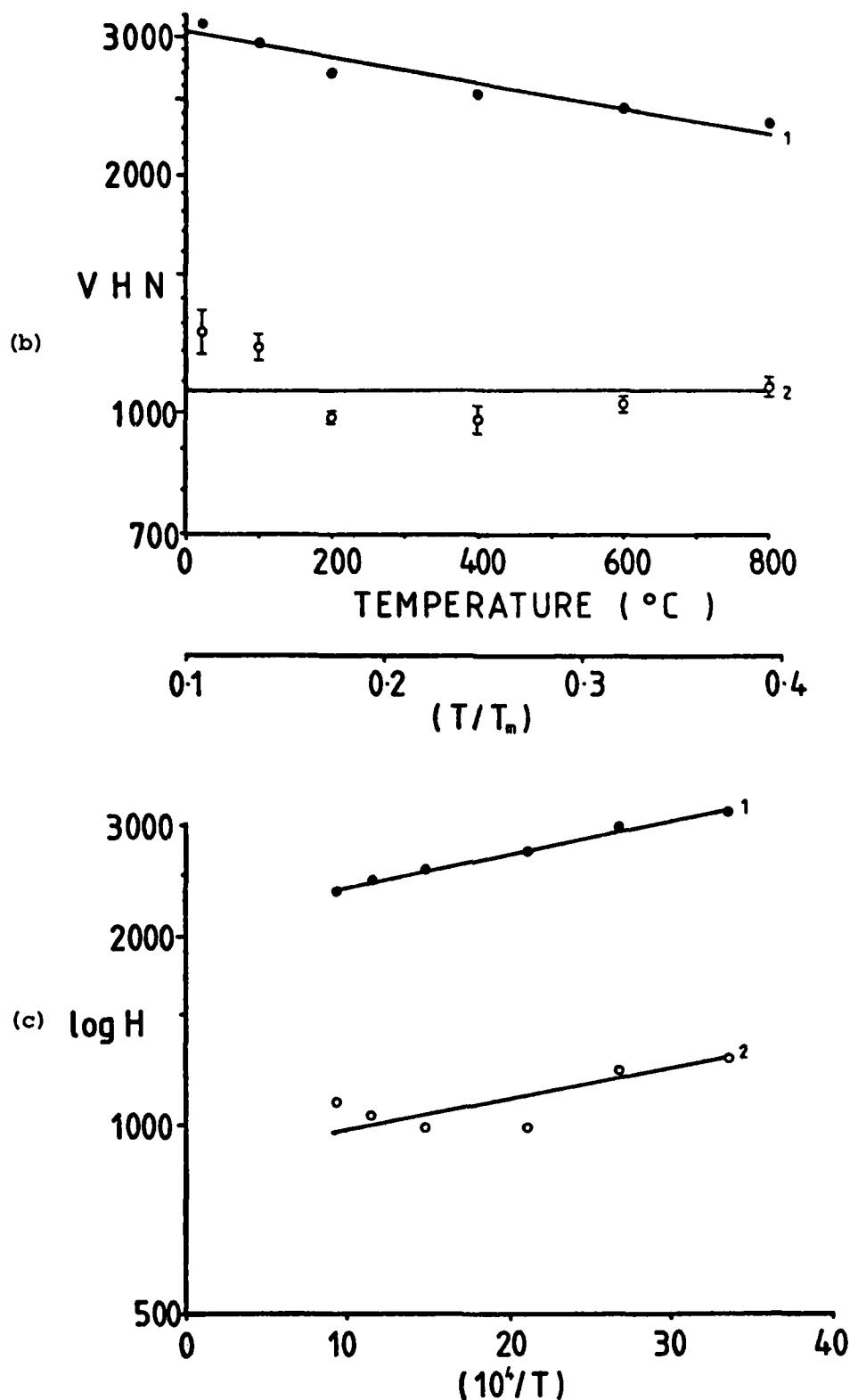


Fig. 26 (b) Hot-hardness plots ( logarithmic hardness scale ) for sintered boron carbides, (c) activation energy plots of log H against (10<sup>4</sup>/T). Curve 1 = Le Carbone grade S1143 ( density 2.4 gcm<sup>-3</sup> ), curve 2 = Le Carbone grade S1138 ( density 2.05 gcm<sup>-3</sup> ).

Material	Activation Energy ( $\text{kJmol}^{-1}$ )	
	Vickers	Knoop
<u>SILICON CARBIDE</u>		
(0001) blue-black single crystal ( $\langle 11\bar{2}0 \rangle$ orientation)	6.3 ( $\pm 0.5$ )	7.5 ( $\pm 1.3$ )
Hot-pressed (Norton NC203)	7.3 ( $\pm 0.8$ )	6.0 ( $\pm 0.9$ )
Sintered (Carborundum) (Suzuki)	8.9 ( $\pm 0.7$ ) 7.2 ( $\pm 0.2$ )	6.0 ( $\pm 0.6$ ) -
Reaction-bonded (REFEL-a) (REFEL-b)	10.4 ( $\pm 2.4$ ); 9.8 ( $\pm 2.4$ ) * 8.4 ( $\pm 0.8$ ); 8.0 ( $\pm 0.8$ ) *	11.2 ( $\pm 1.4$ ) -
<u>SILICON NITRIDE</u>		
Pyrolytically-deposited (AMTE)	2.8 ( $\pm 0.3$ )	-
Hot-pressed (Norton NC132) (Norton NCX34)	2.9 ( $\pm 0.6$ ) 3.1 ( $\pm 0.2$ )	- -
Reaction-bonded (Ford '2.7') (Norton NC350)	0.89 ( $\pm 0.19$ ) 1.08 ( $\pm 0.07$ )	-
<u>SIALON</u>		
Sintered (Lucas Syalon 342)	1.84 ( $\pm 0.05$ )	-
<u>BORON CARBIDE</u>		
Sintered (Le Carbone $\rho=2.4\text{gcm}^{-3}$ ) (Le Carbone $\rho=2.05\text{gcm}^{-3}$ )	1.00 ( $\pm 0.04$ ) 0.70 ( $\pm 0.30$ )	- -
<u>SILICON</u>		
{111} single crystal ( $\langle 11\bar{1}0 \rangle$ orientation)	35 ( $\pm 3$ ) <sup>†</sup>	-

**Table 8** Activation energies for the variation of hardness (at 1 kgf load and 15s dwell time) with temperature above  $T_c$  for a variety of ceramic materials. Errors are one standard error in the mean. N.B. REFEL(a) had grain size  $\sim 10\mu\text{m}$ , REFEL (b) had grain size  $\sim 5\mu\text{m}$ .

\* corrected for residual silicon content.    † 100gf applied load

22.5 vol % porosity ). The denser material was found to be exceptionally hard at room temperature (  $3100 \text{ kgf mm}^{-2}$  ): slightly harder than both (0001) single crystal SiC and PDSN. The temperature sensitivity of hardness was very low for both forms of boron carbide.

The highly porous material was much softer ( by a factor of  $\sim 3$  at  $25^{\circ}\text{C}$  ) than the dense form, showing almost no systematic variation of hardness with temperature ( N.B. the measured hardness of this specimen showed considerable scatter because the porosity was not distributed uniformly ).

Activation energies were thus low for both samples ( table 8 ), values being comparable to those for RBSN materials. The activation energy plots ( fig. 26c ) showed no change in slope in the temperature range investigated (  $0.1 - 0.4 T_m$  ).

### 3.6.5 The Effects of Grain Size

It is difficult to isolate the effects of grain size on hot-hardness behaviour from figs. 22 - 26 because of variations in other microstructural features. For example, RBSN materials had smaller grain sizes than other forms of  $\text{Si}_3\text{N}_4$ , but the effects of porosity are thought to be more important for these materials ( section 3.6.7 ). PDSN ( grain size  $\sim 50\mu\text{m}$ : larger than indentation sizes ) was significantly harder than other  $\text{Si}_3\text{N}_4$  materials ( where grain sizes were always less than the indentation size ), but this might have been partly ( or wholly ) an effect of purity, since the PDSN sample was apparently more pure than other forms of  $\text{Si}_3\text{N}_4$  examined. Although 'REFEL' reaction-bonded silicon carbides appeared to show the opposite effect ( fig. 22c ), a more comprehensive study ( at room temperature ) has established that hardness generally decreases with decreasing grain size and that other microstructural factors are important in these materials ( 158 ).

The observation that single crystal SiC was harder than polycrystalline forms suggests a softening effect due to the presence of grain boundaries in SiC. However, it is not meaningful to compare the polycrystal values with a single crystal value for one indenter orientation, due to the marked hardness anisotropy observed for single crystals ( section 3.4.3 ). For a polycrystalline material with grain size less than the indentation size, anisotropy effects would be

averaged out. Thus, we should compare polycrystal hardness values with a single crystal value averaged over a large number of different orientations in order to establish the effects due to grain boundaries. Average Knoop hardnesses ( 200 gf load ) at room temperature and 800°C were calculated for green SiC single crystals ( figs. 17b, 18, 19 ). However, polycrystalline SiC materials were found to be blue-black in colour, and so likely to be harder due to impurity effects ( 3.5.3 ). Equivalent hardness values for blue-black single crystals were therefore estimated using figs. 17a and 17b. Predicted single crystal and measured polycrystal hardness values are given in table 9 for room temperature and 800°C. The results indicate that there is no consistent grain boundary effect at room temperature, but a marked softening effect due to the presence of grain boundaries seems to occur at 800°C. Similar grain boundary softening effects have been found in MgO ( 86 ) and BeO ( 159 ). The opposite effect has been found in Al<sub>2</sub>O<sub>3</sub> ( 160 ) and other materials ( 155 ).

Grain size effects have been considered in detail by Sargent ( 86, 161 ), who concludes that grain boundary hardening may be expected where high back-stresses occur in dislocation pile-ups at grain boundaries ( in order to initiate slip in the next grain ) and strain-hardening occurs due to secondary slip along boundaries ( required to prevent intergranular fracture ( 86 ) ). In this case, a Hall-Petch relation is expected:

$$H = H_0 + k_h g^{-1/2}$$

where  $H_0$  = hardness extrapolated to infinite grain size from the fine-grained regime ( 86 ),  $k_h$  = a constant related to the stress concentration at the grain boundary due to dislocation pile-up,  $g$  = grain size ( e.g. grain boundary surface area per unit volume ( 86, 161 ) ).

Alternatively, a grain boundary softening effect is expected where the five independent slip system requirement is relaxed by a combination of primary slip in each of the differently oriented grains beneath the indenter, with grain boundary separation to accommodate strain mismatch. This mechanism is thought to be favoured where grain boundary fracture energies are low ( 86 ), and evidence for preferential fracture along boundaries is indeed observed in SiC and Si<sub>3</sub>N<sub>4</sub> materials ( section 4.5 ). Provided the grain boundary fracture energy does not change significantly with temperature, as is the case for many

Material	Knoop Hardness at 200 gf load ( kgf mm <sup>-2</sup> )	
	Room temperature	800°C
Blue-black single crystal SiC	Mean value = 2690	Mean value = 1750
Norton NC203 hot-pressed SiC	2880	1420
Carborundum sintered SiC	2630	1290

**Table 9** A comparison between the Knoop hardness ( 200 gf load, 15s dwell time ) of single crystal and polycrystalline SiC materials at room temperature and 800°C. The single crystal value is an estimate of the hardness averaged over all possible indenter:crystal orientations ( see text ). For the polycrystalline materials, grain sizes were less than the sizes of indentations ( the long diagonals were ~30  $\mu\text{m}$  in length at room temperature and ~45  $\mu\text{m}$  in length at 800°C ).

Material	Porosity $p$	Grain Size $D$ ( $\mu\text{m}$ )	$E$ ( GPa )	$\gamma$ ( Jm <sup>-2</sup> )	$H_1$ ( GPa )	$H_2$ ( GPa )	Measured $H$ ( GPa )
<u>Room Temperature</u>							
Boron Carbide	0.025	5	383	11.7	0.18	39.8	33.5
	0.225	5	240	40.3	0.043	12.0	14.1
RBSN ( Ford '2.7' )	0.13	1	210	32.6	0.39	12.2	15.3
( Norton NC350 )	0.21	1	180	21.8	0.13	9.1	8.8
<u>800°C</u>							
Boron Carbide	0.025	5	376	6.9	0.11	39.1	25.0
	0.225	5	235	21.8	0.023	11.8	11.6
RBSN ( Ford '2.7' )	0.13	1	207	33.1	0.40	12.1	13.0
( Norton NC350 )	0.21	1	177	22.1	0.13	8.9	7.1

**Table 10** The effects of porosity on hardness for two sintered boron carbides and two RBSN materials at room temperature and 800°C ( for theory, see text ). Measured and calculated hardness values are projected area Vickers hardness.

of these materials in the range 25 - 1000°C ( section 4.4 ), a uniform softening effect is predicted over the whole temperature range. This seems to be the case for PDSN compared with HPSN materials ( fig. 24 ), where the hot-hardness curves are transposed along the log H axis with no change in either  $T_c$  or activation energy ( fig. 24c ). The reasons for the temperature sensitivity of this behaviour in SiC ( if this is, indeed, a real effect ) are unclear.

### 3.6.6. The Effects of Grain Boundary Phases

Effects due to differences in grain boundary phases are best observed in hot-pressed materials with different pressing additives but constant grain size, etc. ( see sections 1.2.4.2 and 1.2.5 ). Thus, NC132 HPSN ( with ~5 wt% MgO ) was found to be harder than NCX34 HPSN ( with ~8 wt%  $Y_2O_3$  ) at all temperatures, the curves being transposed along the log H axis without change in  $T_c$  or activation energy ( figs. 24 b,c ). Similar results have been observed for a range of hot-pressed silicon nitrides by Huseby and Petzow ( 162 ) and for  $Al_2O_3$  materials by Loladze et al. ( 163 ).

Now the primary slip/grain boundary separation model discussed in the previous section would predict a decrease in hardness with decreasing grain boundary fracture energy (  $\gamma_{gb}$  ) for materials which show a softening effect due to grain boundaries ( e.g. for SiC and  $Si_3N_4$  materials but not for  $Al_2O_3$  ). On this basis, NCX34 HPSN ought to have lower grain boundary cohesion than NC132 HPSN, as found experimentally ( section 4.5 ). The two materials might further be expected ( assuming a general relation of the form  $H \propto \gamma_{gb}^n$  ) to show a constant offset in the semi-logarithmic hot-hardness curves, provided the ratio  $\gamma_1/\gamma_2$  remains constant.

At very high temperatures ( e.g. 1000°C for  $Si_3N_4$  ), softening of grain boundary phases may lead to grain boundary sliding effects ( e.g. 66 ). Evidence for boundary sliding beneath even room temperature indentations in ZnS has been found by Van der Zwaag et al. ( 134 ). If this occurs generally, differences in hardness would be predicted due to variations in boundary phase viscosity or boundary diffusion coefficients. However, in this case, variations in  $T_c$  and activation energy between materials would also be expected and so the results are thought to be more consistent with the former model.

These effects might also occur in 'REFEL' reaction-bonded silicon carbides, where residual silicon is found over much of the grain boundary surface area. Thus, softening effects in addition to the volume fraction effect described in section 3.6.1 may occur in 'REFEL' materials.

### 3.6.7 The Effects of Porosity

The effects of porosity on hot-hardness behaviour have been the subject of some confusion in the literature. Atkins and co-workers ( 93, 164 ) report that for  $\text{TiC}$  and  $\text{TiB}_2$ , porosity acts to decrease the hardness in the low-temperature regime (  $< 0.5 T_m$  ) but at higher temperatures hardness is largely independent of porosity. Rice ( 155 ) has analyzed the data of Koester and Moak ( 165 ) for precisely the same materials and reached the opposite conclusion that porosity has more effect at high temperatures.

The results obtained in this study for porous RBSN and sintered  $\text{B}_4\text{C}$  samples are more in accord with the former observations. It seems likely that softening due to porosity at low temperatures occurs because compaction becomes an easier mode of deformation than plastic flow, whereas this is not so at high temperatures. Direct evidence for compaction effects may be seen in fig. 27, which shows room-temperature Vickers indentations in a range of highly porous  $\text{SiC}$ ,  $\text{Si}_3\text{N}_4$  and  $\text{B}_4\text{C}$  materials. For all these materials, the amount of porosity within the indentation profile is noticeably less than in the undeformed surface. In some materials, networks of microcracks may be observed within the indentation profile, suggesting that compaction occurs by fracture ( probably along grain boundaries since porosity is largely intergranular in these samples ) followed by re-arrangement of the pieces to form a densified region beneath the indenter. In NC350 RBSN ( figure 27c ) a lip of material may be seen to overhang the indentation profile ( this may be seen much more clearly in the stereo pair of this micrograph ( fig. 6f ) ). A possible explanation for this unlikely observation is that elastic recovery of the undensified surface is much more pronounced than for the densified region beneath the indentation.

A simple model for the effects of compaction on hardness has been developed in order to justify the observations that

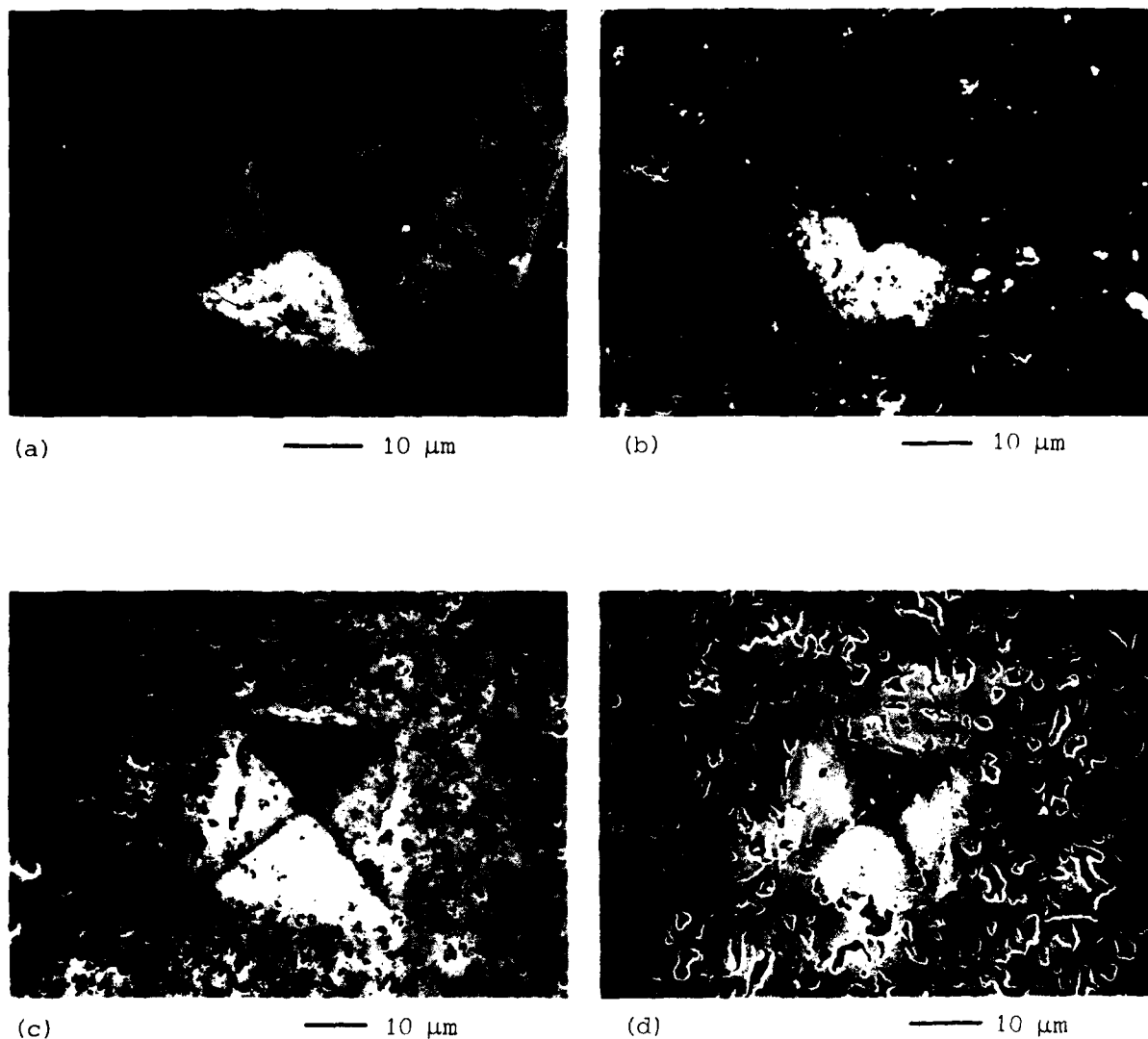


Figure 27 Vickers indentations ( 1 kgf load ) in porous materials. (a) 'Suzuki' sintered SiC ( 9 vol% porosity ), 800°C. (b) Ford '2.7' reaction-bonded  $\text{Si}_3\text{N}_4$  ( 13 vol% porosity ), room temperature. (c) Norton NC350 reaction-bonded  $\text{Si}_3\text{N}_4$  ( 21 vol% porosity ), room temperature. (d) Le Carbone sintered  $\text{B}_4\text{C}$  ( 22.5 vol% porosity ), room temperature. All materials exhibit less porosity within the indentation than in the rest of the surface, suggesting compaction may have occurred. Also, fine cracks, which may have been caused by grain boundary fracture during compaction, are evident within some of the indentations ( especially in (d) ). The stereo pair of image (c) is shown in figure 6f.

(a) hardness decreases with increasing porosity and (b) the temperature sensitivity of hardness is much lower for porous than for dense materials ( figs. 24 and 26 ). The model assumes that deformation occurs entirely by a combination of elasticity and compaction of the porous material ( density  $\rho$  ) to form a fully dense zone ( density  $\rho_T$  ) beneath the indenter. Compaction is assumed to occur by breaking grain boundaries followed by grain re-arrangement, with negligible plastic flow. Thus, the model applies only to materials of small grain size  $D$  ( compared with the indentation size  $a$  ), low grain boundary fracture energy  $\gamma_{gb}$  and high volume fraction of porosity  $p$ .

(a) The Size of the Compacted Zone

A simple mass balance may be applied by assuming that all the mass displaced by the indenter ( volume  $v_i$ , radius  $a$  ) is accommodated in the densified region ( volume  $v_d$ , radius  $b$  ).

$$\text{Hence } \rho_T v_d = \rho ( v_d + v_i )$$

$$\text{and } (\rho/\rho_T) = (1 - p)$$

For a Vickers indentation (  $v_i = 4a^3/21$  ), this reduces to:

$$(b/a) = \left[ \frac{6}{21\pi p} \right]^{1/3}$$

i.e for sintered  $B_4C$ ,  $(b/a) = 1.5$  for  $p = 0.025$  and  $(b/a) = 0.74$  for  $p = 0.225$ .

(b) The Energy Balance

Assuming negligible plastic deformation, specimen heating, etc., work done by indenter ( $W$ ) = work of fracture ( $V$ ) + elastic energy ( $U$ )

Work Done by the Indenter

$$W = Lh \quad \text{where } L = \text{force on the indenter,} \\ h = \text{indentation depth ( } 2a/7 \text{ for Vickers ).}$$

Fracture Energy

If the grains are equiaxed and of mean diameter  $D$ , then

$$\text{the number of grains affected} = N \approx \frac{6v_d}{\pi D^3}$$

The total area fractured =  $\pi D^2 N (1 - p)$  assuming an area fraction  $p$  of porosity at the grain boundaries.

$$\begin{aligned} \text{Hence } V &= \pi D^2 N (1 - p) \gamma \\ &= \frac{24 (1 - p)^2 \gamma a^3}{21 p D} \end{aligned}$$

#### Elastic Energy

$$U = \oint (\text{stress} \times \text{strain}) dV$$

Assuming a Boussinesq elastic stress field (section 4.2.2):

$$U = \frac{1}{E} \int_0^{2\pi} \int_{-\pi/2}^{\pi/2} \int_b^{\infty} \left[ \frac{L}{4\pi r^2} \right]^2 f^2(\theta) r^2 dr d\theta d\phi$$

where  $r, \theta, \phi$  are the spherical polar co-ordinates defined in fig. 31.  $f(\theta)$  is a function of the type of stress (e.g.  $\sigma_r, \sigma_\theta, \sigma_\phi$ , etc.) (see section 4.2.2).

$$\text{Thus } U = \frac{L^2}{8\pi E b} \int_{-\pi/2}^{\pi/2} f^2(\theta) d\theta$$

The integral has been evaluated numerically for various stresses, giving

$$U = \frac{53L^3}{8\pi E b}$$

Applying the energy balance and substituting for  $b$  and for  $H$  ( $= L/2a^2$  for projected area Vickers hardness), we obtain a quadratic in  $H$ :

$$\frac{Ap^{1/3} H^2}{E} - H + \frac{2(1-p)^2 \gamma}{p D} = 0$$

where  $A$  is a constant, calculated to be  $\sim 32.8$ .

This equation has been applied to experimental data for porous boron carbide and RBSN materials (at room temperature and  $800^\circ\text{C}$ ) (table 10). Values of grain boundary fracture energy were calculated using  $\gamma_{gb} = (K_{IC}^2/2E)$  and  $K_{IC}$  values listed in table 18 (section 4.4.2), assuming that indentation fracture was entirely intergranular in the experiments performed to determine  $K_{IC}$ . In table 10, the two roots  $H_1$  and  $H_2$  of the quadratic equation are shown,

and it is evident that  $H_2$  values were ( surprisingly ) close to measured hardness values,  $H_1$  values being  $\sim 2$  orders of magnitude smaller. The discrepancy between calculated  $H_2$  and measured values was greatest for the denser boron carbide at  $800^\circ\text{C}$ , for which plasticity may have become more favourable than compaction. Obviously, further measurements on a range of materials with varying porosity will be required to test the theory properly.

Now  $H_2$  is the root corresponding to the situation where the elastic energy is much greater than the fracture energy, for which

$$H_2 \approx ( E / A p^{1/3} )$$

Thus, the dependence of hardness on porosity and Young's modulus are predicted theoretically, and the observed lack of temperature-sensitivity for porous materials may be explained since  $E$  is only a weak function of temperature for these materials. Interestingly, grain size and grain boundary fracture energy are predicted to have little effect on hardness because the elastic stresses depend on the size of the compacted zone, which depends only on the amount of porosity. Porosity has a weak influence on hardness through the  $p^{-1/3}$  term above, but a much stronger one through the effect of porosity on Young's modulus ( see e.g. 155 ).

### 3.6.8 Summary

Microstructure has been found to have large effects on hardness for  $\text{SiC}$ ,  $\text{Si}_3\text{N}_4$  and  $\text{B}_4\text{C}$  materials. Generally, hot-hardness curves for the different microstructural forms were transposed along the hardness axis ( on a logarithmic scale ) from each other, with little variation in activation energies or in  $T_c$ . For polycrystalline forms of  $\text{SiC}$ ,  $T_c$  was found to be  $\sim 0.18 T_m$  (  $300^\circ\text{C}$  ), whilst for fully-dense polycrystalline  $\text{Si}_3\text{N}_4$ ,  $T_c$  was  $\sim 0.28 T_m$  (  $330^\circ\text{C}$  ). These values are at the lower end of the observed ranges in  $T_c$  for single crystals ( section 3.3.1 ). Sintered sialon also showed a weak transition at  $T_c \approx 240^\circ\text{C}$ . Sintered  $\text{B}_4\text{C}$  showed no transition below the maximum temperature used (  $0.4 T_m$  ).

Grain boundaries are thought to produce softening effects in these materials by allowing deformation to occur by a combination

of primary slip and grain boundary separation, facilitated by low boundary fracture energy. Grain boundary phases have been found to affect the hardness of hot-pressed materials, presumably by changing the grain boundary cohesion.

Evidence for compaction has been found in porous materials and a model developed to quantify the effect which fits the data well with no adjustable parameters.

In all cases, there is a need for further research to verify the proposed mechanisms.

### 3.7 INDENTATION SIZE EFFECTS

Up to this point, it has been tacitly assumed that hardness is a characteristic of the bulk material irrespective of the size of the indentation (or, correspondingly, of the applied load). For many materials, this is not found to be the case (e.g. 166). For ductile materials, hardness tends to a constant value at high loads, but for ceramics this effect is not generally observed because indentations cannot be measured at very high loads due to massive indentation fracture (e.g. above ~100 gf in silicon - see fig. 37). Thus, it is important to quantify the indentation size effect when measuring the hardness of a ceramic material.

#### 3.7.1 The Meyer Index

The indentation size effect is best quantified empirically by the Meyer Index ( $n$ ) defined by (e.g. 86, 161):

$$P = k a^n$$

where  $P$  = applied load,  $k$  = constant,  $a$  = indentation radius.

A value of  $n = 2$  indicates no variation of hardness with load since  $H \propto P/a^2 = \text{constant}$  with respect to load. For  $n < 2$ , the hardness decreases with increasing load, for  $n > 2$ , the converse is true. The amount by which  $n$  differs from 2 measures the magnitude of the indentation size effect. For many materials,  $n$  is in the range 1.8 - 2 (167), although significantly different values have been found for some materials (e.g.  $n = 4$  for PbTe alloys (168)).

The Meyer index is calculated by, for example, least squares

fit to a  $\log a : \log P$  plot, minimizing the errors in  $\log a$ . Detailed statistical techniques for calculating  $n$  and also the hardness at a given indentation size ( rather than at fixed load ) have been given by Sargent ( 86, 161 ).

It is important to realize that the relation described above is merely an empirical function which best describes the effect for most materials: it makes no assumptions about the cause(s) of the effect.

### 3.7.2 Theoretical Interpretations

#### (a) Elastic Recovery

Early workers ( e.g. 169 ) considered that elastic recovery of the indentation on removal of the load might be proportionately more severe for smaller indentations ( making  $n < 2$  ). Whilst this effect might be significant in very hard, stiff solids, it is not thought to account for the full indentation size effect observed in these materials, probably because elastic recovery of indentations does not alter the diagonal lengths significantly ( 86 ).

#### (b) Surface Effects

Clearly, small indentations will be more sensitive to surface effects than large indentations, which sample more of the bulk. Thus, surface layers of, for example, different composition or strain are likely to cause an indentation size effect. Sargent ( 86 ) has shown that even a very thin layer ( compared with the indentation size ) may produce a measurable effect. Surface effects might also arise due to the chemical environment above the specimen surface, as discussed in section 3.9.

Additionally, the free surface is expected to influence plasticity mechanisms even in the absence of other effects, because of differences in atomic structure, electronic band structure, purity, vacancy concentration, etc. ( e.g. 2 ). For example, dislocations in the bulk experience image forces which attract them towards the surface and perhaps facilitate near-surface dislocation nucleation. Oxide layers of high elastic modulus present on the surface may attract distant dislocations but repel close ones, and also impede the exit of dislocations at the surface, perhaps causing dislocation pile-ups ( 86 ). Where dislocations intersect the surface, pinning or drag

effects must be considered. In short, both dislocation nucleation and propagation processes are likely to be modified to a large extent by the surface.

(c) Scale Effects

The scale of the indentation with regard to the deformation may produce an indentation size effect in the following way. Small indentations require nearby dislocation loops to be of greater curvature than do large indentations, thus increasing the stress required to propagate such loops ( 86 ). Mott ( 170 ) considers that slip interpenetration might be more difficult for smaller indentations. Sargent ( 86 ), by a process of elimination, considers that such effects provide the most likely explanation of the indentation size effect in single crystal MgO.

In addition to these effects, the scale of the indentation with regard to the specimen microstructure may be important ( 86, 161 ). In polycrystalline materials, for example, a transition from pseudo-single crystal to polycrystalline behaviour is expected as the indentation size increases from less than to greater than the grain size. Such effects have been measured by Sargent and Page ( 161 ) for MgO. None of the experiments described here should show such an effect because indentation sizes were always either less than or greater than the grain size over the whole load range used.

(d) Indentation Fracture Effects

As described in Chapter 5, above a critical value of applied load (  $P^*$  ), indentation fracture occurs, which might well change the stress state beneath the indentation. An indentation size effect might therefore be observed if  $P^*$  falls within the load range used. However, it has been estimated that the energy of fracture is usually negligible compared with the energy of deformation ( 0.1% for SiC at 100gf ( 90 ) ), so this effect should be small.

In this section, a variety of theoretical interpretations of the indentation size effect has been presented. Few, if any of the models described above have been quantified, and it is difficult to assess the relative contributions of each mechanism to observed indentation

size effects in real materials. Accordingly, experimental results for the materials investigated in this study will be presented with relatively little discussion. Clearly, further understanding of these effects must await more detailed knowledge of the deformation mechanisms operating beneath the indenter and the ways in which the free surface modifies the deformation.

### 3.7.3 Temperature Effects

Meyer indices calculated from Vickers hot-hardness data for Si, SiC,  $\text{Si}_3\text{N}_4$ , sialon and  $\text{B}_4\text{C}$  materials are shown in table 11. Values were calculated from least-squares fits to  $\log a : \log P$  plots, as described in reference 161, only without the statistical weighting, which was found to have little effect on the results. The load range was 100 - 1000 gf in each case.

Most of the indices were found to lie in the range 1.8 - 2, indicating relatively little indentation size effect over this load range (the effect is generally more pronounced at lower loads (86)). Si and SiC materials were found to show little consistent change in  $n$  with temperature, whilst  $\text{Si}_3\text{N}_4$  materials showed a small increase, with  $n > 2$  (by varying amounts) at  $800^\circ\text{C}$ . Sargent (86) similarly observed that  $n$  increased towards 2 with increasing temperature for single crystal MgO.

Meyer indices calculated from Knoop hot-hardness data (same load range) for various forms of SiC are shown in table 12:  $n$  was found to be significantly lower ( $\sim 1.6 - 1.8$ ) for this indenter profile.

Somewhat lower values of Meyer index have been reported for a few of these materials: for example, workers in Cambridge (86, 89, 90, 161) have found  $n \approx 1.65$  for NC203 hot-pressed SiC and  $n \approx 1.7$  for NC132 hot-pressed  $\text{Si}_3\text{N}_4$ . Chakraborty and Mukerji (171) have reported  $n \approx 1 - 1.5$  for various reaction-bonded and single crystal silicon nitrides. All these studies were made at lower loads than used here (e.g. up to 100 gf (161) and 100 - 500 gf (171)), so these differences are not unexpected.

Porosity effects have been described by Chakraborty and Mukerji (171): for RBSN materials,  $n$  was found to decrease with

Temp (°C)	SILICON CARBIDE						SILICON NITRIDE				SIALON	BORON CARBIDE		SILICON
	(0001) SiC	HPSC (NC203)	Sintered SiC		RBSC*		PDSN	HPSN		Sintered Lucas 342		Sintered		
			Carb- orundum	Suzuki	REFEL (a)	REFEL (b)		NC132	NCX34			ρ=2.4	ρ=2.05	
					{111} Si									
25	1.89	1.88	1.87	1.93	1.81	1.80	1.78	1.97	1.89	1.94	1.96	1.83	1.85	1.92
200	-	1.96	1.92	1.92	-	1.87	1.77	1.98	2.00	2.07	-	-	-	-
400	2.06	1.88	1.96	1.97	1.89	1.89	1.85	2.11	1.94	2.02	1.98	-	-	1.86
600	-	1.86	2.02	1.99	-	1.99	1.89	2.01	1.95	2.09	-	-	-	1.95
800	1.94	1.99	1.88	1.97	1.82	1.91	2.05	2.23	2.04	2.11	-	-	-	1.95

Table 11 Variation of Meyer index (n) with temperature for Vickers indentations in the load range 100gf - 1kgf. Standard errors typically  $\pm 0.03$  \*REFEL (a) had grain size  $\sim 10\mu\text{m}$ , REFEL (b) had grain size  $\sim 5\mu\text{m}$ .

TEMPERATURE (°C)	(0001) SiC	HPSC (NC203)	Sintered (Carborundum)	RBSC REFEL (a)
25	1.75	1.70	1.69	1.69
200	1.68	1.72	1.64	1.65
400	1.71	1.75	1.71	1.63
600	1.71	1.77	1.63	1.65
800	1.53	1.80	1.87	1.79

**Table 12** Variation of Meyer index (n) with temperature for Knoop indentations in SiC materials. Standard errors typically  $\pm 0.03$

increasing porosity. No such effect has been found here- porous materials ( sintered silicon carbides, RBSN and sintered  $B_4C$  ) had Meyer indices similar to those of the fully-dense materials.

Finally, it is emphasized that all hardness measurements were made in vacuo in order to minimize chemomechanical effects as far as possible.

#### 3.7.4 The Effects of Surface Abrasion Damage

Hardening effects due to mechanical abrasion have previously been found in sapphire ( 172 ) and in  $MgO$  ( 173, 174 ). The damage induced by abrasion is near-surface ( e.g. 113 - 115 ), hence an indentation size effect is expected when the plastic zone beneath the indenter is of the order of the scale of the damage. This was investigated for alpha 'REFEL' reaction-bonded  $SiC$ , the abrasion damage being induced by diamond polishing to various surface finishes. The aims of the investigation were three-fold: firstly to establish whether or not surface abrasion affects the hardness, secondly to determine whether such effects were significant for the surface finishes commonly used for hardness testing and thirdly to measure the indentation size effect.

The same specimen was used throughout the experiment, using a Kent polishing machine equipped with automatic polishing arm and utilizing constant wheel speed and applied weight ( 1.75 kg ). The sequence described represents typical polishing procedure for this and similar materials ( section 2.1 ), starting with coarse diamond compound on metal laps and finishing with fine ( in this case  $0.1 \mu m$  ) diamond compound on soft cloth polishing wheels. Additionally, the material was polished for a longer period of time ( 2 hours in total ) at the  $0.1 \mu m$  stage, in case the normally used time of 15 minutes proved insufficient to remove all the damage from the coarser polishing stages. The surface was then roughened to  $6 \mu m$  and then to  $14 \mu m$  ( cloth ) finishes as a consistency check.

At each stage in the polishing procedure, the amount of damage in the specimen surface was assessed by optical microscopy ( attempts to quantify this by measuring the cathodoluminescent output in a SEM failed, since the material showed no output whatever ).

Indentations were made at 100 gf and 1 kgf loads at room temperature and under ambient conditions using a Leitz 'Miniload' microhardness tester with Vickers indenter. Since the measured effect was likely to depend on the sampling depth of the plastic zone, estimates of the plastic zone size  $b$  were made using the equation

$$(b/a) = 0.4 (E/H)^{1/2}$$

( see section 3.3.2.3 ). For 100 gf indentations in 'REFEL',  $b$  was estimated as  $\sim 14 \mu\text{m}$ , whilst for 1 kgf indentations,  $b \approx 52 \mu\text{m}$ .

It was found impossible to resolve indentations on the coarsely-finished surfaces (  $14 \mu\text{m}$  and  $6 \mu\text{m}$  cast iron laps ) due to surface roughness, the material being severely chipped and scratched. After the  $6 \mu\text{m}$  copper lap, the sample showed small unchipped regions and, macroscopically, a slight lustre. When polished on the  $6 \mu\text{m}$  cloth, the specimen appeared shiny, optical examination revealing only tiny (  $\sim 1 \mu\text{m}$  ) chips in the surface, especially around the SiC:Si interfaces present in this material. After the  $1 \mu\text{m}$  and subsequent stages, no damage could be resolved by optical microscopy, until roughened to  $6 \mu\text{m}$  and finally  $14 \mu\text{m}$  cloth finish, where the damage was again marked, although not as severe as with the  $6 \mu\text{m}$  copper lap.

The results ( table 13 ) show that at 1 kgf applied load, the macroscopically shiny surfaces (  $6 \mu\text{m}$  -  $0.1 \mu\text{m}$  cloths ) all had similar hardness values (  $\sim 2050 \text{ kgf mm}^{-2}$  ) to well within experimental errors. Only the highly damaged  $6 \mu\text{m}$  copper-lapped and  $14 \mu\text{m}$  cloth-polished surfaces showed a hardening effect, in proportion to the amount of damage observed.

The 100 gf indentations provided a slightly more sensitive test, revealing hardening effects at the  $6 \mu\text{m}$  and  $14 \mu\text{m}$  cloth stages with respect to the highly-polished  $1 - 0.1 \mu\text{m}$  finishes. In neither case did the hardness change significantly on polishing for a long time at the  $0.1 \mu\text{m}$  stage.

For this material, an indentation size effect (  $n \approx 1.84$  ) was found even where abrasion damage had no effect. The same effect was observed where abrasion damage was severe enough to affect both 100 gf and 1 kgf indentations ( i.e. for the  $14 \mu\text{m}$  cloth finish ). A larger indentation size effect (  $n \approx 1.74$  ) occurred at the intermediate surface finish (  $6 \mu\text{m}$  cloth ), where presumably the damage depth was a significant fraction of the  $14 \mu\text{m}$  plastic zone size for

Polishing Sequence	Polishing Time (min.)	Vickers Hardness (kgfmm <sup>-2</sup> )		Meyer Index n
		(100gf load)	(1kgf load)	
14μm diamond compound on cast iron lap	5	-	-	-
6μm " " " "	10	-	-	-
6μm " " " copper lap	15	-	2690 (±250)	-
6μm " " " Hyprocel Pellon cloth	45	2930 (±190)	2070 (±100)	1.74
1μm " " " micro cloth	15	2440 (±110)	2010 (±100)	1.84
$\frac{1}{4}\mu\text{m}$ " " " "	15	2570 (±150)	2090 (±50)	1.84
$\frac{1}{10}\mu\text{m}$ " " " "	15	2470 (±200)	2060 (±85)	1.85
$\frac{1}{10}\mu\text{m}$ " " " "	120	2560 (±160)	2040 (±50)	1.82
*6μm " " " Hyprocel Pellon cloth	15	2710 (±190)	-	-
*14μm " " " "	15	2970 (±310)	2430 (±190)	1.84

Table 13 The effect of surface finish on the room temperature Vickers hardness of alpha REPEL reaction-bonded silicon carbide. Plastic zone sizes were calculated to be ~ 14μm for 100gf and ~ 52μm for 1 kgf loads. \*Indicates the surface was roughened from 1/10μm finish. Errors are 95% confidence limits (10 indentations).

100 gf indentations, but not of the 52  $\mu\text{m}$  plastic zone size for 1 kgf indentations.

In conclusion, a hardening effect has been observed on the surface of alpha 'REFEL' reaction-bonded SiC when subjected to optically resolvable amounts of abrasion damage. The effect was insignificant for the surface finishes commonly used for microhardness tests ( at loads above 100 gf ) in this investigation ( see section 2.1 ). It has been demonstrated that hard surface layers can cause an indentation size effect over and above that normally obtaining in the material. The mechanism(s) responsible for the hardening effect have not been determined ( although strain-hardening is an obvious possibility ) - detailed TEM observations of the deformation structures involved in both indentation and abrasion processes will be required to do this.

### 3.8 INDENTATION CREEP

Indentation creep is defined as the increase in indentation size ( i.e. decrease in hardness ) with increasing time of loading at constant applied load. In this section, high-temperature creep is discussed. So-called 'anomalous indentation creep' phenomena, which occur at low temperatures and are thought to be caused by chemomechanical effects, are discussed in section 3.9.

#### 3.8.1 Theoretical Analysis

As described in section 3.3.2, deformation in the high-temperature regime (  $T > T_c$  ) is thought to occur by dislocation glide plus climb controlled by vacancy diffusion ( either along dislocation cores or through the lattice at very high temperatures ). This mechanism is essentially a creep process, for which the typical tensile-creep behaviour has been described ( e.g. 175 ) by a relation of the form:

$$\dot{\epsilon}_s = A \sigma^m \exp ( -Q/RT )$$

where  $\dot{\epsilon}_s$  is the steady strain rate, A is a constant,  $\sigma$  is the tensile stress, m is a stress exponent and Q is the activation energy for the process.

A similar form of the relation may be derived for the variation

of hardness  $H$  with time  $t$  and temperature  $T$ :

$$(A'/t) = H^m \exp(-Q/RT)$$

Such a relation has been derived by Mulhearn and Tabor (176) assuming steady-state viscous creep, for which the strain rate was assumed to be proportional to (stress)<sup>m</sup> and the imposed strain proportional to the indentation diagonal length  $d$ . Atkins et al. (177) preferred a transient creep approach where the creep rate is proportional to (stress)<sup>m/3</sup> but the effective strain behaves as if proportional to  $d^3$ . These (and other) approaches give the same form of relation.

For small stresses ( $\sigma \lesssim 10^{-4} E$ ), the stress exponent  $m$  has a value of approximately 5, whilst for the high stresses found in indentation ( $\sigma > 10^{-3} E$ ),  $m$  is approximately 10 (177). Stress exponents found in compressive creep experiments with ceramic materials are usually in the range 2 - 3 (e.g. 178 - 180), which is consistent with the transient creep model, which predicts a hardness exponent three times larger (177).

For constant load time, the variation of hardness with temperature in the high-temperature regime is given by

$$H \propto \exp(Q/mRT)$$

Hence the activation energy derived from a  $\log H$  versus  $(1/T)$  plot (as in tables 3, 4 and 8) is smaller than that relevant to the deformation mechanism(s) by a factor of  $m$ . Alternatively, the variation of hardness with load time at constant temperature is given by

$$H \propto t^{-(1/m)}$$

Thus, a plot of  $\log H$  against  $\log t$  should have constant slope  $-(1/m)$ , although such plots are often found in practice to show a deviation from linearity for indentation times below about 10 seconds (177). Generally, the slope increases slightly with increasing temperature (177), indicating a decrease in  $m$  (which has not been explained).

A complete description of hot-hardness behaviour above  $T_c$  is therefore obtained by a combination of hardness versus temperature at constant load time and hardness versus load time at constant temperature experiments. In particular, the activation energy for deformation must be obtained from both experiments, as described in the following section.

### 3.8.2 Results for {111} silicon

Figure 28 shows the results of indentation creep experiments on n-type {111} single crystal silicon in the temperature range 600 - 800°C at loading times up to 300 seconds ( Vickers indenter, 100 gf load in all cases ). For loading times greater than 15 s, the log H versus log t plots were linear, as described above. However, the results are a little suspect, in that the gradients appeared to decrease significantly with increasing temperature, notably between 700 and 800°C. The reason for this is thought to be that a second specimen ( cut from the same crystal ) was used for the 800°C experiments because of insufficient space on the original section after performing hardness tests at lower temperatures. The second specimen was possibly indented in a slightly different orientation to the first ( both were aligned such that indenter diagonals were parallel to  $\langle 1\bar{1}0 \rangle$  and  $\langle \bar{1}\bar{1}2 \rangle$  directions, within about 10 - 15° ). Such orientation effects on creep plots have been postulated by Atkins et al. ( 177 ). The slopes of the plots in fig. 28 correspond to  $m = 5$  ( 600°C ),  $m = 6$  ( 700°C ) and  $m = 19$  ( 800°C ).

The procedure used for obtaining activation energies was similar to that described by Atkins et al. ( 177 ). By extrapolating back from the linear portions of log H versus log t plots, values of  $H_0$  at a time of  $t_0 = 1$  second ( chosen arbitrarily ) were obtained by linear regression using the method of least squares. These values were 508 kgf mm<sup>-2</sup> at 600°C, 291 kgf mm<sup>-2</sup> at 700°C and 115 kgf mm<sup>-2</sup> at 800°C. The data were then re-plotted as  $\log ( H^{-3} - H_0^{-3} )$  against  $\log ( t^{1/3} - t_0^{1/3} )$  for each temperature, which effectively assumes a constant value of  $m = 9$  ( this seems to be standard procedure, even when it is known that  $m$  must vary over the temperature range ). Best-fit lines of unit slope were obtained ( again by least squares ), the interval between two lines ( for  $T_1$  and  $T_2$  ) being a measure of  $( 1/T_2 - 1/T_1 )Q/3R$ . Thus,  $Q$  was calculated to be 270 kJ mol<sup>-1</sup> between 600 and 700°C, 250 kJ mol<sup>-1</sup> between 700 and 800°C and 260 kJ mol<sup>-1</sup> over the whole range 600 - 800°C. Despite the earlier misgivings, it is reassuring that these values are fairly constant for each pair of lines. As may be seen from table 14, these values are in good agreement with the expected value of activation energy for core diffusion-the proposed dislocation climb mechanism at these temperatures ( 72 ). Lattice diffusion is evidently not dominant in this temperature range.

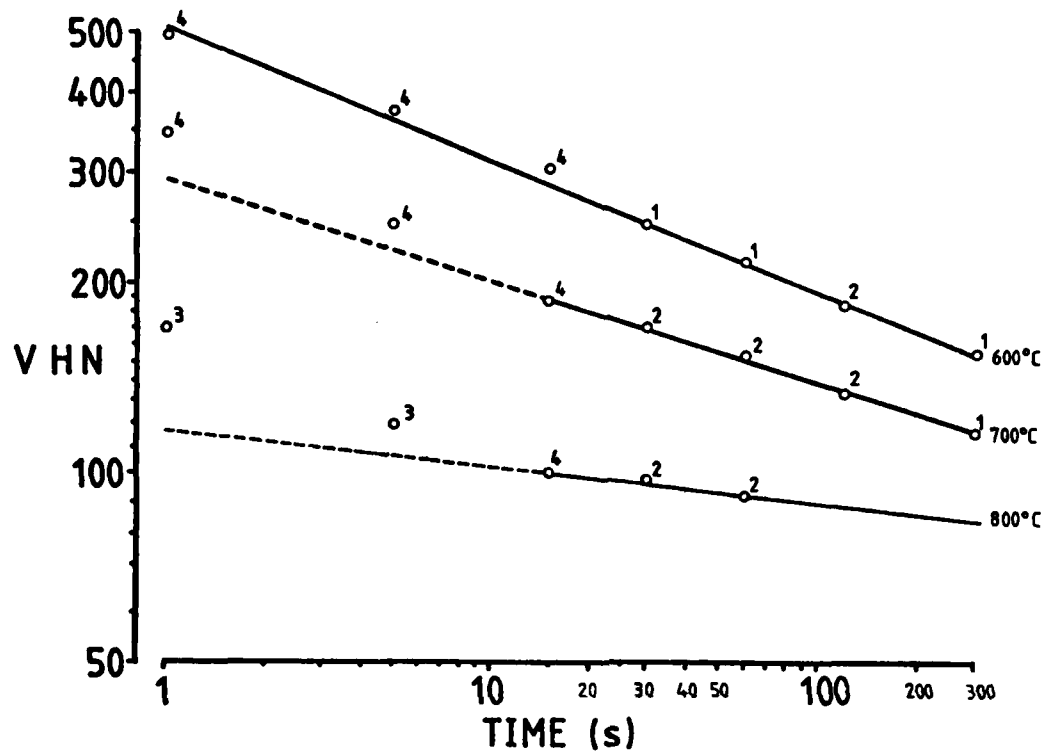


Figure 28. Indentation creep in {111} single crystal silicon at 600°C, 700°C and 800°C, plotted as log H against log t, where H = Vickers hardness at 100gf applied load and t = indenter dwell time. The number of indentations used to determine the hardness is indicated by the side of each data point.

	Activation Energy ( $\text{kJmol}^{-1}$ )		
	Silicon	$\alpha$ -SiC	$\text{Si}_3\text{N}_4$
Lattice-controlled glide	219 (ref. 17)	550 (ref. 17)	980 (ref. 17)
Core diffusion	300 (ref. 72)	-	-
Grain boundary diffusion	300 (ref. 72)	306 (ref. 182)*	-
Lattice diffusion	496 (ref. 72)	700-800 (refs. 183,184)	-
Grain boundary sliding	-	230 (ref. 178) <sup>†</sup>	550-650 (refs. 179,180)*

Table 14 Activation energies taken from the literature for various deformation mechanisms in Si, SiC and  $\text{Si}_3\text{N}_4$  materials.

\* hot-pressed materials

† REFEL reaction-bonded SiC

Although indentation creep experiments were not performed for SiC and Si<sub>3</sub>N<sub>4</sub> materials ( largely because of the problems of maintaining furnace operation for reasonable times at high temperatures ), it may be estimated from tables 3, 4 and 8 that activation energies for SiC materials would be in the range 50 - 100 kJ mol<sup>-1</sup> and for Si<sub>3</sub>N<sub>4</sub> materials in the range 10 - 30 kJ mol<sup>-1</sup> at temperatures between T<sub>C</sub> and 800°C ( assuming m = 9 ). These values are substantially less than the expected values for various deformation modes ( table 14 ). However, the activation energy plots ( e.g. figs. 13e, 15 ) for many of these materials show that the activation energy increases steadily over a temperature interval extending to considerably higher than T<sub>C</sub>. This suggests that athermal deformation mechanisms may still play a significant role, even above T<sub>C</sub>. This is in accord with the ideas of Gerk ( 181 ), who considers that the 'instantaneous' hardness attained immediately after full loading is reached is constant at all temperatures, the instantaneous deformation always occurring by athermal mechanisms as discussed in section 3.3.3. Subsequent deformation ( whilst the indenter is still in contact with the surface ) may then occur at temperatures above T<sub>C</sub><sup>\*</sup> by glide/climb of dislocations ( at substantially lower strain rate ) away from the indentation. Thus, for a fixed load time, creep effects should become progressively more dominant with increasing temperature. This effect would be most marked for small dwell times ( as used here ).

Finally, activation energies obtained from indentation creep experiments performed on various SiC and Si<sub>3</sub>N<sub>4</sub> materials are available in the literature. Atkins and Tabor ( 93 ) measured a relatively low value of 188 kJ mol<sup>-1</sup> at 1280°C ( 0.5 T<sub>m</sub> ) for a sintered SiC ( 2% porosity ), whilst Hirai and Niihara ( 99 ) measured Q = 523 kJ mol<sup>-1</sup> in the range 1400 - 1500°C ( ~0.6 T<sub>m</sub> ) for single crystals of 6H SiC ( their data suggesting m = 18 - 20 ). These differences are probably due to grain boundary effects such as boundary sliding. Atkins and Tabor ( 93 ) also measured Q = 130 - 170 kJ mol<sup>-1</sup> for polycrystalline Si<sub>3</sub>N<sub>4</sub> ( 4% porosity ) at 0.5 T<sub>m</sub> ( ~800°C ).

Clearly, there is a need for further study of high-temperature indentation creep in these materials. In particular, the variations of stress exponent with material and temperature should be considered more carefully.

---

\* Creep rates below T<sub>C</sub> were considered to be negligible ( 93, 177, 181 ).

### 3.9 EFFECTS OF CHEMICAL ENVIRONMENT

Beyond establishing that the Knoop hardness of (0001) blue-black SiC was the same in vacuo ( 2370 ( $\pm 20$ ) kgf mm<sup>-2</sup> at  $2 \times 10^{-6}$  mm Hg ) as measured under ambient conditions ( 2410 ( $\pm 40$ ) kgf mm<sup>-2</sup> ), no study has been made here of the effects of chemical environment on hardness. However, such effects are known to occur in a wide range of ceramic materials ( e.g. 185 ) and so a brief review of the subject is included here.

Two types of chemomechanical ( or 'Rebinder' ) effect on hardness have been observed, with changes in hardness at fixed load time and in the rate of room temperature indentation creep ( often termed anomalous indentation creep ) occurring in the presence of certain polar solvents, especially water ( e.g. 185, 186 ). All the proposed interpretations of these effects have considered the influence of adsorbed species on the behaviour of near-surface dislocations ( e.g. 187, 188 ).

Originally, Rebinder ( 189 ) proposed that adsorbed layers reduced the surface free energy, facilitating the formation of both the indentation and surface slip steps and hence reducing the hardness. However, hardening effects have also been observed for many material/environment combinations, and so dislocation pinning by adsorbed molecules at the point of emergence was postulated ( 190 ).

For ionic crystals, where dislocation mobility at room temperature is often controlled by interactions with point defects such as vacancies or impurity atoms ( section 3.3.2.1 ), Westwood et al. ( 191 ) postulated that chemisorption involves electron/hole transfer between near-surface point and line defects and the adsorbate, leading to a surface charge. This can also lead to bending of energy bands at the surface and so influence the occupation of dislocation energy levels ( see also Hirsch ( 21 ) ). It has been demonstrated ( 192 ) that such effects must influence both dislocation-impurity and either dislocation-dislocation or dislocation-lattice interactions.

A critical observation ( e.g. 187, 188 ) is that hardness correlates well with the  $\zeta$ -potential of non-metallic solids when immersed in electrolyte environments: hardness is maximum at  $\zeta = 0$ . This has been established for a wide range of materials, including

$\text{Al}_2\text{O}_3$ ,  $\text{MgO}$  and possibly  $\text{Si}$  ( 193 ). Detailed mechanisms for this effect are not yet understood, since the relations between  $\zeta$ -potential, surface charge and near-surface electronic structure are unclear. Cuthrell ( 194, 195 ), for example, considers that  $\zeta = 0$  corresponds to the greatest concentration of free hydrogen ions near to the surface and that chemomechanical effects are generally caused by a form of 'hydrogen embrittlement'. However, no mechanism was put forward, and further evidence suggests that hydrogen adsorption is unlikely to provide the basis of a universal explanation of such phenomena ( 188 ).

### 3.10 CONCLUSIONS

In this chapter, plasticity in single crystal and polycrystalline forms of various highly brittle ceramic materials (  $\text{Si}$ ,  $\text{SiC}$ ,  $\text{Si}_3\text{N}_4$ , sialon and  $\text{B}_4\text{C}$  ) has been studied as a function of temperature using hot indentation techniques performed in vacuo. The main results of the investigation were as follows:

(a)  $\{111\}$  single crystal silicon was found to show a transition from largely stress-activated behaviour at low temperatures to largely thermally activated behaviour at high temperatures, the transition temperature  $T_c$  being  $\sim 0.36 T_m$  (  $350^\circ\text{C}$  ), confirming earlier studies.

(b) Single crystals of  $\alpha$ - $\text{SiC}$  were found to show a similar transition at  $T_c \approx 0.15 - 0.25 T_m$  (  $200 - 550^\circ\text{C}$  ), depending on indenter: crystal orientation and probably on specimen impurity.

(c) Hot-hardness data obtained from the literature for single crystal  $\alpha$ - $\text{Si}_3\text{N}_4$  were re-examined and a ( more gradual ) transition in behaviour was found to occur over the range  $T_c \approx 0.3 - 0.45 T_m$  (  $400 - 700^\circ\text{C}$  ), being largely independent of orientation.

(d) Surface slip steps on single crystals of  $\text{Si}$  ( slip plane  $\{111\}$  ) and  $\text{SiC}$  ( slip plane  $(0001)$  ) were observed to form at critical temperatures which were higher than  $T_c$ , and it is suggested that this occurs at a critical  $(E/H)$  value of approximately 30, where the plastic zone size equals the indentation radius. This value is not reached for  $\text{Si}_3\text{N}_4$  until very high temperatures (  $>1500^\circ\text{C}$  ).

(e) The Gilman theory for low-temperature plastic flow has been applied to hot-hardness data for single crystal  $\text{SiC}$ . The theory fits the shape of the hardness/temperature plots nicely, but

an explanation of the variation in  $T_c$  must await detailed knowledge of the variation of phonon energy with orientation and specimen purity.

(f) The anisotropy in Knoop hardness of single crystals of  $\alpha$ -SiC has been measured over a wide range of orientations as a function of temperature in order to obtain information about active slip systems. The anisotropy may be explained in terms of a combination of basal (  $(0001)\langle 11\bar{2}0 \rangle$  ) and prismatic (  $\{10\bar{1}0\}\langle 11\bar{2}0 \rangle$  ) slip, the CRSS for basal slip decreasing with increasing temperature much more rapidly than for prismatic slip. The ratio  $(CRSS)_{\text{basal}} : (CRSS)_{\text{prismatic}}$  was established to be 0.7 - 1.1 at room temperature and 0.3 - 0.6 at 800°C.

(g) A preliminary investigation of impurity effects in Si and SiC materials has been made. It seems that p-type SiC is harder than n-type material, with differences in  $T_c$  and in the activation energy for high-temperature deformation.

(h) Microstructure was found to have a pronounced effect on the hot-hardness behaviour of polycrystalline materials, especially for  $\text{Si}_3\text{N}_4$ . For dense materials, the hot-hardness curves ( on a logarithmic scale ) were generally transposed from each other along the  $\log H$  axis, with little variation in  $T_c$  or activation energy. Grain boundaries are thought to produce a softening effect in these materials, with the amount/composition of boundary phases also having an effect. These observations are thought to be consistent with deformation occurring by a combination of primary slip and grain boundary separation, facilitated by low grain boundary cohesion. Large amounts of porosity are thought to facilitate compaction in preference to plasticity, decreasing the temperature-sensitivity of hardness. A quantitative model for this has been developed which fits the data well with no adjustable parameters.

(i) For polycrystalline forms of SiC,  $T_c$  was found to be  $\sim 0.18 T_m$  ( 300°C ), whilst for fully-dense polycrystalline  $\text{Si}_3\text{N}_4$ ,  $T_c$  was  $\sim 0.28 T_m$  ( 330°C ). These values are at the lower ends of the observed ranges in  $T_c$  values for single crystals. Sintered sialon also showed a weak transition in hot-hardness behaviour at  $T_c \approx 240^\circ\text{C}$ . Sintered  $\text{B}_4\text{C}$  showed no transition below the maximum temperature used (  $0.4 T_m$  ).

(j) The variation of hardness with load ( or indentation size effect ) was found to be relatively small for all materials in

the load range 100 - 1000 gf. For  $\text{Si}_3\text{N}_4$  materials, the effect reversed from higher hardness at low loads to higher hardness at high loads as the temperature was raised.

(k) Abrasion damage was found to produce a hardening effect in 'REFEL' reaction-bonded SiC, being more pronounced for small indentations, which sampled more of the surface-affected layer.

(l) Indentation creep of {111} single crystal silicon was studied in the range 600 - 800°C ( i.e. above  $T_c$  ). The activation energy for deformation was estimated to be  $\sim 260 \text{ kJ mol}^{-1}$ , which is likely to correspond to dislocation climb by pipe diffusion of vacancies along dislocation cores. Although similar experiments were not performed for SiC and  $\text{Si}_3\text{N}_4$  materials, it is likely that activation energies would have been somewhat lower ( by up to an order of magnitude ) than expected, suggesting that athermal or weakly thermally activated processes may still operate at temperatures in excess of  $T_c$ .

### 3.11. REFERENCES

1. R.C. Bradt and R.E. Tressler (Eds.), 1974, "Deformation of Ceramic Materials", Proc. Symposium held at Penn. State University, July 17-19, 1974, Plenum Press.
2. R.M. Latanision and J.T. Fourie (Eds.), 1977, "Surface Effects in Crystal Plasticity", Nato Advanced Study Inst. Series E (Nordhoff, Leyden).
3. A. Kelly, 1966, "Strong Solids", Clarendon Press, Oxford.
4. P.C. Dokko and J.A. Pask, 1976, Mater. Sci. Eng. 25, 77.
5. J.W. Edington, D.J. Rowcliffe and H.L. Henshall, 1975. Powder Met. Int. 7, 82.
6. A.G. Evans and J.V. Sharp, 1971, J. Mater. Sci. 6, 1292.
7. G.R. Sawyer, P.M. Sargent and T.F. Page, 1980, J. Mater. Sci. 15, 1001.
8. R. Von Mises, 1928, Z. Angew. Math. Mech. 8, 161.
9. G.W. Groves and A. Kelly, 1963, Phil. Mag. 8, 877.
10. H. Alexander and P. Haasen, 1968, Solid State Physics 22, 27.
11. H.L. Fotedar and T.G. Stoebe, 1975, Phys. Stat. Sol. (a) 31, 399.
12. M. Srinivasan and T.G. Stoebe, 1974, J. Mater. Sci. 9, 121.
13. A.G. Evans and T.G. Langdon, 1976, Progress in Materials Science 21, 214.
14. P.B. Hirsch, 1980, J. Microscopy 118, 3.
15. A.G. Cullis and D.C. Joy (Eds.), 1981, Inst. Phys. Conf. Ser. No. 60: Section 1, Proceedings of Microscopy of Semiconducting Materials Conference, Oxford, 6-10 April, 1981.
16. J.J. Gilman, 1968, J. Appl. Phys. 39, 6086.
17. Idem, 1975, Ibid 46, 5110.
18. H.L. Frisch and J.R. Patel, 1967, Phys. Rev. Lett. 18, 784.
19. P. Haasen, 1979, J. de Physique, Colloque C6, Supplem. 6, 40, C6-111.
20. P.B. Hirsch, 1979, ibid. C6-117.
21. P.B. Hirsch, 1981, ibid., Colloque C3, Supplem. 6, 42, C3-149.

22. Idem, 1981, in "Defects in Semiconductors", Ed. J. Narayan and T.Y. Tan, North-Holland, p.257.
23. R. Jones, 1980, Phil. Mag. B42, 213.
24. C.H. Woo and M.P. Puls, 1977, Phil. Mag. 35, 1641.
25. H.L. Fotedar and T.G. Stoebe, 1971, Phil. Mag. 23, 859.
26. M. Srinivasan and T.G. Stoebe, 1970, J. Appl. Phys. 41, 3726.
27. H.G. Brion, H. Siethoff and W. Schröter, 1981, Phil. Mag. A43, 1505.
28. C. Zener, 1948, Trans. A.S.M. 40, 3.
29. A.N. Stroh, 1957, Adv. Phys. 6, 418.
30. A.H. Cottrell, 1958, Trans. Met. Soc. AIME 212, 192.
31. R.W. Davidge and A.G. Evans, 1970, Mater. Sci. Eng. 6, 281.
32. A.R.C. Westwood, 1961, Phil. Mag. 6, 195.
33. R.C. Ku and T.L. Johnston, 1964, Phil. Mag. 9, 231.
34. J. Moriyoshi, W.D. Kingery and J.B. Van der Sande, 1977, J. Mater. Sci. 12, 1062.
35. J.T. Hagan, M.Y. Swain and J.E. Field, 1979, in "The Science of Ceramic Machining and Surface Finishing II", Eds. B.J. Hockey and R.W. Rice, National Bureau of Standards Special Publication 562 (U.S. Government Printing Office, Washington, D.C.), p.15.
36. J.T. Hagan, 1979, J. Mater. Sci. 14, 2975.
37. B.R. Lawn and T.R. Wilshaw, 1975, "Fracture of Brittle Solids", Cambridge University Press.
38. B.R. Lawn, B.J. Hockey and S.M. Wiederhorn, 1970, J. Mater. Sci. 15, 1207.
39. D.A. Koss and K.S. Chan, 1980, Acta. Metall. 28, 1245.
40. J.C. Jaeger and N.G.W. Cook, 1979, "Fundamentals of Rock Mechanics," Chapman and Hall, London.
41. A.H. Heuer, 1970, Proc. Brit. Ceram. Soc. 15, 173.
42. Y.G. Eremenko and V.I. Nikitenko, 1972, Phys. Stat. Sol. (a) 14, 317.
43. H. Föll and D. Aat, 1979, Phil. Mag. A40, 589.

44. C.B. Carter, H. Föll, D.G. Ast and S.L. Sass, 1981, Phil. Mag. A43, 441.
45. C.B. Carter, J. Rose and D.G. Ast, 1981, Inst. Phys. Conf. Ser. No. 60: section 3, paper presented at Microsc. Semicond. Mater. Conf., Oxford, 6-10 April 1981, p.153.
46. J.-J. Bacmann, G. Silvestre, M. Petit and W. Bollmann, 1981, Phil. Mag. A43, 189.
47. W. Bollmann, G. Silvestre and J.J. Bacmann, 1981, Phil. Mag. A43, 201.
48. P. Chaudhari and J.W. Matthews, 1971, J. Appl. Phys. 42, 3063.
49. W.D. Kingery, 1974, J. Am. Ceram. Soc. 57, 1.
50. C.B. Carter, D.L. Kohlstedt and S.L. Sass, 1980, J. Am. Ceram. Soc. 63, 623.
51. R.W. Balluffi, P.D. Bristowe and C.P. Sun, 1981, J. Am. Ceram. Soc. 64, 23.
52. N.W. Jepps, W.M. Stobbs and T.F. Page, 1981, Inst. Phys. Conf. Ser. No. 61: Chapter 10, paper presented at EMAG, Cambridge, 7-10 September, 1981, p.453.
53. H. Suzuki and T. Hase, 1980, J. Am. Ceram. Soc. 63, 349.
54. Z. Inoue, Y. Uemura and Y. Inomata, 1981, J. Mater. Sci. 16, 2297.
55. D.R. Clarke and G. Thomas, 1977, J. Am. Ceram. Soc. 60, 491.
56. Idem, 1978, *ibid.* 61, 114.
57. O. Kriyanek, T.M. Shaw and G. Thomas, 1979, *ibid.* 62, 585.
58. A.H. Heuer, V. Lou, L. Ogbuji and T.E. Mitchell, 1977, J. Microsc. Spectrosc. Electron 2, 475.
59. L.K.Y. Lou, T.E. Mitchell and A.H. Heuer, 1978, J. Am. Ceram. Soc. 61, 392.
60. P. Drew and M.H. Lewis, 1974, J. Mater. Sci. 9, 261.
61. B.S.B. Karunaratne and M.H. Lewis, 1980, *ibid.* 15, 1781.
62. P.E.D. Morgan, F.F. Lange, D.R. Clarke and B.I. Davis, 1981, J. Am. Ceram. Soc. 64, C-77.
63. P.L. Farnsworth and R.L. Coble, 1965, J. Mater. Sci. 9, 270.
64. F.R.N. Nabarro, 1948, "Report of a Conference on Strength of Solids", The Physical Society, London, p.75.

65. C. Herring, 1950, J. Appl. Phys. 21, 437.
66. A.G. Evans and A. Rana, 1980, Acta. Metall. 28, 129.
67. A.G. Evans and S.M. Wiederhorn, 1974, J. Mater. Sci. 9, 270.
68. R.L. Tsai and R. Raj, 1980, J. Am. Ceram. Soc. 63, 513.
69. R.B. Day and R.J. Stokes, 1966, *ibid.* 49, 345.
70. M.N. Sinha, D.J. Lloyd and K. Tangri, 1973, J. Mater. Sci. 8, 116.
71. T.G. Langdon and F.A. Mohamed, 1976, J. Mater. Sci. 11, 317.
72. H.J. Frost and M.F. Ashby, 1981, "Deformation Maps for Ceramics", Cambridge University Engineering Department Internal Report No. CUED/C/MATS/TR.79, May 1981.
73. D. Tabor, 1951, "The Hardness of Metals", Clarendon Press, Oxford.
74. D. Tabor, 1970, Reviews of Physics in Technology 1, 145.
75. D.M. Marsh, 1964, Proc. Roy. Soc. A279, 420.
76. R. Hill, 1950, "The Mathematical Theory of Plasticity", Clarendon Press, Oxford.
77. K.L. Johnson, 1970, J. Mech. Phys. Solids 18, 115.
78. W. Hirst and M.G.J.W. Howse, 1969, Proc. Roy. Soc. Lond. A311, 429.
79. C.J. Studman, M.A. Moore and S.E. Jones, 1977, J. Phys. D. 10, 949.
80. A.P. Gerk, 1976, J. Phys. D. 9, L179.
81. C.M. Perrott, 1977, Wear 45, 293.
82. J. Boussinesq, 1885, discussed in S.P. Timoshenko and J.N. Goodier, 1970, "Theory of Elasticity", McGraw-Hill, New York, p.398.
83. E.H. Yoffe, 1982, to be published in Phil. Mag. A.
84. J.J. Gilman, 1973, in "The Science of Hardness Testing and its Research Applications", American Society for Metals, Metals Park, Ohio, USA, p.51.
85. A.P. Gerk, 1977, J. Mater. Sci. 12, 735.
86. P.M. Sargent, 1979, Ph.D. thesis, University of Cambridge.
87. J.J. Gilman, 1959, Acta. Met. 7, 608.
88. C.A. Brookes, 1970, Nature 228, 660.

89. O.O. Adewoye, 1976, Ph.D. thesis, University of Cambridge.
90. G.R. Sawyer, 1979, Ph.D. thesis, University of Cambridge.
91. I.V. Gridneva, Yu.V. Milman and V.I. Trefilov, 1972, Phys. Stat. Sol. (a) 14, 177.
92. J.H. Westbrook, reported in ref. 17.
93. A.G. Atkins and D. Tabor, 1966, Proc. Roy. Soc. Lond. A292, 441.
94. B.J. Hockey, 1973, as ref. 84, p.21.
95. H. Kotake and S. Takasu, 1981, J. Mater. Sci. 16, 767.
96. S.M. Hu, 1975, J. Appl. Phys. 46, 1470.
97. A.T. Churchman, G.A. Geach and J. Winton, 1956, Proc. Roy. Soc. Lond. A238, 194.
98. V.I. Trefilov, V.A. Borisenko, G.G. Gnesin, I.V. Gridneva, Yu.V. Milman and S.I. Chugunova, 1978, Sov. Phys. Dokl. 23, 207.
99. T. Hirai and K. Niihara, 1979, J. Mater. Sci. 14, 2253.
100. K. Niihara and T. Hirai, 1979, *ibid.* 14, 1952.
101. R. Wagatsuma, K. Sumino, W. Uchida and S. Yamamoto, 1971, J. Appl. Phys. 42, 222.
102. J. Lankford and D.L. Davidson, 1979, J. Mater. Sci. 14, 1669.
103. M.M. Chaudhri, J.T. Hagan and J.K. Wells, 1980, J. Mater. Sci. 15, 1189.
104. M.A. Velednitskaya, V.N. Rozhanskii, L.F. Comolova, G.F. Saparin, J. Schreiber and O. Brümmer, 1975, Phys. Stat. Sol. (a) 32, 123.
105. K. Sumino and J. Hasegawa, 1968, Trans. Japan. Inst. Metals. Suppl. 9, 749.
106. A.S. Keh, 1960, J. Appl. Phys. 31, 1538.
107. S.M. Hu, 1977, Appl. Phys. Letters 31, 139.
108. O.O. Adewoye and T.F. Page, 1976, J. Mater. Sci. 11, 981.
109. T.F. Page, G.R. Sawyer, O.O. Adewoye and J.J. Wert, 1978, Proc. Brit. Ceram. Soc. 26, 193.
110. M.J. Hill and D.J. Rowcliffe, 1974, J. Mater. Sci. 9, 1569.
111. B.J. Hockey, 1971, J. Am. Ceram. Soc. 54, 223.

112. B.J. Hockey and B.R. Lawn, 1975, J. Mater. Sci. 10, 1275.
113. R. Stickler and G.R. Booker, 1962, Phil. Mag. 8, 859.
114. M. Kitada, 1980, J. Mater. Sci. 15, 1684.
115. J. Lankford and D.L. Davidson, 1979, as ref. 35, 395.
116. B.J. Hockey, S.M. Wiederhorn and H. Johnson, 1978, in "Fracture Mechanics of Ceramics", Vol. 3, Eds. R.C. Bradt, D.P.H. Hasselman and F.F. Lange, Plenum Press, p.379.
117. B.J. Hockey and S.M. Wiederhorn, 1979, Proceedings of the Fifth International Conference on Erosion by Liquid and Solid Impact (ELSI V), 3-6th September, 1979, Newnham College, Cambridge, Publ. Cavendish Laboratory, Cambridge, paper 26.
118. L. Garbato and A. Rucci, 1977, Phil. Mag. 35, 1681.
119. R.C. Marshall, J.W. Faust, Jr. and C.E. Ryan (Eds.), 1973, Silicon Carbide-1973, Proc. 3rd. Int. Conf. on SiC, Florida, University of South Carolina Press.
120. F.M. Ernsberger, 1968, J. Am. Ceram. Soc. 51, 545.
121. K.W. Peter, 1970, J. Non-Crystalline Solids 5, 103.
122. A. Arora, D.B. Marshall and B.R. Lawn, 1979, *ibid.* 31, 415.
123. M. Imaoka and I. Yasui, 1976, *ibid.* 22, 315.
124. A.J. Miller, G.A. Saunders and Y.K. Yogortcu, 1981, Phil. Mag. A 43, 1447.
125. Y.K. Yogortcu, A.J. Miller and G.A. Saunders, 1981, J. Phys. Chem. Solids 42, 49.
126. V.N. Rozhanskii, M.P. Nazarova, I.L. Svetlov and L.K. Kalashnikova, 1970, Phys. Stat. Sol. (a) 41, 579.
127. J.A. Van Vechten, 1973, Phys. Rev. B 7, 1479.
128. S. Minomura and H.G. Drickamer, 1962, J. Phys. Chem. Solids 23, 451.
129. R.A. Graham, O.E. Jones and J.R. Holland, 1965, J. Appl. Phys. 36, 3955.
130. G. Rosenberg, 1980, J. Phys. Chem. Solids 41, 561.
131. T.Y. Tan, H. Föll and S.M. Hu, 1981, Phil. Mag. A. 44, 127.
132. J. Lankford, 1978, as ref. 116, p.245.
133. N.W. Jepps and T.F. Page, 1979, J. Microscopy 116, 159.

134. S. Van der Zwaag, J.T. Hagan and J.E. Field, 1980, J. Mater. Sci. 15, 2965.
135. N.W. Thibault and H.L. Nyquist, 1947, Trans. Am. Soc. Metals 38, 271.
136. P.T.B. Shaffer, 1964, J. Am. Ceram. Soc. 47, 466.
137. Idem., 1964, *ibid.* 48, 601.
138. C.A. Brookes, J.B. O'Neill and B.A.W. Redfern, 1971, Proc. Roy. Soc. Lond. A322, 73.
139. R.D. Arnell, 1974, J. Phys. D. 7, 1225.
140. F.W. Daniels and C.G. Dunn, 1949, Trans. Am. Soc. Metals 41, 419.
141. Y. Kumashiro, A. Itoh, T. Kinoshita and M. Sobajima, 1977, J. Mater. Sci. 12, 595.
142. R.H.J. Hannink, D.L. Kohlstedt and M.J. Murray, 1972, Proc. Roy. Soc. Lond. A326, 409.
143. D.J. Rowcliffe and G.E. Hollox, 1971, J. Mater. Sci. 6, 1261.
144. Idem., 1971, *ibid.* 6, 1270.
145. G. Morgan and M.H. Lewis, 1974, *ibid.* 9, 349.
146. R.W. Davidge, 1967, *ibid.* 2, 339.
147. B.J. Busoyne Jr., D.M. Kotchick and R.E. Tressler, 1979, Phil. Mag. A 39, 265.
148. F. Sato and K. Sumino, 1980, J. Mater. Sci. 15, 1625.
149. J.R. Patel and A.R. Chaudhuri, 1966, Phys. Rev. 143, 601.
150. J.R. Patel and L.R. Testardi, 1977, Appl. Phys. Lett. 30, 3.
151. A. George and G. Champier, 1979, Phys. Stat. Sol. (a) 53, 529.
152. S.G. Roberts, 1982, private communication.
153. N.K. Gibbs and T.F. Page, 1982, unpublished research.
154. B. North and K.E. Gilchrist, 1981, Am. Ceram. Soc. Bull. 60, 549.
155. R.W. Rice, 1977, Treatise on Materials Science and Technology 11, ed. R.K. MacCrone, Academic Press, p.199.
156. R.W. Davidge, 1974, in "Fracture Mechanics of Ceramics" Vol. 2, eds. R.C. Bradt, D.P.H. Hasselman and F.F. Lange, Plenum Press, p.447.
157. K.C. Pitman and D.J. Godfrey, 1978, Proc. Brit. Ceram. Soc. 26, 225.

158. M.G.S. Naylor, 1978, M. Phil. thesis, University of Cambridge, Department of Metallurgy and Materials Science.
159. R.W. Armstrong, E.L. Raymond and R.R. Vandervoort, 1963, J. Am. Ceram. Soc. 53, 529.
160. S.D. Skrovanek and R.C. Bradt, 1979, J. Am. Ceram. Soc. 62, 215.
161. P.M. Sargent and T.F. Page, 1978, Proc. Brit. Ceram. Soc. 26, 209.
162. I.C. Huseby and G. Petzow, 1974, Powder Met. Int. 6, 17.
163. T.N. Loladze, G.V. Bokuchava and G.E. Davidova, 1973, as ref. 84, p.251.
164. C.A. Brookes and A.G. Atkins, 1965, Proc. 5th. Plansée Seminar, "Metals for the Space Age", ed. F. Benesovsky, June 22-26, 1964, Reutte, Springer-Verlag, p.712.
165. R.D. Koester and D.P. Moak, 1967, J. Am. Ceram. Soc. 50, 290.
166. G.P. Upit and S.A. Varchenya, 1973, as ref. 84, p.135.
167. R.P. Burnand, 1974, Ph.D. thesis, University of Exeter.
168. A.J. Crocker and M. Wilson, 1978, J. Mater. Sci. 13, 833.
169. L.P. Tarazov and N.W. Thibault, 1947, Trans. ASM 38, 331.
170. B.W. Mott, 1956, "Microindentation Hardness Testing", Butterworths.
171. D. Chakraborty and J. Mukerji, 1980, J. Mater. Sci. 15, 3051.
172. P.F. Becher, 1974, J. Am. Ceram. Soc. 57, 107.
173. C.A. Brookes and M.P. Shaw, 1976, Nature 263, 760.
174. C.A. Brookes, 1977, in ref. 2, p.671.
175. A.M. Brown and M.F. Ashby, 1980, Scripta Metall. 14, 1297.
176. T.O. Mulhearn and D. Tabor, 1960-61, J. Inst. Metals 89, 7.
177. A.G. Atkins, A. Silvério and D. Tabor, 1966, *ibid.* 94, 369.
178. P. Marshall and R.B. Jones, 1969, Powder Met. 12, 193.
179. R. Kossowsky, D.G. Miller and E.S. Diaz, 1975, J. Mater. Sci. 10, 983.
180. P.J. Dixon-Stubbs and B. Wilshire, 1979, *ibid.* 14, 2773.
181. A.P. Gerk, 1975, Phil. Mag. 32, 355.
182. P.L. Farnsworth and R.L. Coble, 1965, J. Am. Ceram. Soc. 49, 264.

183. J.D. Hong and R.F. Davis, 1980, *ibid.* 63, 546.
184. J.D. Hong, R.F. Davis and D.E. Newbury, 1981, *J. Mater. Sci.* 16, 2485.
185. A.R.C. Westwood and N.H. Macmillan, 1973, as ref. 84, p.377.
186. J.H. Westbrook and P.J. Jorgensen, 1965, *Trans. AIME* 233, 425.
187. N.H. Macmillan, 1977, in ref. 2, p.629.
188. A.R.C. Westwood, J.S. Ahearn and J.J. Mills, 1981, *Colloids and Surfaces* 2, 1.
189. P.A. Rebinder, 1928, *Proc. Sixth Phys. Conf.*, State Press, Moscow, p.29.
190. A.R.C. Westwood, 1962, *Phil. Mag.* 7, 633.
191. A.R.C. Westwood, D.L. Goldheim and R.G. Lye, 1967, *Phil. Mag.* 16, 505.
192. J.S. Ahearn, 1978, reported in A.R.C. Westwood, "Mechanisms of Environment-Sensitive Cracking of Materials", *Metals Soc. Lond.* 1978, p.283.
193. G.B. Yost and W.S. Williams, 1978, *J. Am. Ceram. Soc.* 61, 139.
194. R.E. Cuthrell, 1979, *J. Mater. Sci.* 14, 612.
195. *Idem*, 1979, *ibid.* 14, 2563.
196. S.S. Chiang, D.B. Marshall and A.G. Evans, 1982, *J. Appl. Phys.* 53, 298.
197. R.A. Dugdale, 1954, *J. Mech. Phys. Solids* 2, 265.

## CHAPTER 4

### CRACK PROPAGATION

Whilst plastic flow is often the dominant response of a material to indentation, tensile stresses generated beneath an indenter may also cause arrested fracture in brittle solids. Indentation fracture occurs only above a critical value of applied load ( $P^*$ ), which is low (e.g. 0.1 N) for very brittle solids and high (e.g. 800kN) for ductile materials. This reflects the relative ease of crack nucleation, discussed in Chapter 5. As the load is increased above  $P^*$ , so indentation fracture becomes increasingly more severe, i.e. cracks propagate further from the indentation. This effect, together with its temperature sensitivity, is discussed and quantified in this chapter. In particular, application of the principles of fracture mechanics (section 4.3) enables valuable materials information about the resistance of a material to crack propagation (i.e. toughness) to be obtained as a function of temperature, etc. This leads ultimately to the concept of 'brittleness': the resistance of a material to plastic deformation relative to its resistance to brittle fracture (discussed in Chapter 6). In addition, the introduction of well-defined crack patterns into a test surface allows the study of preferred fracture paths within the specimen microstructure (section 4.5), which may lead to the design of microstructure for optimum toughness.

Firstly, a brief description of brittle fracture in general is presented, which serves to define many of the terms used in subsequent sections and indicates why we might expect factors such as temperature, specimen microstructure, etc. to influence strength and toughness.

#### 4.1 BRITTLE FRACTURE

The theoretical tensile strength ( $\sigma_{th}$ ) of a perfect material has been estimated (1,2) to be  $\sim(E/10)$ , where  $E$  = Young's modulus. Ductile materials have much lower shear strengths\* because deformation by plastic flow, involving movement of dislocations at shear stresses much lower than  $\tau_{th}$  is possible. For ceramic materials, where dislocation activity in conventional tensile tests is usually negligible,

---

\* For uniaxial tension or compression, the maximum shear stress  $\tau$  is simply related to the tensile/compressive stress  $\sigma$  according to  $\sigma = 2\tau$ .

carefully-prepared fibres or whiskers may have strengths approaching  $\sigma_{th}$  (1), yet bulk materials are generally weaker by approximately two orders of magnitude (e.g. 2,3]. Broadly, two approaches may be taken to account for this latter behaviour (e.g. 4,5). The basis of both schemes is that brittle materials contain flaws which act as initiation sites for crack development under the applied stress.

i) Stress Concentration

This approach is based on the Inglis (6) analysis of the stress field at the tip of an elliptical crack of length  $c$  and tip radius  $\rho$ , subjected to uniform tensile stress  $\sigma$ . Stress concentrations at the crack tip cannot be relieved by plastic flow in a ceramic, so the material fails when the stress at the tip reaches  $\sigma_{th}$ .

$$\sigma_{tip} = 2\sigma(c/\rho)^{1/2} \quad (\text{Inglis (6)})$$

$$\text{and} \quad \sigma_{th} \approx (E\gamma_o/a)^{1/2} \quad (\text{Kelly (2)}),$$

where  $\gamma_o$  = thermodynamic surface energy of the material

$a$  = cleavage plane spacing

Hence the fracture stress for constant  $\rho$  is given by

$$\sigma_f \propto (E\gamma_o/c)^{1/2}$$

ii) The Griffith Energy Balance

In this approach, the propagation of a well-developed crack is considered to occur spontaneously when the decrease in mechanical energy caused by a crack extension  $\delta c$  just exceeds the increase in surface energy  $V$ . The mechanical energy is the difference between the elastic stored energy  $U$  and external work  $W$  performed by the applied load due to the displacements caused by crack extension. Thus, the Griffith energy balance (1) may be written as:

$$\frac{\partial}{\partial c} \{ (U-W) + V \} = 0$$

always assuming  $\frac{\partial^2}{\partial c^2} \{ (U-W) + V \}$  is negative: where this does not apply, crack growth is arrested. Due to the localized nature of tensile stresses beneath an indenter (section 4.2.3), indentation fracture falls into this category (section 4.3.1).

Considering the example of an elliptical crack of length  $2c$

in a thin, infinite sheet under tensile stress:

$$U = \frac{\pi c^2 \sigma^2}{E} \quad (\text{plane stress})$$

$$W = 2U \quad (\text{for constant load})$$

and  $V = 4c\gamma_0$

Then the Griffith criterion predicts crack extension at

$$\sigma_f = \left[ \frac{2E\gamma_0}{\pi c} \right]^{\frac{1}{2}}$$

as predicted by the Inglis approach assuming constant  $\rho$  (3a) (see ref.5).

Now, defining a mode I (e.g. ref.4) crack opening stress intensity

factor  $K_I = \sigma(\pi c)^{\frac{1}{2}}$ , crack propagation will occur at

$$K_{IC} = \sigma_f(\pi c)^{\frac{1}{2}} \quad \text{hence} \quad K_{IC} = (2E\gamma_0)^{\frac{1}{2}}$$

where  $K_{IC}$  is the critical stress intensity factor: a measure of the resistance to crack propagation, i.e. toughness, of the material.

For most ceramic materials,  $K_{IC} \approx 0.5 - 10 \text{ MPam}^{\frac{1}{2}}$ , whilst for metals,  $K_{IC} \approx 50 - 200 \text{ MPam}^{\frac{1}{2}}$ .

For many materials, the fracture surface energy measured by experiment turns out to be much higher than  $\gamma_0$ . This occurs when energy is dissipated at the crack tip by mechanisms such as crack tip plasticity (e.g. 5), crack branching (e.g. 4), stress-induced microcracking (e.g. 7-9), phase transformations (e.g. 9), etc. In this case, we may simply re-formulate the above expressions in terms of a new parameter  $G$ , the strain energy release rate, or force per unit length normal to the crack front:

$$K_{IC} = (EG_{IC})^{\frac{1}{2}} = \sigma_f(\pi c)^{\frac{1}{2}}$$

For highly brittle covalent solids at low temperatures, where fracture is thought (10) to occur by sequential bond rupture at the crack tip with little or no energy dissipation,  $G_{IC} \approx 2\gamma_0$ . For semi-brittle materials, which show some crack tip plasticity (2),  $G_{IC} > 2\gamma_0$  and for metals,  $G_{IC} \gg 2\gamma_0$ . Thus, on heating a brittle material,  $G_{IC}$  tends to increase due to increasing crack tip plasticity. Other deformation mechanisms may also operate at high temperatures, notably grain boundary sliding, which may cause either a further increase in  $G_{IC}$  (due to crack blunting) or alternatively a decrease in

$G_{Ic}$  (due to lower grain boundary fracture energy). We may note here that microstructural effects may have a strong influence on  $G_{Ic}$  (e.g. 3, 11). For example,  $\gamma_0$  may be lowered where fracture is intergranular rather than transgranular (i.e. for small grain sizes and weak boundaries (3)), or where porosity decreases the actual area of fracture (3). Such effects are discussed in section 4.5.

From the above analysis, it is apparent that the tensile strength of a ceramic is influenced not only by the inherent toughness of the material, but also by the critical flaw size  $c$ , which is generally the largest suitably-oriented flaw within the stressed volume. Critical flaws are often surface defects induced by handling/machining damage (12), particle impact (4), etc. Even in the absence of these, microstructural flaws may exist, e.g. pores or grain-sized cracks originating from anisotropic thermal contraction effects on cooling the specimen after fabrication (13). Generally, commercial materials will have a wide distribution of flaw sizes, which may result in variations in strength from specimen to specimen, hence strengths (e.g. moduli of rupture) of ceramic materials are usually determined statistically (e.g. 14-16). Fracture may not always initiate from pre-existing flaws, however: as will be described in Chapter 5, cracks may be (and often are) nucleated by plastic flow processes occurring in response to the applied stress (this is especially so for indentation).

#### 4.2. INDENTATION FRACTURE

##### 4.2.1 Crack Geometries

Indentation fracture geometries have been characterized and modelled principally by Lawn, Evans and co-workers (e.g. 17-27). In the case of surface contact by sharp indenters (e.g. Vickers, Knoop, etc.) at loads greater than  $P^*$ , penny-shaped median cracks, perpendicular to the specimen surface, are created beneath the plastic zone during loading of the indenter (illustrated in fig. 29a) (e.g. 17-19). In some (not all) materials, surface radial cracks, also perpendicular to the surface but separate from the median cracks, may also form during loading (e.g. 20, 28). On unloading the indenter, radial cracks extend outward and downward and median cracks extend upward and outward, such that the crack systems merge to form a composite semicircular median/radial system (fig. 29b) (e.g. 23).

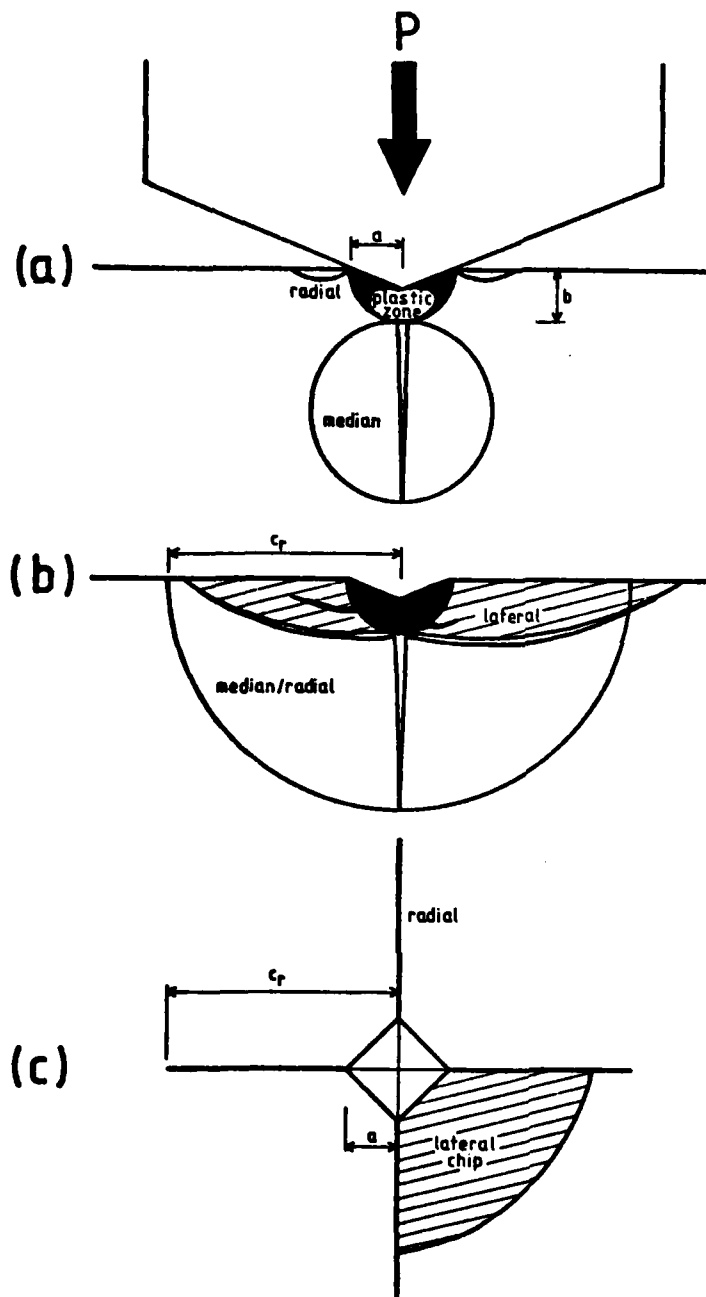


**Figure 29.** Schematic diagrams of crack geometries formed by Vickers indentations. (a) On loading the indenter above a critical load  $P^*$ , penny-shaped median cracks, orthogonal to the specimen surface, are nucleated at the plastic zone boundary and propagate downwards. Surface radial cracks may also form in some materials. (b) On removing the load, median cracks extend upwards and radial cracks outwards, the two crack types merging to form a composite median/radial system. In addition, lateral cracks, approximately parallel to the surface, may nucleate at the plastic zone boundary and propagate away from the indentation, forming chips of removed material where they intersect radial cracks and the specimen surface. (c) Plan view of a Vickers indentation after removal of the load, showing four radial cracks and one lateral chip.

This final configuration seems to be attained whether radial cracks form on loading or not (20). The depth of median cracks does not change during unloading (25). For a Vickers indenter, two orthogonal median/radial systems, usually extending out from the indentation corners, are often formed in homogeneous, isotropic materials (17). Also formed during unloading of the indenter are lateral cracks which lie approximately parallel to the specimen surface and originate from the plastic zone boundary (fig.29b) (e.g. 17). Where lateral cracks intersect the specimen surface, chips of material may be removed (fig.29c and see also stereo pair images in fig. 6).

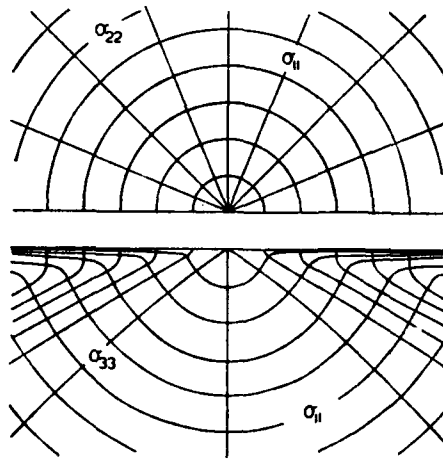
The precise sequence of microfracture events depends on the material, its surface preparation and the applied load (e.g. 20). Lankford (28) has studied indentation fracture in Si, Ge, SiC, Al<sub>2</sub>O<sub>3</sub> and NaCl materials by means of in situ observation, acoustic emission and post facto examination of indentations subsequently fractured along the median/radial cracks. Lankford concluded that, for many materials, radial cracks are generally the first to form and that median cracks often do not form at all at loads close to P\*. Evans and Wilshaw (20) observed that as the ratio (E/H) increases, surface radial fracture becomes more dominant with respect to subsurface median cracking in the earlier stages of loading. The materials examined in this investigation were all highly brittle, with low (E/H) values, at room temperature.

Finally, an entirely different pattern of fracture occurs beneath blunt indenters, involving the formation of Hertzian ring and cone cracks (e.g. 18). Although these crack geometries have also been observed beneath Vickers indentations in certain 'anomalous' glasses (29, 30), they were not observed in the materials examined in this investigation and will not be discussed in detail.

#### 4.2.2 Elastic Stress Fields

Early attempts to model indentation fracture (e.g. 17, 18) considered only the elastic stress field beneath an indenter. For blunt indenters, the Hertzian stress field is used (e.g. 18), whilst for sharp contact the Boussinesq field, illustrated in fig. 30, applies. Firstly, a spherical polar co-ordinate system is defined (fig. 31 insert). Tensile/compressive stresses along radial directions from the point of contact are termed  $\sigma_r$ , whilst stresses tangential to the

(a)



(b)

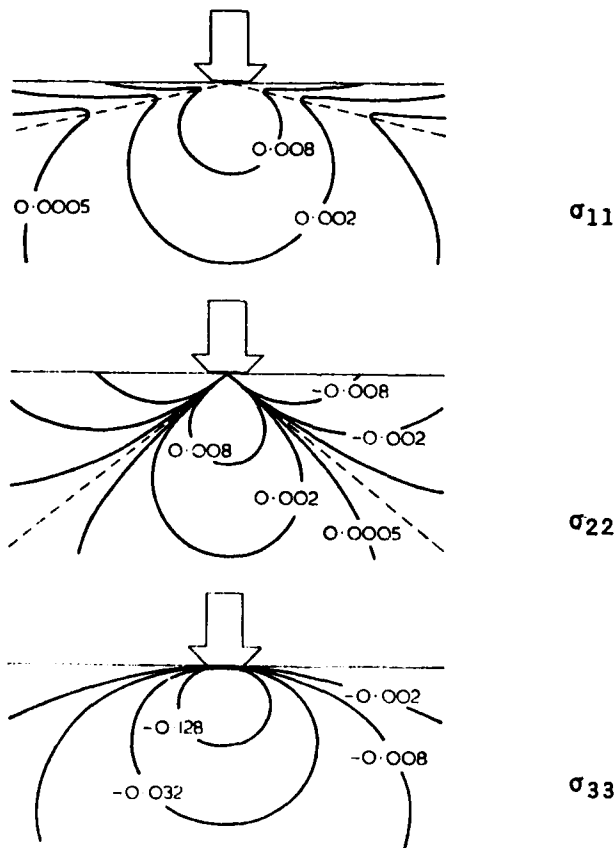


**Figure 30.** The Boussinesq elastic stress field: (a) stress trajectories and (b) contours of principal normal stresses ( after Lawn and Wilshaw ( 18 ) ). A value of  $\nu = 0.25$  is assumed. Stresses are measured in units of  $H$ .

angles  $\theta$  and  $\phi$  are termed  $\sigma_\theta$  and  $\sigma_\phi$  respectively ( $\sigma_\phi$  are hoop stresses). Shear stresses  $\sigma_{r\theta}$ ,  $\sigma_{r\phi}$ , etc. may also be defined in the usual way (e.g. 17). For the Boussinesq field:

$$\begin{aligned}\sigma_r &= \frac{P}{4\pi r^2} (1 - 7 \cos \theta) \\ \sigma_\theta &= \frac{P}{4\pi r^2} \left[ \frac{\cos^2 \theta}{1 + \cos \theta} \right] \\ \sigma_\phi &= \frac{P}{4\pi r^2} \left[ \cos \theta - \frac{1}{1 + \cos \theta} \right]\end{aligned}$$

for  $\nu = 0.25$  and where  $P$  = applied load.

The stresses are proportional to  $(1/r^2)$  and are therefore very high near  $r = 0$ , such that some sort of yielding occurs over a region  $r \leq b$ , spreading the load to a uniform pressure over the indentation radius  $a$ . Effects due to the plastic zone are discussed in section 4.2.3.

Figure 30 illustrates the Boussinesq stress field in terms of the principal stresses  $\sigma_{11}$ ,  $\sigma_{22}$  and  $\sigma_{33}$  ( $\sigma_{11} \geq \sigma_{22} \geq \sigma_{33}$ ), whose trajectories vary, as shown in fig. 30a. Thus,  $\sigma_{11} = \sigma_\theta$  at  $\theta = 0^\circ$  and  $\sigma_{11} = \sigma_r$  at  $\theta = 90^\circ$ . Similarly,  $\sigma_{33} = \sigma_r$  at  $\theta = 0^\circ$  and  $\sigma_{33} = \sigma_\theta$  at  $\theta = 90^\circ$ .  $\sigma_\phi \equiv \sigma_{22}$ . Contours of equal stress for each principal stress are shown in fig. 30b, tensile stresses being positive, compressive stresses negative. Thus,  $\sigma_{11}$  is everywhere tensile, whilst  $\sigma_{33}$  is everywhere compressive.  $\sigma_{22}$  is tensile in the range  $|\theta| \leq 51.8^\circ$  but compressive for larger  $\theta$ .

Cracks in isotropic materials are thought to follow paths of maximum tensile stress (e.g. 17,18), median cracks propagating downwards under the action of the  $\sigma_{11}$  stress and outwards under the action of  $\sigma_{22}$  (hence they must be confined within  $\theta = \pm 51.8^\circ$ ). Fracture is arrested because of the  $(1/r^2)$  decrease in stress.

For comparison, cone cracks are observed to follow the direction of maximum  $\sigma_{11}$  in the Hertzian stress field (e.g. 18).

The elastic stress field does not account for radial and lateral cracks, which form as a result of residual stresses introduced by the permanent deformation occurring within the plastic zone (33).

#### 4.2.3. Residual Stress

Whilst elastic stresses have been well characterized,

elastic/plastic stresses are less well understood (e.g. 20, 23, 24). Stress fields derived from the expanding spherical cavity models discussed in section 3.2. are inaccurate because the far-field stresses vary as  $(1/r^3)$  and therefore do not reduce to the elastic values (decreasing as  $(1/r^2)$ ), as required by St. Venant's principle (e.g. 24). This problem has been partially overcome by combining the two solutions, the results being supported by finite element calculations (24).

Near-surface hoop stresses calculated in this way are shown as a function of  $(r/a)$  in fig. 31, after Evans (24). The main features of the stress distribution are:

- peak tensile stress  $(\sim \sigma_y/3)$ , where  $\sigma_y$  is the uniaxial yield stress) at the elastic/plastic boundary, where radial cracks are thought to nucleate;
- large compressive stresses within the plastic zone, close to the indenter;
- compressive far-field stresses (causing crack arrest).

The  $\sigma_\theta$  stresses along the load axis ( $\theta = 0^\circ$ ) are, by comparison, always tensile because the elastic  $\sigma_{11}$  stresses are always tensile. Peak tension is again expected at the elastic/plastic boundary, where median cracks are observed to nucleate (e.g. 17).

The stresses described above (termed 'indentation stresses') are those obtaining whilst the indenter is loaded onto the surface, and may be thought of as a combination of elastic and residual stresses. On removal of the load, the elastic stresses relax, leaving only residual stresses (23-25). This is especially important where the elastic stresses are compressive and the residual stresses tensile, as for the near-surface hoop stresses (fig. 31). In this case, tensile stresses are enhanced on removal of the load and cracks formed on loading may then extend, or new ones nucleate. This occurs for both radial cracks (propagating due to  $\sigma_\phi$  enhancement as above) and lateral cracks (propagating due to enhancement of  $\sigma_r$  at  $\theta = 0^\circ$  and  $\sigma_\theta$  near  $\theta = 90^\circ$ , due to compressive  $\sigma_{33}$  elastic stresses). Median cracks do not grow on unloading because  $\sigma_\theta$  becomes less tensile near  $\theta = 0^\circ$  (the load axis) on relaxation of the tensile  $\sigma_{11}$  stresses.

Perrott (31) has calculated that residual tensile hoop stresses may be of the order of the yield stress ( $\sigma_y$ ) in the near-surface region, but only  $\sim (\sigma_y/13)$  at the elastic/plastic boundary on

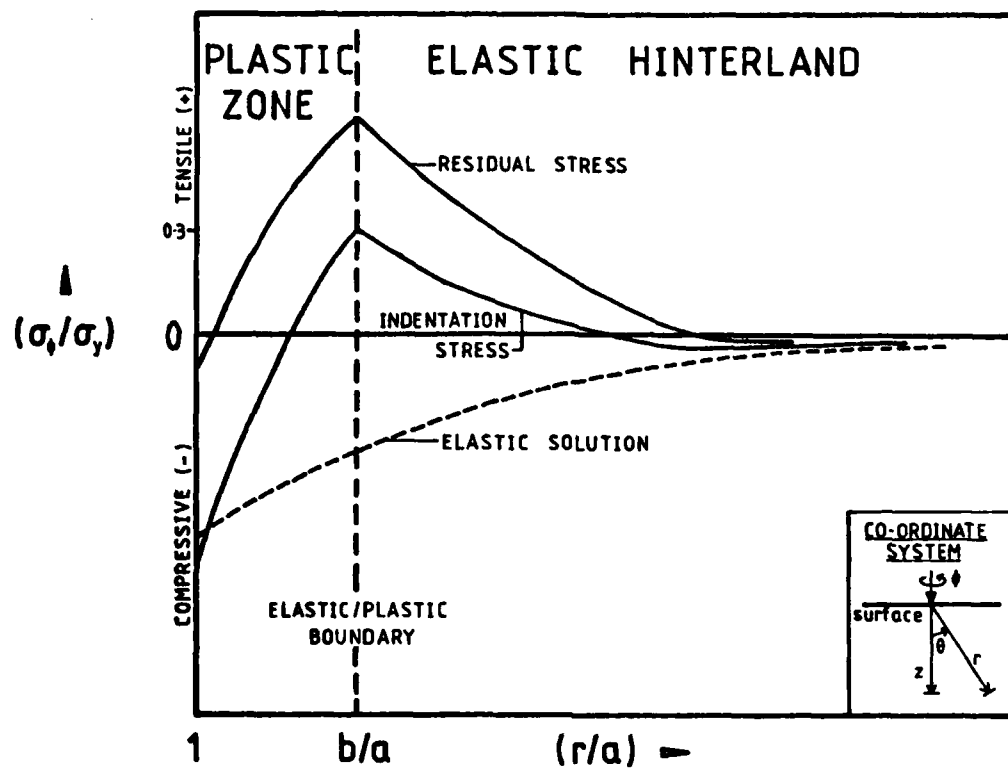


Figure 31. Surface hoop stress distributions ( elastic, plastic and residual ) proposed by Evans ( 24 ) for indentation of brittle materials.

the load axis. Thus, Lankford and Davidson (32) considered that radial cracking was much more likely than median crack formation because of both greater tensile stress and greater likelihood of encountering pre-existing flaws near to the surface. In the Perrott model (31), radial cracks formed during indenter loading were predicted to nucleate at the indentation boundary (where tensile stresses are maximum) whilst those forming on unloading were predicted to nucleate at the elastic/plastic boundary (for the same reason). Further, radial cracks were predicted to be contained within  $\sim 19^\circ$  of the surface on removal of the indenter. Perrott's model applies to brittle materials such as WC/Co which show substantial surface and subsurface plasticity (with  $(b/a) \gtrsim 1.65$  at the surface). The occurrence of 'Palmqvist radial' cracks in such materials has been well-documented (e.g. 33-35). Lankford and Davidson (32) proposed that even highly brittle solids such as single crystal SiC might behave in the same way, an electron channelling study of near-surface plasticity around indentations in SiC indicating  $(b/a) \sim 4$  at the surface. However, such observations are not confirmed by TEM or dislocation etch-pitting experiments (see section 3.3.2) and, as will be seen in following sections, the quantitative indentation fracture behaviour of SiC conforms largely to the Lawn/Evans model rather than to that of Perrott.

#### 4.3. INDENTATION FRACTURE MECHANICS

##### 4.3.1. The Dependence of Crack Size on Contact Load

When cracks are formed around an indentation in the surface of a brittle material, the extent of cracking  $c$  is found to increase with applied load  $P$ . For many crack patterns, an empirical relation

$$P = \lambda c^{3/2}$$

obtains (e.g. 19,36), where  $\lambda$  is constant. This relation has been observed for cone cracks in silicate glasses (36) and for median and radial cracks in many ceramic materials (e.g. 19, 21-28).

As pointed out by Roesler (36) in 1956, the above relation may be deduced from the Griffith criterion for growth of a single crack in the elastic field of a concentrated load. Whilst Roesler considered the specific case of cone cracks formed in silicate glasses by punch indenters, his arguments apply generally to stable crack

growth in an elastic material. The only necessary assumptions are (a) the Griffith energy balance and (b) the Boussinesq field of displacements proportional to  $(P/r)$  and stresses or strains (stress  $\propto$  strain for an elastic field) proportional to  $(P/r^2)$  (requiring fully-developed cracks such that  $c \gg b$ ).

Then, at equilibrium, a very small increase  $\delta c$  in the extent of a crack is associated with changes in the elastic strain energy ( $U$ ) and the potential energy of the load ( $W$ ), which must just balance the fracture surface energy of the crack extension ( $V$ ). These three quantities may be expressed in terms of  $P$  and  $c$ , as follows (following Lawn and Fuller (19) and Yoffe (37)).

#### Elastic Strain Energy

The strain energy is proportional to the volume integral of the product of stress and strain in the surrounding elastic material, hence:

$$U \propto \int_c^{\infty} (P/r^2)^2 r^2 dr = (P^2/c)$$

#### External Work

The opening of the crack near  $r = c$  relaxes stresses of order  $(P/c^2)$  and involves displacements of order  $(P/c)$ . The load therefore moves down, losing potential energy.

$$W \propto (P^2/c)$$

#### Fracture Surface Energy

The total surface energy is proportional to the area of crack opened  $V \propto c^2$

Applying the Griffith energy balance gives  $(P^2/c^2) \propto c$ .

Hence  $P \propto c^{3/2}$  is derived making no assumptions about crack geometry and associated stress intensity factors. The same reasoning applies to growth of several cracks (e.g. two medians) or any other pattern of cracks whose main area of growth is in the region  $r = c$ .

Whilst the above argument applies to a median crack system developing under a purely elastic Boussinesq stress field, it may not be applied directly to radial or lateral crack extension, which occurs due to residual stresses (section 4.2.3). However, Lawn et al. (e.g. 23) have observed that, for high applied loads, the median/radial system attains a near semicircular configuration on complete removal of the

load, where the extent of surface radial cracks is roughly equal to the depth of the associated medians. Thus, the relation  $P \propto c^{3/2}$  still be expected to hold where radial cracks develop from a median system (which might not always be the case (e.g. 28, 32)).

Strictly, the above analysis applies only to the extension of a particular crack configuration (e.g. two medians, one cone, etc.) with increasing load. In some materials, it is observed that the number of cracks increases rapidly with load, not merely the extent of the larger ones. Dense microcracking may occur close to the indentation, with only a few cracks extending out to radius  $c$ . This behaviour is typical of polycrystalline ceramic materials containing weak interfaces, along which preferred fracture takes place. Examples include Si : SiC phase boundaries in reaction-bonded 'REFEL' SiC (fig. 42) and grain boundaries in various sintered (24) and hot-pressed (38) materials. In such cases, the relation  $P \propto c^{3/2}$  is not expected, since the total crack area  $A$  is no longer related simply to the extent of cracking  $c$ . Thus, crack areas rather than crack extents should be estimated for these materials, which poses an interesting problem in stereological analysis. A simple analysis (as yet untested) is suggested below.

In order to estimate the total crack area around an indentation, we can effectively rotate the surface crack distribution through  $180^\circ$  about any axis in the plane of the specimen surface. This operation transforms a surface crack element  $dl$  at radius  $r$  from the indentation centre and angle  $\theta$  from the rotation axis into a surface of area  $\pi r |\sin\theta| dl$ . We can estimate the crack length contained within an element of surface area defined by  $(r, \theta) \rightarrow (r + dr, \theta + d\theta)$  as  $dl = \frac{Lr dr d\theta}{(\pi c^2 - 2a^2)}$  where  $L$  = total crack length on the specimen surface and  $c$  = maximum extent of cracking. The total fracture surface area  $A$  is then given by:

$$\begin{aligned}
 A &= \int_0^{2\pi} \int_a^c \frac{\pi L r^2 |\sin\theta| dr d\theta}{(\pi c^2 - 2a^2)} \\
 &= \frac{4}{3} \left[ \frac{\pi L (c^3 - a^3)}{(\pi c^2 - 2a^2)} \right]
 \end{aligned}$$

Thus,  $A$  may be estimated from measurements of the total line length and maximum extent of cracks on the surface. The analysis

assumes that the crack traces observed at the surface are typical of those which would be observed on a random section through the cracked volume, and that the surface crack distribution is independent of  $\theta$  (probably valid) and  $r$  (probably invalid).

#### 4.3.2. Fracture Toughness

The most successful quantitative fracture mechanics model for the dependence of radial/median crack extent on contact load and on materials parameters ( $K_{Ic}$ ,  $E$ ,  $H$ , etc.) is that developed by Lawn, Evans and co-workers (e.g. 17-27). Initially, Lawn and Fuller (19) modelled the median crack as a centre-loaded penny crack (assuming an essentially elastic stress field), for which the stress intensity factor could be obtained from standard fracture mechanics text books, leading to the relation

$$K_{Ic} = \frac{P_{cm}}{\beta_0} c^{-3/2} \quad (\text{hence } P \propto c^{3/2})$$

where the constant of proportionality  $\beta_0$  was subsequently found by experiment (e.g. 22) to be  $\sim 7$ .

Evans and Wilshaw (20) combined dimensional analysis with an empirical curve fitting scheme to obtain a calibration curve in which  $\log(K_{Ic} H^{-1} a^{-1/2})$  was plotted against  $\log(c/a)$  for a variety of ceramic materials and indentation loads. The curve was found to be linear for  $(c/a) \gtrsim 3$ . A rather better correlation was found by Evans and Charles (21) by introducing the dimensionless ratio  $(H/E)^{2/5}$ , such that  $\log(K_{Ic} H^{-1} a^{-1/2} (H/E)^{2/5})$  was found to be a linear function (with slope  $-3/2$ ) of  $\log(c/a)$  for  $(c/a) \gtrsim 2.5$ . Thus, fracture toughness could be estimated from crack length data by comparison with this 'universal indentation fracture curve'.

The importance of residual stresses, originating in mismatch between the plastic zone and the surrounding elastic matrix, was later recognized (e.g. 23), especially in the propagation of surface radial cracks (which are most conveniently measured for experimental  $K_{Ic}$  determination). Thus, Evans (24) proposed that the  $(E/H)^{2/5}$  term found empirically might be related to the size of the plastic zone, which should determine the magnitude of residual stresses. This was justified theoretically by Lawn, Evans and Marshall (25), who made a full analysis of the elastic and residual components of stress

intensity factors for median and radial cracks, based on an indentation stress field derived from the expanding spherical cavity model (section 3.2), and allowing for stress variation over the crack front (not considered previously). Thus:

$$\begin{aligned} K_r &= \chi_r P c^{-3/2} & \chi_r &= \xi_r(\theta) (E/H)^{1-m} (\cot\psi)^{2/3} \\ K_e &= \chi_e P c^{-3/2} & \chi_e &= \xi_e(\theta) \ln(2c/b) \quad \text{for } c \gg b \end{aligned}$$

where  $K_r$ ,  $K_e$  are residual and elastic stress intensity factors for radial or median cracks,  $\xi_r(\theta)$ ,  $\xi_e(\theta)$  are dimensionless geometrical terms independent of the indenter/specimen system but dependent on the type of crack (i.e. median:  $\theta = 0^\circ$  or radial:  $\theta = 90^\circ$ ),  $\psi$  = indenter half-angle and  $m \approx \frac{1}{2}$  (ref. 15).

For peak load:  $K_{Ic} = (\chi_e + \chi_r) P c_m^{-3/2}$   
 For complete unloading:  $K_{Ic} = \chi_r P c_r^{-3/2}$

where  $c_m$  = median crack radius and  $c_r$  = radial crack radius.

Calibrating this latter relation for soda-lime glass and silicon, Lawn et al. (25) obtained an expression for  $K_{Ic}$ :

$$K_{Ic} = 0.0139 (E/H)^{1/2} P c_r^{-3/2}$$

Anstis et al. (26) later obtained a more accurate calibration by means of indentation fracture measurements on a wide range of materials, the constant of proportionality being determined as 0.016 ( $\pm 0.004$ ). A recent comment by Marshall and Evans (27) suggests that the original Evans and Charles (21) relation

$$K_{Ic} = 0.027 (E/H)^{2/5} P c_r^{-3/2} \quad \text{for } (c/a) \gtrsim 2.5$$

is probably the most accurate for  $K_{Ic}$  determination, especially for SiC and B<sub>4</sub>C materials, for which the precise value of the (E/H) exponent  $m$  becomes important. This latter relation has therefore been used for all  $K_{Ic}$  calculations in this investigation.

Before considering other indentation fracture models, it is instructive to examine some of the assumptions behind the above analyses. Firstly, the stresses under which fracture takes place are assumed to be those predicted by expanding spherical cavity models, which may not be applicable to all materials (section 3.2). In particular, the stresses will be modified where pile-up of material

occurs around indentations (section 3.2) and where deformation occurs by densification or compaction rather than by plastic flow (e.g. 25), as in some anomalous glasses (e.g. 30) or in porous materials (section 3.6.7) or perhaps in sphalerite materials in the low-temperature hardness regime (section 3.3.3). In addition, the (possibly considerable) changes in stress which must occur as a result of crack nucleation and propagation have not been considered. The effects of elastic recovery and indentation size effect (section 3.7) on the measured hardness are similarly not included in any of the above models. Test materials are also assumed to be isotropic and homogeneous, such that cracks nucleate and propagate along planes of maximum tensile stress, rather than along preferred fracture paths within the material (note that crack initiation probably occurs at points of maximum shear stress rather than tensile stress- see Chapter 5).

The possible effects of variations in Poisson's ratio ( $\nu$ ) and in indenter:specimen friction have been discussed, but not quantified, by Evans and co-workers (e.g. 24, 27). In particular, indentation fracture theories often assume  $\nu = 0.25$  as found for many materials (e.g. Si,  $\text{Si}_3\text{N}_4$  and  $\text{B}_4\text{C}$ - table 2), however  $\nu$  is generally substantially lower (0.15 - 0.2) for SiC materials. Marshall and Evans (27) suggest that Poisson's ratio effects are small, but that modelling of frictional effects must await numerical (finite element) indentation analyses.

Finally, the above theory is only valid for conditions in which  $c < b$ , i.e. where radial cracks are driven into the elastic hinterland by the residual stress. This may not be the case for low applied loads or relatively soft materials (e.g. WC/Co), in which Palmqvist radial cracks (with no median component) are formed around indentations (e.g. 28, 31, 32). Plastic zone effects are thought to dominate crack behaviour for  $(c/a) \lesssim 2.5$  for most materials (21, 24, 39). In this case the relation  $P \propto c$  is often found empirically (24, 33-35, 39) and the indentation stress field due to Perrott (31) may be more applicable. An empirical relation has recently been obtained by Niihara et al. (39) from experimental data obtained by Dawihl and Altmeyer (34) for WC/Co materials:

$$K_{\text{IC}} = 0.013 (E/H)^{2/5} H^{1/2} P^{1/2} \ell^{-1/2} \quad \text{for } 0.25 \lesssim \ell \lesssim 2.5$$

where  $\ell$  = radial crack extent from the edge of the indentation to the crack tip i.e.  $\ell = (c-a)$ . Thus,  $K_{Ic}$  may also be determined from indentation fracture measurements at relatively low indenter loads.

The Niihara et al. relation shows  $P \propto \ell$  for WC/Co. Lankford (28), on the other hand, has found that the relation  $P \propto c^{3/2}$  applies to Palmqvist radial cracks in brittle materials (including Si, Ge, SiC,  $Al_2O_3$  and NaCl) near to the threshold fracture load  $P^*$ , the radial cracks of length  $\ell$  behaving as composite cracks of length  $(\ell+a) = c$ . As will be seen in the following section, this behaviour was confirmed for most of the materials examined in this investigation, for which  $(c/a)$  was often less than 2.5 (table 15) and  $(c/b) \lesssim 1$  (table 16) in some cases.

#### 4.4. TEMPERATURE EFFECTS

##### 4.4.1 The Variation of Crack Sizes with Temperature

Figures 32-36 show the variation of radial crack radius ( $c_r$ , defined in fig.29) with temperature for silicon, silicon carbide, silicon nitride, sialon and boron carbide materials respectively. All materials showed some increase in  $c_r$  with increasing temperature. The form of the variation was linear for most of the nitrides, for REFEL reaction-bonded SiC, for (0001) single crystal and Carborundum sintered silicon carbides at high indenter loads and for {111} silicon above  $\sim 300^\circ\text{C}$ . For sintered boron carbides and the majority of SiC materials (except as above), the plot of  $c_r$  against temperature was a curve of decreasing slope with increasing temperature. The variation was particularly interesting for {111} Si (fig. 32), which showed no change in  $c_r$  up to  $\sim 300^\circ\text{C}$ , followed by a steep linear increase up to  $700^\circ\text{C}$ . Above  $700^\circ\text{C}$ , no radial cracking was observed (fig. 37), even for 1kgf indentations, presumably due to the increase in  $P^*$  with increasing temperature (section 5.3).

The variation of lateral crack extent  $c_l$  (for 1kgf applied load) with temperature was also measured for {111} Si (fig. 32 - dashed curve). Despite the relatively large statistical spread in results,  $c_l$  was observed to peak at  $\sim 200^\circ\text{C}$ , with  $c_l \approx c_r$ , and then to die away with increasing temperature, such that surface lateral cracks were rarely observed above  $300^\circ\text{C}$ . This was probably because the depth at which cracks formed increased as the plastic zone size increased (only those lateral cracks which broke through to the surface

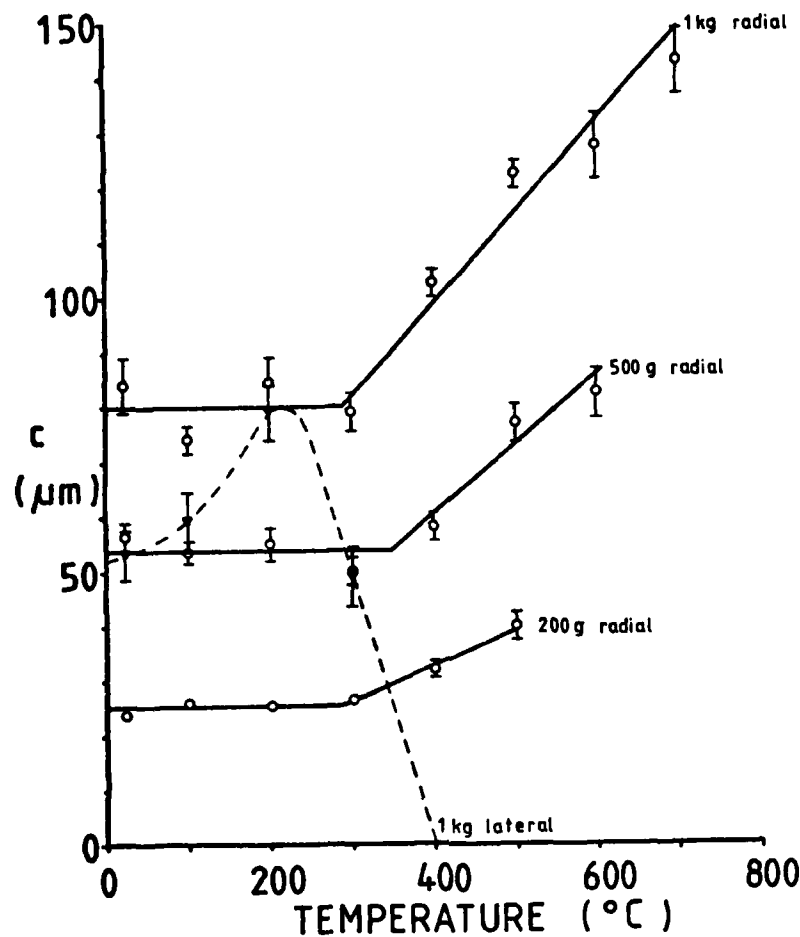


**Figure 32.** Radial and lateral crack radii as functions of temperature and load for {111} single crystal silicon. Solid curves - radial cracks, dashed curve - lateral cracks. Error bars indicate one standard error in the mean.

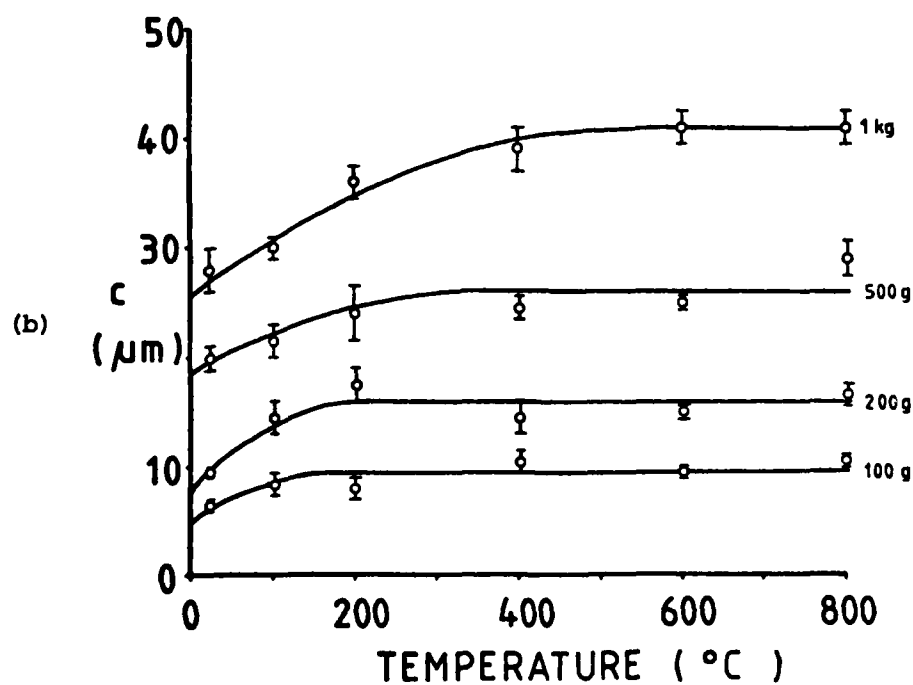
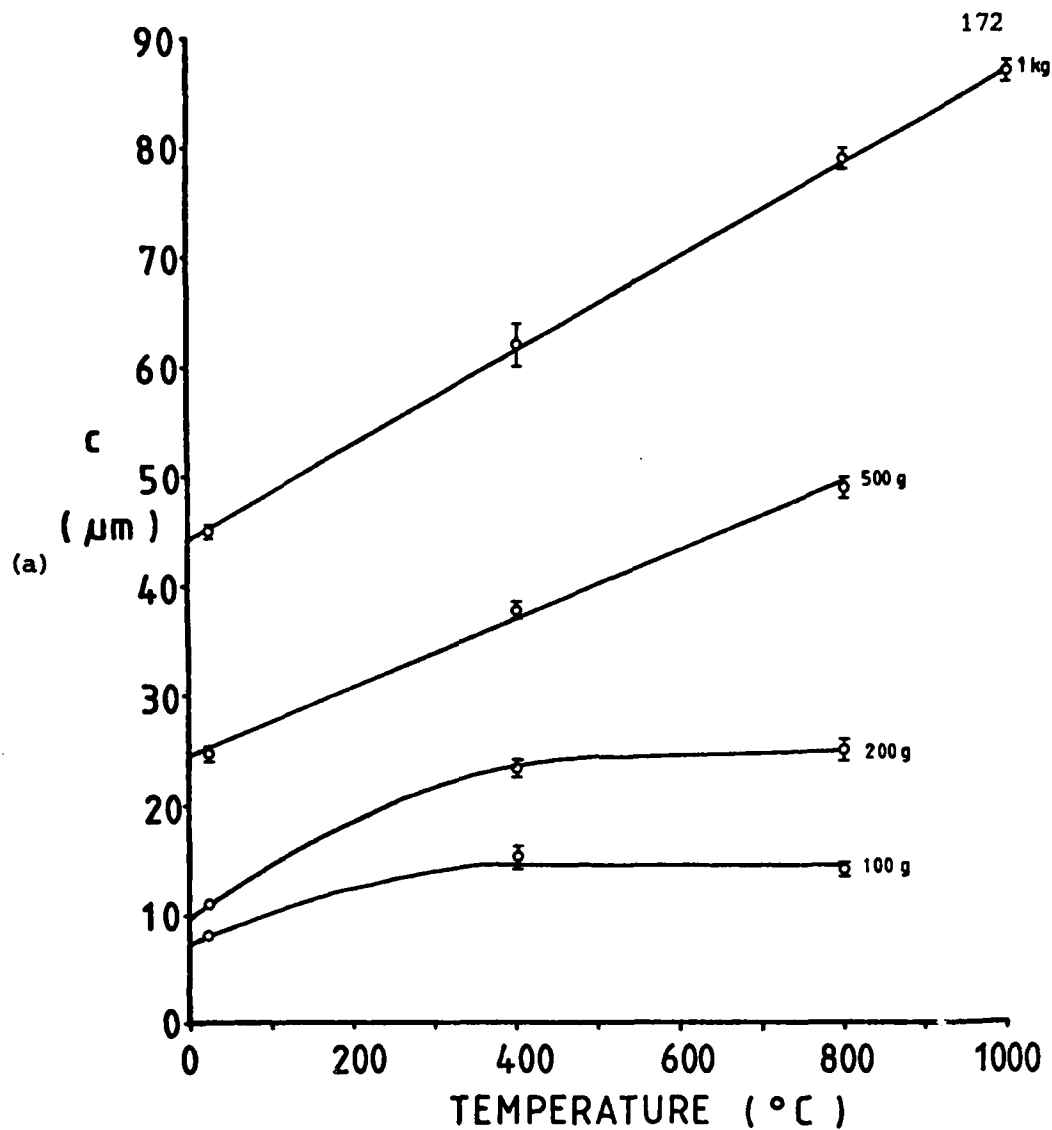
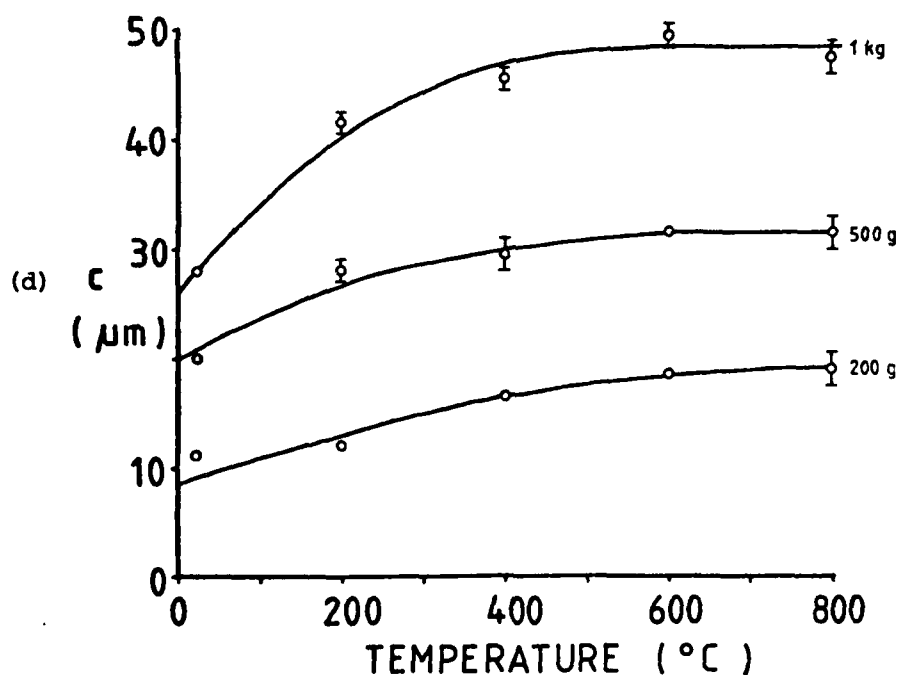
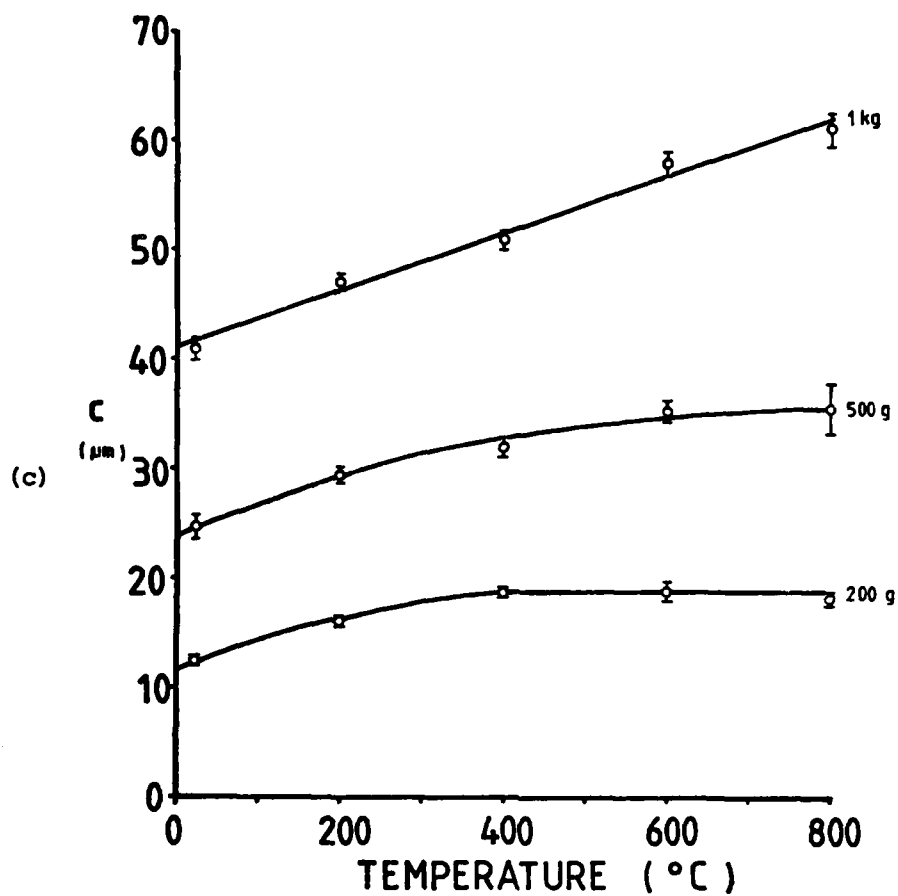


Figure 33. Radial crack radius  $c$  as a function of temperature and load for SiC materials: (a) blue-black (0001) single crystal SiC, (b) Norton NC203 hot-pressed SiC. Error bars indicate one standard error in the mean.



**Fig. 33** Radial crack radius  $c$  as a function of temperature and load for SiC materials: (c) Carborundum sintered SiC, (d) 'Suzuki' sintered SiC.

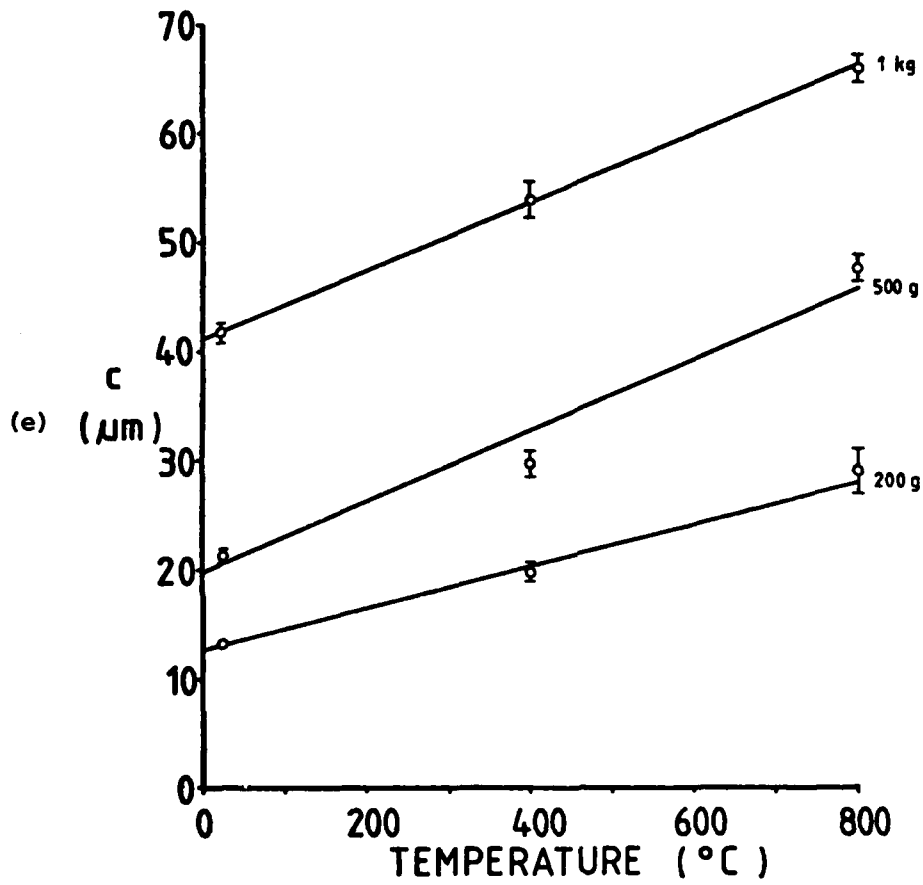
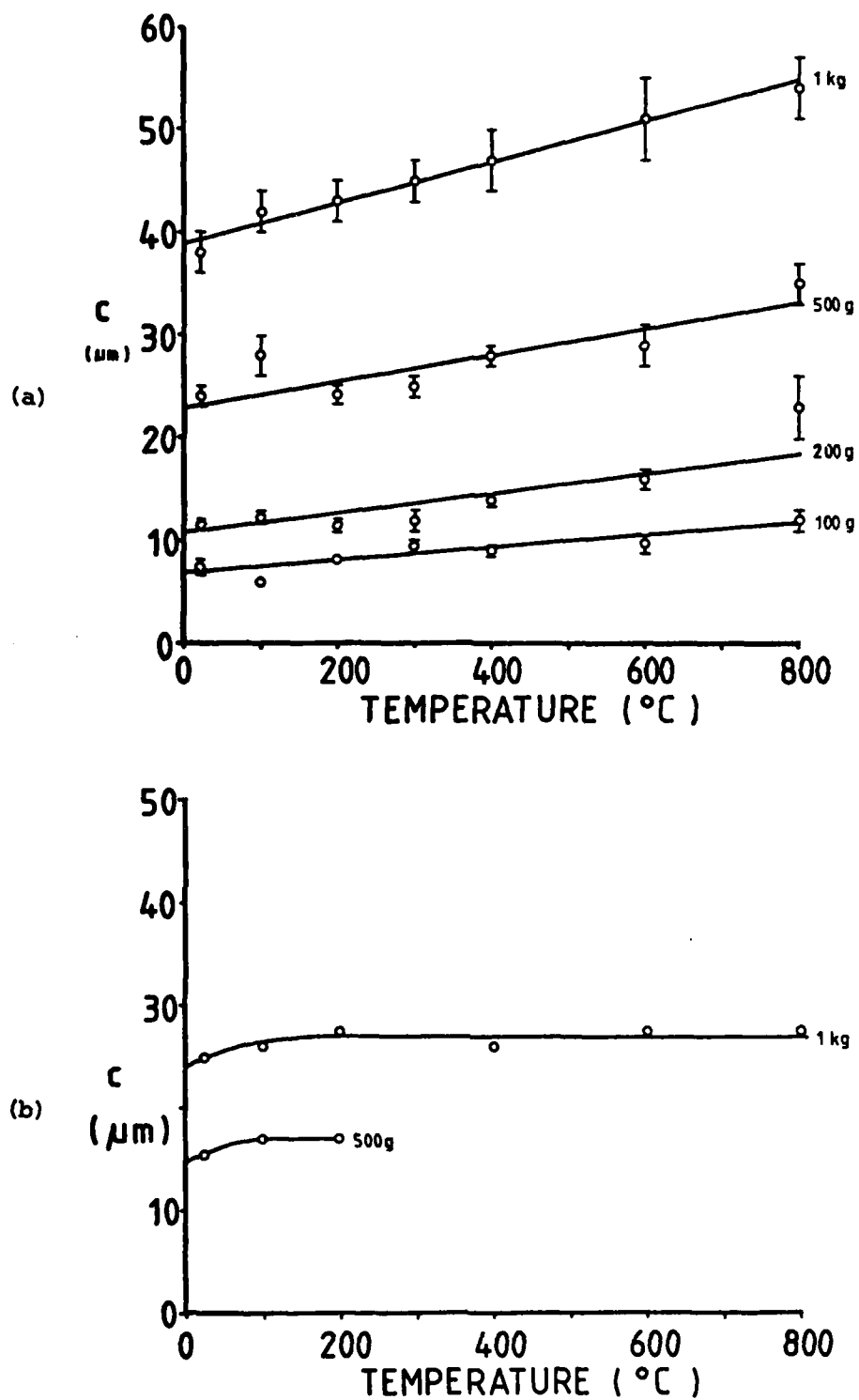
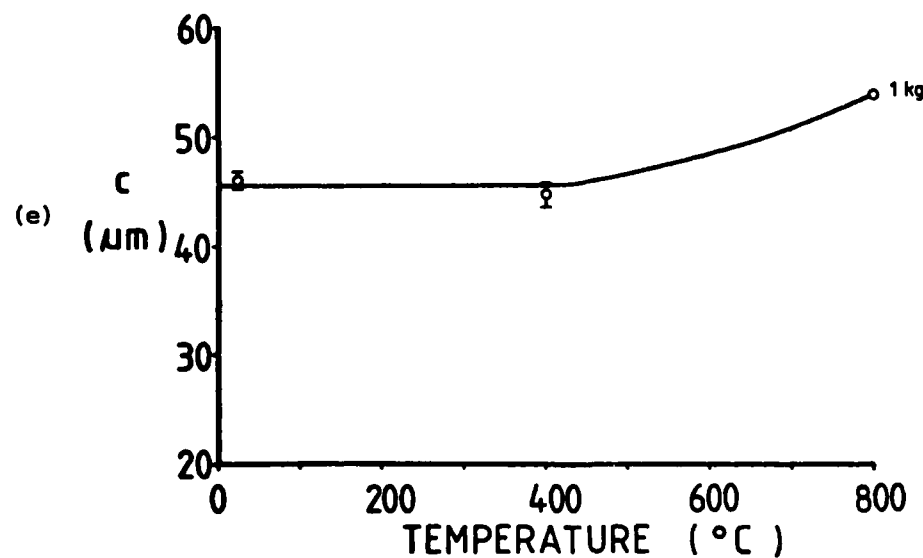
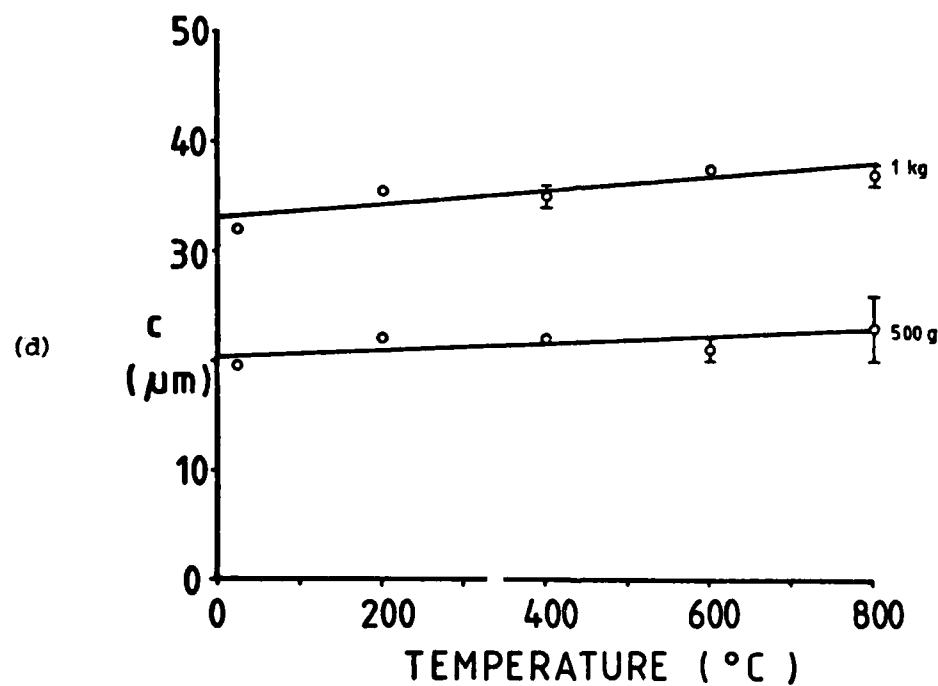
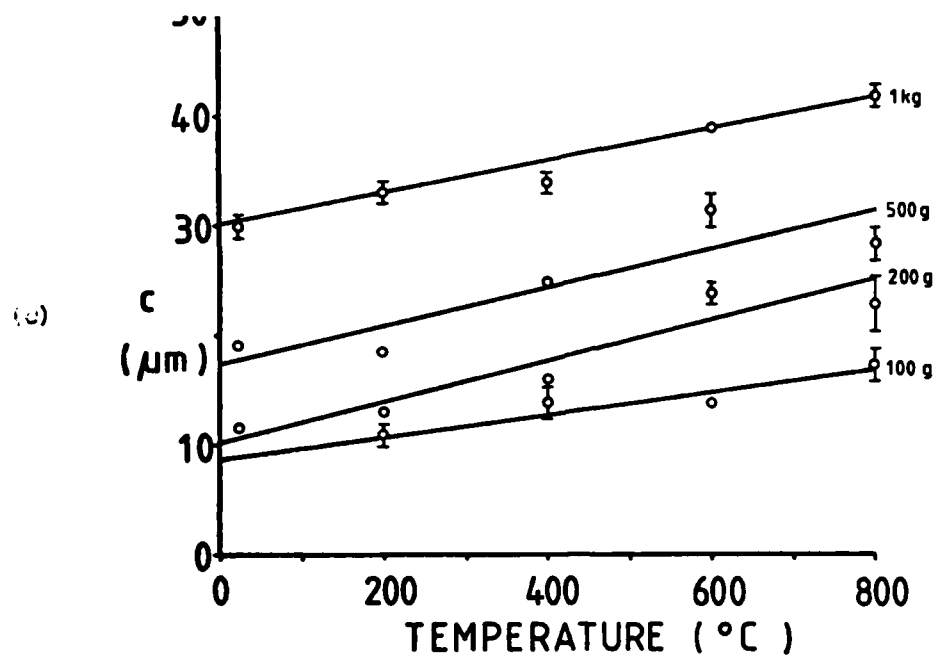


Fig. 33 Radial crack radius  $c$  as a function of temperature and load for SiC materials: (e) 'REFEL' reaction-bonded SiC ( 10  $\mu\text{m}$  grain size ).



**Figure 34.** Radial crack radius  $c$  as a function of temperature and load for  $\text{Si}_3\text{N}_4$  materials: (a) pyrolytically-deposited  $\text{Si}_3\text{N}_4$ , (b) Norton NC132 hot-pressed  $\text{Si}_3\text{N}_4$ . Error bars indicate one standard error in the mean.



**Fig.34** Radial crack radius as a function of temperature and load for  $\text{Si}_3\text{N}_4$  materials: (c) Norton NCX34 hot-pressed  $\text{Si}_3\text{N}_4$ , (d) Ford '2.7' RBSN, (e) Norton NC350 RBSN.

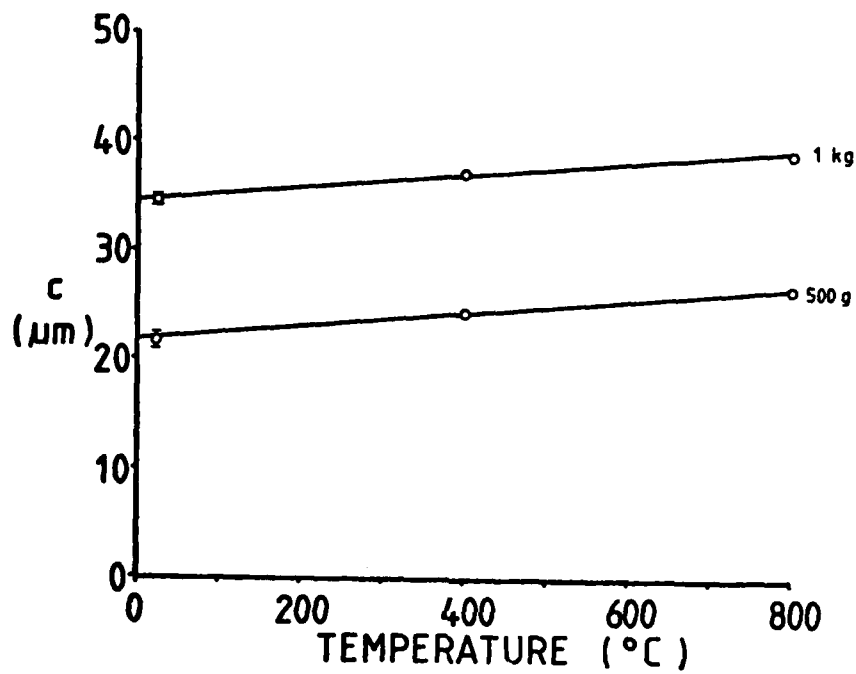


**Figure 35.** Radial crack radius  $c$  as a function of temperature and load for a sintered sialon ( Lucas SYALON 342 ). Error bars indicate one standard error in the mean.

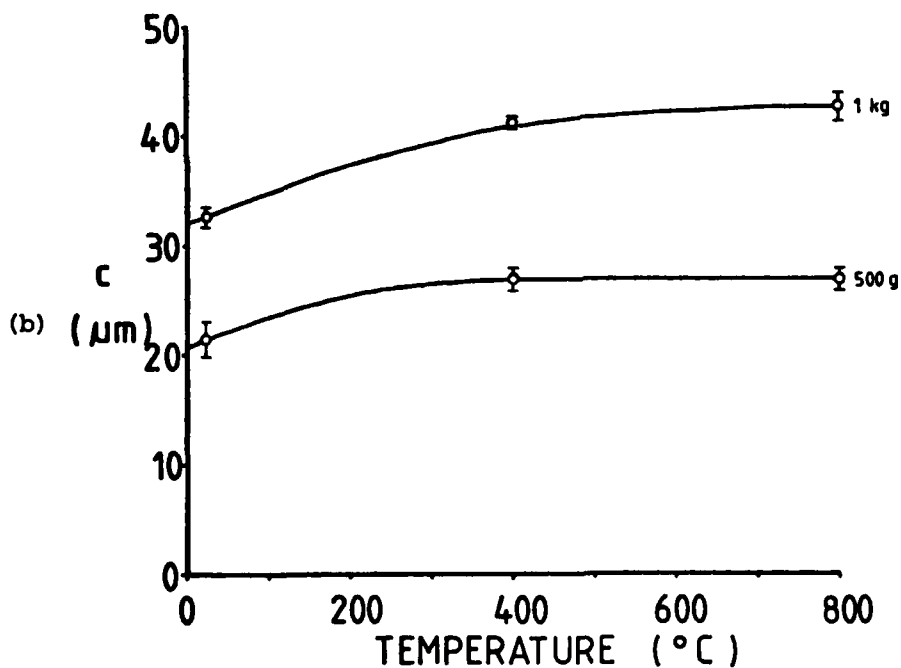
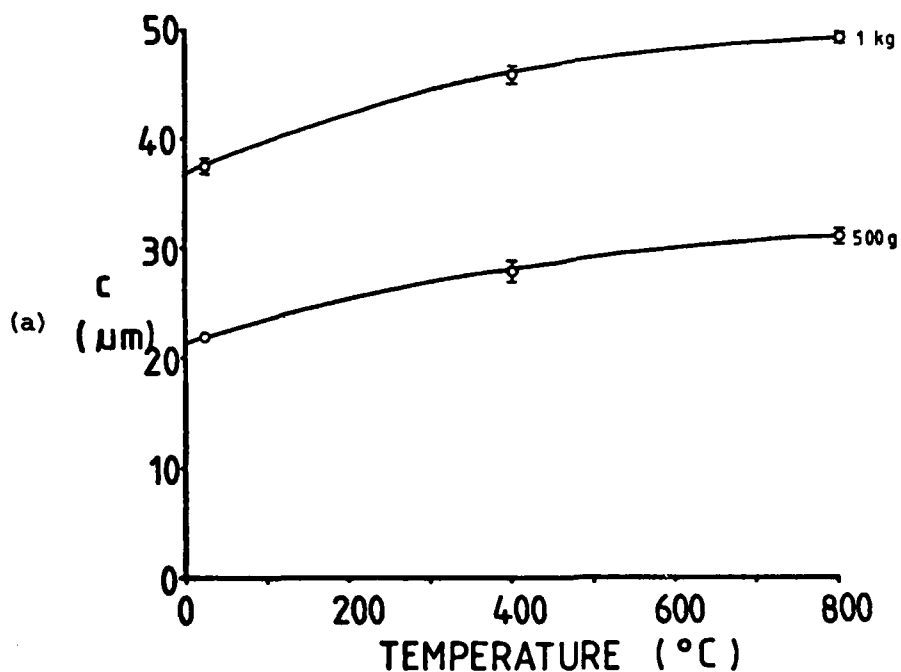


**Figure 36.** Radial crack radius  $c$  as a function of temperature and load for two forms of sintered  $\text{B}_4\text{C}$ : (a) Le Carbone grade S1143 ( density  $2.4 \text{ gcm}^{-3}$  ), (b) Le Carbone grade S1138 ( density  $2.05 \text{ gcm}^{-3}$  ). Error bars indicate one standard error in the mean.

AD-A136 242

MICROHARDNESS FRICTION AND WEAR OF SIC AND Si3N4  
MATERIALS AS A FUNCTION OF (U) CAMBRIDGE UNIV (ENGLAND)  
DEPT OF METALLURGY AND MATERIALS SCI.

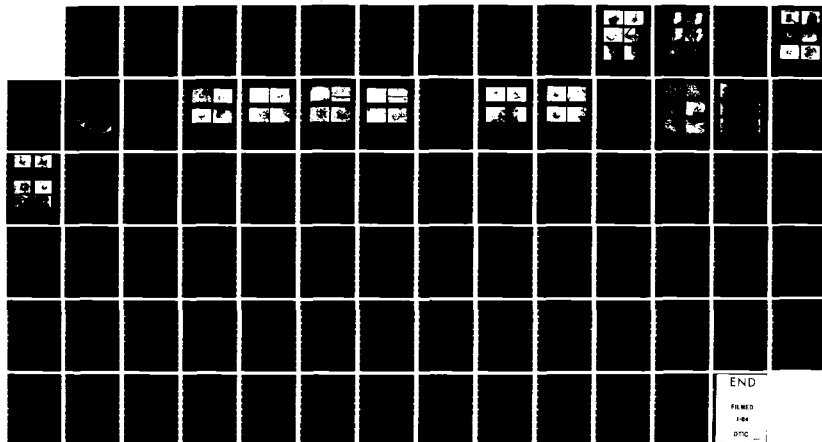
3/3

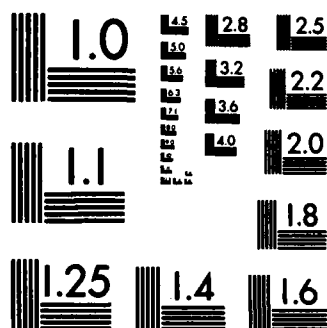
UNCLASSIFIED

M G NAYLOR ET AL. OCT 81 DA-ERD-78-G-010

F/G 11/2

NL





MICROCOPY RESOLUTION TEST CHART  
NATIONAL BUREAU OF STANDARDS-1963-A

to form a chip of removed material were measured).

A similar dependence of crack size on temperature has been reported by Trefilov et al. (40) for both radial and lateral\* cracks around Vickers indentations in (0001) SiC (c.f. fig. 33a):  $c$  was found to increase with increasing temperature above  $\sim 400^{\circ}\text{C}$  and to decrease above  $\sim 800^{\circ}\text{C}$  (radials) (see also ref. 41) or  $\sim 1000^{\circ}\text{C}$  (laterals). Veldkamp and Hattu (42) report a similar type of variation for lateral cracks around scratches in a  $\text{PbO-SiO}_2$  based glass. Otherwise, there have been relatively few studies of the variation of indentation fracture behaviour with temperature.  $\text{MgO}$ , for example, has been found to exhibit substantial fracture up to  $800^{\circ}\text{C}$ , "dislocation interaction cracks" between 800 and  $1000^{\circ}\text{C}$ , with no fracture above  $1000^{\circ}\text{C}$  (43, 44). Dynamic hardness tests by Fitzgerald (45) have revealed an increase with temperature in the number of cleavage cracks in single crystal  $\text{TiC}$ , and the onset of ring cracking in polycrystalline  $\text{B}_4\text{C}$  above  $1340^{\circ}\text{C}$ . Shockey et al. (46) studied crack geometries around particle impact sites in NC132 hot-pressed  $\text{Si}_3\text{N}_4$  as a function of temperature ( $20^{\circ}\text{C}$  and  $1400^{\circ}\text{C}$ ), finding a transition from ring and cone cracking at  $20^{\circ}\text{C}$  to ring, cone, radial and lateral cracking (for impact by WC spheres) at  $1400^{\circ}\text{C}$ . Inoue and Matzke (47) report a decrease in ring crack radius (corresponding to a decrease in fracture surface energy) with increasing temperature for Hertzian indentation of  $\text{ThO}_2$ .

The increases in radial crack length with increasing temperature found in this investigation were most pronounced for {111} Si ( $\sim 75\%$  increase in  $c_r$  over the temperature range  $25-700^{\circ}\text{C}$ ) and for SiC materials ( $\sim 50\%$  increase in  $c_r$  between 25 and  $800^{\circ}\text{C}$ ).  $\text{B}_4\text{C}$  and especially  $\text{Si}_3\text{N}_4$  and sialon materials displayed comparatively little variation in  $c_r$  with temperature (N.B. NC132 HPSN - fig. 34b).

On the basis of the Lawn/Evans et al. indentation fracture model, there are two immediately apparent interpretations of the increase in  $c_r$  with increasing temperature: (i) that the fracture toughness decreases with increasing temperature and (ii) that the

---

\*Trefilov et al. described a subsurface "damaged zone" of radius roughly equal to the length of radial cracks (see fig. 38). Although this was interpreted as circular Hertzian cone cracking, it is more likely to be lateral fracture.

residual stresses around indentations increase. The first of these hypotheses is examined in the following section.

#### 4.4.2 The Variation of Fracture Toughness with Temperature

Before calculating  $K_{IC}$  values from indentation fracture measurements, it is essential to check that the relevant model is valid for the experimental conditions obtaining. In particular, the Lawn/evans et al. analysis generally requires  $(c/a) \geq 2.5$  (e.g. 21, 24, 27, 39), which was not achieved for many of the less brittle materials used in this investigation in the available indenter load range (maximum 1kgf) (table 15). In some cases, particularly for some  $Si_3N_4$  materials and some silicon carbides at high temperatures, radial cracks were calculated to be entirely contained within the plastic zone around the indentation (table 16). Under such conditions, Palmqvist radial crack geometries are anticipated (section 4.2.1), for which the relation  $P \propto c^{3/2}$  might not hold (section 4.3.2). Whilst no attempt was made to establish whether median cracks were present or not, the above relation was confirmed for all but one material - NCX34 hot-pressed  $Si_3N_4$  - for which the exponent  $q$  in the expression  $P \propto c^q$  was found to be greater than 1.5, and to increase with temperature (table 17). In addition, REFEL reaction-bonded SiC was found to have a high value of  $q = 1.9$  at  $800^\circ C$ . This behaviour is discussed in section 4.4.3. For no material was the relation  $P \propto c$  ( $q=1$ ) found.

Thus, the expression suggested by Marshall and Evans (27) (quoted in section 4.3.2) was used to determine  $K_{IC}$  values as a function of temperature for each material investigated (except NCX 34 HPSN). Data were analyzed by determining the gradients of  $c^{3/2}$  versus  $P$  plots (least squares, minimizing errors in  $c^{3/2}$  rather than in  $P$ ). These, together with projected area Vickers hardness values averaged over the relevant load range (table 2) and values of Young's modulus obtained from the literature (table 2), were used to calculate  $K_{IC}$  values (table 18).

The results show that, with a few exceptions,  $K_{IC}$  did not vary systematically with temperature, confirming results of bulk mechanical tests (e.g. 48, 49) which suggest that  $K_{IC}$  is temperature-insensitive below  $\sim 1000^\circ C$  for these materials. In passing, it is apparent that  $K_{IC}$  values calculated from these indentation fracture experiments agree fairly well with values measured in more

Material	Indenter Load Range (gf)	(c/a)	
		25°C	800°C
<u>SILICON</u>			
{111} single crystal	200 - 1000	2.6 - 3.8	0; 2.1 at 1kgf load, 700°C
<u>SILICON CARBIDE</u>			
(0001) single crystal	100 - 1000	2.1 - 3.6	2.6 - 4.4
Hot-Pressed (Norton NC203)	100 - 1000	1.8 - 2.3	1.6 - 2.0
Sintered (Carborundum)	200 - 1000	2.2 - 3.2	2.1 - 2.9
(Suzuki)	200 - 1000	1.8 - 2.0	1.9 - 2.1
Reaction-Bonded (REFEL-a)	200 - 1000	2.1 - 2.7	2.5 - 2.3
<u>SILICON NITRIDE</u>			
Pyrolytically-Deposited (AMTE)	100 - 1000	2.2 - 3.3	2.5 - 3.6
Hot-Pressed (Norton NC132)	500-1000; 1000*	1.4 - 1.7	1.5*
(Norton NCX34)	100 - 1000	1.6 - 1.8	2.6 - 2.0
Reaction-Bonded (Ford '2.7')	500 - 1000	1.5 - 1.8	1.7 - 1.9
(Norton NC350)	1000	1.9	2.0
<u>SIALON</u>			
Sintered (Lucas SYALON 342)	500 - 1000	1.8 - 2.0	1.9 - 1.9
<u>BORON CARBIDE</u>			
Sintered (Le Carbone $\rho = 2.4$ )	500 - 1000	2.5 - 3.1	3.2 - 3.5
(Le Carbone $\rho = 2.05$ )	500 - 1000	1.7 - 1.7	1.9 - 2.1

**Table 15** The ratio (c/a) of radial crack radius to Vickers indentation radius at room temperature and 800°C over the stated indenter load ranges for various Si, SiC, Si<sub>3</sub>N<sub>4</sub>, Sialon and B<sub>4</sub>C materials.

Material	(c/b)	
	25°C	800°C
<b><u>SILICON</u></b>		
{111} single crystal	2.4	0; 0.5 at 700°C
<b><u>SILICON CARBIDE</u></b>		
(0001) single crystal	2.5	2.1
Hot-Pressed (Norton NC203)	1.5	0.8
Sintered (Carborundum)	2.2	1.3
(Suzuki)	1.3	0.9
Reaction-Bonded (REFEL-a)	1.6	0.7
<b><u>SILICON NITRIDE</u></b>		
Pyrolytically-Deposited (AMTE)	2.8	2.5
Hot-Pressed (Norton NC132)	1.1	0.8
(Norton NCX34)	1.1	1.0
Reaction-Bonded (Ford '2.7')	1.2	1.2
(Norton NC350)	1.1	1.0
<b><u>SIALON</u></b>		
Sintered (Lucas SYALON 342)	1.2	0.9
<b><u>BORON CARBIDE</u></b>		
Sintered (Le Carbone $\rho = 2.4$ )	2.3	2.3
(Le Carbone $\rho = 2.05$ )	1.0	1.2

Table 16 The ratio (c/b) of radial crack radius to calculated plastic zone radius for 1 kgf Vickers indentations in a variety of brittle materials at room temperature and at 800°C. b was calculated from the relation  $(b/a) = 0.4 (E/H)^{1/2}$  (section 3.3.2.3).

Material	Temperature (°C)								
	25	100	200	300	400	500	600	700	800
<b><u>SILICON</u></b>									
{111} single crystal	1.3	1.5	1.4	1.5	1.4	1.4	1.6	-	-
<b><u>SILICON CARBIDE</u></b>									
(0001) single crystal	1.3	-	-	-	1.6	-	-	-	1.3
Hot-Pressed (Norton NC203)	1.6	1.9	1.6	-	1.7	-	1.6	-	1.7
Sintered (Carborundum)	1.4	-	1.5	-	1.6	-	1.4	-	1.3
(Suzuki)	1.7	-	1.3	-	1.6	-	1.6	-	1.7
Reaction-Bonded (REFEL-a*)	1.4	-	-	-	1.6	-	-	-	1.9
(REFEL-a*)	1.4								
(REFEL-b*)	1.3								
<b><u>SILICON NITRIDE</u></b>									
Pyrolytically-Deposited (AMTE)	1.4	1.2	1.4	1.4	1.4	-	1.4	-	1.6
Hot-Pressed (Norton NC132)	1.4	1.5	1.4	-	-	-	-	-	-
(Norton NCX34)	1.7	-	2.0	-	2.4	-	2.5	-	2.6
Reaction-Bonded (Ford '2.7')	1.4	-	1.4	-	1.5	-	1.2	-	1.3
<b><u>SIALON</u></b>									
Sintered (Lucas SYALON 342)	1.5	-	-	-	1.6	-	-	-	1.8
<b><u>BORON CARBIDE</u></b>									
Sintered (Le Carbone $\rho=2.4$ )	1.3	-	-	-	1.4	-	-	-	1.5
(Le Carbone $\rho=2.05$ )	1.6	-	-	-	1.6	-	-	-	1.5

**Table 17** The exponent  $q$  in the relation  $Pac^q$  calculated from indentation fracture data for various brittle materials as a function of temperature. Values close to  $3/2$  indicate that the Lawn, Evans et al. model is applicable, whilst values close to 1 would suggest the Palmqvist relation (see text). Typical errors  $\pm 0.1$ .

\*See footnote to table 18.

Material	$K_{IC}$ (MPa $m^{1/2}$ )										Typical Errors (MPa $m^{1/2}$ )
	25°C	100°C	200°C	300°C	400°C	500°C	600°C	700°C	800°C	1000°C	
{111} Silicon	0.99	1.22	1.02	1.22	0.95	0.80	0.91	1.01	-	-	± 0.07
(0001) SiC (blue-black)	2.45	-	-	-	1.80	-	-	-	1.41	1.28	± 0.06
Hot-pressed SiC (Norton NC203)	5.0	4.9	3.7	-	3.7	-	3.8	-	4.3	-	± 0.2
Sintered SiC (Carborundum)	2.9	-	2.4	-	2.4	-	2.2	-	2.2	-	± 0.1
" " (Suzuki)	5.3	-	3.1	-	3.1	-	3.1	-	3.4	-	± 0.2
Reaction-Bonded SiC (REFEL-a*)	3.2	-	-	-	2.7	-	-	-	2.5	-	± 0.1
" " (REFEL-a*)	4.4	-	-	-	-	-	-	-	-	-	± 0.2
" " (REFEL-b*)	4.4	-	-	-	-	-	-	-	-	-	± 0.2
Pyrolytically-Deposited Si <sub>3</sub> N <sub>4</sub> (AMTE)	2.6	2.3	2.3	2.1	2.1	-	1.9	-	1.9	-	± 0.1
Hot-Pressed Si <sub>3</sub> N <sub>4</sub> (Norton NC132)	6.3	6.0	5.7	-	6.2	-	6.1	-	6.2	-	± 0.2
Reaction-Bonded Si <sub>3</sub> N <sub>4</sub> (Ford 2.7)	4.2	-	3.6	-	3.8	-	3.4	-	3.6	-	± 0.2
" " Norton NC350)	2.8	-	-	-	3.1	-	-	-	2.4	-	± 0.2
Sintered SYALON (Lucas 342)	4.2	-	-	-	4.1	-	-	-	4.0	-	± 0.1
Sintered B <sub>4</sub> C (Le Carbone p=2.4)	3.0	-	-	-	2.5	-	-	-	2.3	-	± 0.1
" (Le Carbone p=2.05)	4.4	-	-	-	3.5	-	-	-	3.2	-	± 0.2

Table 18 The variation of indentation fracture toughness with temperature for various Si, SiC, Si<sub>3</sub>N<sub>4</sub>, sialon and B<sub>4</sub>C materials.  $K_{IC}$  values were calculated using the relation recently suggested by Marshall and Evans (27) - see text.

\*three different REFEL samples were tested, two having grain size ~ 10  $\mu$ m (a) and one with grain size ~ 5  $\mu$ m (b).

conventional tests (table 2).

Materials which did appear to show a systematic change in  $K_{IC}$  with temperature were (0001) SiC and the two sintered boron carbides,  $K_{IC}$  decreasing with increasing temperature in all cases. Such an effect has been reported for  $B_4C$  (50), but single crystal SiC has previously been found to show no change in  $K_{IC}$  up to  $\sim 800^\circ C$ , followed by an increase in toughness with increasing temperature (48).

#### 4.4.3 Discussion

The important point about the above results is that radial crack lengths increase with increasing temperature, not due to any decrease in  $K_{IC}$  (in most cases), but due to increasing residual stress around indentations. This, in turn, is due to the increase in  $(E/H)$  ratio which results in greater crack opening forces (e.g. 25). This factor is likely to be important in wear situations in which high temperatures are reached, since increasing temperature results in both increased plasticity and more severe indentation fracture (Chapter 6).

Considering only temperature as a variable, the Evans et al. relation  $c_r^{3/2} \propto (E/H)^{2/5} PK_{IC}^{-1}$  (section 4.3.2) predicts  $c_r \propto H^{-4/15}$  for constant load  $P$  (since  $E$  and  $K_{IC}$  are only weakly dependent on temperature). The variations of  $c_r$  with temperature in figs. 32-36 were indeed found to follow the corresponding variations in  $H^{-4/15}$ , except for those SiC materials which showed a levelling out in the plot of  $c_r$  against temperature at high temperatures -  $H^{-4/15}$  varies almost linearly with temperature for all these materials. It is apparent from fig. 33 that the  $c/T$  plots for these anomalous materials level out at increasingly high temperatures for increasing indenter loads: for example, (0001) single crystal and Carborundum sintered silicon carbides display linear  $c/T$  plots (with no levelling off) at high indenter loads but curved plots at low loads. The reasons for this behaviour remain unclear, but are possibly connected with the increase in plastic zone size ( $b$ ) relative to crack sizes as the temperature increases:  $(c/b)$  is a much weaker function of temperature for  $Si_3N_4$ , sialon and  $B_4C$  materials - see table 16. Similar behaviour was not, however, observed for {111} silicon, which showed an even greater variation in  $(b/a)$  with temperature than did SiC.

For some materials,  $K_{IC}$  was observed to decrease with increasing temperature. This may be a real effect in some cases

(e.g.  $B_4C$ ) or may be due to a breakdown in any of the assumptions made in the Lawn/Evans et al. model (section 4.3.2). In particular, it is suggested that subcritical crack growth effects may become more severe with increasing temperature for polycrystalline materials with boundary phases (see section 3.1.2). Such effects, which are likely to be most severe over short time spans immediately following indentation (26), would result in larger cracks and hence apparently low values of  $K_{IC}$ . Subcritical crack growth effects were not investigated in detail in this study, although measurements made several hours after indentation were found to be consistent with those made within minutes of indentation. Such effects are unlikely to account for the decrease in  $K_{IC}$  with increasing temperature measured for (0001) single crystal SiC, which is as yet unexplained.

The anomalous behaviour of NCX 34 hot-pressed  $Si_3N_4$  and 'REFEL' reaction-bonded SiC at  $800^\circ C$ , where the exponent  $q$  in the relation  $P \propto c^q$  was much higher than predicted, probably reflects the nature of indentation fracture in these materials. NCX 34 HPSN was observed to form networks of cracks along grain boundaries (fig. 45), whilst 'REFEL' SiC formed cracks along SiC:Si interfaces, especially at high temperatures (fig. 42). These materials probably become increasingly susceptible to this type of behaviour at high temperatures because of grain boundary phase softening in NCX 34 or softening of residual silicon in REFEL. Indentation fracture in these materials was not true radial fracture, and so the Lawn/Evans et al. analysis was invalid, for reasons discussed in section 4.3.1. Microstructural effects on indentation fracture are discussed in detail in the following section.

#### 4.5. MICROSTRUCTURAL EFFECTS

In this section, the effects of microstructure on crack paths are investigated for each material (sections 4.5.1 - 4.5.5) and influences on fracture toughness are discussed (section 4.5.6).

##### 4.5.1 Fracture of Single Crystals

Crack patterns around Vickers indentations in {111} silicon

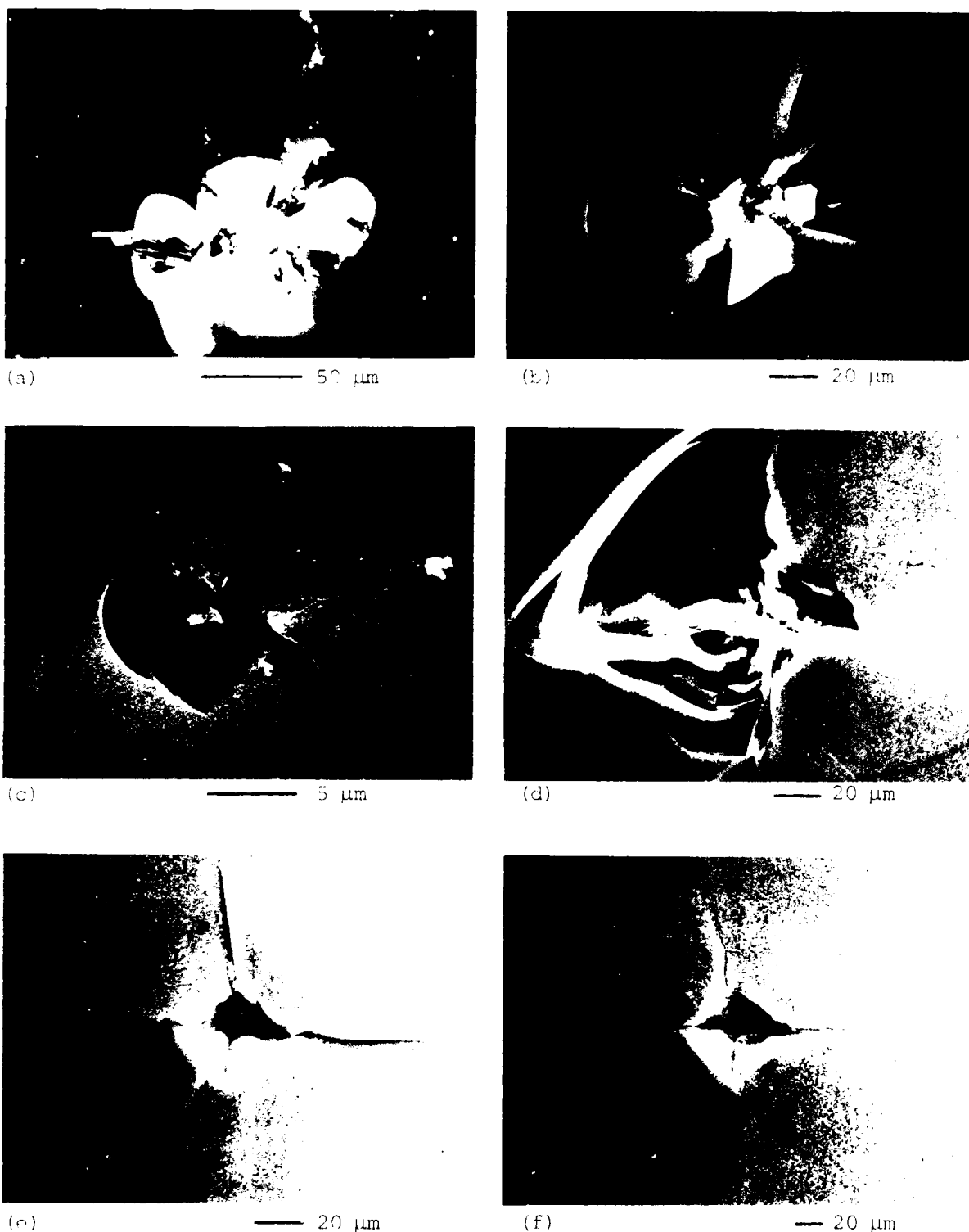
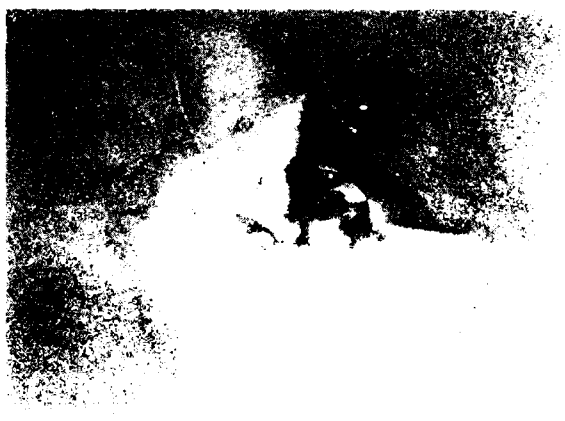


**Figure 37** Vickers indentations made at various temperatures on {111} single crystal Si ( n-type ) with one indenter axis parallel to  $\langle 1\bar{1}0 \rangle$ . All indentations made at 1 kgf applied load except for (c), which was made at 100 gf load. (a) Room temperature indentation with severe radial and lateral fracture ( surface and subsurface ) ( Nomarski ). (b) Secondary electron SEM image of the indentation shown in (a). The lateral vents may be seen more clearly ( for stereo pair of this image, see figure 6a ). (c) Room temperature indentation showing less extensive radial and lateral cracking at 100 gf load. (d) 200°C indentation with massive lateral vents and radial cracks ( SEM secondary image ). (e) 400°C indentation showing extensive radial fracture and one subsurface lateral crack ( SEM ). (f) 500°C indentation showing extensive radial cracking without lateral fracture ( SEM ).



are shown as a function of temperature in fig. 37. In the temperature range 24-300°C, cracking was a combination of both radial and lateral fracture at all the loads used (figs. 37 a-d). Above 300°C, breakout of lateral cracks to the surface to form 'chips' of removed material was seldom observed (figs. 37 e-l). Below 700°C, radial crack traces were often along near  $\langle \bar{1}\bar{1}2 \rangle$  directions (e.g. fig. 37i), however many cracks were not perfectly straight (e.g. fig. 37g) or were several degrees away from  $\langle \bar{1}\bar{1}2 \rangle$ , some even being nearly parallel to  $\langle \bar{1}\bar{1}0 \rangle$  directions (e.g. fig. 37d). At 700°C, radial cracks formed exclusively along  $\langle \bar{1}\bar{1}0 \rangle$  directions and were contained wholly within the plastic zone (fig. 37j).

Surface crack traces along largely  $\langle \bar{1}\bar{1}2 \rangle$  directions suggests  $\{ \bar{1}\bar{1}0 \}$  rather than  $\{ 11\bar{1} \}$  cleavage, in agreement with observations by Puttick and Hosseini (51). Although  $\{ 11\bar{1} \}$  cleavage has been calculated to be energetically favourable (52), arguments in favour of  $\{ \bar{1}\bar{1}0 \}$  fracture around indentations and scratches on  $\{ 11\bar{1} \}$  planes have been put forward (51): the resolved maximum tensile stress on  $\{ \bar{1}\bar{1}0 \}$  planes perpendicular to the surface is greater than that on  $\{ 11\bar{1} \}$  planes lying at 70.5° to the surface, and consideration of shear stresses and elastic anisotropy further tilts the balance in favour of  $\{ \bar{1}\bar{1}0 \}$  cleavage. Radials formed at 700°C were, by contrast, exclusively along  $\langle \bar{1}\bar{1}0 \rangle$  directions, parallel to the slip plane traces, and were wholly contained within the plastic zone (fig. 37j). Further study is required to establish the effects of slip on crack propagation at these elevated temperatures (e.g. 53).

Whilst radial crack propagation became more extensive with increasing temperature (as described in section 4.4.1), the number of radials formed around indentations decreased, from which it is surmized that nucleation became more difficult. Thus, at 500°C there were very few radials around 100gf indentations; at 600°C, few radials were observed around 100gf and 200gf indentations; at 700°C, radial cracks were only observed at 1kgf load and, on average, there were only two or three around each indentation (fig. 37j). Finally, at 800°C, no radial fracture occurred at even 1kgf load, merely occasional small chips in and around the indentation profile (fig. 37l). The effects of temperature on crack nucleation are discussed in section 5.3.

Indentation fracture around Vickers and Knoop indentations



in (0001) single crystal SiC (blue-black) is shown in fig. 38. Knoop indenter profiles generally promote lateral cracking, whereas radial fracture is favoured around Vickers indentations, thus a combination of indentation techniques may be used to completely characterize indentation fracture behaviour.

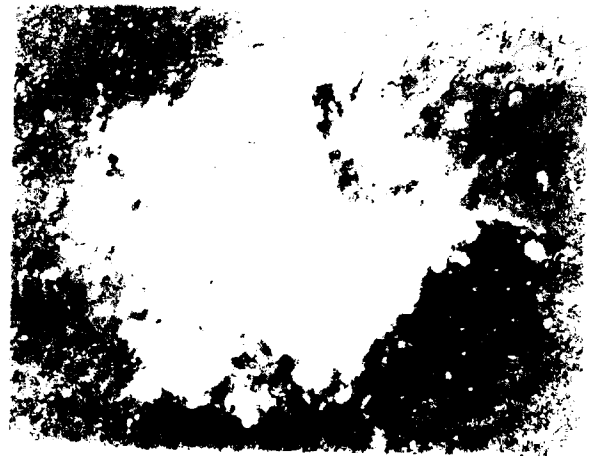
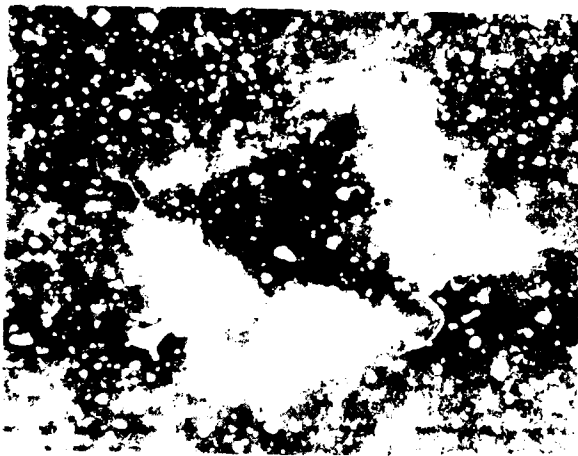
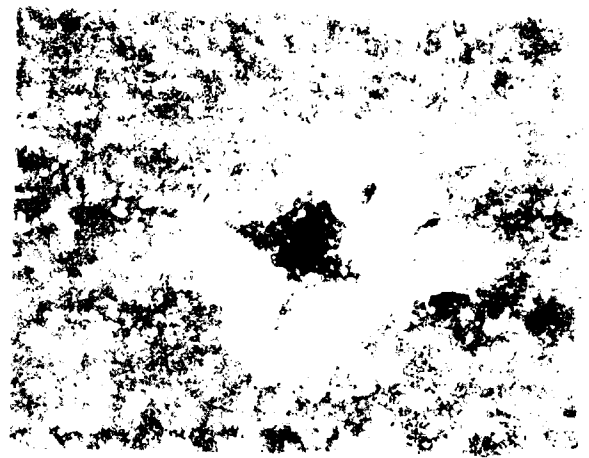
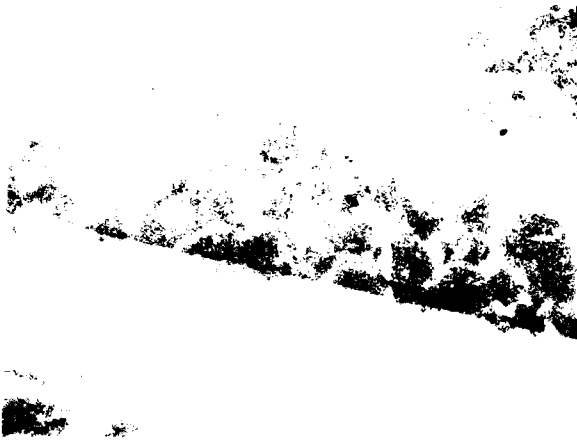
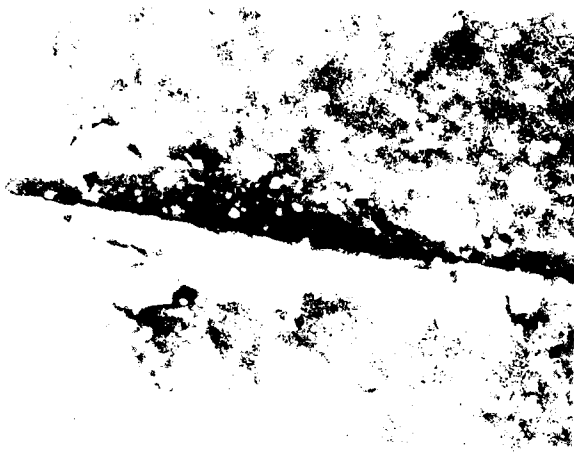
Room temperature Knoop indentations often showed subsurface lateral fracture, seen optically as a white 'halo' around indentations (see figs. 38e,f), with relatively little surface fracture. This was, however, evident where an indentation intersected an obvious flaw such as a surface scratch (fig. 38a). On increasing the temperature, both the incidence and extent of lateral cracking increased dramatically above about 400°C until, by 800°C, almost all the 500gf indentations had large lateral vents associated with them (fig. 38b), even 100gf indentations often being badly cracked. Lateral crack paths often appeared to be along (0001), confirming observations by Adewoye (54), who showed that even general conchoidal fracture surfaces through single crystals could be resolved into a series of cleavage steps.

Radial fracture around Vickers indentations was found to form preferentially along  $\langle 11\bar{2}0 \rangle$  directions ( $\{10\bar{1}0\}$  traces) and to a lesser extent along  $\langle 10\bar{1}0 \rangle$  directions ( $\{11\bar{2}0\}$  traces) (figs. 38c, ). Subsurface lateral fracture was visible in the SEM (as dark shadowing around indentations) and optically, especially when viewed in reflection between crossed polars (figs. 38e,f). Lateral cracks were observed to extend to approximately the length of the radial cracks.

#### 4.5.2 Fracture of Polycrystalline Silicon Carbides

##### (i) Hot-Pressed SiC (Norton NC203)

Both Vickers and Knoop indentations showed relatively inextensive fracture at room temperature (figs. 39 a, d). For the Knoop indenter, cracking took the form of networks of small, largely intergranular cracks and chips around the indentation profile, becoming more pronounced with increasing temperature (figs. 39 a-c). Vickers indentations also showed such crack networks in addition to relatively short radial cracks, which were again largely intergranular, sometimes terminating at the small W-rich particles situated at grain boundaries in this material (figs. 39 d,e). Nomarski differential interference micrographs of 800°C indentations revealed slip steps in



several grains and surface rumpling of grains adjacent to the indentation (fig. 39f). The incidence of grain boundary fracture in this material suggests a low value of grain boundary cohesive energy.

(ii) Carborundum Sintered SiC

Around Vickers indentations, this material formed extensive radial cracks (fig. 40) with only occasional lateral chips. Crack paths were sometimes branched, in many cases appearing to pass preferentially along grain boundaries for parts of their lengths. Often, cracks appeared to have changed direction in order to pass through pores, which sometimes (by no means always) acted as termination sites (fig. 40c). Slip steps and surface rumpling were again observed in grains immediately adjacent to indentations made at 800°C.

(iii) 'Suzuki' Sintered SiC

This material formed shorter radial cracks than the above sample, which were generally straight, passing non-preferentially through several pores over their lengths (note the greater amount of porosity in this material) (fig. 41). Often, crack paths were deflected slightly on passing through pores (e.g. fig. 41d), and again pores occasionally formed crack termination sites. Sometimes, where the needle- or plate-like grains were suitably oriented, cracks propagated preferentially along grain boundaries (figs. 41c,d).

(iv) 'REFEL' Reaction-Bonded SiC

Figure 42 shows fracture around Knoop and Vickers indentations made at various temperatures in REFEL SiC (sample (a)). Knoop indentations promoted a mixture of lateral chipping and networks of small cracks which were of no particular geometry with regard to the indentation, but were clearly related to the microstructure. Vickers indentations also produced these crack networks in addition to radial cracks (often ill-defined). Cracking was clearly observed to occur preferentially along interfaces between SiC and residual silicon (confirming observations by Page et al. (38)) and along grain boundaries (although intragranular fracture was also commonly observed). Interfaces between original grit 'seed' particles and epitaxially deposited material were not found to provide preferred fracture paths. Microstructural deviation of crack paths occurred to a remarkable

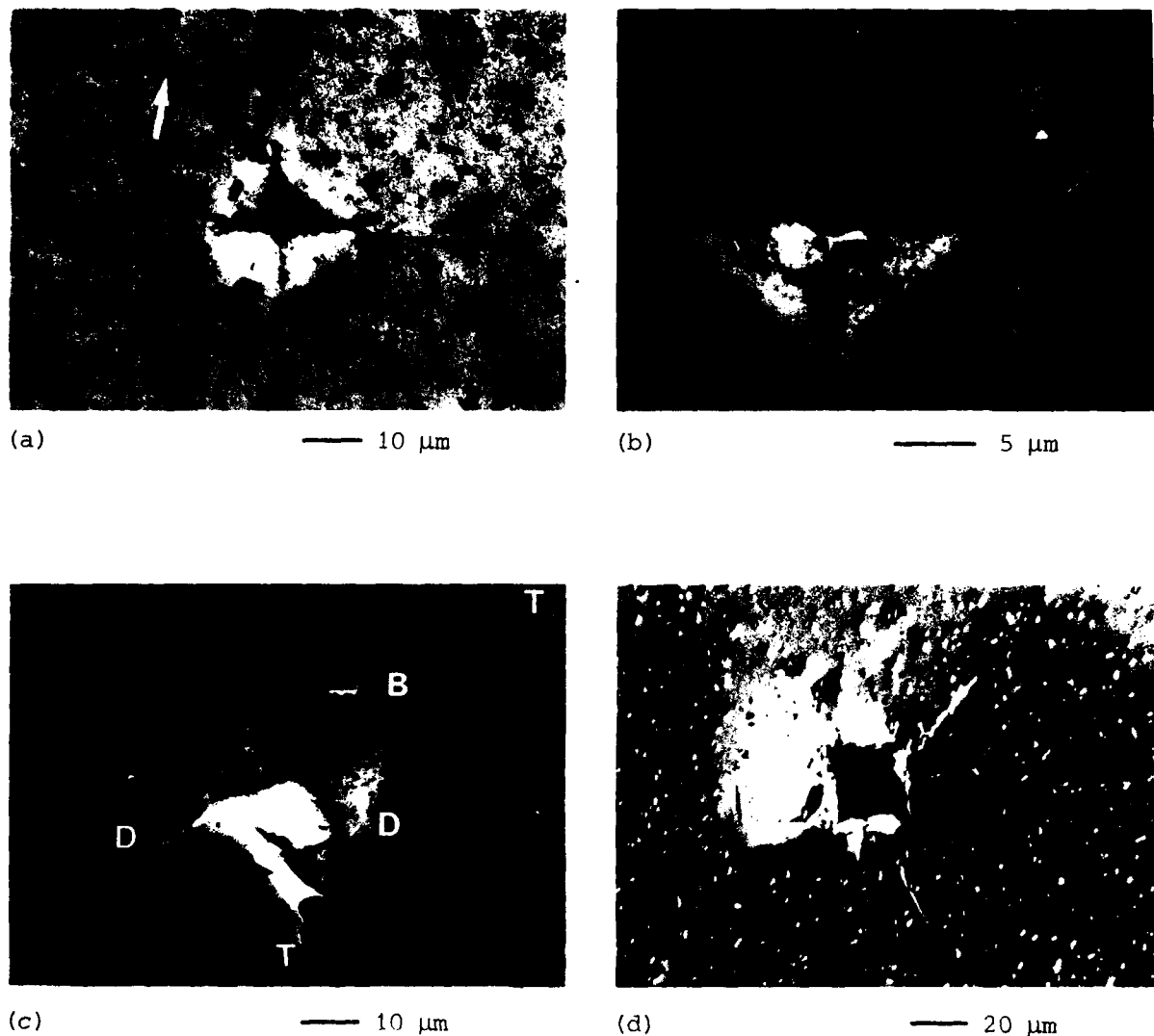


**Figure 40** Fracture around 1 kgf Vickers indentations in Carborundum sintered  $\alpha$ -SiC. Micrographs a, b and c are secondary electron SEM images, whilst micrograph d is a Nomarski differential interference contrast image. (a) Room temperature indentation showing radial fracture, partly along grain boundaries (arrowed). (b) as (a) showing radial and lateral cracking and cracks running along the indentation profile. (c) 800°C indentation exhibiting large-scale radial and lateral cracking. Porosity is seen to cause crack deflection (D), branching (B) and termination (T). The stereo pair of this image is shown in figure 6d. (d) as (c) revealing slip steps in grains adjacent to the indentation.

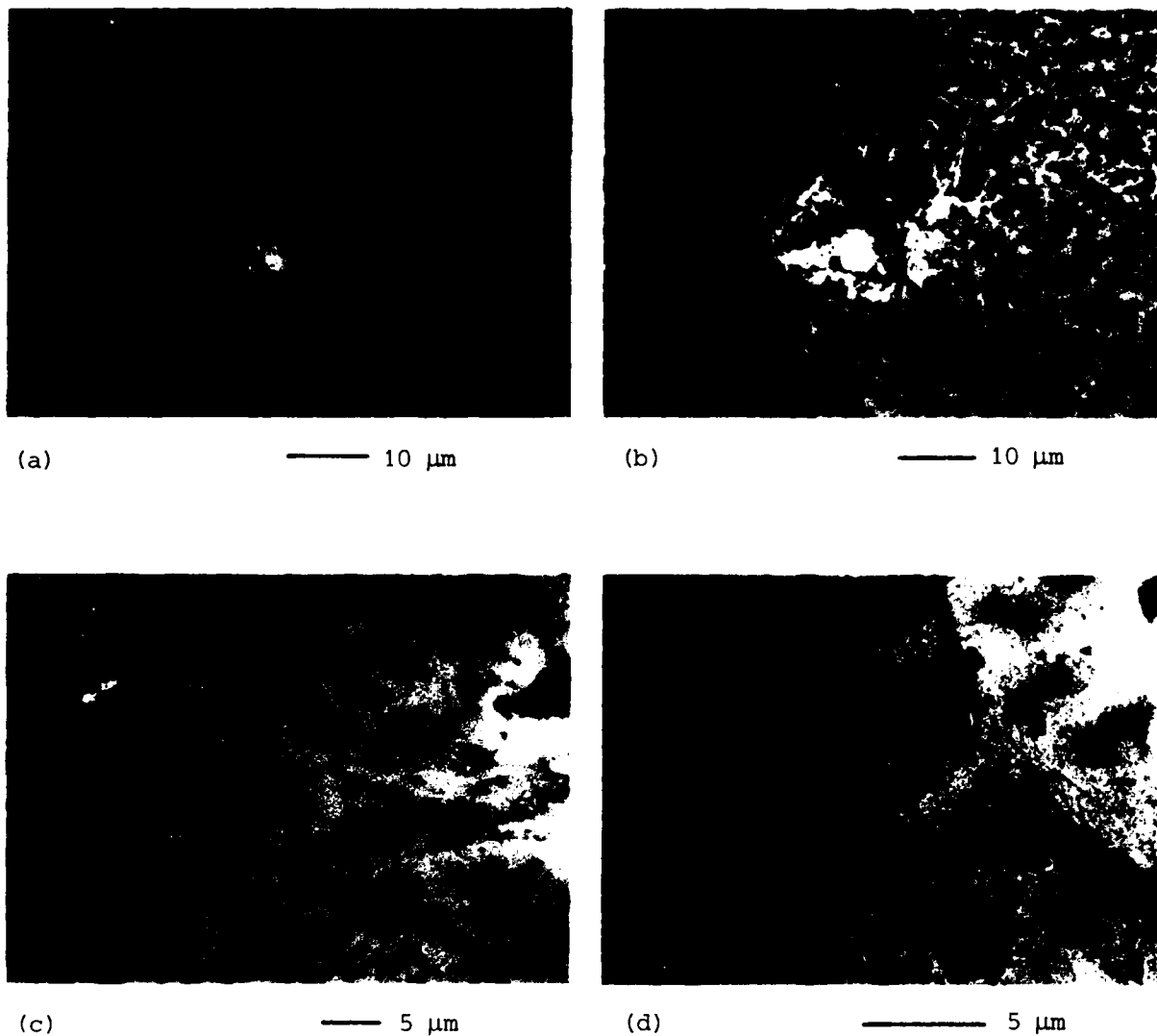
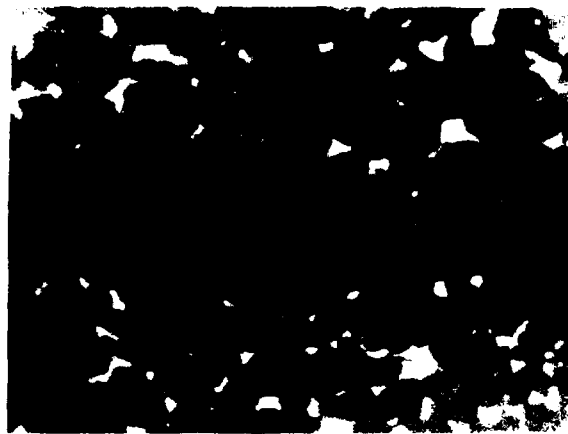


**Figure 41** Fracture around 1 kgf Vickers indentations in 'Suzuki' sintered  $\beta$ -SiC. All micrographs are secondary electron SEM images. (a) Room temperature indentation showing radial cracks. Note the long needle- or plate-like grains surrounded by porosity. (b) 800°C indentation with more extensive radial cracks. (c) as (b) showing radial fracture along a suitably oriented grain boundary. (d) as (b) and (c) with preferred fracture along an apparently weak grain boundary.



(a)

— 10  $\mu\text{m}$ 

(b)

— 10  $\mu\text{m}$ 

(c)

— 10  $\mu\text{m}$ 

(d)

— 10  $\mu\text{m}$ 

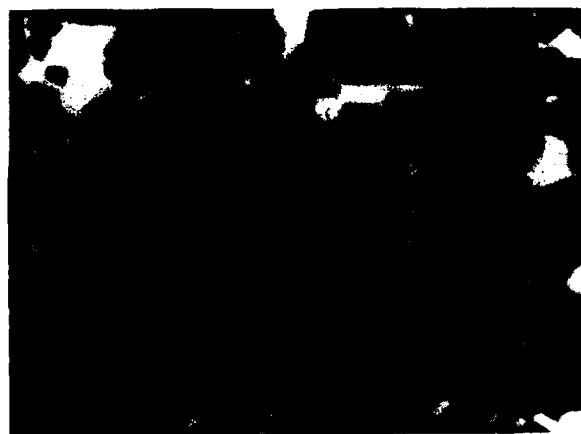
**Figure 42** Fracture around 1 kgf Knoop and Vickers indentations in 'REFEL' reaction-bonded SiC. Micrographs a, c and e are reflected light images, whilst micrographs b, d, f, g and h are secondary electron SEM images. (a) Room temperature indentation showing limited cracking which often passes along interfaces between SiC ( darker phase ) and Si ( lighter phase ). (b) SEM image of the same indentation as in (a), showing that some of the cracking is intergranular. (c) and (d) 400°C indentation showing extensive lateral chipping, much of which is intragranular ( note the impurity contrast on the fracture facets in the secondary electron SEM image ) or along Si:SiC boundaries.



(e)

— 10  $\mu\text{m}$ 

(f)

— 10  $\mu\text{m}$ 

(g)

— 10  $\mu\text{m}$ 

(h)

— 10  $\mu\text{m}$ 

Figure 42 continued. (e) Reflected light micrograph of a 900°C Knoop indentation exhibiting extensive networks of cracks predominantly along Si:SiC interfaces. Striations in occasional grains are attributed to massive slip steps. (f) SEM image of the same indentation as shown in (e) showing both inter- and intragranular fracture. Slip steps are visible in different grains to those observed in (e). (g) Room temperature Vickers indentation showing large amounts of fracture near to the indentation. Microstructural deflection of cracks is very noticeable. (h) 800°C Vickers indentation with extensive networks of largely intergranular and inter-phase cracking. The crack pattern could neither be described as radial nor as lateral.

extent (with deflections greater than  $90^\circ$  in some cases), with crack branching common. The susceptibility of the material to the network pattern of fracture became more marked with increasing temperature, such that well-defined radial or lateral cracks were seldom observed at  $800^\circ\text{C}$  (fig. 42h). Thus, the cohesion between SiC and Si appears to decrease with increasing temperature. Slip steps were observed in a number of grains immediately adjacent to Knoop indentations made at  $900^\circ\text{C}$  (figs. 42e,f).

#### 4.5.3 Fracture of Polycrystalline Silicon Nitrides

##### (i) Pyrolytically-Deposited $\text{Si}_3\text{N}_4$

Vickers indentations in PDSN showed extensive, well-defined radial cracks at all temperatures (fig. 43). Lateral fracture was generally infrequent, becoming more noticeable at high temperatures and high applied loads. Radial cracks often appeared to pass preferentially through the very small amounts of porosity (probably intergranular) found to be present in this material. Viewing the specimen optically between crossed polars revealed both the grain structure and sub-surface indentation fracture (figs. 43c,d). Occasionally, grain boundaries appeared to form preferred fracture paths when suitably situated with respect to the indentation, however the cracking was for the most part intragranular due to the large grain size of the material.

##### (ii) Hot-Pressed $\text{Si}_3\text{N}_4$ (Norton NC132: with ~5wt% MgO)

Vickers indentations in NC132 HPSN produced comparatively short radial cracks (figs. 44a,c) at and above 500gf load, the cracks being macroscopically straight but 'meandering' on a submicron scale (fig. 44b). Cracks were often seen to pass around grain boundary WC or WSi particles, often being deflected slightly, and occasionally terminating at a particle. These observations suggest that crack paths were at least partly intergranular. At high temperatures, small crack networks were observed around indentation profiles (fig. 44d), together with short radial cracks for 1kgf indentations. Below this load, radial cracks were either absent or too small to be distinguishable at temperatures  $\gtrsim 300^\circ\text{C}$ . Lateral cracks were not observed at any temperature or load.

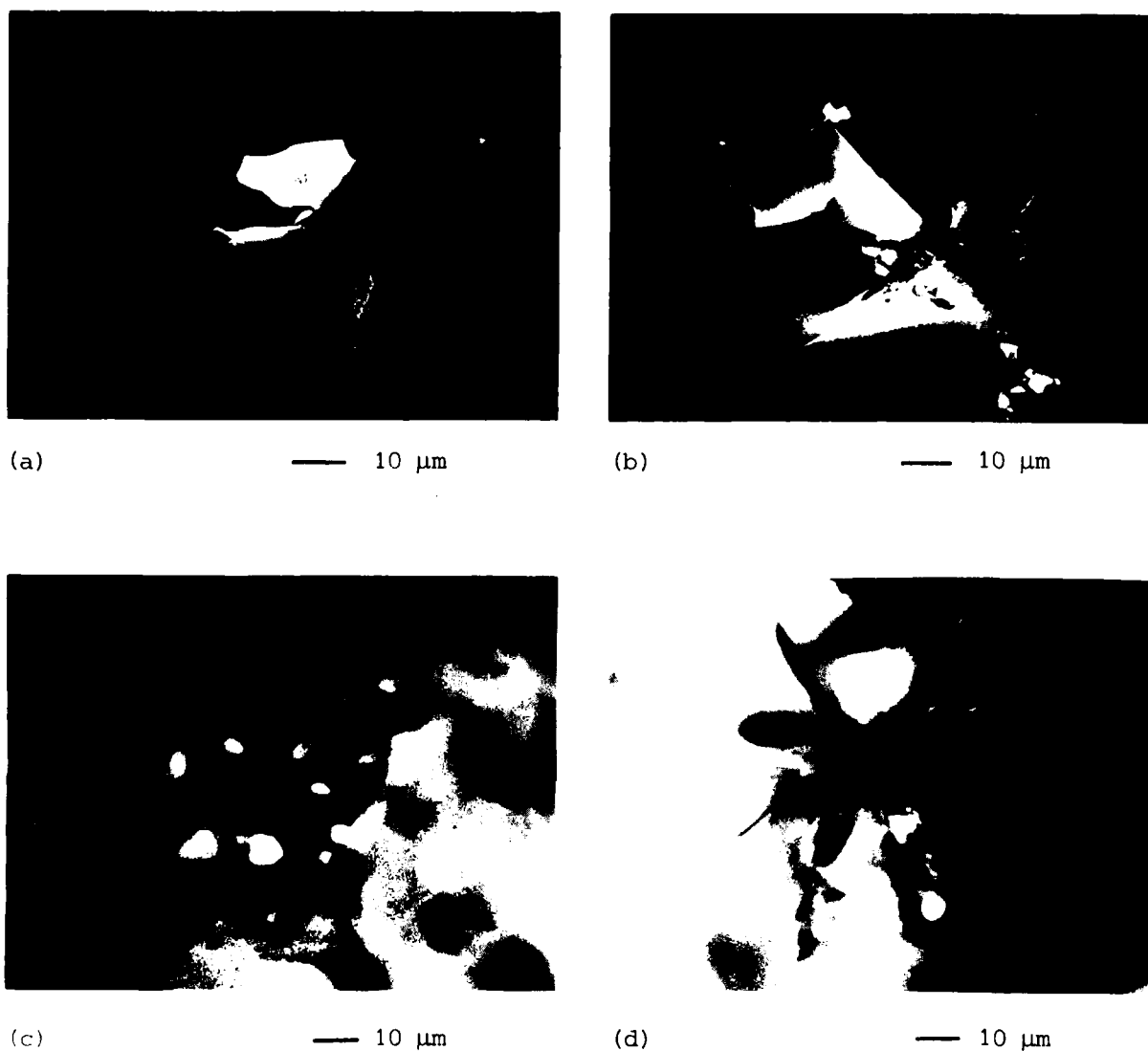


**Figure 43** Fracture around 1 kgf Vickers indentations in pyrolytically-deposited  $\text{Si}_3\text{N}_4$ . (a) Secondary electron SEM image of a room temperature indentation showing radial cracking and a lateral chip. (b) as (a) showing more extensive fracture around an 800°C indentation ( the stereo pair of this image is shown in figure 6e ). (c) Crossed polar reflected light micrograph of a room temperature indentation showing surface and subsurface radial/median and lateral fracture. The grain structure of the material is revealed by orientation-dependent grain-to-grain contrast. (d) as (c), showing an 800°C indentation with more extensive fracture.

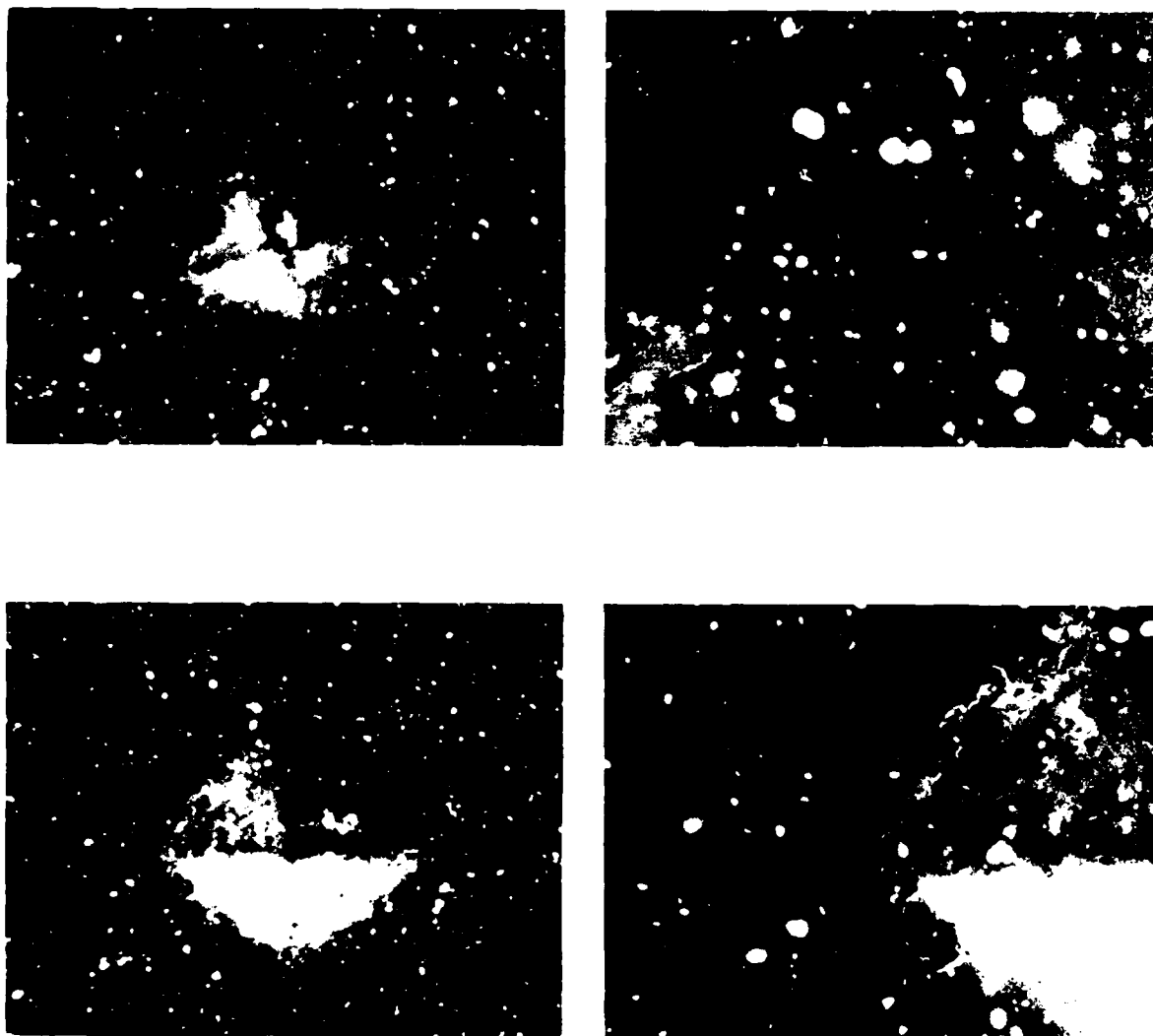


**Figure 44** Fracture around 1 kgf Vickers indentations in Norton NC132 hot-pressed  $\text{Si}_3\text{N}_4$  ( with MgO additive ). All micrographs are secondary electron SEM images. (a) Room temperature indentation with 'meandering' radial cracks which are occasionally deflected by grain boundary particles. (b) as (a) showing a radial crack path at higher magnification. (c) 800°C indentation showing radial fracture as above. (d) Higher magnification image of part of (c). Radial cracks appear to be predominantly intergranular, passing around several grain boundary inclusions. The indentation has a ragged appearance due to several small cracks and chips which have formed along the edge of the indentation.

(iii) Hot-Pressed  $\text{Si}_3\text{N}_4$  (Norton NCX34: with ~8wt%  $\text{Y}_2\text{O}_3$ )

The fracture behaviour of NCX34 HPSN was similar to that of NC132 but more pronounced, radial cracks being measurable over the whole load range at all temperatures. Again, cracks were meandering (figs. 45 a,c) and in this case clearly intergranular (figs. 45 b-f). At  $800^\circ\text{C}$ , networks of grain boundary cracks were formed (figs. 45 d,e), more extensively than in NC132, but not as pronounced as in NC203 hot-pressed SiC. Thus, it is unclear why NC203 appears to show normal indentation fracture behaviour, with  $P \propto c^{3/2}$ , yet NCX34 behaves anomalously. Possibly the crucial difference is the large amount of  $\text{Y}_2\text{O}_3$ -based grain boundary phase present in NCX34, giving rise to some progressively thermally-activated grain boundary deformation mechanism (e.g. grain boundary sliding). Clearly, further work is required to elucidate this matter.

(iv) Reaction-Bonded  $\text{Si}_3\text{N}_4$  (Ford '2.7')

This RBSN sample formed radial cracks at loads of 500gf and above, no lateral fracture being observable (figs. 46 a,c). Crack paths were generally free from branches, but appeared a little 'meandering', possibly around the  $\sim 1\mu\text{m}$  sized grains. Cracks often passed through, and were deflected by, the substantial (intergranular) porosity in this material (figs. 46 b,d) and were sometimes terminated by pores.

(v) Reaction-Bonded  $\text{Si}_3\text{N}_4$  (Norton NC350)

NC350 RBSN formed radial cracks around 1kgf Vickers indentations (only one indenter load was used for this sample) over the whole temperature range (figs. 46 e,f). The cracks were fairly straight and free from branches, but more extensive than in Ford '2.7' RBSN. Crack-pore interactions were observed to occur as above, and cracking appeared to be in some degree intergranular. At low temperatures, cracks were observed to run along the indentation profile, such that surface material overhung the indentation (figs. 46e and 6f (stereo pair)), as discussed in section 3.6.7.

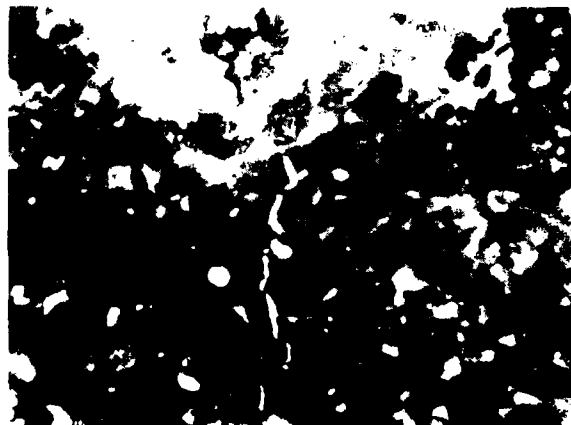
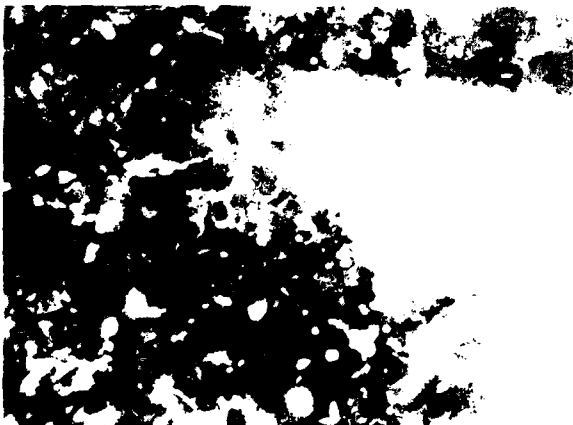
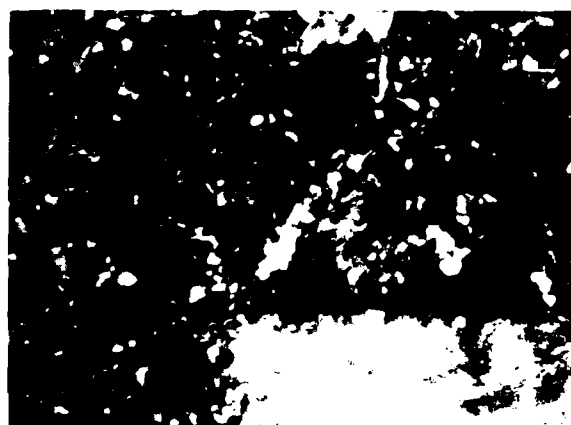
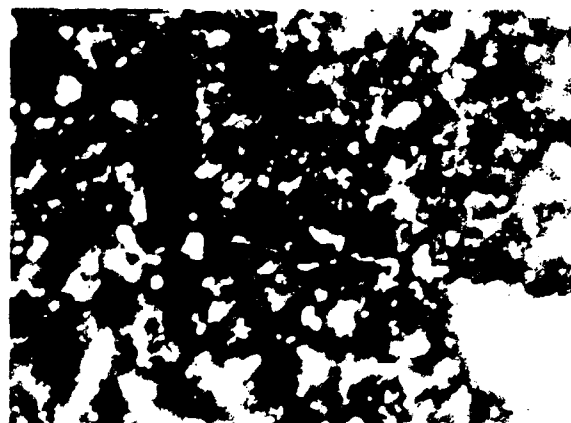
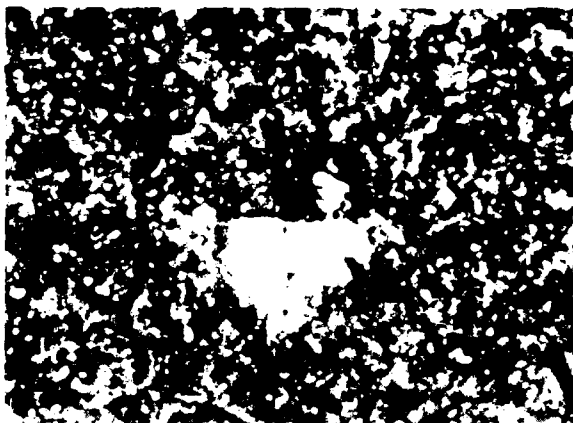


Figure 1. Micrograph showing a bright, irregularly shaped inclusion within a dark, granular matrix. The inclusion is roughly triangular with some internal texture. Below the image is a horizontal scale bar.

Figure 2. Micrograph showing a bright, irregularly shaped inclusion within a dark, granular matrix. The inclusion is roughly triangular with some internal texture. Below the image is a horizontal scale bar.



#### 4.5.4 Fracture of Polycrystalline Sialon

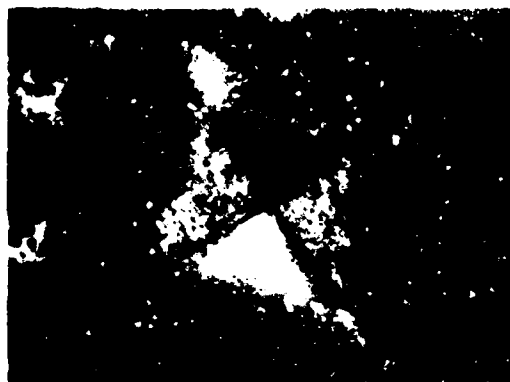
Vickers indentations in Lucas SYALON 342 produced radial cracking (with few laterals) at loads of 500gf and 1kgf. Cracks generally had a meandering appearance, occasionally being subjected to large deflections (fig. 47). Due to the fine scale of the microstructure relative to the width of cracks, it was difficult to ascertain preferred crack paths in this material, although it seemed that fracture was partly intergranular and partly transgranular. Certainly, grain boundary crack networks were not observed in this material (which had  $Y_2O_3$ -based grain boundary phases as observed in NCX 34 HPSN), even at high temperatures (fig. 47b).

#### 4.5.5. Fracture of Polycrystalline Boron Carbide

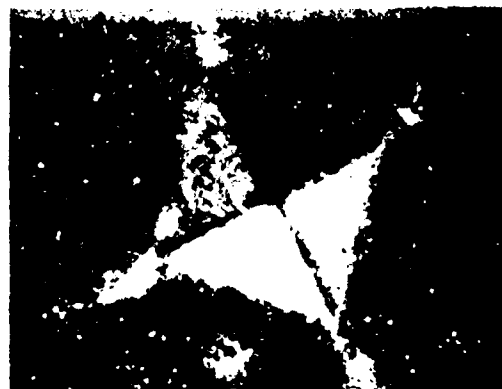
Crack patterns around Vickers indentations (made at  $25^\circ C$  and  $800^\circ C$ ) in two sintered boron carbides, of different densities, are shown in fig. 48. In both forms, fracture was largely radial, crack paths in between the pores being generally irregular with several deflections (up to  $\sim 90^\circ$  in some cases) over their lengths. This suggests that fracture may have occurred preferentially along grain boundaries, although clear contrast between grains was not visible by SEM or optical microscopy in this material. Crack-pore interactions (deflection and termination) were apparent in both specimens, especially in the less dense material (figs. 48c,d - note the inhomogeneity in porosity across the sample), where cracks were often terminated by pores quite close to the indentation. Crack branching was common in the highly porous material (fig. 48c) but seldom observed in the denser form (figs. 48a,b).

#### 4.5.6. Microstructural Control of Fracture Toughness

Firstly, it is apparent that  $K_{IC}$  values measured by indentation techniques (table 18) generally lie within the experimental ranges found by more conventional bulk mechanical testing techniques (table 2), as has been established by other workers (e.g. 21,24,26,27). If anything,  $K_{IC}$  values calculated for some SiC materials (e.g. (0001) single crystal and Carborundum sintered SiC) are lower than those reported in the literature, whilst some of the results for  $Si_3N_4$  materials (e.g. NC350 RBSN) are a little high. It is unclear whether these differences are significant or not, since measurements were



(a) ——— 10 μm



(b) ——— 10 μm

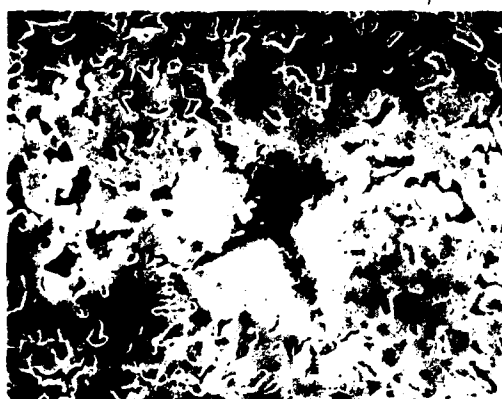
Figure 47 Fracture around 1 kgf Vickers indentations in a sintered sialon ( Lucas SYALON 342 ) as revealed by secondary electron SEM images. (a) Room temperature indentation showing radial fracture which is, on average, straight, but is subject to sub-micron scale deflections. Cracking appears to be partly inter- and partly transgranular. The microstructure is similar to that observed in Norton NCX 34 Y<sub>2</sub>O<sub>3</sub> hot-pressed Si<sub>3</sub>N<sub>4</sub>, but on a finer scale. (b) 800°C indentation showing radial fracture as in (a) with no intergranular crack networks as formed in some of the hot-pressed silicon carbides and nitrides.



(a) ——— 10 μm



(b) ——— 10 μm



(c) ——— 10 μm



(d) ——— 10 μm

Figure 48 Fracture around 1 kgf Vickers indentations in two forms of B<sub>4</sub>C sintered to different densities ( SEM secondary images ). (a) Room temperature indentation in Le Carbone grade S1111 material ( 15 vol% porosity ). Extensive radial fracture is evident, but is subject to several large deflections and occasional termination by pores. (b) as (a), 800°C indentation showing similar fracture behavior to that observed at room temperature. (c) Room temperature indentation in Le Carbone grade S1132 material ( 22.5 vol% porosity, but more evenly distributed ). Radial cracking is highly irregular in form, frequently changing direction or branching and often being terminated by pores close to the indentation. Crack networks have been formed within the indentation pit, as shown in figure 27d. (d) as (c), 800°C indentation in a low porosity region, cracks being less prone to termination by pores. Fracture within the

generally made on only one sample of each material in this investigation, whereas bulk mechanical test data are usually averaged over a number of specimens. Agreement between indentation fracture toughness and conventional  $K_{Ic}$  values is not necessarily expected in any case: indentation cracks grow stably under equilibrium conditions until diminishing stresses cause crack arrest. In bulk mechanical tests, cracks are generally propagated unstably across the test specimen at the fracture stress.

Despite this, certain general trends emerge from table 18 - for instance, hot-pressed materials have relatively high  $K_{Ic}$  values, whilst single crystals and coarse-grained materials have low values, as do porous materials. Microstructural effects on toughness have been reviewed by several authors (e.g. 3-5, 11, 13, 48-50, 55-69), and some relevant points are summarized below.

Crack paths in single crystals and large-grained materials were generally straighter over much of their lengths than in fine-grained materials, where cracks often passed preferentially along grain boundaries, giving rise to a 'meandering' appearance. This latter effect presumably results in more difficult crack propagation, hence higher  $K_{Ic}$ . A corresponding effect is observed in large-scale fracture tests, where the ratio of transgranular to intergranular cleavage (which may be related to grain size in many cases (3)) is important (56). Since preferential fracture along grain boundaries was often observed in the materials investigated here, grain boundary cohesion (which must depend on the amount and composition of boundary phases (e.g. 3, 56, 59)) is thought to be an important parameter. Grain shape effects have also been reported for hot-pressed silicon nitrides (e.g. 60-62), more elongated grains resulting in higher toughness. This may explain the relatively high value of  $K_{Ic}$  for 'Suzuki' sintered SiC compared with the denser Carborundum material.

As mentioned in section 2.3, all the hot-pressed materials examined here contained small W-rich inclusions at the grain boundaries. Such inclusions are thought to be capable of interacting with cracks to produce a toughening effect (e.g. 56, 64-66), although this will generally depend on the nature of the particles (e.g. 56, 65). Direct evidence for such interactions may be seen in the case of NC132 HPSN in figure 44.

Porosity is known to have a marked influence on toughness

(e.g. 70). Detrimental effects include stress concentration (pore size and shape being important), reduction of the effective area of fracture (effectively a decrease in  $\gamma_0$ ) and grain boundary weakening (if the porosity is intergranular) (e.g. 3, 55, 67). Beneficial effects may arise from interactions resulting in crack deflection or crack arrest (e.g. 66-68). Although these latter effects were observed in many materials, the overall effect of porosity appears (table 18) to have been to reduce the toughness, except in the case of the two sintered boron carbides, where crack-pore interactions seem to have resulted in a higher  $K_{IC}$  value for the more porous sample. However, this might not be a real effect since the Lawn/Evans et al. model for calculating  $K_{IC}$  assumes that deformation beneath the indenter occurs entirely by plastic flow. As has been demonstrated in section 3.6.7, compaction effects are probably dominant in porous materials, hence residual stresses are almost certainly less than those assumed by the model. Thus,  $K_{IC}$  has probably been overestimated for porous materials, as is indicated by comparison of  $K_{IC}$  values in tables 2 and 18.

Finally, subcritical crack growth effects, which may dominate the high-temperature fracture behaviour of these materials, depending on grain size, grain boundary phases, etc. (e.g. 58, 69) were not thought to be significant over the temperature range studied here (maximum temperature  $1000^{\circ}\text{C}$ ). Hot-pressed silicon nitrides, for example, are found not to undergo significant subcritical crack growth in conventional mechanical tests below  $\sim 1200^{\circ}\text{C}$  (63).

#### 4.6 SUMMARY

Radial fracture around indentations has been found to become more extensive with increasing temperature, presumably due to an increase in crack-opening residual stress caused by the concomitant increase in  $(E/H)$  ratio. The effect was most marked for  $\{111\}$  single crystal silicon, followed by silicon carbide materials (which often showed an anomalous levelling off in the variation of  $c_r$  with temperature, especially for low indenter loads), then sintered boron carbides and finally silicon nitride and sialon materials, which showed relatively little increase in crack extent with temperature.

$K_{IC}$  values were calculated using recently-developed

indentation fracture mechanics theories, and were found to be independent of temperature for most materials over the temperature range 25-800°C, exceptions being (0001) SiC and sintered boron carbides, for which  $K_{Ic}$  was found to decrease with increasing temperature.  $K_{Ic}$  values were found to compare well with those reported from bulk mechanical tests.

The toughest materials investigated were found to be the hot-pressed samples, despite their high susceptibility to grain boundary fracture. Possible reasons for this are: (i) crack deflection along grain boundaries which may not be planes of maximum tensile stress, (ii) grain shape effects, (iii) interaction with boundary inclusions and (iv) the absence of porosity.

$K_{Ic}$  values were low for single crystals and coarse-grained materials, where crack paths were relatively unaffected by the microstructure, although cracks often propagated along preferred cleavage planes.

Porous materials were generally less tough than dense ones, hence stress concentration or reductions in  $\gamma_o$  or  $\gamma_{gb}$  must outweigh the toughening effects of crack-pore interactions. For these materials, it is believed that  $K_{Ic}$  values calculated from the Lawn/Evans et al. model are overestimates because of compaction effects beneath the indenter.

Certain materials were found not to obey the relation  $P \propto c^{3/2}$ , the crack size exponent being somewhat higher than 3/2 and increasing with increasing temperature. It has been suggested that cracks generated in these materials were not true radial cracks, but were networks of cracks along weak microstructural paths (e.g. grain or phase boundaries).

Finally, lateral fracture was found to be favoured in single crystals and coarse-grained materials. The extent of surface lateral fracture around Vickers indentations in {111} silicon was found to peak at ~200°C, decreasing to zero by ~400°C. This was thought to be due to increases in lateral crack depth with increasing temperature (laterals generally nucleate at the bottom of the plastic zone on the load axis (e.g. 17)), this resulting in less frequent breakout of cracks to the specimen surface.

4.7. REFERENCES

1. A.A. Griffith, 1920, Phil. Trans. Roy. Soc. Lond. A221, 163.
2. A. Kelly, 1966, "Strong Solids", Clarendon Press, Oxford.
3. R.W. Davidge, 1974, in "Fracture Mechanics of Ceramics, Vol.2" eds. R.C. Bradt, D.P.H. Hasselman and F.F. Lange, Plenum Press, p.447.
4. B.R. Lawn and T.R. Wilshaw, 1975, "Fracture of Brittle Solids", Cambridge University Press.
5. R.W. Davidge and A.G. Evans, 1970, Mater. Sci. Engng. 6, 281.
6. C.E. Inglis, 1913, Trans. Inst. Naval Archit. 55, 219.
7. R.G. Hoagland and J.D. Embury, 1980, J. Am. Ceram. Soc. 63, 404.
8. A.G. Evans and K.T. Faber, 1981, *ibid.* 64, 394.
9. W. Kreher and W. Pompe, 1981, J. Mater. Sci. 16, 694.
10. B.R. Lawn, B.J. Hockey and S.M. Wiederhorn, 1980, *ibid.* 15, 1207.
11. R.W. Rice, S.W. Freiman and P.F. Becher, 1981, J. Am. Ceram. Soc. 64, 345.
12. R.W. Rice and J.J. Mecholsky Jr., 1979, U.S. Naval Research Laboratory Report 4077, September 25, 1979.
13. R.W. Davidge, 1981, Acta Metall. 29, 1695.
14. W. Weibull, 1939, Ingeriörsvetenskapsakad Handl. 151, 45.
15. A. De S. Jayatilaka and K. Trustrum, 1977, J. Mater. Sci. 12, 1426.
16. D.G. Rickerby, 1980, *ibid.* 15, 2466.
17. B.R. Lawn and M.V. Swain, 1975, *ibid.* 10, 113.
18. B.R. Lawn and R. Wilshaw, 1975, *ibid.* 10, 1049.
19. B.R. Lawn and E.R. Fuller, 1975, *ibid.* 10, 2016.
20. A.G. Evans and T.R. Wilshaw, 1976, Acta. Metall. 24, 939.
21. A.G. Evans and E.A. Charles, 1976, J. Am. Ceram. Soc. 59, 371.
22. B.R. Lawn and D.B. Marshall, 1979, *ibid.* 62, 347.
23. D.B. Marshall and B.R. Lawn, 1979, J. Mater. Sci. 14, 2001.
24. A.G. Evans, 1979, ASTM Special Technical Publication No. 678, Philadelphia, p.112.
25. B.R. Lawn, A.G. Evans and D.B. Marshall, 1980, J. Am. Ceram. Soc. 63, 574.

26. G.R. Anstis, P. Chantikul, B.R. Lawn and D.B. Marshall, 1981, *ibid.* 64, 533.
27. D.B. Marshall and A.G. Evans, 1981, *ibid.* 64, C-182.
28. J. Lankford, 1981, *J. Mater. Sci.* 16, 1177.
29. J.T. Hagan, 1979, *ibid.* 14, 462.
30. A. Arora, D.B. Marshall, B.R. Lawn and M.V. Swain, 1979, *J. Non-Crystalline Solids* 31, 415.
31. C.M. Perrott, 1977, *Wear* 45, 293.
32. J. Lankford and D.L. Davidson, 1979, *J. Mater. Sci.* 14, 1669.
33. S. Palmqvist, 1962, *Arch. Eisenhüttenwes.* 33, 629.
34. W. Dawihl and G. Altmeyer, 1964, *Z. Metallk.* 55, 231.
35. C.T. Peters, 1979, *J. Mater. Sci.* 14, 1619.
36. F.C. Roesler, 1956, *Proc. Phys. Soc.* B69, 981.
37. E.H. Yoffe, 1981, private communication.
38. T.F. Page, G.R. Sawyer, O.O. Adewoye and J.J. Wert, 1978, *Proc. Brit. Ceram. Soc.* 26, 193.
39. K. Niihara, R. Morena and D.P.H. Hasselman, 1982, *J. Mater. Sci. Letters* 1, 13.
40. V.I. Trefilov, V.A. Borisenko, G.G. Gnesin, I.V. Gridneva, Yu. V. Milman and S.I. Chugunova, 1978, *Sov. Phys. Dokl.* 23, 207.
41. T. Hirai and K. Niihara, 1979, *J. Mater. Sci.* 14, 2253.
42. J.D.B. Veldkamp and N. Hatttu, 1981, *ibid.* 16, 1273.
43. A.G. Atkins and D. Tabor, 1966, *Proc. Roy. Soc. Lond.* A292, 441.
44. A.G. Atkins, 1971, in "The Science of Hardness and its Research Applications", eds. J.H. Westbrook and H. Conrad, American Society for Metals, Metals Park, Ohio. p.223.
45. L.M. Fitzgerald, 1963, *J. Less-Common Metals* 5, 356.
46. D.A. Shockey, D.C. Erlich and K.C. Dao, 1981, *J. Mater. Sci.* 16, 477.
47. T. Inoue and H.J. Matzke, 1981, *J. Am. Ceram. Soc.* 64, 355.
48. J.L. Henshall, 1975, Ph.D. Thesis, University of Cambridge.
49. J.W. Edington, D.J. Rowcliffe and J.L. Henshall, 1975, *Powder Met. Int.* 7, 136.
50. G.W. Hollenberg and G. Walther, 1980, *J. Am. Ceram. Soc.* 63, 610.

51. K.E. Puttick and M.M. Hosseini, 1980, J. Phys. D. 13, 875.
52. B.R. Lawn, 1968, J. Appl. Phys. 39, 4828.
53. B.R. Lawn, B.J. Hockey and S.M. Wiederhorn, 1980, J. Mater. Sci. 15, 1207.
54. O.O. Adewoye, 1976, Ph.D. Thesis, University of Cambridge.
55. R.W. Rice, 1977, Treatise on Materials Science and Technology 11, ed. R.K. MacCrone, Academic Press, p.199.
56. J.D.B. Veldkamp and N. Hattu, 1979, Philips Journal of Research 34, 1.
57. F.P. Knudsen, 1959, J. Am. Ceram. Soc. 42, 376.
58. B.J. Dalgleish, A. Fakhr, P.L. Pratt and R.D. Rawlings, 1979, J. Mater. Sci. 14, 2605.
59. G. De With and N. Hattu, 1981, *ibid.* 16, 841.
60. F.F. Lange, 1973, J. Am. Ceram. Soc. 56, 518.
61. *Idem.*, 1979, *ibid.* 62, 428.
62. G. Himsolt, H. Knoch, H. Huebner and F.W. Kleinlein, 1979, *ibid.* 62, 29.
63. R.K. Govila, K.R. Kinsman and P. Beardmore, 1979, J. Mater. Sci. 14, 1095.
64. R.L. Tsai and R. Raj, 1980, J. Am. Ceram. Soc. 63, 513.
65. C. Greskovich and J.A. Palm, 1980, *ibid.* 63, 597.
66. C.T. Forwood and A.J. Forty, 1965, Phil. Mag. 11, 1067.
67. J.B. Kessler, J.E. Ritter Jr. and R.W. Rice, 1974, Mater. Sci. Res. 7, 529.
68. D.R. Biswas, 1981, J. Mater. Sci. 16, 2434.
69. J.B. Wachtman Jr., 1974, J. Am. Ceram. Soc. 57, 509.
70. J.C. Knight, T.F. Page and J.E. Weston, 1982, Proc. Brit. Ceram. Soc. 32, "Engineering with Ceramics", Proceedings B.C.S. Conference, London, Dec. 15-17, 1981.

## CHAPTER 5

### CRACK INITIATION

#### 5.1 INTRODUCTION

In the previous Chapter, the extent of fracture around indentations was related to the resistance of the test material to crack propagation, or toughness (quantified in terms of  $K_{IC}$ ). In this Chapter, we consider the number of cracks formed around indentations. For conical or spherical indenters, this is related to the ease of crack nucleation and increases with increasing indenter load (1,2), no cracks being formed below a threshold value of load  $P^*$  (e.g. 1,3). However, fracture around Vickers indentations seems often to be constrained to emanate from the four indentation corners, hence four radials or two orthogonal median/radial systems are generally formed (except where microstructural effects dominate: section 4.5). Thus, for the study of crack initiation, Vickers indenters are useful only in determining whether cracks are nucleated or not, in terms of the threshold load  $P^*$ . This is examined here as a function of temperature and specimen microstructure.

#### 5.2. CRACK NUCLEATION THEORIES

The transition from plasticity-dominated behaviour (at low indenter loads) to fracture-dominated (high-load) behaviour was first quantified by Lawn et al. (4). Taking the crack propagation relation  $K_{IC} \propto P c^{-3/2}$  and the hardness relation  $H \propto P a^{-2}$ , indentation and radial crack dimensions were plotted as a function of applied load, the two curves crossing at a critical applied load  $P^*$ , for which  $c = c^* = a^*$ . From the above relations, it is easy to see that

$$P^* \propto (K_{IC}^4 / H^3)$$

$$\text{and } c^* \propto (K_{IC} / H)^2$$

Crack initiation in elastic/plastic indentation fields was first treated theoretically by Lawn and Evans (5), using a simple approximation for the tensile stress distribution beneath an indenter, in which the maximum tensile stress on the load axis was taken to occur at the elastic/plastic boundary and to be proportional to the hardness. The stress was further assumed to decrease linearly to zero over a distance proportional to the indentation radius  $a$ . The

interaction of this stress with pre-existing flaws within the test specimen was then considered. Assuming a sufficiently high density of flaws, such that the elastic/plastic boundary always has available flaws which may or may not develop into well-defined median cracks, two initiation criteria were obtained. Firstly, the applied load should exceed a threshold value:

$P^* = \lambda_0 (K_{IC}^4/H^3)$ ;  $\lambda_0$  calculated to be  $\sim 2.2 \times 10^4$  for Vickers indentations.

Below this value, the spatial extent of the tensile stress is always too small for extension of flaws.

Secondly, the initial flaw size required for formation of a median crack should exceed a threshold value:

$c^* = \mu_0 (K_{IC}/H)^2$ ;  $\mu_0$  calculated to be  $\sim 44$  for Vickers indentations.

Flaws smaller than this cannot extend spontaneously because the stress levels ( $\propto H$ ) are too low.

It is emphasized that this model considers the development of median cracks from pre-existing near-surface defects (see section 4.1) rather than true median crack nucleation. Where the density of large ( $>c^*$ ) flaws is low, the model requires that the applied load be increased so that the expanding tensile front may sample deeper-lying flaws in order to form a median crack. Effectively, this means an increase in  $P^*$  above that predicted theoretically.

The coefficients  $\lambda_0$  and  $\mu_0$  were later modified by Lawn and Marshall (6) using a 'universal deformation/fracture plot' approach for a wide range of materials. As in the earlier study of Lawn et al. (4), a graph of indentation and crack sizes against applied load was plotted on a log-log scale, this time dividing by the normalizing parameters  $(K_{IC}/H)^2$  (for  $a$  and  $c$ ) and  $(K_{IC}^4/H^3)$  (for  $P$ ):

$$(a/c^*) = (P/P^*)^{1/2}; \quad (c/c^*) = (P/P^*)^{2/3}, \text{ for all materials.}$$

A further modification was the incorporation of the variation of  $c$  with applied load predicted by Lawn and Evans (5) for loads close to  $P^*$ . In this way,  $\lambda_0 \sim 1.6 \times 10^4$  and  $\mu_0 \sim 120$  were found experimentally for Vickers indentations, although the theory was considered to be too inexact to enable absolute results to be derived to within approximately an order of magnitude. However, Lankford and Davidson (7) used high-resolution SEM and acoustic emission techniques

to establish that theoretical values of  $P^*$  and  $c^*$  were close to those observed experimentally.

More recently, Hagan (8) has shown that pre-existing flaws are not necessary for crack formation because suitably-sized flaws may be nucleated by the deformation processes occurring during indentation (thus removing the  $c^*$  criterion for nucleation). Hagan's analysis was based on crack nucleation by interaction of dislocations on two intersecting slip planes or by one slip plane blocking another (e.g. 9-11). A critical load for crack nucleation was derived which followed the form of the earlier result, with only a difference in the coefficient  $\lambda_0$  (4885 in this case). Crack nucleation was thus considered to be governed by shear deformation rather than tensile stresses as above. Dislocation-induced fracture is thought to occur in nucleation of  $\{1\bar{1}0\}$  cracks in near  $\{111\}$  silicon (12), and has been considered in general terms by various authors (e.g. 9-11, 13,14).

A similar mechanism was also postulated for soda-lime glass, in which cracks are observed to nucleate at the intersections of inhomogeneous shear bands within the deformed regions beneath Vickers indentations (3,8,15). Such flow lines have also been observed in ZnS, where cavities produced as a result of grain boundary sliding may also act as crack nuclei (16).

In polycrystalline materials, fracture may also be initiated by dislocation pile-up at grain boundaries, as has been demonstrated for MgO bicrystals (17-19). In such cases, a Hall-Petch relationship may apply:

$$\sigma_F = \sigma_0 + KD^{-1/2}$$

where  $\sigma_F$  = stress to form a crack,  $\sigma_0$  = stress required for dislocation multiplication (rather than the lattice friction stress (18)),  $K$  = a measure of the effective surface energy for localized crack initiation (proportional to  $(E\gamma_{gb})^{1/2}$  for intergranular crack initiation (14)) and  $D$  = glide band length (assuming  $D \propto$  the number of dislocations in the glide band), often approximated by the grain size  $g$ . This relation assumes that large dislocation pile-ups are possible, which may not be the case for the highly brittle materials studied here (see section 3.6.5), or for materials with high stacking fault energy.

A precisely analogous relation is obtained if crack nucleation occurs by twin interactions (14). Twinning is favoured at large grain sizes in materials with low stacking fault energy (14). Lateral cracking in  $\text{Al}_2\text{O}_3$  is thought to be nucleated by twinning (15).

### 5.3. TEMPERATURE EFFECTS

Crack nucleation was generally observed to become more difficult at high temperatures. For example, NC132 HPSN formed few, if any, radial cracks below 500gf ( $\sim 5\text{N}$ ) load at temperatures up to  $200^\circ\text{C}$ , above which no radial cracks formed below 1kgf ( $\sim 10\text{N}$ ) load. {111} single crystal silicon was observed to have  $P^*$  values in the range 1-2N at  $500^\circ\text{C}$ , 2-5N at  $600^\circ\text{C}$ , 5-10N at  $700^\circ\text{C}$  and  $>10\text{N}$  at  $800^\circ\text{C}$ . A decrease in the number of cracks formed around indentations was clearly visible with increasing temperature for this material (fig. 37), although those cracks which did form at high temperatures were more extensive than those formed at low temperature (section 4.4.1).

A value of  $\lambda_0 = 2 \times 10^4$  was found to give the best consistency between calculated and observed values of  $P^*$  (c.f.  $\lambda_0 = 1.6 \times 10^4$  (6)), the agreement being at least order of magnitude and often much better. This is reasonable, considering that typical errors in estimating  $P^*$  were calculated to be of the order of 30% due to the dependence on high powers of  $K_{\text{IC}}$  and  $H$  (5% error in  $H$  and  $K_{\text{IC}}$  would result in a possible 35% error in  $P^*$ ).

Despite the inaccuracy of absolute values, a clear idea of both the temperature and microstructural variations of  $P^*$  may be obtained from figs. 49-52, which show calculated values of  $P^*$  as a function of temperature for Si, SiC,  $\text{Si}_3\text{N}_4/\text{sialon}$  and  $\text{B}_4\text{C}$  materials respectively. A semi-logarithmic scale has been used for these plots since  $P^*$  varied by several orders of magnitude for different materials/temperatures.

The {111} silicon crystal showed the most dramatic increase in  $P^*$  with temperature (fig. 49): by 3 orders of magnitude over the temperature range  $25-700^\circ\text{C}$  ( $P^*$  being of the order of 1gf at  $25^\circ\text{C}$ !). The slope of the curve increased sharply at  $\sim 500^\circ\text{C}$ , reflecting the increase in slope of the hardness/temperature plot at approximately this point (fig. 10),  $K_{\text{IC}}$  remaining constant over the whole temperature range. The observed increase in  $P^*$  with temperature

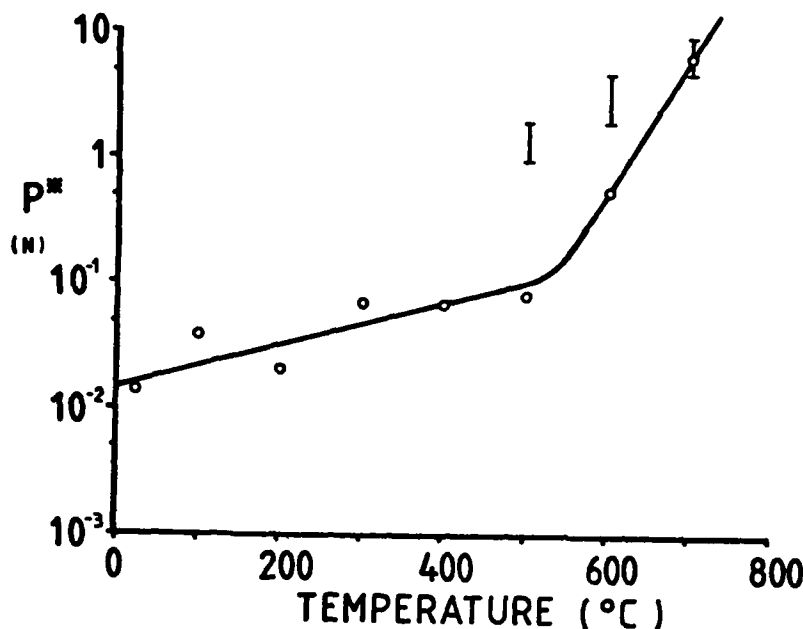


Figure 49. The temperature sensitivity of  $P^*$ , the critical load required for radial crack nucleation: {111} single crystal silicon. Estimated errors typically  $\pm 30\%$ . Observed values of  $P^*$  were within the ranges indicated by the bars at 500, 600 and 700°C.

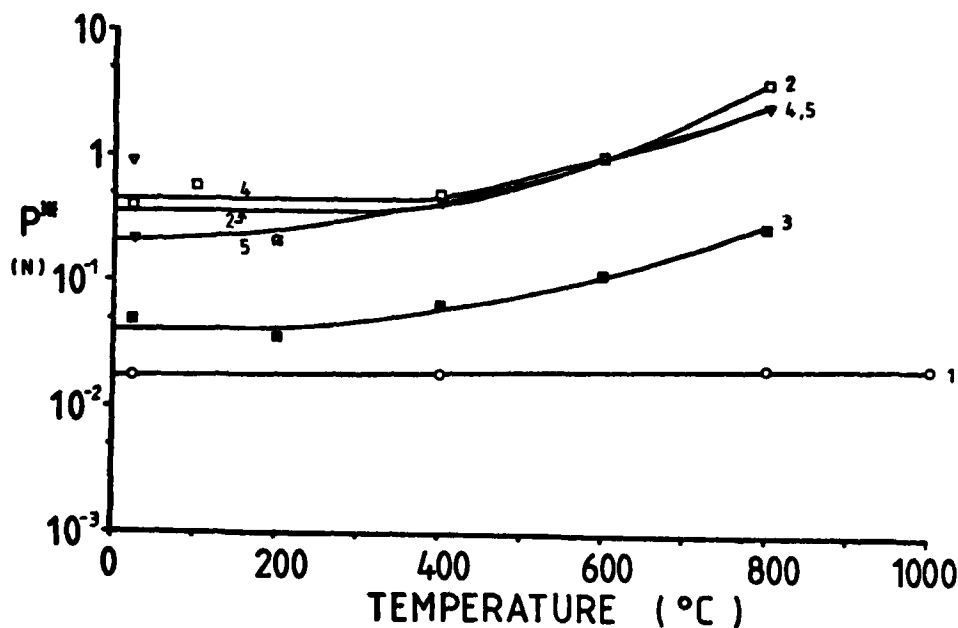


Figure 50. The temperature sensitivity of  $P^*$ , the critical load required for radial crack nucleation: SiC materials. Curve 1 = blue-black (0001) single crystal SiC (open circles), curve 2 = Norton NC203 hot-pressed SiC (open squares), curve 3 = Carborundum sintered SiC (filled squares), curve 4 = 'Suzuki' sintered SiC (open triangles), curve 5 = 'REFEL' reaction-bonded SiC (grain size 10  $\mu\text{m}$ ) (filled triangles). Estimated errors typically  $\pm 30\%$ .

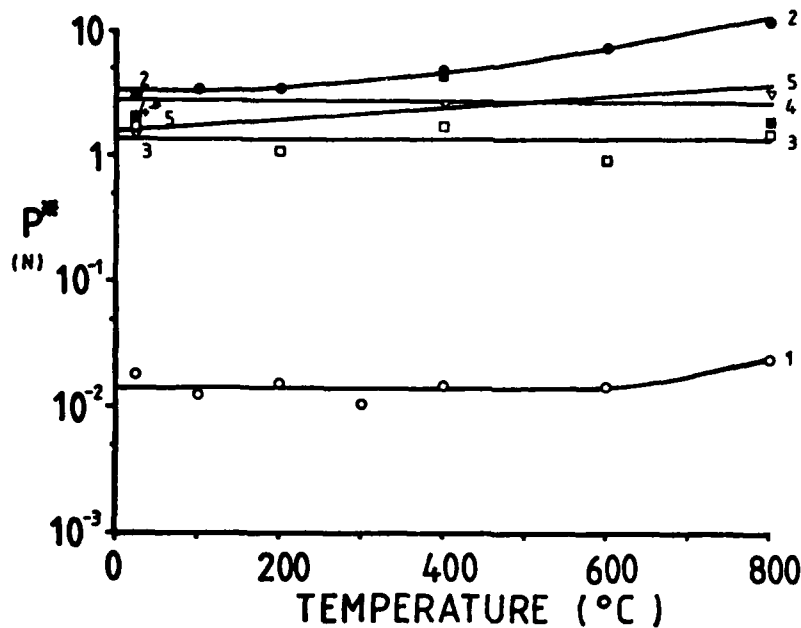


Figure 51. The temperature sensitivity of  $P^*$ , the critical load required for radial crack nucleation:  $\text{Si}_3\text{N}_4$  and sialon materials. Curve 1 = pyrolytically-deposited  $\text{Si}_3\text{N}_4$  ( open circles ), curve 2 = Norton NC132 hot-pressed  $\text{Si}_3\text{N}_4$  ( filled circles ), curve 3 = Ford '2.7' RBSN ( open squares ), curve 4 = Norton NC350 RBSN ( filled squares ), curve 5 = Lucas sintered SYALON 342 ( open triangles ). Estimated errors typically  $\pm 30\%$ .

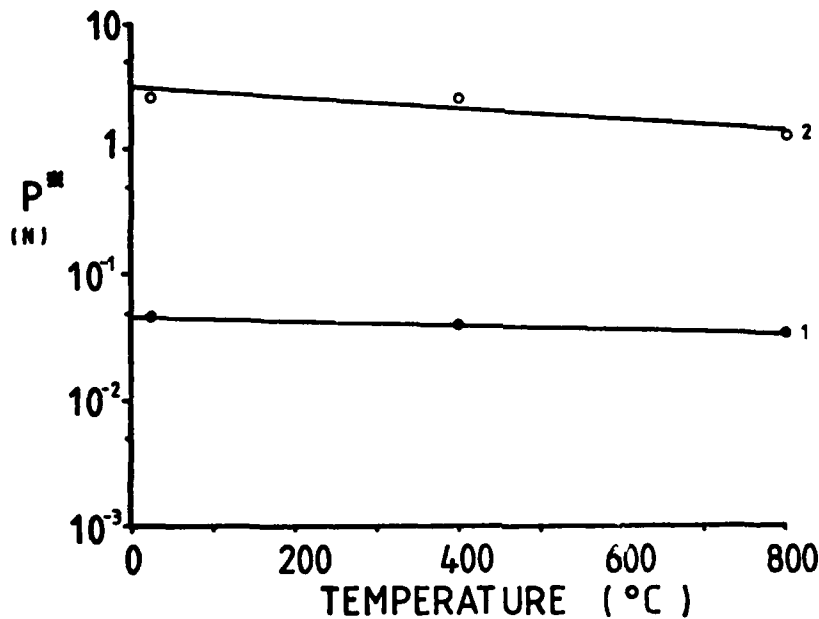


Figure 52. The temperature sensitivity of  $P^*$ , the critical load required for radial crack nucleation:  $\text{B}_4\text{C}$  materials. Curve 1 = Le Carbone sintered  $\text{B}_4\text{C}$  grade S1143 ( density  $2.4 \text{ gcm}^{-3}$  ) ( filled circles ), curve 2 = Le Carbone sintered  $\text{B}_4\text{C}$  grade S1138 ( density  $2.05 \text{ gcm}^{-3}$  ) ( open circles ). Estimated errors typically  $\pm 30\%$ .

(described above) seems to be less rapid than that predicted theoretically.

SiC materials generally showed no change in  $P^*$  with temperature up to  $\sim 300-400^\circ\text{C}$ , followed by a modest ( $\times 2-3$ ) increase between  $400^\circ\text{C}$  and  $800^\circ\text{C}$  (fig. 50). (0001) single crystal SiC showed no change in  $P^*$  at all, since the decrease in hardness was compensated by a decrease in  $K_{\text{IC}}$  for this material (perhaps fortuitously).

$\text{Si}_3\text{N}_4$  and sialon materials showed comparatively little increase in  $P^*$  with increasing temperature (fig. 51), due to their lower temperature sensitivity of hardness (especially marked for RBSN materials).

Sintered boron carbide materials showed a slight decrease in  $P^*$  with increasing temperature, the decrease in  $K_{\text{IC}}^4$  outweighing the decrease in  $H^3$ .

In all cases, microstructural factors are discussed in the following section.

Changes in  $P^*$  with temperature may be explained in terms of each of the crack nucleation theories discussed in section 5.2. If fracture initiates at pre-existing flaws, the effect of increasing temperature will be to decrease the magnitude of sub-indentation tensile stresses ( $\propto H$ ) but to increase their extent ( $\propto a$ ), the former effect predominating, such that  $P^*$  generally increases (except where  $K_{\text{IC}}$  decreases) with increasing temperature. The temperature sensitivity of crack initiation by dislocation pile-up is more difficult to predict theoretically. The parameters  $\sigma_0$  and  $K$  in the Hall-Petch relation (section 5.2) will generally decrease with increasing temperature, but the stress concentration at the tips of glide bands will also decrease due to increasing glide band width and lower dislocation density within the glide bands (e.g. 14), and also because of dislocation climb effects above the critical temperature  $T_c$  (Chapter 3). If these latter effects predominate, the stress required to form a crack at the tip of a glide band ( $\sigma_F$ ) will increase with increasing temperature, rendering crack nucleation more difficult, as observed. Finally, grain boundary sliding effects would tend to facilitate crack initiation by triple point cavitation at high temperatures, but this was not thought to occur in the temperature range used here (see sections 3.6.6. and 4.4.3).

Although the  $c^*$  criterion for crack nucleation may be relaxed by the possibility of nucleating suitably sized flaws by plasticity mechanisms, it is instructive to consider the approximate values required (table 19). (The magnitudes of  $c^*$  in relation to the scale of the microstructures are discussed in the following section).  $c^*$  generally increases with increasing temperature (except for sintered  $B_4C$ ), by a factor of 6 at most (often much less) between 25 and  $800^\circ C$ . It is anticipated that, in the limit of very high temperatures, where a material is fully plastic,  $P^*$  and  $c^*$  values would both be very high indeed.

#### 5.4 MICROSTRUCTURAL EFFECTS

From figs. 49-52, the most obvious microstructural effect on  $P^*$  was that of grain size, coarse-grained and single crystal materials showing relatively easy crack nucleation due to their high hardness (section 3.6.5) and low toughness (section 4.5.6). Thus, Carborundum sintered and (0001) single crystal SiC (fig.50) and PDSN (fig.51) all had lower values of  $P^*$  (by 1-2 orders of magnitude) than other SiC and  $Si_3N_4$  materials. For polycrystalline materials, this is consistent with both the pre-existing flaw model (where microstructural flaws of the order of the grain size are expected (e.g. 14)) and the plasticity-induced flaw mechanism (setting  $D$  equal to the grain size in the Hall-Petch relation, i.e. assuming that large dislocation pile-ups are possible).

Porosity in SiC and  $Si_3N_4$  materials appears to decrease both  $H$  and  $K_{IC}$ , leaving  $P^*$  unchanged relative to dense hot-pressed materials (figs. 50,51). For the two sintered boron carbides, however, the effect of porosity was to decrease  $H$  but increase  $K_{IC}$ , resulting in a higher value of  $P^*$  for the less dense material (fig.52). As discussed in section 4.5.6,  $K_{IC}$  values may have been overestimated for porous materials due to compaction effects, in which case  $P^*$  values would have been significantly lower than shown in figs.50-52.

The values of  $c^*$  quoted in table 19 are interesting because they are less than the grain size for all materials (except the two forms of RBSN) at room temperature and for many materials (except for NC203 and REFEL silicon carbides, NC132 HPSN, both forms of RBSN and the sialon) at  $800^\circ C$ . This suggests that crack nucleation

Material	c* ( $\mu\text{m}$ )	
	25°C	800°C
<u>SILICON</u>		
{111} single crystal	1.0	5.8 (700°C)
<u>SILICON CARBIDE</u>		
(0001) single crystal (blue-black)	0.6	1.0
Hot-pressed (Norton NC203)	3.0	15.7
Sintered (Carborundum)	1.1	4.1
(Suzuki)	5.1	13.3
Reaction-Bonded (REFEL-a)	2.7	17.2
(REFEL-a)	4.5	-
(REFEL-b)	4.5	-
<u>SILICON NITRIDE</u>		
Pyrolytically-Deposited (AMTE)	0.6	0.9
Hot-Pressed (Norton NC132)	10.1	25.3
Reaction-Bonded (Ford '2.7')	9.0	9.2
(Norton NC350)	12.1	13.9
<u>SIALON</u>		
Sintered (Lucas SYALON 342)	8.1	14.3
<u>BORON CARBIDE</u>		
Sintered (Le Carbone $\rho = 2.4$ )	1.0	1.0
$\rho = 2.05$ )	11.7	9.1

Table 19. The critical flaw sizes (c\*) required for median crack nucleation in a variety of Si, SiC, Si<sub>3</sub>N<sub>4</sub>, sialon and B<sub>4</sub>C materials at 25°C and 800°C. Values were calculated from the relation  $c^* = 120 (K_{Ic}/H)^2$  (see text).

Typical errors estimated to be  $\pm 15\%$ .

in the majority of polycrystalline materials was almost certainly from pre-existing microstructural flaws, without the need for initiation by plasticity mechanisms. This is especially likely given that microstructural features such as grain boundaries provide preferred fracture paths in all of these materials (section 4.5). Provided  $c^*$  is always less than the grain size, any increase in the difficulty of nucleating cracks with increasing temperature must be due to an increase in  $P^*$  rather than in  $c^*$ . This was perhaps also true for single crystals, where it is speculated that crack initiation by slip interpenetration may well have predominated (especially at high temperatures), thus removing the necessity for pre-existing flaws of size greater than or equal to  $c^*$ . However, for those polycrystalline materials (e.g. NC132 HPSN) in which  $c^*$  became much larger than the grain size at high temperatures, crack initiation might have become more difficult because of the scarcity of suitably-sized pre-existing flaws, since dislocation pile-up at grain boundaries is unlikely to produce cracks larger than the grain size (unless crack linkage occurs).

Despite the above generalizations, a full understanding of the role of crack nucleation in indentation fracture must await detailed characterization of the micro-mechanics of crack genesis in a variety of materials.

## 5.5 CONCLUSIONS

The effects of temperature and microstructure on crack nucleation processes are often difficult to predict but, using the parameter  $P^* = \lambda_o (K_{IC}^4/H^3)$ , may easily be compared. Thus,  $P^*$  was generally observed to increase with increasing temperature due to the decrease in  $H$  (except where  $K_{IC}$  also decreased), predicting more difficult crack nucleation at high temperatures, as observed directly in some cases. This was especially marked for {111} single crystal silicon, for which  $P^*$  increased by 3 orders of magnitude over the temperature range 25-700°C. Rather more modest increases ( $\times 2-3$ ) were found for SiC materials,  $Si_3N_4$  and sialon materials showing comparatively little change in  $P^*$ , with sintered boron carbides showing a slight decrease in  $P^*$  with increasing temperature.

Single crystals and coarse-grained materials were found to

show easy crack nucleation (low  $P^*$ ) compared to finer grained materials such as the hot-pressed samples, which were therefore superior to other microstructural forms in their resistance to both crack nucleation and propagation. The effects of porosity on crack nucleation beneath indentations are as yet unclear.

The form of the above expression for  $P^*$  is believed to be generally valid (it may be derived dimensionally), but the coefficient of proportionality ( $\lambda_0$ ) perhaps depends on the process responsible for crack nucleation (e.g. sampling of pre-existing flaws, slip band interpenetration, blocking of glide bands by grain boundaries, grain boundary separation, etc.). Thus, a better approach\* might be to measure  $P^*$  directly and derive  $\lambda_0$  values for a range of materials/temperatures in order to assess which mechanisms operate. In this investigation, a value of  $\lambda_0 \sim 2 \times 10^4$  was found to give reasonable agreement with the limited number of  $P^*$  values observed directly.

It is believed that for many of the polycrystalline materials investigated here, cracks originated from microstructural flaws (e.g. weak grain boundaries) without the need for nucleation by plasticity mechanisms, since the critical flaw size  $c^*$  required for median crack formation was generally less than the grain size. For some (single crystal and polycrystalline) materials, this might not have been the case, especially at high temperatures, and further study is required to establish the nucleation mechanisms operating here.

---

\* This approach has been followed in a recent paper by Chiang et al. (21). The parameter  $\Omega^* = P^* H^3 / K_{IC}^4$  was calculated (and found experimentally) to decrease with increasing plastic zone size: indentation size ratio ( $b/a$ ). Flaw nuclei initiated by slip interpenetration were calculated to show an initial stable growth region for increasing indenter load prior to unstable growth at some critical value of ( $c/b$ ) to form well-developed cracks. Radial cracks were thought likely to initiate from pre-existing flaws, whilst median and lateral cracks were considered to nucleate by slip interpenetration. Thus, radial, median and lateral cracks should have different values of  $P^*$ , with  $P^*_r < P^*_m < P^*_l$ . The implications of this study to the present work will require further analysis.

5.6. REFERENCES

1. A.G. Evans and T.R. Wilshaw, 1976, Acta. Metall. 24, 939.
2. M.M. Chaudhri, 1981, private communication.
3. J.T. Hagan and M.V. Swain, 1978, J. Phys. D. 11, 2091.
4. B.R. Lawn, T. Jensen and A. Arora, 1976, J. Mater. Sci. 11, 573.
5. B.R. Lawn and A.G. Evans, 1977, ibid. 12, 2195.
6. B.R. Lawn and D.B. Marshall, 1979, J. Am. Ceram. Soc. 62, 347.
7. J. Lankford and D.L. Davidson, 1979, J. Mater. Sci. 14, 1662.
8. J.T. Hagan, 1979, ibid. 14, 2975.
9. C. Zener, 1948, Trans. ASM 40, 2.
10. A.N. Stroh, 1957, Adv. Phys. 6, 192.
11. A.H. Cottrell, 1958, Trans. Met. Soc. AIME 212, 192.
12. K.E. Puttick and M.M. Hosseini, 1980, J. Phys. D. 13, 875.
13. B.R. Lawn and T.R. Wilshaw, 1975, "Fracture of Brittle Solids", Cambridge University Press.
14. R.W. Davidge and A.G. Evans, 1970, Mater. Sci. Engng. 6, 281.
15. J.T. Hagan, 1980, J. Mater. Sci. 15, 1417.
16. S. Van der Zwaag, J.T. Hagan and J.E. Field, 1980, ibid. 15, 2965.
17. A.R.C. Westwood, 1961, Phil. Mag. 6, 195.
18. R.C. Ku and T.L. Johnston, 1964, ibid. 9, 231.
19. J. Moriyoshi, W.D. Kingery and J.B. Van der Sande, 1977, J. Mater. Sci. 12, 1062.
20. J. Lankford, 1978, in "Fracture Mechanics of Ceramics" Vol.3, eds. R.C. Bradt, D.P.H. Hasselman and F.F. Lange, Plenum Press, p.245.
21. S.S. Chiang, D.B. Marshall and A.G. Evans, 1982, J. Appl. Phys. 53, 312.

## CHAPTER 6

### FRICTION AND WEAR

#### 6.1 INTRODUCTION

Many of the surface and near-surface plasticity and fracture processes which occur in friction and wear situations involving surface contact by hard, sharp asperities or particles may be studied in a more controlled manner using indentation tests. It is therefore the aim of this chapter to try to indicate how the results of the present investigation might be relevant in predicting friction and wear behaviour of ceramic materials and, in particular, its dependence on temperature and specimen microstructure. ( N.B. this chapter contains no additional experimental data. )

Firstly, a brief review of friction and wear processes is presented in order to provide some background to this discussion. For more detailed discussion, the reader is referred to reviews by a number of authors ( e.g. 1 - 9 ).

#### 6.2 FRICTION

The frictional force  $F$  between two contacting bodies when subjected to an external force tending to cause relative motion is related to the load  $P$  normal to their interface according to the classical relation  $F = \mu P$ , where  $\mu$  is the coefficient of sliding friction.  $F$  is found to be independent of the apparent area of contact ( $A'$ ) and is only a weak function of sliding speed. Two major approaches have been used to model friction: interlocking of surface asperities and interatomic adhesion between surfaces ( e.g. 1 - 4 ). In the Bowden and Tabor model ( 1,2 ), surface asperities adhere to form junctions and  $F$  is directly related to the stress ( $\tau_j$ ) needed to shear these junctions. The normal load  $L$  is supported by the actual contact area  $A$  of elastically and plastically deformed asperities.

Then:  $F = A\tau_j = L\tau_j/p_o$       thus  $\mu_a = (\tau_j/p_o)$

where  $p_o$  is the yield pressure ( related to the hardness ) of the softest of the two contacting materials. However, there are difficulties in interpreting the above relation, in that  $\tau_j$  may be taken as the shear strength of the interface or of the weaker material or of the

deformed material near to the interface. Also, the actual contact area during sliding is found to be larger than the contact area predicted by assuming  $p_0 = H$  ( e.g. 3 ), i.e. the model predicts values of  $\mu$  (  $\sim 0.2 - 0.3$  ) which are too low. This is especially so for contact between clean surfaces of similar metals, where values of  $\mu \approx 100$  are possible ( e.g. 11 ). Thus, Rabinowicz ( 3 ) considered the effects of surface energy, deriving a relation

$$\mu = \frac{\tau_j}{H} \left[ \frac{1}{1 - (2W_{ab} \cot \theta) / rH} \right]$$

where  $\theta$  is the average surface roughness angle,  $r$  is the average junction radius and  $W_{ab}$  is the surface energy of adhesion for the contacting materials:  $W_{ab} = ( \gamma_a + \gamma_b - \gamma_{ab} )$ , where  $\gamma_a$  = surface energy of material a, etc. Thus,  $\mu$  is high for small  $\theta$  and for large  $( W_{ab} / H )$ .

Ploughing of the surface(s) by hard asperities may contribute to the friction. Usually, this is incorporated with the adhesive component by writing  $\mu = \mu_a + \mu_p$  ( 3, 10 ). In reality, the two effects must interact, but there is as yet no good model for this. The form of the expression for  $\mu_p$  has been considered by Bowden and Tabor ( 10 ), who derived the relation  $\mu_p \propto \cot \theta$ , where  $\theta$  is the semi-apical angle of the ( assumed ) conical asperities. For smooth sliding, the adhesive component of friction may dominate, whilst for abrasive processes, ploughing effects are more important ( section 6.3.2 ).

More recently, Challen and Oxley ( 11 ) have proposed a friction model based on slip line field analyses of hard asperities contacting and deforming softer ones. The model predicted  $\mu$  as a function of asperity contact angle (  $\alpha$  ) ( i.e. surface roughness ) and the ratio (  $f$  ) of the interfacial shear stress to the shear flow stress of the softer material. Three regimes of friction and wear were considered: (a) asperity rubbing with no wear loss, (b) asperity fracture by shearing off the plastically deformed regions from the softer asperities and, above a critical value of  $\alpha$ , (c) wear by asperity cutting ( see section 6.3.2 ).  $\mu$  was predicted to increase with increasing  $\alpha$  in all three regimes and to increase with increasing  $f$  in regions (a) and (b) but to decrease with increasing  $f$  in region (c) ( as observed ). N.B. even in the absence of adhesion ( i.e.  $f = 0$  ), friction could still occur for non-zero asperity contact angles due to asperity deformation, thus we should include the deformation contribution to friction by writing

$$\mu = \mu_a + \mu_p + \mu_d \quad ( \text{e.g. 53} ).$$

Rigney and co-workers ( e.g. 12, 13 ) prefer to use an energy-based model for describing friction, based on the hypothesis that plastic deformation is the most important factor in frictional energy dissipation for many materials ( including metals and ceramics ). Using analytical expressions for the shear stress-shear strain relation and for the variation of shear strain with depth below the surface and finally equating the frictional work with the work of plastic deformation during steady-state sliding, an expression for  $\mu$  was obtained ( 13 ):

$$\mu = (A/L) \tau_{\max} f(\tau_s / \tau_{\max})$$

$$f(u) = 1 - 2 \left[ \frac{\ln(1+u) - u}{\ln(1-u^2)} \right]$$

where  $\tau_{\max}$  = the ultimate shear strength of the material,  
 $\tau_s$  = the average shear stress at the interface during sliding,  
 $(L/A)$  = applied normal load / actual asperity contact area, which may perhaps be approximated by the indentation hardness ( under the same conditions of surface strain and temperature obtaining during sliding ).

As yet, there are insufficient experimental measurements of these three parameters to enable fair comparison between theory and experiment ( 13 ).

Whilst friction models generally involve only a limited number of variables for simplicity, a complete description would account for important ( but complex ) effects such as differences between steady-state and "running-in" behaviour, frictional heating effects, environmental effects, crystallographic anisotropy in  $\mu$ , etc. In particular, microstructural changes occurring in the near-surface layer during sliding must be considered ( e.g. 14, 15 ). This is important, since the original microstructure, degree of strain-hardening, etc. may or may not then influence the subsequent friction/wear behaviour of the material.

Finally, it is tempting to try to correlate coefficients of friction with wear rates. Whilst the two are often related, the correlation is by no means perfect ( e.g. 16 ). This is perhaps to be expected, since friction probably involves mainly plastic deformation, whilst the formation of wear debris involves both deformation and fracture processes ( the energy of fracture being expected to be

much lower than the plastic deformation energy ).

### 6.3 WEAR MODELS

#### 6.3.1 Adhesive Wear

Adhesive wear models have been extensively reviewed in the literature ( e.g. 1 - 9, 17 - 20 ), and so only a brief outline is presented here. Probably the best-known model is that due to Archard ( 15 ), which is closely related to the adhesion model of Bowden and Tabor ( 1,2 ) described previously. By assuming that a constant fraction of the volume of material displaced by a sliding asperity is removed, the wear volume per unit sliding distance (  $w$  ) was related to the normal load  $L$  and the yield pressure  $p_0$  of the wearing material:

$$w = \frac{k' L}{3 p_0}$$

where  $k'$  is a factor related to the probability of forming a wear particle. If the hardness  $H$  is taken to be proportional to  $p_0$ , the wear law becomes  $w = k L/H$ . Values of  $k$  are generally low, spanning the range  $10^{-8} - 10^{-3}$  between mild and severe wear ( e.g. 20 ).

The only materials' parameter in the above relation is hardness, yet a good many additional parameters are known to be important ( e.g.  $K_{IC}$ , crystal structure, bonding type, chemical reactivity, etc. ). Indeed, as will be seen, increases in hardness may sometimes result in increases in wear rates.

Another major drawback to the Archard model is that no mechanism is provided for generation of loose debris. Rather, the model considers only adhesive transfer of material to the opposing surface. It is observed ( e.g. 51 ) that wear particle sizes vary considerably and may be much larger than asperity contact dimensions. Rabinowicz ( 3 ) obtained an expression for the minimum wear particle size (  $D$  ) by equating the stored elastic energy with the nett surface energy required to form the particle, such that  $D \propto k E \gamma / H^2$ , where  $k$  = constant,  $E$  = Young's modulus,  $\gamma$  = surface energy,  $H$  = hardness. Rabinowicz also made the simplifying assumption  $H \propto E$ , which is invalid since  $(E/H)$  ratios vary significantly between materials and with changing temperature ( sections 3.2, 3.3 ). Wear particle sizes predicted by this relation turn out to be larger than many of the

particles actually formed ( e.g. 22 ).

### 6.3.2 Abrasive Wear

Abrasive wear is defined as the displacement or removal of material on one of two contacting surfaces in relative motion either by hard asperities fixed on the opposing surface ( two-body abrasive wear ) or by loose particles between the surfaces ( three-body abrasive wear ). Abrasion is a very common form of industrial wear because abrasives such as  $\text{SiO}_2$  ,  $\text{Al}_2\text{O}_3$  and iron oxides, which form a high proportion of the earth's crust, may not easily be excluded from the moving parts of machinery ( e.g. 9, 32 ).

Abrasion of ductile materials is usually considered in terms of two mechanisms: ploughing and machining ( or 'cutting' ) ( 23 - 25 ). Ploughing may occur by displacement of material to the sides of grooves and by formation of a prow of material ahead of the asperity ( i.e. pile-up of material - see section 3.2 ). Ploughing models have predicted wear laws similar in form to the Archard law ( 1-3, 9, 31 ). Cutting dominates abrasive wear for asperity contacts above a critical value of rake angle ( defined as the angle between the normal to the wear surface and the face of the tool or asperity along which a chip slides ) ( 23 - 25 ). The critical rake angle  $\alpha_c$  depends markedly on material ( e.g.  $\alpha_c \approx 0^\circ$  for steel but  $\alpha_c \approx -40^\circ$  for copper under the same conditions ) and also on a wide range of operating conditions ( e.g. temperature, lubricant, cutting speed, tool shape, etc. ). Cutting is a more efficient means of removing material than ploughing, the deformed surface layer being less deep and coefficients of friction lower where cutting dominates ( 11, 23 - 25 ).

In abrasive wear, the relative hardnesses of the wearing material (  $H_m$  ) and the abrasive (  $H_a$  ) are important: for ratios of (  $H_a/H_m$  )  $\gtrsim 1.3 - 1.7$ , abrasion rates are relatively high and show comparatively little sensitivity to  $H_a$ . For (  $H_a/H_m$  )  $\lesssim 0.7 - 1.1$  ( depending on abrasive particle size ), wear rates are lower and depend strongly on  $H_a$  ( 26, 9 ).

The Archard equation has been successfully applied to abrasive wear of pure metals ( 27 ), particularly when grouped according to crystal structure ( 28, 29 ). For covalent and ionic ceramics, a similar relation has been found, but the plot of wear

resistance against hardness has a much lower slope for brittle materials than for pure metals ( 30, 31 ). Wear data for metal alloys lie between these two limiting plots. Attempts to increase the wear resistance of a given material by means of changing the microstructure or degree of strain-hardening are often unsuccessful ( e.g. 32 ): for example, cold-worked steels offer little improvement over pure iron over a wide range of hardness. Heat-treated steels show some improvement over pure iron, but the variation of wear resistance with hardness is not as great as for pure metals.

At high hardness levels, wear resistance tends to fall off, which is thought to be consistent with the concomitant decreases in fracture toughness ( e.g. 33, 34 ). Fracture mechanics approaches have only recently been applied to wear processes ( e.g. 33 - 41 ), their justification being that wear debris formation must involve fracture events. Thus, materials' parameters such as  $K_{IC}$ ,  $K_{IIC}$ , etc. are introduced in addition to the hardness. Thus, for ferrous alloys, wear rates are found to depend on  $K_{IC}$  for values below approximately  $10 - 15 \text{ MPam}^{3/2}$  ( 34 ). Zum-Gahr ( 34 ) has suggested that wear rates can be described by a ploughing term (  $\alpha(1/H)$  ) plus a fracture term (  $\alpha(H^{1/2}/K_{IC}^2)$  ). In the theory due to Rosenfield ( 37 ), ploughing and cutting are important above a critical value of  $(K_{IC}/H)$  whilst, below this value, flaking, chipping and spalling ( i.e. brittle fracture ) processes dominate. This is very similar to the predictions of indentation fracture mechanics models concerning abrasive wear behaviour of brittle ceramics ( section 6.4 ). However, more recent work ( e.g. 38 ) suggests that  $K_{IIC}$  might be a more appropriate parameter than  $K_{IC}$ , since wear debris ( in metal systems, at least ) is probably formed by shear cracks ( e.g. 54 ).

### 6.3.3 Corrosive Wear

Corrosive wear, i.e. wear controlled or influenced by the effects of chemical environment, will not be discussed in detail here, since the subject is immensely complex and, as yet, poorly understood. In general terms, the surface chemistry of a material can influence friction and wear processes in a number of ways, possible mechanisms including: (a) formation of ( hard or soft ) surface layers ( e.g. oxides, metal-lubricant soaps, etc. ); (b) selective removal of certain components

of the material ( e.g. decarburization of steels ); (c) penetration of various species into the material, causing changes in structure and properties ( e.g. hydrogen embrittlement, internal oxidation at grain boundaries ); (d) changing the chemical composition of debris particles; (e) changing the electronic properties of the near-surface region ( see section 3.10 ).

Equally, wear processes may influence the surface chemistry, by, for example: (a) providing highly deformed sites with enhanced chemical reactivity; (b) continuously removing oxide layers; (c) causing surface transfer layers of different composition to that of either of the bulk materials in contact; (d) introducing highly diffusive paths ( e.g. cell boundaries ) into the near-surface region.

Thus, predicting the effects of chemical environment on friction and wear processes is not generally feasible: such effects must be determined experimentally for each material/ environment system ( e.g. 42 ).

#### 6.3.4 Surface Fatigue Wear

Fatigue effects in wear processes have been postulated by a number of workers ( e.g. 43 - 50 ), both in rolling contacts and in sliding. Assuming that  $N$  cycles of loading for a given asperity lead to fatigue fracture, a wear law similar to Archard's law may be derived ( e.g. 45, 46 ), where the wear coefficient  $k$  is related to  $(1/N)$ .

Similarities between wear and fatigue processes have been summarized by Hirth and Rigney ( 48, 49 ), among others. Both processes are thought to produce similar microstructures at high strains and display similar sensitivity to environment ( 44 ). On this basis, it has been speculated ( e.g. 48, 49 ) that correlations between wear rates and fatigue resistance might be expected, however there are as yet insufficient data to establish this. Effects such as transfer of material between the two surfaces might spoil the correlation. In addition, most fatigue data is based on alternating tension/compression tests, whilst wear involves predominantly compressive and shear loading, with localized tensile stresses playing an important role in brittle materials.

### 6.3.5 Delamination

Based on the observation that wear debris is often lamellar in form, Suh and co-workers have proposed a new wear model, termed 'the delamination theory of wear' ( e.g. 51 - 55 ). In the original model ( 51 ), a soft surface layer, formed as a result of dislocation image forces, was postulated. Immediately beneath this layer was thought to be a region of much higher dislocation density, which would result in void nucleation during wear, especially in the presence of particles or inclusions. Formation of wear debris was then thought to occur by void coalescence to form a crack which would propagate at a critical length, running parallel to the surface.

A problem with this model was that the soft surface layer would only be a few tens of nm thick, whilst wear particles can be much thicker ( e.g. tens of  $\mu\text{m}$  ) ( 48, 49 ). In later versions ( e.g. 52 - 55 ), Suh omitted the soft surface layer, suggesting instead that cracks nucleate below the surface because near-surface stresses are highly compressive. Repeated asperity interactions were thought to contribute incremental plastic strains per cycle of loading, leading to crack nucleation and propagation by a fatigue process. Cracks would propagate parallel to the surface because (i) the principal plastic shear stress acts on that plane in the subsurface region ( 48, 54 ) and (ii) cracks may follow preferred microstructural paths within the highly textured surface region ( see below ). Cracks would either propagate under tensile stresses acting normal to the surface ( 52 - 54 ) or due to shear stresses ( mode II fracture ) ( 54 ). It is uncertain whether a shear crack would extend in the wake of an asperity ( in the tensile region ) ( 52 - 54 ) or in advance of the asperity in the direction of sliding ( in the compressive region ), where shear stresses would be highest ( e.g. 48 ). Further uncertainties in delamination theory arise in the nucleation stage, especially for single-phase materials without inclusions ( e.g. 55 ).

Rigney and Glaeser ( 15 ) suggest that cracks propagate parallel to ( and possibly within ) dislocation cell and sub-grain boundaries within the highly deformed surface layer, these being flattened out parallel to the surface, providing more crack paths in this plane. Thus, the finest wear particles would correspond to

one sub-structure unit and the largest would have thickness equal to that of the highly deformed layer. The model may then incorporate materials' properties such as stacking fault energy and may account for modifications to crack paths due to microstructural factors such as phase transformations ( e.g. in austenitic steels ). Adhesion effects ( e.g. build-up of a transfer-layer ) may also be considered in addition to delamination. A prior requirement in the Rigney and Glaeser model is the presence of a suitable microstructure before delamination debris can be produced, which may account for the 'break-in' period prior to steady-state wear.

Delamination models such as the above could be made very elaborate indeed by incorporating a large number of variables. As yet, no simple quantitative wear law has been derived which satisfactorily predicts wear rates for all materials ( e.g. 48 ). What has been achieved by such models is a better insight into how wear debris forms and how materials' parameters other than hardness might become important in controlling wear behaviour.

#### 6.3.6 Erosion

Erosive wear is generally divided into three major categories—erosion by impact of hard, solid particles or by liquid drop impact or by cavitating liquids ( e.g. 56 ). Only the first of these is considered in this section, since solid impact is more analogous to the quasi-static indentation test. Broadly, the features of erosion which distinguish it from any other form of wear or surface deformation are the enormous strain rates produced ( e.g.  $10^6 \text{ s}^{-1}$  ) and the small contact times ( e.g. microseconds ) between the impacting particle and the material surface. Despite these differences, erosive damage in ceramics is found to show the same qualitative features as in quasi-static hardness experiments, viz. intense plastic deformation at the impact site often surrounded by localized crack arrays ( e.g. 57 - 62 ).

Solid particle erosion involves many variables relating to both the target and the impacting particles, including particle velocity, size, shape and hardness, impact angle, etc. Empirical wear laws based on these parameters have been determined ( e.g. 63 ), but there is, as yet, little detailed understanding of wear mechanisms.

Differences in erosive wear behaviour have been established between metals and ceramics ( e.g. 60 ), particularly in the dependence of wear rate on impact angle and particle size. Whilst most metals show a maximum wear rate for impact angles in the range  $20 - 30^\circ$ , ceramics wear most quickly at normal incidence. For small particle sizes, wear rates increase with increasing particle size for both metals and ceramics, but the increase saturates at larger particle sizes for metals, yet not for ceramics. Wear loss in ceramics is controlled by brittle fracture for large particles at high impact velocity and by plastic deformation for small particles at low impact velocity ( e.g. 58, 60, 64 ).

Erosive wear loss in the brittle regime has been considered by Evans et al. ( 58 ) using an indentation fracture mechanics approach, assuming that wear loss is primarily due to the formation of lateral cracks. Wear loss ( $w$ ) at normal incidence was found to depend on hardness  $H$  and toughness  $K_{IC}$  according to the relation  $w \propto K_{IC}^{-4/3} H^{-1/4}$  for constant particle velocity, radius and density. Thus, hardness and toughness are important parameters, although only the dynamic ( high strain-rate ) values are strictly relevant ( e.g. 57, 58, 60 ).

Erosive wear mechanisms for ductile materials are thought to include such processes as ploughing, cutting, melting, lip extrusion and fracture, fatigue and adhesive transfer. It is uncertain which, if any, of these mechanisms might apply to ceramic materials in the plasticity-controlled regime.

Without considering detailed mechanisms for material removal, Hutchings ( 65 ) has proposed that material may become detached after accumulating a fixed amount of plastic strain  $\epsilon_c$ . For normal impact of spherical particles, Hutchings derived a wear loss equation

$$w \propto v^3 / \epsilon_c^2 H^{3/2} \quad \text{where } v = \text{particle velocity.}$$

The number of impacts per unit area required to initiate material loss ( $N_f$ ) was shown to vary as  $N_f \propto \epsilon_c^2 H R v^{-2}$  where  $R$  = particle radius. Again, dynamic hardness appears to be a key materials' parameter, in theory at least.

#### 6.4 ABRASIVE WEAR OF CERAMICS

As for erosive wear, abrasive wear of brittle materials may be divided into two regimes: in severe wear situations involving high contact loads and large abrasive particles, material removal occurs primarily by brittle fracture, whilst for mild wear conditions ( e.g. polishing ), material is removed by some form of plastic deformation process(es) ( e.g. 9, 32, 39, 40, 66-74 ).

The effect of abrasive particle size may be rationalized as follows. Large particles are capable ( assuming sufficient load normal to the surface of the test material ) of producing indentations or scratches of sufficient size ( i.e. radius  $> c^*$  )<sup>†</sup> to initiate cracks ( section 5.2 ). Particles with radii less than  $c^*$  cannot induce fracture because they cannot produce large enough indentations. Equally, values of the normal load on each abrasive particle or asperity are required to exceed the critical load  $P^*$  for fracture to occur.<sup>†</sup> Since the number of particles or asperities that contact the surface per unit area is given by  $N \propto D^{-2}$  ( e.g. 9 ), where  $D$  = particle diameter, larger particles would produce smaller values of  $N$  such that each contacting particle would have to support a larger proportion of the total applied load normal to the surface. Thus, it is reasonable to suppose that a critical mean particle size exists, above which contact loads/indentation sizes are sufficient to cause fracture of the wearing surface.

The 'ductile-brittle' wear transition discussed above is important because it is accompanied by a rapid increase in wear rate ( e.g. 74 ). Materials which are superior in one wear regime may often prove to be inferior in the other ( e.g. 40 ). Thus, in addition to the variables which control wear rates in each wear regime,  $P^*$  and  $c^*$  are important materials' parameters.

---

<sup>†</sup> Both  $P^*$  and  $c^*$  should be lower for dynamic scratching situations than in quasi-static indentation tests. Swain ( 69 ) has shown that the frictional forces involved in sliding increase the stress intensity factor at median crack tips by a factor of  $\sqrt{4(1 + \mu^2)}$ .<sup>1/2</sup> Thus, for small  $\mu$ ,  $P^*$  values should be lower than in the quasi-static case by a factor of  $\sqrt{4}$ , or 256 and  $c^*$  should be lower by a factor of  $\sqrt{16}$ . For a highly brittle material such as silicon at room temperature,  $P^*$  for sliding contacts could therefore be as low as a few milligrams!

#### 6.4.1 The Fracture-Controlled Wear Regime

Abrasive wear in the fracture-controlled regime is comparatively well-understood ( e.g. 40 ). Debris formation is thought to occur primarily by means of indentation fracture events at contacting asperities, combinations of median/radial and, especially, lateral chipping leading to material removal. Various indentation fracture mechanics analyses of this situation have been attempted ( e.g. 39, 40, 69, 75, 76 ), the most recent ( 40 ) predicting an expression for the volume of material removed per unit sliding distance (  $w$  ):

$$w \propto P^{9/8} K_{IC}^{-1/2} H^{-5/8} (E/H)^{4/5}$$

Evans ( 40 ) reports good correlations between the parameter  $K_{IC}^{-1/2} H^{-5/8}$  and wear rates determined in diamond grinding and sawing experiments on a variety of ceramics ( 77, 78 ). Moore and King ( 74 ), however, report a poor correlation between a similar parameter  $K_{IC}^{-3/4} H^{-1/2}$  and wear rates during abrasion by flint and SiC abrasive papers or cloths, although the  $K_{IC}$  values used in this study are suspect ( 40 ). An important factor in Moore and King's experiments may also have been degradation of abrasive particles, especially the softer flint abrasive with very hard test materials ( e.g. 26 ). Rounding of abrasive particles could, for example, cause a change in crack morphology from median/radial and lateral to ring and cone cracking. Particle fracture would decrease the mean particle size until a lower limit (  $c^*$  ) is reached, below which particles cannot fracture ( e.g. 79 ). Depending on whether  $c^*$  for the abrasive is greater than or less than  $c^*$  for the wearing material, wear may then proceed either by brittle fracture or plasticity mechanisms.

#### 6.4.2 The Plasticity-Controlled Wear Regime

Very little is known about wear of ceramics in the plasticity-controlled ( polishing ) regime. Moore and King ( 74 ) have plotted wear rates versus (  $1/H$  ) for various ceramics based on polishing experiments with fine grit abrasives, but the plots showed a fair amount of scatter. An interesting effect has been observed by Gibbs ( 80 ) in diamond polishing of  $Al_2O_3$  materials. Wear rates were found not to depend consistently on microhardness ( e.g. at 100 gf load ), but to correlate well with the Meyer index ( section 3.7.1 ) for the

load sensitivity of hardness. This is justifiable, in that wear processes generally involve surface contacts at low applied loads, and so only the hardness values measured at these loads are strictly appropriate to the Archard equation. Materials with Meyer indices less than two are harder at low loads and should therefore have high wear resistance. Richardson ( 81 ) has demonstrated that the correlation between relative wear resistance and hardness is improved ( for metals ) if the hardness of the worn surface is measured, rather than that of the undeformed material. As has been demonstrated in section 3.7.4, abrasion of even a highly brittle ceramic material can cause an increase in surface hardness.

Mechanistically, there seem to be few good models for plastic wear of ceramics. The tacit assumption is often that such mechanisms may be similar to those observed in metals, but clearly this requires further clarification. In the remainder of this section, two classes of wear will be considered: conventional abrasive wear and delamination. Whilst other types of wear can almost certainly occur in ceramics, it is felt that there is, as yet, insufficient theoretical or experimental basis for discussion of how these models might be applied specifically to wear of ceramics.

The two commonly observed abrasive wear processes in metals ( ploughing and cutting ) have previously been described in section 6.3.2. Cutting may only take place above a critical value of asperity or particle rake angle (  $\alpha_c$  ) which, for metals, generally increases with increasing hardness. Extrapolating this trend,  $\alpha_c$  should be quite large and positive for ceramics: only very sharp abrasive particles in a small range of orientations with respect to the wear surface would cause cutting. Particle rounding, which for wear of hard ceramics might be quite severe ( 26 ), would effectively render cutting impossible. Equally, ploughing of ceramics in the same way as for metals is possible only for very sharp particles or asperities because indenters of large semi-apical angle promote material flow radially outwards from the point of contact, which does not involve 'pile-up' around the indentation or groove to form a lip of material which might subsequently be removed ( see section 3.2 ). Again, particle rounding would reduce, or even eliminate the possibility of lip or prow formation during asperity or particle sliding. To summarize, it is the author's unproved opinion that conventional abrasive wear

processes are unlikely to contribute significantly to steady-state plastic wear of ceramics, although evidence for these mechanisms might be found in single-pass or low-cycle experiments ( 89 ).

Wear by what appears to be delamination has been observed in scratch and wear tests in various ceramics ( e.g. 67, 68, 74, 82 ). For example, multi-pass sliding cone-on-flat scratch tests on NC203 hot-pressed SiC have revealed wear by a combination of delamination ( i.e. removal of sheets of material ) and intergranular fracture leading to grain pullout ( 68 ). Swain ( 82 ) proposed that delamination in  $\text{Al}_2\text{O}_3$  occurs by increasing dislocation pile-up at near-surface grain boundaries leading to eventual grain boundary failure.

A likely mechanism for delamination in ceramics would involve build-up of residual stresses with progressive abrasion ( i.e. repeated contacts over the same surface area ). Eventually, the residual stresses could reach a critical level at which failure would take place, probably by the nucleation and propagation of a crack at the elastic-plastic boundary, where tensile stresses are greatest. Thus, fracture might occur by accumulation of residual stress even though individual contact loads are below  $P^*$ . Clearly, further thought must be given to the problem of how repeated surface contacts could lead to plastic strain accumulation in these materials.

## 6.5 APPLICATION OF QUASI-STATIC INDENTATION RESULTS

### 6.5.1 Friction

Information about coefficients of friction may not be derived from any of the hardness/temperature data in this thesis. This follows from the findings of Brookes and co-workers ( 83-85 ) that coefficients of friction measured in vacuo on a variety of ceramic materials in self-contact varied with temperature but the variations were entirely independent of the hot-hardness behaviour ( especially of the "ductile-brittle" transition ). Typically, materials with a significant degree of metallic bonding ( WC, TiC,  $\text{TiO}_2$  ) showed a decrease in  $\mu$  up to a certain material-dependent temperature, above which  $\mu$  increased with increasing temperature. Highly covalent materials ( SiC,  $\text{Si}_3\text{N}_4$ ,  $\text{B}_4\text{C}$  ) generally showed a slight but continuous decrease in  $\mu$  with increasing temperature over the temperature range

investigated ( up to  $1000 - 1500^{\circ}\text{C}$  ).

These results were thought to be inconsistent with the Bowden and Tabor theory of adhesive friction ( section 6.2 ), which would predict that  $\mu$  should be fairly independent of temperature ( since  $\tau_j$  and  $H$  are both likely to depend on temperature in the same way ). The high-temperature increase in  $\mu$  observed for the more 'metallic' materials was thought to be a consequence of increased adhesion facilitated by enhanced diffusion rates, leading to asperity junction strengthening by a mechanism analogous to sintering. This effect would not be observed for highly covalent materials, where diffusion rates would be too low ( c.f. section 1.2.4.1 ). The initial decrease in  $\mu$  with increasing temperature observed for both classes of material is not easily explainable - it is not, for example, thought to be due to thermal desorption of surface contaminants ( 84 ).

#### 6.5.2 Wear in the Plasticity-Controlled Regime

As has previously been intimated ( section 6.4.2 ), correlations between plastic wear resistance and hardness are by no means well-established, so predictions concerning wear behaviour based solely on hardness criteria are highly tentative. However, until further theoretical developments establish more reliable parameters, hardness will continue to be used as a convenient yardstick for predicting wear performance in the plasticity-controlled regime.

Based on the hardness data in figures 22 - 26, dense forms of SiC and  $\text{B}_4\text{C}$  would be less susceptible to plastic wear at room temperature than silicon nitrides ( with the exception of PDSN ). Single crystals and coarse-grained materials would be predicted to have superior wear resistance to other microstructural forms of the same material and porous materials would have especially low wear resistance.

At high temperatures, which in a wear situation might be generated by frictional heating, dense boron carbide would be expected to retain its wear resistance better than the other materials studied here, although oxidation problems have been reported on heating  $\text{B}_4\text{C}$  above  $450^{\circ}\text{C}$  in air ( 86 ). Silicon nitrides ( especially PDSN ) should be more wear resistant than corresponding forms of SiC at high

temperatures, due to the lower temperature-sensitivity of hardness of the former.

It is emphasized, however, that strain rate effects may have a marked effect on the temperature-sensitivity of hardness. High strain rates should result in higher values of the transition temperature  $T_c$  than found in quasi-static indentation tests, so the rapid decrease in hardness with increasing temperature observed for Si, SiC and, to a lesser extent,  $Si_3N_4$  materials might not be observed until very high temperatures in wear situations. This is especially likely in erosive impact, in which particle contact times are so small that creep processes involving dislocation vacancy climb would not be important. However, even in this case it is still possible to envisage a high-temperature transition from stress-activated to thermally activated dislocation glide controlled by the Peierls' barrier.

Finally, the correlation between plastic wear rate and load sensitivity of hardness observed by Gibbs ( 80 ) may be significant for high-temperature wear of silicon nitrides, which were often found to have Meyer indices greater than two at  $800^\circ C$  ( table 11 ). This would predict lower hardness values, hence greater wear susceptibility, for small contact loads. The effect is difficult to quantify since this would involve extrapolation of the hardness:load relation well beyond the experimental load range used here, which is not thought to be meaningful ( 87 ).

#### 6.5.3 The Fracture-Controlled Wear Regime

As discussed in section 6.4.1,  $P^*$  and  $c^*$  are important materials' parameters in that they define the most severe conditions of load under which a material will wear by plastic deformation without brittle fracture. Thus, from figs. 50 - 52, silicon nitrides ( except PDSN ) would be more resistant to the onset of brittle wear than other materials, although the relative temperature-sensitivities of  $P^*$  are such that many SiC materials have values approaching those for the nitrides at  $800^\circ C$  and {111} single crystal Si has even higher values of  $P^*$  above  $700^\circ C$ . With the exception of  $B_4C$ , which showed a slight decrease in  $P^*$ , the effect of increasing temperature is to increase  $P^*$ , favouring plastic wear. Of the various microstructural

forms, fine-grained materials, especially hot-pressed forms, are predicted to have greater resistance to fracture-controlled wear than other materials.

The parameter  $(H/K_{IC})$  has been proposed ( e.g. 88 ) as a measure of "brittleness" in wear situations since, in general terms, it relates the scale of plastic deformation to the scale of fracture. However, as described in section 6.4.1, wear rates in the fracture-controlled regime are thought to depend mainly on the extent of cracking. Indentation crack sizes were generally found to increase with increasing temperature for the materials studied here ( section 4.4.1 ), yet the parameter  $(H/K_{IC})$  generally decreases with increasing temperature, as shown in figures 53 - 56, predicting less brittle behaviour. Thus,  $(H/K_{IC})$  is probably not a good parameter for predicting wear behaviour of ceramics.

Perhaps the best parameter which can be measured to predict the susceptibility of a material to crack propagation around indentations ( and possibly scratches ) is the directly measurable quantity  $c^{3/2}P^{-1}$  where  $c$  = crack size and  $P$  = applied load. The parameter has dimensions of inverse toughness  $(MPa\sqrt{m})^{-1}$ .  $c^{3/2}P^{-1}$  is plotted as a function of temperature for each material studied in this investigation in figures 57 - 60. Indentation fracture mechanics analyses predict  $c^{3/2}P^{-1} \propto (E/H)^{2/5} K_{IC}^{-1}$  ( section 4.3.2 ), hence both hardness and fracture toughness should be maximized for optimum wear resistance in the fracture-controlled regime, although these are often conflicting requirements. A similar conclusion may be drawn from the analysis due to Evans ( 40 ), which predicts that wear rates should vary as  $K_{IC}^{-1/2} H^{-5/8}$ .

From figures 57 - 60, it seems that microstructural effects on the parameter  $c^{3/2} P^{-1}$  are more important than differences in material for the range of materials investigated ( excepting, of course, single crystal silicon, which was highly 'brittle' compared with other materials ). Hot-pressed materials are less susceptible to both initiation and propagation of indentation fracture than all other microstructural forms in the temperature range 25 - 800°C. Single crystals and coarse-grained materials are the most susceptible to fracture.

The results obtained in this investigation suggest increasing

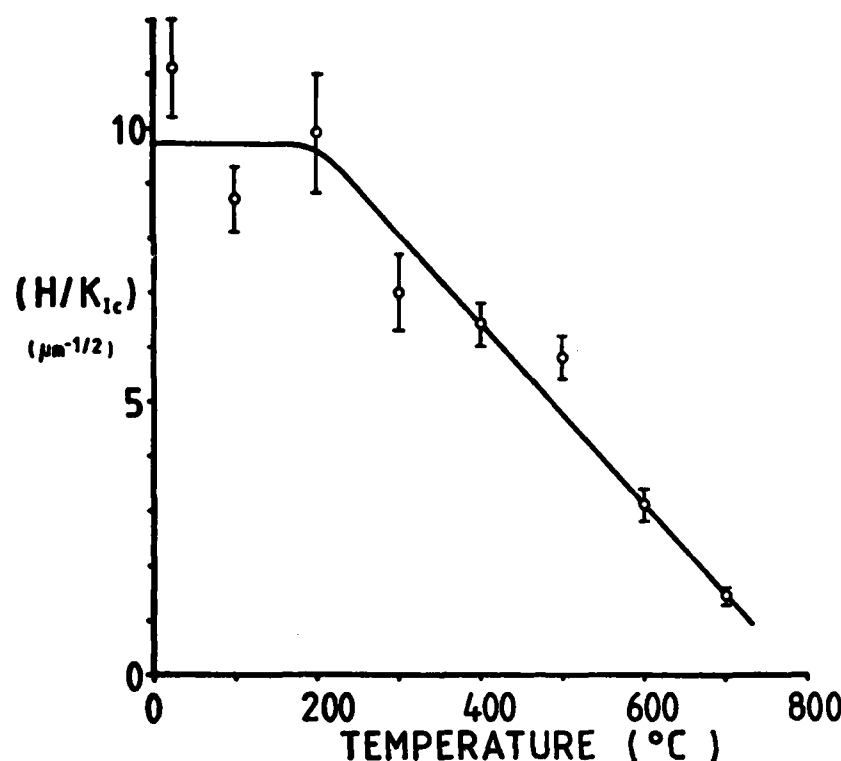


Figure 53. The variation of  $(H/K_{IC})$  with temperature for  $\{111\}$  silicon. Error bars indicate one standard error in the mean.

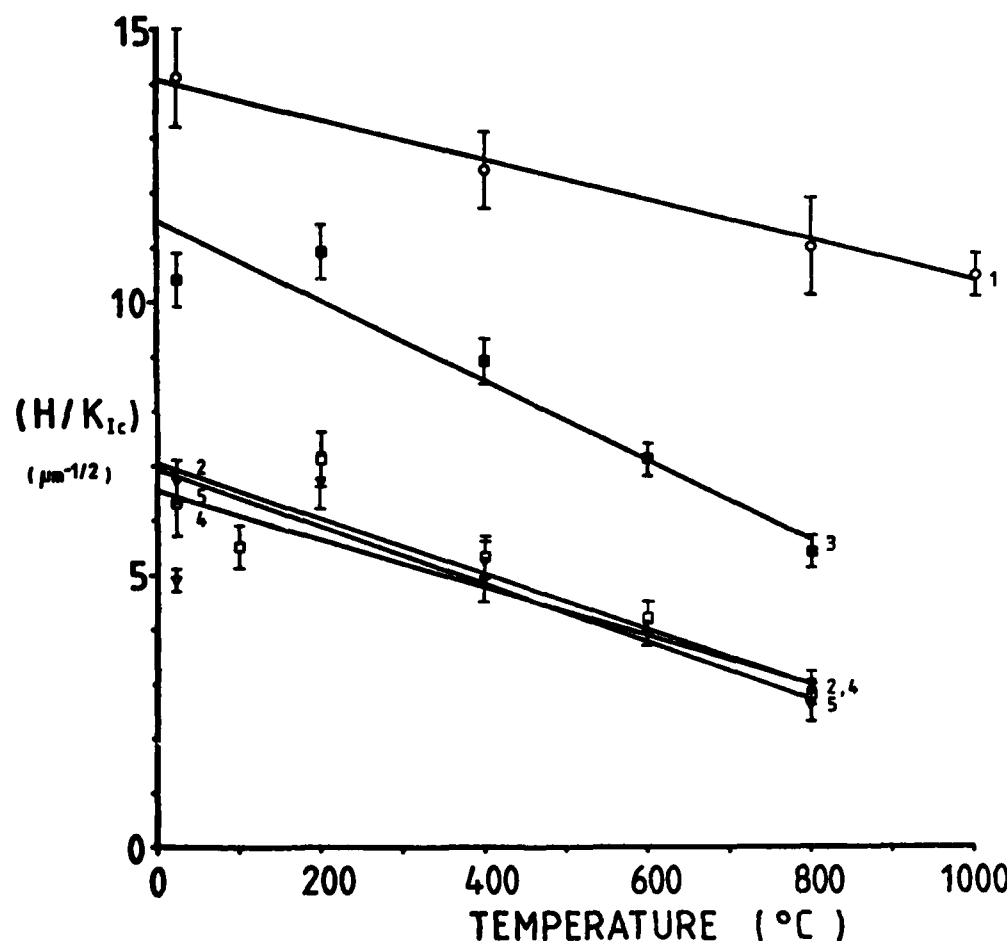


Figure 54. The variation of  $(H/K_{IC})$  with temperature for SiC materials: curve 1 = blue-black (0001) single crystal SiC (open circles), curve 2 = Norton NC203 hot-pressed SiC (open squares), curve 3 = Carborundum sintered SiC (filled squares), curve 4 = 'Suzuki' sintered SiC (open triangles), curve 5 = 'REFEL' reaction-bonded SiC (filled triangles). Error bars indicate one standard error in the mean.

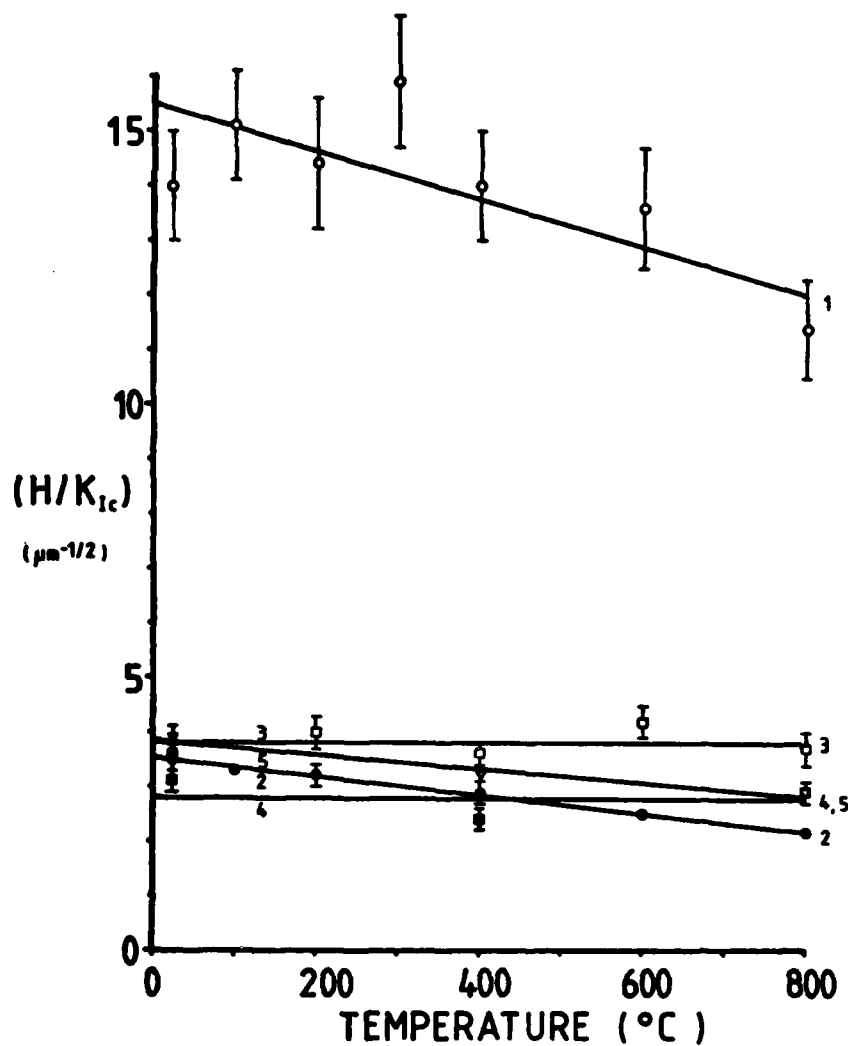
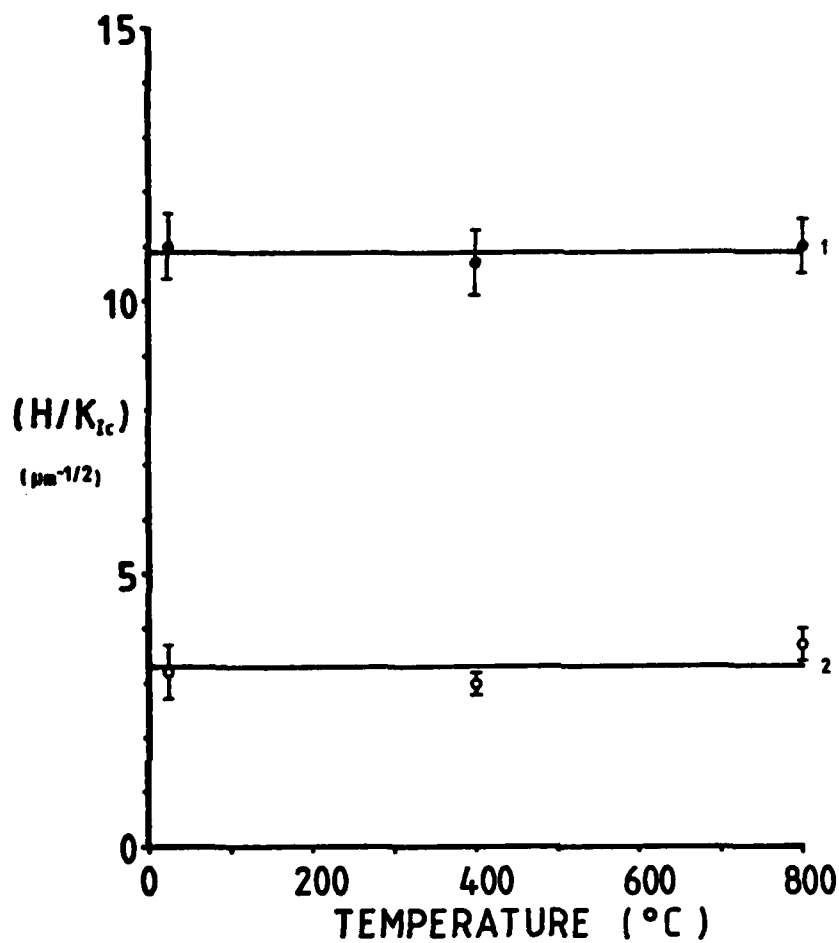


Figure 55. The variation of  $(H/K_{IC})$  with temperature for  $Si_3N_4$  and sialon materials: curve 1 = pyrolytically-deposited  $Si_3N_4$  ( open circles ), curve 2 = Norton NC132 hot-pressed  $Si_3N_4$  ( filled circles ), curve 3 = Ford '2.7' RBSN ( open squares ), curve 4 = Norton NC350 RBSN ( filled squares ), curve 5 = Lucas sintered SYALON 342 ( open triangles ). Error bars indicate one standard error in the mean.



**Figure 56.** The variation of  $(H/K_{IC})$  with temperature for  $B_4C$  materials: curve 1 = Le Carbone sintered  $B_4C$ , grade S1143 ( density  $2.4 \text{ gcm}^{-3}$  ) ( filled circles ), curve 2 = Le Carbone sintered  $B_4C$ , grade S1138 ( density  $2.05 \text{ gcm}^{-3}$  ) ( open circles ). Error bars indicate one standard error in the mean.

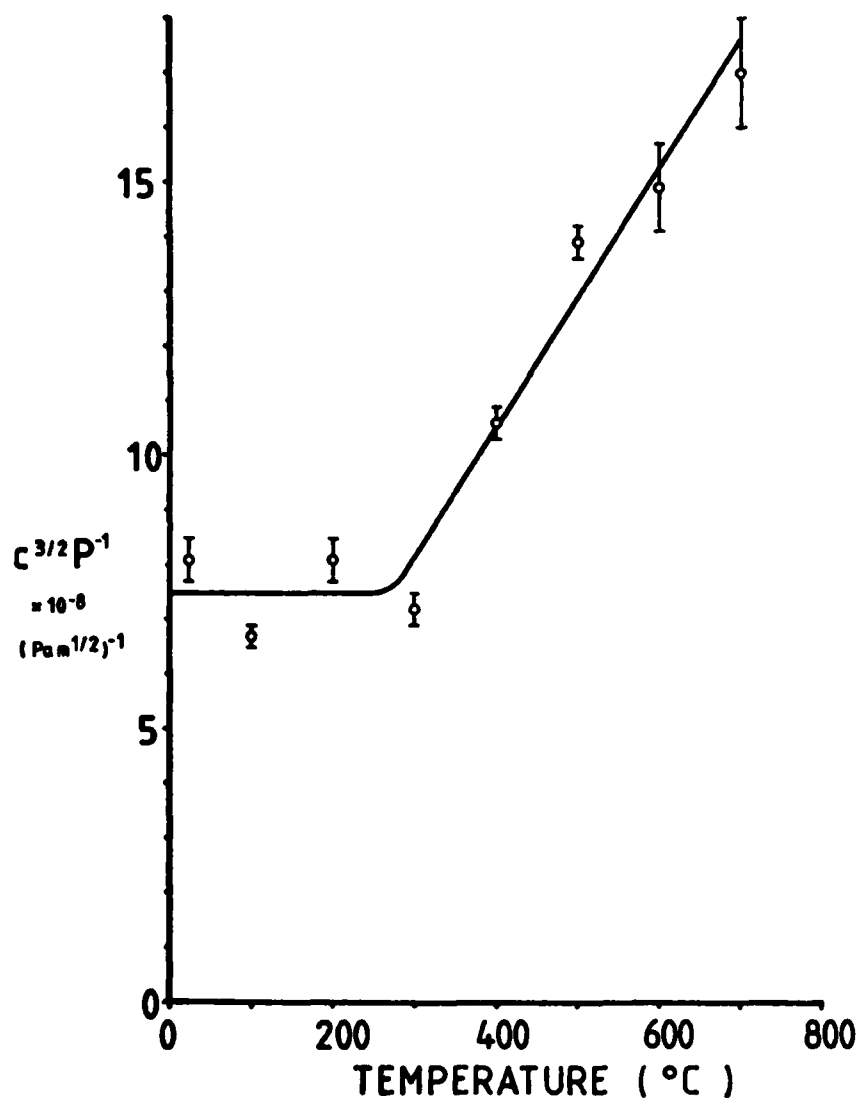


Figure 57. The variation of 'indentation brittleness' ( $c^{3/2}P^{-1}$ ) with temperature for {111} single crystal silicon. Error bars indicate one standard error in the mean.

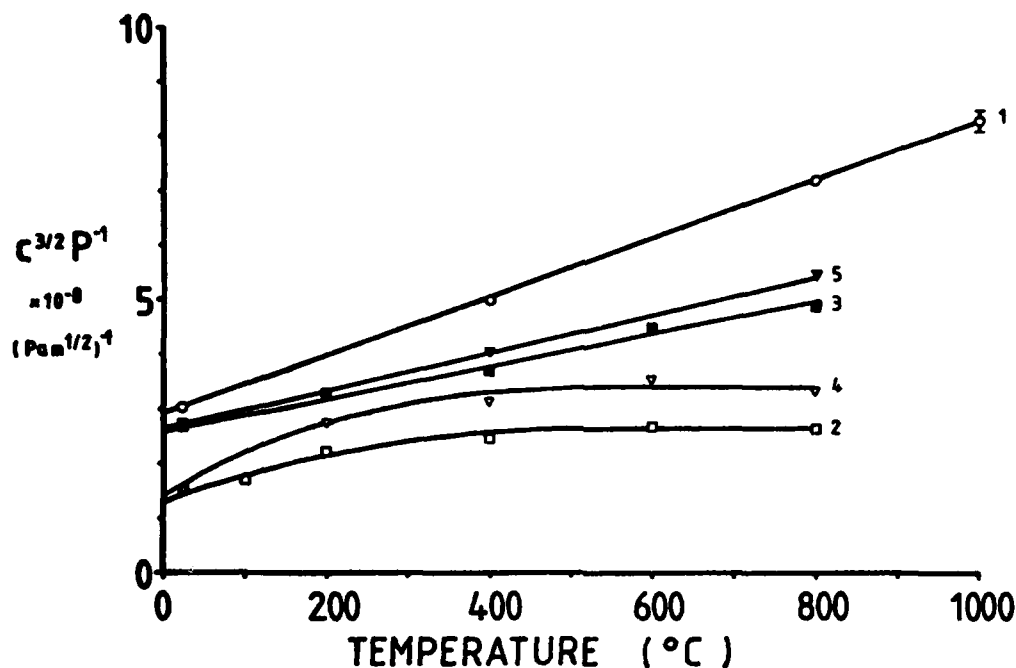


Figure 58. The variation of 'indentation brittleness' ( $c^{3/2}P^{-1}$ ) with temperature for SiC materials: curve 1 = blue-black (0001) single crystal SiC (open circles), curve 2 = Norton NC203 hot-pressed SiC (open squares), curve 3 = Carborundum sintered SiC (filled squares), curve 4 = 'Suzuki' sintered SiC (open triangles), curve 5 = 'REFEL' reaction-bonded SiC (grain size 10  $\mu\text{m}$ ) (filled triangles). Error bars indicate one standard error in the mean.

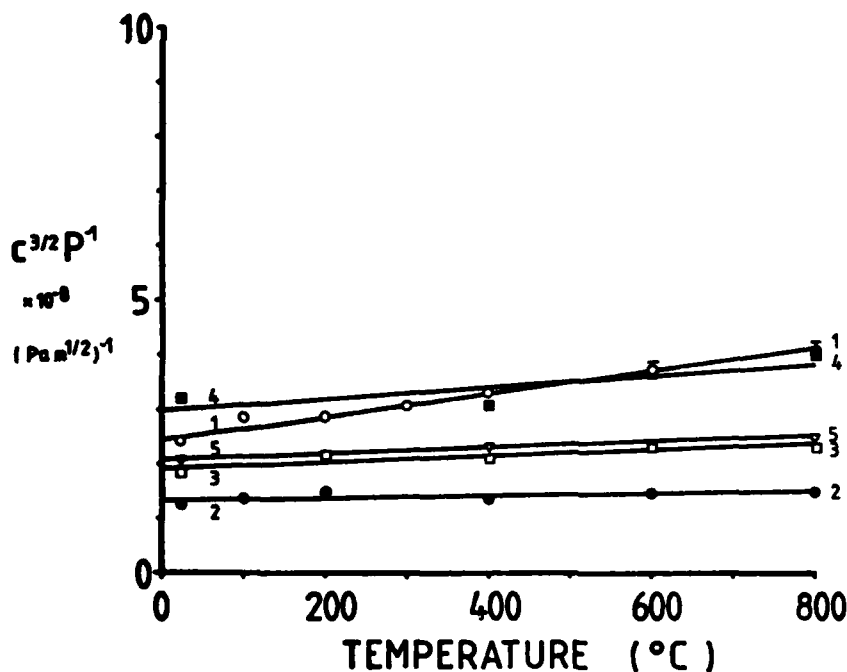
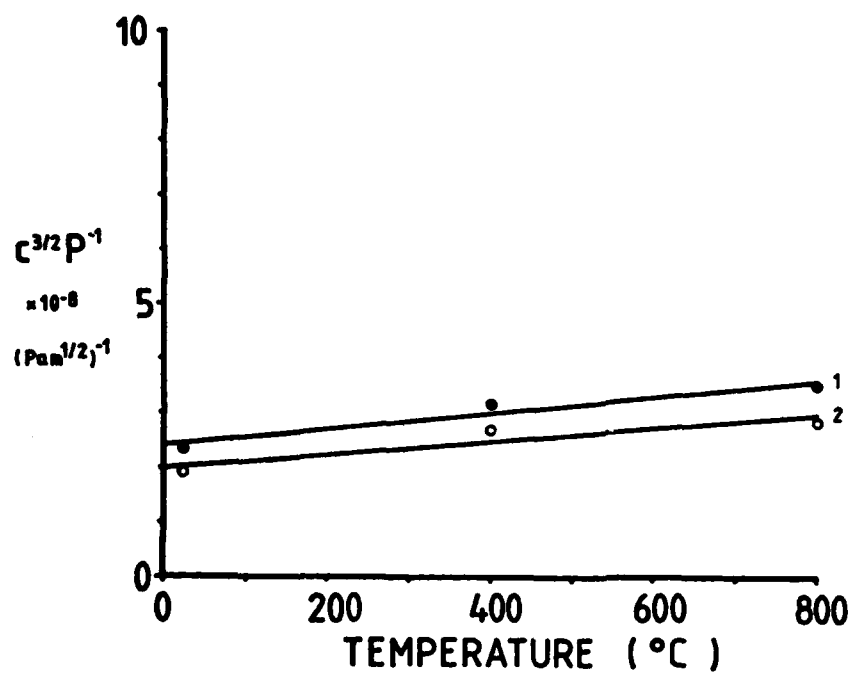


Figure 59. The variation of 'indentation brittleness' ( $c^{3/2}P^{-1}$ ) with temperature for  $\text{Si}_3\text{N}_4$  and sialon materials: curve 1 = pyrolytically-deposited  $\text{Si}_3\text{N}_4$  (open circles), curve 2 = Norton NC132 hot-pressed  $\text{Si}_3\text{N}_4$  (filled circles), curve 3 = Ford '2.7' RBSN (open squares), curve 4 = Norton NC350 RBSN (filled squares), curve 5 = Lucas sintered SYALON 342 (open triangles). Error bars indicate one standard error in the mean.



**Figure 60.** The variation of 'indentation brittleness' ( $C^{3/2}P^{-1}$ ) with temperature for  $B_4C$  materials: curve 1 = Le Carbone sintered  $B_4C$ , grade S1143 ( density  $2.4 \text{ gcm}^{-3}$  ) ( filled circles ), curve 2 = Le Carbone sintered  $B_4C$ , grade S1138 ( density  $2.05 \text{ gcm}^{-3}$  ) ( open circles ). Error bars indicate one standard error in the mean.

wear rates should be observed with increasing temperature in both plasticity- and fracture-controlled regimes. Again, care must be exercised in making this prediction, since the dynamic hardness is probably less sensitive to temperature than the quasi-static hardness, which would result in less variation in crack sizes or in  $P^*$  and  $c^*$  with temperature. Thus, Hockey et al. ( 59, 61 ) observed no change in erosive wear behaviour at normal particle incidence for SiC,  $Al_2O_3$  and other materials up to  $1000^\circ C$ , although for  $15^\circ$  particle incidence, changes in the particle velocity exponent for wear loss were observed, suggesting that increasing plasticity has at least some effect at high temperatures. Clearly, the dynamic situations obtaining under real wear conditions are much more complex than in the quasi-static case, making predictions about wear behaviour from the results obtained in this study difficult.

6.6. REFERENCES

1. F.P. Bowden and D. Tabor, 1950, "The Friction and Lubrication of Solids I", Oxford University Press.
2. Idem, 1964, "The Friction and Lubrication of Solids II", Oxford University Press.
3. E. Rabinowicz, 1965, "Friction and Wear of Materials", Wiley, N.Y.
4. J.V. Kragelskii, 1965, "Friction and Wear", English Translation L. Ronson and J.K. Lancaster, Butterworths, London.
5. J. Halling (Ed.), 1975, "Principles of Tribology", MacMillan, London.
6. D. Scott (Ed.), 1979, Treatise on Materials Science and Technology 13, "Wear", Academic Press.
7. D.A. Rigney (Ed.), 1981, "Fundamentals of Friction and Wear", ASM Materials Science Seminar, 4-5 Oct. 1980, Pittsburgh Pa., ASM, Metals Park, Ohio.
8. D.H. Buckley, 1972, "A Fundamental Review of the Friction and Wear Behaviour of Ceramics", NASA Technical Memorandum NASA-TM-X-68046.
9. M.A. Moore, 1978, Materials in Engineering Applications, 1, 97.
10. F.P. Bowden and D. Tabor, 1966, Brit. J. Appl. Phys. 17, 1521.
11. J.M. Challen and P.L.B. Oxley, 1979, Wear 53, 229.
12. D.A. Rigney and J.P. Hirth, 1979, Wear 53, 345.
13. P. Heilmann and D.A. Rigney, 1981, Wear 72, 195.
14. A.W. Ruff, L.K. Ives and W.A. Glaeser, 1981, in ref. 7, p.235.
15. D.A. Rigney and W.A. Glaeser, 1978, Wear 46, 241.
16. J.F. Archard, 1953, J. Appl. Phys. 24, 981.
17. J.T. Burwell, 1957/58, Wear 1, 119.
18. E.F. Finkin, 1979, Materials in Engineering Applications 1, 154.
19. T.S. Eyre, 1978, Tribology International 11, 91.
20. R. Holm, 1946, "Electrical Contacts". H. Gerbers, Stockholm, p.214.
21. L.E. Samuels, E.D. Doyle and D.M. Turley, 1981, in ref. 7, p.13.

22. N. Soda, Y. Kimura and A. Tanaka, 1976, Wear 40, 23.
23. L.E. Samuels, 1968, "Metallographic Polishing by Mechanical Methods", Pitman and Sons Ltd., London.
24. Idem, 1978, Scientific American, Nov. 1978, 110.
25. T.O. Mulhearn and L.E. Samuels, 1962, Wear 5, 478.
26. R.C.D. Richardson, 1968, Wear 11, 245.
27. M.M. Khrushov and M.A. Babichev, 1956, Friction and Wear in Machinery, Vol. 11, NEL translation no. 831, National Engineering Laboratory, East Kilbride, 5.
28. M.Y. Gurleyik, 1970, Z. Metallk. 61, 422.
29. K. Bhansali and A.E. Miller, 1981, Wear 71, 375.
30. M.M. Khrushov and M.A. Babichev, 1960, Research on the Wear of Metals, Chap. 13, NEL translation no. 891, National Engineering Laboratory, East Kilbride.
31. M.M. Khrushov, 1974, Wear 28, 69.
32. M.A. Moore, 1981, in ref. 7, p. 73.
33. E. Hornbogen, 1975, Wear 33, 251.
34. K.H. Zum-Gahr, 1979, in "Wear of Materials II", ASME, p.266.
35. J.R. Fleming and N.P. Suh, 1977, Wear 44, 39.
36. D.A. Hills and D.W. Ashelby, 1979, Wear 54, 321.
37. A.R. Rosenfield, 1980, Wear 61, 125.
38. Idem, 1981, Wear 72, 97.
39. A.G. Evans, 1979, in "The Science of Ceramic Machining and Surface Finishing II", eds. B.J. Hockey and R.W. Rice, National Bureau of Standards Special Publication 562 (U.S. Government Printing Office, Washington D.C.), p.1.
40. Idem, 1981, in ref. 7, p.439.
41. A.G. Atkins, 1980, Wear 61, 183.
42. R.M. Bentley and D.J. Duquette, 1981, in ref. 6, p.439.
43. Y. Kimura, 1981, in ref. 7, p.187.
44. N. Soda, Y. Kimura and A. Tanaka, 1975, Wear 33, 1.
45. J. Malling, 1975, Wear 34, 239.
46. E.F. Finkin, 1978, Wear 47, 107.

47. N.P. Suh, N. Saka and S. Jahanmir, 1977, *Wear* 44, 127.
48. J.P. Hirth and D.A. Rigney, 1980, in "Strength of Metals and Alloys Vol. 3", eds. P. Haasen, V. Gerold and G. Kostorz, Proc. 5th. Int. Conf., Aachen, W. Germany, August. 27-31, 1979, Pergamon Press, p.1483.
49. Idem, 1981, in "Dislocations in Solids", ed. F.R.N. Nabarro, North-Holland Press.
50. P. Heilmann and D.A. Rigney, 1981, *Met. Trans. A.* 12, 686.
51. N.P. Suh, 1973, *Wear* 25, 111.
52. Idem, 1977, *Wear* 44, 1.
53. N.P. Suh and co-workers, 1977, "The Delamination Theory of Wear", Elsevier Sequoia, Lausanne.
54. J.R. Fleming and N.P. Suh, 1977, *Wear* 44, 57.
55. N.R. Suh, in ref. 7, p.43.
56. C.M. Preece (Ed.), 1979, *Treatise on Materials Science and Technology* 16, Academic Press.
57. A.G. Evans and T.R. Wilshaw, 1977, *J. Mater. Sci.* 12, 97.
58. A.G. Evans, M.E. Gulden and M. Rosenblatt, 1978, *Proc. Roy. Soc. Lond.* A361, 343.
59. B.J. Hockey, S.M. Wiederhorn and H. Johnson, 1978, in "Fracture Mechanics of Ceramics Vol. 3". Eds. R.C. Bradt, D.P.H. Hasselman and F.F. Lange, Plenum Press, p.379.
60. A.W. Ruff and S.M. Wiederhorn, 1979, in ref. 56, p.69.
61. B.J. Hockey and S.M. Wiederhorn, 1979, *Proceedings of the Fifth International Conference on Erosion by Liquid and Solid Impact (ELSI V)*, 3-6th September 1979, Newnham College, Cambridge. Publ. Cavendish Laboratory, Cambridge, paper 26.
62. D.A. Shockey, D.C. Erlich and K.C. Dao, 1981, *J. Mater. Sci.* 16, 477.
63. G.P. Tilly, 1979, in ref. 6, p.287.
64. G.L. Sheldon and I. Finnie, 1966, *Trans. ASME* 88B, 387.
65. I.M. Hutchings, 1981, *Wear* 70, 269.
66. R. Stickler and G.R. Booker, 1962, *Phil. Mag.* 8, 859.
67. T.F. Page, G.R. Sawyer, O.O. Adewoye and J.J. Wert, 1978, *Proc. Brit. Ceram. Soc.* 26, 193.
68. O.O. Adewoye and T.F. Page, 1981, *Wear* 70, 37.

69. M.V. Swain, 1979, Proc. Roy. Soc. Lond. A366, 575.
70. J.D.B. Veldkamp and R.J. Klein Wassink, 1976, Philips Res. Repts. 31, 156.
71. A. Broese van Groenou, J.D.B. Veldkamp and D. Snip, 1977, J. de Physique C1, 285.
72. J.D.B. Veldkamp, N. Hattu and V.A.C. Snijders, 1978, as ref. 59, p.273.
73. A. Broese van Groenou, N. Maan and J.D.B. Veldkamp, 1979, as ref. 39, p.43.
74. M.A. Moore and F.S. King, 1980, Wear 60, 123.
75. B.R. Lawn, 1975, Wear 33, 369.
76. A.G. Evans and T.R. Wilshaw, 1976, Acta. Metall. 24, 939.
77. R.W. Rice and B.K. Speronello, 1976, J. Am. Ceram. Soc. 59, 330.
78. B.G. Koepke and R.J. Stokes, 1979, as ref. 39, p.75.
79. J.T. Hagan, 1981, J. Mater. Sci. 16, 2909.
80. N.K. Gibbs, 1982, Ph.D. thesis, University of Cambridge, in preparation.
81. R.C.D. Richardson, 1967, Wear 10, 353.
82. M.V. Swain, 1975, Wear 35, 185.
83. C.A. Brookes, 1962, in "Special Ceramics 1962", ed P. Popper, Brit. Ceram. R.A., Stoke-on-Trent, p.221.
84. C.A. Brookes and M. Imai, 1964, in "Special Ceramics 1964", ed. P. Popper, Brit. Ceram. R.A., Stoke-on-Trent, p.259.
85. C.A. Brookes and A.G. Atkins, 1965, Proc. 5th Plansée seminar, ed. F. Benesovsky, June 22-26, 1964, Reutte, Springer-Verlag Press, p.712.
86. F.H. Norton, 1974, "Elements of Ceramics, Addison Wesley, p.256.
87. P.M. Sargent, 1979, Ph.D. thesis, University of Cambridge.
88. B.R. Lawn and D.B. Marshall, 1979, J. Am. Ceram. Soc. 62, 347.
89. R.L. Aghan and R. McPherson, 1973, *ibid.* 56, 46.

## CHAPTER 7

### CONCLUSIONS

In this thesis, plasticity and fracture mechanisms in a variety of highly brittle covalent materials have been investigated principally as functions of temperature ( in the range 25 - 1000°C ) and specimen microstructure. The main experimental technique used in this study was controlled-temperature/environment indentation microhardness testing, backed up by a range of microscopical techniques ( e.g. reflected light microscopy, Nomarski differential interferometry, scanning electron microscopy ) for examining specimen microstructures and surface deformation structures. The results of this investigation, which are summarized below, are thought to be especially relevant to studies of wear processes in ceramic materials, and provide greater insight into the concept of 'brittleness'.

#### 7.1 SUMMARY OF HOT-HARDNESS RESULTS

The majority of the materials investigated here ( including single crystals of Si and SiC and polycrystalline SiC, Si<sub>3</sub>N<sub>4</sub> and sialon ) showed two regimes of hardness behaviour in the temperature range 25 - 800 or 1000°C. At lower temperatures, hardness was found to be a weak function of temperature whilst at higher temperatures, hardness was strongly thermally activated. The transition temperatures between the two regimes have been determined as 350°C (  $\sim 0.36 T_m$  ) for {111} single crystal Si, 200 - 550°C (  $\sim 0.15 - 0.25 T_m$  ) for single crystal  $\alpha$ -SiC ( depending on orientation and probably on specimen purity ), 300°C (  $\sim 0.18 T_m$  ) for polycrystalline SiC, between 400 and 700°C (  $0.3 - 0.45 T_m$  ) for single crystal  $\alpha$ -Si<sub>3</sub>N<sub>4</sub>, 330°C (  $\sim 0.28 T_m$  ) for polycrystalline Si<sub>3</sub>N<sub>4</sub> and  $\sim 240^\circ\text{C}$  for a sialon material. Sintered B<sub>4</sub>C was found to show no transition over the temperature range investigated ( up to  $0.4 T_m$  ), hardness being a relatively weak function of temperature for this material.

These results have been examined in the light of a variety of indentation plasticity theories, but firm conclusions are not possible without a clearer picture of the plastic deformation mechanisms actually operating ( especially in the low-temperature regime ) ( see section 7.3 ).

Examination of slip steps formed around high-temperature indentations in single crystals established that  $\{111\}\langle 1\bar{1}0 \rangle$  slip systems operated in silicon (above  $500^{\circ}\text{C}$ ) and that  $(0001)\langle 11\bar{2}0 \rangle$  slip occurred in SiC (above  $800^{\circ}\text{C}$ ). Slip steps were also formed around indentations in polycrystalline silicon carbides at  $800^{\circ}\text{C}$ . Formation of surface slip steps occurs only where the plastic zone size exceeds the indentation radius, which is suggested to occur as a critical value of  $(E/H)$  of approximately 30 is exceeded. This value is not generally attained until temperatures substantially in excess of  $T_c$  are reached: for  $\text{Si}_3\text{N}_4$ , very high temperatures indeed ( $>1500^{\circ}\text{C}$  at least) would be required.

Further indentation experiments were performed in an attempt to provide more information about plasticity mechanisms in these materials. Thus, the anisotropy in Knoop hardness of single crystals of  $\alpha$ -SiC was measured over a wide range of orientations as a function of temperature. The results were explained in terms of a combination of basal ( $(0001)\langle 11\bar{2}0 \rangle$ ) and prismatic ( $\{10\bar{1}0\}\langle 11\bar{2}0 \rangle$ ) slip, the CRSS for basal slip decreasing with increasing temperature much more rapidly than for prismatic slip. The ratio  $(\text{CRSS})_{\text{basal}} : (\text{CRSS})_{\text{prismatic}}$  was estimated to be in the range 0.7 - 1.1 at room temperature and 0.3 - 0.6 at  $800^{\circ}\text{C}$ .

Attempts were made to study the effects of various impurities on the hardness of Si and SiC materials. Whilst direct evidence for impurity effects was not obtained, such effects were thought to account for the higher hardness of blue-black single crystal  $\alpha$ -SiC (presumed to be p-type) compared with green SiC (presumed to be n-type).

The variation of hardness with applied load (or indentation size effect) was found to be small for all the materials investigated here over the load range 100 - 1000gf. For many  $\text{Si}_3\text{N}_4$  materials, the effect reversed from higher hardness at low loads to lower hardness at low loads as the temperature was raised. Abrasion damage was found to cause a surface hardening effect in 'REFEL' reaction-bonded SiC, this being more pronounced for small indentations, which sampled more of the surface-affected layer. The relevance of these findings to abrasive wear in the plasticity-controlled (polishing) regime has been discussed.

In order to measure meaningful activation energies for high-temperature ( $T > T_c$ ) deformation processes, indentation creep

experiments were performed on {111} single crystal silicon in the temperature range 600 - 800°C. The activation energy was estimated to be  $\sim 260 \text{ kJmol}^{-1}$ , which is similar to the value predicted for dislocation climb by pipe diffusion of vacancies along dislocation cores.

Specimen microstructure was found to influence the temperature-sensitivity of hardness to a large extent, especially for  $\text{Si}_3\text{N}_4$  materials. For dense materials, hot-hardness curves for different microstructural forms were transposed from each other along the log H axis, with little variation in  $T_c$  or activation energy. Grain boundaries were thought to produce a softening effect in these materials, the amount and composition of boundary phases being important in addition to the grain size. A model for this behaviour involving deformation by primary slip with grain boundary separation was discussed. Highly porous materials were found to be comparatively soft at low temperatures, the hardness displaying very little temperature-sensitivity. Microstructural evidence for compaction was found in these materials and a quantitative model was developed which fitted the experimental hardness data well, with no adjustable parameters.

Finally, this thesis illustrates the importance of hardness and its temperature-sensitivity in reflecting not only plasticity effects, but also crack nucleation and propagation processes, as summarized in the following section.

## 7.2 SUMMARY OF INDENTATION FRACTURE RESULTS

The study of indentation fracture enabled conclusions to be drawn concerning crack nucleation and propagation processes as functions of temperature and specimen microstructure.

Considering the propagation stage firstly, it was found that increasing temperature generally resulted in more extensive radial fracture, the effect being most pronounced for {111} single crystal silicon ( above  $\sim 300^\circ\text{C}$  ) and for SiC materials.  $\text{Si}_3\text{N}_4$ ,  $\text{B}_4\text{C}$  and sialon materials showed comparatively little increase in crack radius with increasing temperature. It was established that, in most cases, the effect was due to increases in crack-opening residual stresses caused by increasing amounts of plasticity ( reflected in a decrease in  $(E/H)$  ratio ) with increasing temperature. Applying

the results of currently-available indentation fracture mechanics analyses,  $K_{IC}$  values were calculated and found to be independent of temperature for most materials over the temperature range investigated, exceptions being (0001) single crystal SiC and sintered  $B_4C$ , for which  $K_{IC}$  was found to decrease with increasing temperature.  $K_{IC}$  values calculated from indentation fracture experiments were found to compare well with those reported in studies using more conventional mechanical tests.

Certain materials ( a hot-pressed  $Si_3N_4$  and a reaction-bonded SiC ) were found not to obey the theoretically predicted relationship  $P \propto c^{3/2}$  between crack size  $c$  and applied load  $P$ . For these materials, exponents greater than  $3/2$  were found, values increasing with increasing temperature. Cracks formed in these materials were not true radial cracks, but networks of cracks along weak microstructural paths ( e.g. grain or phase boundaries ).

Microstructural control of crack paths was investigated for each material and the effects of such behaviour on  $K_{IC}$  discussed. The toughest materials investigated here were found to be hot-pressed samples, despite ( or perhaps because of ) their high susceptibility to grain boundary fracture. Porous materials were found to be less tough than dense materials, although crack-pore interactions were common in the former. The least tough materials were found to be single crystals and coarse-grained materials, in which cracks propagated along preferred cleavage planes.

Lateral fracture was found to be favoured in single crystal and coarse-grained materials. Whilst increasing temperature promoted more extensive lateral cracking around Knoop indentations in (0001) single crystal SiC, lateral crack extents around Vickers indentations in {111} single crystal Si peaked at  $\sim 200^\circ C$ , decreasing to zero by  $\sim 400^\circ C$ . This latter effect was thought to be due to increases in lateral crack depth with increasing temperature, resulting in less frequent breakout to the specimen surface.

The relative resistance of a material to crack nucleation has been quantified in terms of  $P^*$ , the critical load required to form ( radial ) cracks around Vickers indentations. Theoretically,  $P^*$  is predicted to be a strong function of both  $H$  and  $K_{IC}$  since  $P^* \propto K_{IC}^4 / H^3$ , so materials with high toughness and low hardness should be less susceptible to crack nucleation. Thus, coarse-grained

materials and single crystals were predicted to show easy crack nucleation compared with fine-grained materials, especially hot-pressed samples.

The effect of increasing temperature should be to increase  $P^*$  (largely due to the decrease in  $H$ ), making crack nucleation more difficult, as observed in some materials (notably {111} silicon).

Corresponding to the critical load  $P^*$  is a critical flaw size  $c^*$  which describes the smallest flaw which may grow into a fully-developed crack. Since  $c^*$  was calculated to be less than the grain size for many of the materials investigated here, it is believed that cracks probably originated from microstructural flaws (e.g. weak grain boundaries) without the need for nucleation by plasticity mechanisms. For some materials, this might not have been the case, especially at high temperatures (since  $c^*$  is thought to vary as  $(K_{IC}/H)^2$ , which increases with increasing temperature), and further study is required to establish the nucleation mechanisms operating here.

### 7.3 SUGGESTIONS FOR FURTHER WORK

Listed below are a series of points for future investigation, based on observations or speculations contained in the present work. The list is by no means all-inclusive.

#### (a) Microstructural Examination of Indentation Plasticity

This is crucial to the further development of indentation plasticity theories, but is likely to be a highly difficult and controversial field of research. Use of high resolution techniques such as transmission electron microscopy (TEM) may not necessarily achieve the most useful results: previous TEM studies have been claimed to provide evidence for a variety of deformation mechanisms (see section 3.3.3) and it is difficult, if not impossible, to establish from post facto observations which were the most important mechanisms during the indentation test. It is suggested that a broad combination of techniques, including light microscopy, etching, cathodoluminescence, selected area electron channelling, X-ray topography, TEM and other techniques may be necessary for this study and that 'in situ' observations, where feasible, would be highly desirable. The investigation should aim to answer the following questions:

- How does the plastic zone size vary as a function of material and of temperature?
- What are the dominant deformation mechanisms ( as a function of material, temperature, etc. )?
- If slip is important, is it, for example, controlled by the Peierls' barrier or by strain-hardening effects ( in which case a correlation between hardness and stacking fault energy might be expected ) or by pinning effects or by cross-slip or climb?
- What are the slip systems and is the von Mises criterion satisfied?
- For polycrystalline materials, is there any evidence for dislocation pile-up at grain boundaries or for grain boundary separation?
- What is the precise mechanism for compaction of porous materials?

(b) Indentation Creep Experiments

As discussed in section 3.8, high-temperature indentation creep experiments are essential in order to determine reliable activation energies for the deformation mechanisms. Particular attention should be paid to the stress exponent for creep and to the effects of crystallographic orientation for single crystals ( section 3.8 ).

(c) Impurity Effects

The preliminary investigations described in section 3.5 could be extended to include both highly pure and more heavily doped materials, ideally with more accurately known dopant levels.

(d) Hardness Anisotropy Experiments as a Function of Temperature

Such techniques ( described in section 3.4 ) would provide valuable information concerning the dominant slip systems and their respective activation energies, etc. as a back-up to microstructural characterization of dislocation structures.

(e) Environmental Effects

Study of the effects of chemical environment on plasticity mechanisms would be very useful, both from a fundamental standpoint and from the practical one of predicting wear behaviour in typical operating environments.

(f) The Effects of Strain Rate

Dynamic hardness tests performed as a function of temperature

would provide a more reliable basis for predicting wear behaviour from the Archard equation or from indentation fracture mechanics formulations involving hardness ( section 6.5 ).

(g) Microstructural Investigation of Crack Nucleation Mechanisms

These are required to establish which ( if any ) of the proposed crack nucleation mechanisms ( such as growth from pre-existing flaws or nucleation by slip interaction ) actually occur in the materials studied here, and how the mechanisms are influenced by changing temperature, microstructure, etc.

(h) Subcritical Crack Growth Effects

These may be important in certain chemical environments and at high temperatures. Such effects could be investigated by measuring radial crack lengths as a function of time after indentation. If the rate of subcritical crack growth is high, this must be allowed for in determination of  $K_{IC}$  from crack length data.

(i) Friction Tests

Since the results obtained here provide no information about coefficients of friction ( section 6.5.1 ), independent friction tests as a function of temperature and specimen microstructure are required.

(j) Wear Tests

There is a great need for more wear test data in order to verify the theoretically-predicted correlations between wear rates and hardness, toughness and other parameters. This is especially true for wear in the plasticity-controlled regime. On a more fundamental level, investigations of how repeated asperity or particle contacts lead to strain accumulation in the surface of a brittle material are required before further theoretical advances may be made in the fields of delamination or surface fatigue wear. To this end, any or all of the techniques mentioned in point (a) may prove useful.

END

FILMED

1-84

DTIC